Compact-Size Wideband Antennas and Arrays for Wireless Communications

By

Lehu Wen

A Thesis Submitted to the University of Kent
For the Degree of Doctor of Philosophy
In Electronic Engineering

September 2020

Abstract

Polarization is an important parameter for characterizing antenna systems. Dual-polarized and circularly-polarized wideband antennas with compact size are very useful for mobile communications and satellite communications. Due to the multipath propagation and shadowing in urban environment, radio signals received by mobile terminals can become very weak. Dual-polarized antennas can achieve better signal quality in mobile communications by using polarization diversity. Wideband circularly polarized antennas are very important for mobile satellite communications as circularly polarized signals are immune to Faraday rotation effects. Circular polarization also enables mobile satellite communications without strict alignment between transmit and receive antennas. Therefore, dual-polarized antennas and circularly polarized antennas have been drawn increasing popularity in the wireless communication systems.

In this thesis, several novel designs of compact, wideband, and specially functioned antennas and arrays are developed for wireless communication applications. First, wideband antennas and arrays are investigated for base station applications with different appealing features, such as compact radiator size, enhanced upper out-of-band suppression, or low pattern sidelobes. They are designed with different novel design concept, such as shared-dipole, electromagnetic dipoles, shorted dipoles, and fourth-order coupling structure. Then, to directly match to the newly emerged differential circuit systems, several wideband differentially fed dual-polarized antennas are proposed for base station applications. They are designed for high common mode suppression, high harmonic suppression, or compact radiator size by using the idea of orthogonal six-port power divider, multi-resonance structure, and crossed open loop resonators. The final designs are two circularly polarized antennas, which have the wide overlapped impedance and axial ratio bandwidth, or dual circularly polarized radiations realized by using crossed open slot-pairs, orthogonal power diver, and phase shift unit cells.

The working principles of these different antennas are extensively illustrated with the relevant design theories and detailed structure studies. The performances of these antennas and arrays are evaluated first by the full-wave electromagnetics simulations, and followed by the measurements of the corresponding fabricated prototypes. Good agreements between the simulated and measured results are obtained. With these different features to accommodate different requirements, these antennas and arrays can be the good candidates for the wireless communication systems.

Acknowledgement

I am very appreciated for the sincere guidance, support and encouragement from my supervisor, Professor Steven Gao. In the past three years, he has provided me with warm and cozy research atmosphere, well-functioned hardware and software for my PhD study. Furthermore, he has given lots of professional and insightful guidance and comments, which encourage me enormously for my study at University of Kent. I have also learnt many social etiquettes and skills in communication with friends and colleagues, which will benefit me a lot in the future research career and life.

I also would like to express deep gratitude to my co-supervisor, Dr. Benito Sanz-Izquierdo. He helps me a lot in my PhD study. He has provided me a lot of supports and comments in the research and writing of professional papers.

I also would like to especially thank Dr. Qi Luo, the Research Fellow in our group, who impresses and helps me a lot for his professional guidance and many valuable comments in my PhD research life.

Also, many thanks to all my close team members, Qingling Yang, Rui Xu, Hang Xu, Wenting Li, Chao Gu, Chunxu Mao, etc., for their kind helps and suggestions in my PhD study life.

I would like to thank my parents, my wife, my family members, and all my friends for their kind support and accompany in the past few years. Their encouragements help me overcome all kinds of difficulties and finally complete my dissertation.

Finally, thanks very much to the following funding supports to help me finish the designs in this thesis. The works in the thesis were supported in part by China Research Institute of Radiowave Propagation, and in part by EPSRC grants EP/N032497/1, EP/S005625/1, and EP/P015840/1.

Contents

Abstract i

Acknowledgement ii

Contents iii

List of Symbols vi

List of Abbreviations vii

List of Figures viii

List of Tables xvi

Chapter 1. Introduction 1

1.1 Motivation 1

1.2 Main Contributions 2

1.3 Publications 3

1.4 Outline of the Thesis 4

Chapter 2. Literature Review 6

2.1 Introduction 6

2.2 Wideband Dual-Polarized Antennas 7

2.2.1 Wideband Dual-Polarized Patch Antennas 7

2.2.2 Wideband Dual-Polarized Slot Antennas 10

2.2.3 Wideband Dual-Polarized Dipole Antennas 12

2.3 Wideband Circularly Polarized Antennas 16

2.3.1 Wideband Circularly Polarized Patch Antennas 16

2.3.2 Wideband Circularly Polarized Slot Antennas 19

2.3.3 Wideband Circularly Polarized Dipole Antennas 20

2.4 Summary and Objectives 22

Chapter 3. Wideband and Compact Base Station Antennas 24

3.1 Introduction 24

3.2 Compact Dual-Polarized Shared-Dipole Antennas 25

3.2.1 Operation Principle 25

3.2.2 Design I: Four-Port DPSD Antenna 31
3.2.3 Design II: Highly Integrated DPSD Antenna 37
3.3 Dual-Polarized Antenna With Enhanced Upper Out-of-Band Suppression 41
3.3.1 Antenna Configuration 42
3.3.2 Working Principle 44
3.3.3 Results and Discussion 54
3.4 Wideband Dual-Polarized Antenna Using Shorted Dipoles 57
3.4.1 Antenna Configuration 57
3.4.2 Working Principle 59
3.4.3 Results and Discussion 63
3.5 Filtering Array Antenna With Low Sidelobes 65
3.5.1 Antenna Element Design 65
3.5.2 Array Design 72
3.5.3 Results and Discussion 74
3.6 Summary 77
Chapter 4. Wideband and Low-Profile Differentially Fed Antennas 78
4.1 Introduction 78
4.2 Wideband Antenna With High Common Mode Suppression 79
4.2.1 Antenna Configuration 79
4.2.2 Working Principle 81
4.2.3 Results and Discussion 88
4.3 Wideband Antenna With High Harmonic Suppression 91
4.3.1 Antenna Configuration 92
4.3.2 Working Principle 93
4.3.3 Results and Discussion 100
4.4 Low-Profile Differentially Fed Dual-Polarized Array Antenna 103
4.4.1 Antenna Element 104
4.4.2 Array Design 108
4.4.3 Results and Discussion 109

4.5 Summary 114
Chapter 5. Wideband Circularly Polarized Antennas 115
5.1 Introduction 115
5.2 Series-Fed Antenna Using Crossed Open Slot-Pairs 116
5.2.1 Design Principle 116
5.2.2 Antenna Design 122
5.2.3 Results and Discussion 128
5.3 Wideband Dual Circularly Polarized Antenna 132
5.3.1 Antenna Configuration 132
5.3.2 Working Principle 134
5.3.3 Results and Discussion 141
5.4 Summary 145
Chapter 6. Conclusion and Future Work 147
6.1 Conclusion 147
6.2 Future Work 148
References 150

List of Symbols

c	Velocity of light in vacuum
E	Electric field
f	Frequency
H	Magnetic field
H_i	Height of a structure
J	Surface electric current
j	Imaginary unit
L_i	Length of a structure
M	Magnetic current
M_{ij}	Coupling coefficient
m_{ij}	Normalized coupling coefficient
Q_e	External quality
S_a	Size of an aperture
S_{ddij}	Differentially driven S-parameters
S_{ij}	S-parameters
V	Voltage
W_i	Width of a structure
Z_{in}	Input impedance
α	Magnitude of the voltage source
β	Magnitude of the voltage source
Γ_{in}	Reflection coefficient
γ	Phase of the voltage source
$\Delta\omega$	Bandwidth of the angular frequency
ε_r	Relative permittivity
θ	Phase of the voltage source
λ	Wavelength
ϕ	Delayed phase
ω	Angular frequency

List of Abbreviations

AR	Axial Ratio
BW	Bandwidth
CD	Crossed Dipole
CM	Common Mode
Co-pol.	Co-polarization
CP	Circular Polarization
CPS	Coplanar Stripline
DCP	Dual Circular Polarization
DE	Differential Evolution
DM	Differential Mode
DPSD	Dual-Polarized Shared Dipole
FBW	Fractional Bandwidth
HPBW	Half-Power Beamwidth
LHCP	Left-Hand Circular Polarization
LH-TL	Left-Hand Transmission Line
MIMO	Multiple Input, Multiple Output
OPD	Orthogonal Power Divider
PTH	Plated Through Hole
RHCP	Right-Hand Circular Polarization
RH-TL	Right-Hand Transmission Line
RL	Return Loss
SLL	Side Lobe Level
VSWR	Voltage Standing Wave Ratio
XPD	Cross Polarization Discrimination
X-pol.	Cross-polarization

List of Figures

Figure 2.1 Dual-polarized quadruple L-probe single-element square patch antenna [8]..... 8
Figure 2.2 Geometry of the antenna element with dimensions in millimetres [11]. 9
Figure 2.3 Configuration of loop fed patch for single polarization, side view and top view (unit: mm) [14]. 9
Figure 2.4 Geometry of dual-polarized double tuned antenna. Unit: mm 10
Figure 2.5 Configuration and prototype of the proposed antenna [22]. 11
Figure 2.6 Geometry of the proposed dual-polarized antenna element. 13
Figure 2.7 (a) Geometry of antenna. (b) Baluns for different ports [38]. 14
Figure 2.8 Geometry of the proposed antenna [49]. 15
Figure 2.9 Configuration of the proposed differentially fed dual-polarized antenna [62].. 15
Figure 2.10 Wideband CP patch antenna presented in [71]. 17
Figure 2.11 Geometry of the proposed CP array antenna in [75]. 18
Figure 2.12 Configuration of the CP slot antenna presented in [85]. 19
Figure 2.13 Configuration of the CP dipole antenna presented in [90]. 20
Figure 2.14 Self-phased CP dipole antenna presented in [95]. 21
Figure 3.1 Different configurations for dual-polarized antenna. 26
Figure 3.2 Equivalent circuit for the DPSD antenna. 27
Figure 3.3 Four-port single-ended network with common mode excitation. 28
Figure 3.4 Models of simulated DPSD antenna. 29
Figure 3.5 (a) Input impedance of the DPSD antenna and the CD antenna. (b) H-plane radiation patterns of the DPSD antenna and CD antenna. 30
Figure 3.6 Simulated S-parameters of DPSD antenna. 30
Figure 3.7 Geometry of the four-port DPSD antenna. (a) 3D view. (b) Detailed configuration of radiator. (c) Side view. (Unit: mm) 31
Figure 3.8 Equivalent circuit model of the four-port DPSD Antenna. 32
Figure 3.9 Design steps of the four-port DPSD antenna. (a) With ideal lumped port feed. (b) With CPS feed. (c) With balun feed. 32
Figure 3.10 Simulated S-parameters of the four-port DPSD antenna with different feed methods. 33
Figure 3.11 Photographs of the fabricated four-port DPSD antenna without feed network. (a) Top view. (b) Side view. 34

Figure 3.12 Simulated and measured S-parameters for the four-port DPSD antenna. 34
Figure 3.13 The calculated VSWR and isolation by the simulated and measured results for the four-port DPSD antenna without feed network..... 34
Figure 3.14 Photographs of the fabricated four-port DPSD antenna with the feed network. 35
Figure 3.15 Simulated and measured results for the four-port DPSD antenna with the feed network. 35
Figure 3.16 Simulated and measured radiation patterns of the four-port DPSD antenna with the feed network for the H-plane when the feed point 1 excited. (a) 1.7 GHz. (b) 2.2 GHz. (c) 2.7 GHz. 36
Figure 3.17 Simulated and measured gain and HPBW for H-plane when the feed point 1 excited..... 36
Figure 3.18 Geometry of the highly integrated DPSD Antenna. (a) 3D view. (b) Top view of the radiator. (Unit: mm)..... 37
Figure 3.19 Equivalent circuit of highly integrated DPSD antenna. 38
Figure 3.20 Photograph of the fabricated highly integrated DPSD antenna. 39
Figure 3.21 Simulated and measured results for the highly integrated DPSD antenna. 39
Figure 3.22 Simulated and measured radiation patterns of the highly integrated DPSD antenna for the H-plane with the feed point 1 excited. (a) 1.7 GHz. (b) 2.2 GHz. (c) 2.7 GHz..... 39
Figure 3.23 Simulated and measured gain and HPBW of the highly integrated DPSD antenna for H-plane with the feed point 1 excited. 40
Figure 3.24 Equivalent electric dipole and magnetic dipole configurations. (a) Reference [102]. (b) Reference [49]. (c) Proposed antenna..... 41
Figure 3.25 Configuration of the proposed dual-polarized antenna. 43
Figure 3.26 Simulation models of the dual-polarized antenna and single-polarized antenna. (a) Antenna 1. (b) Antenna 2. 44
Figure 3.27 Simulated results of the reference Antenna 1 and Antenna 2. (a) S-parameters. (b) Input impedances. 45
Figure 3.28 Current distributions on the surface of the two antennas: 47
Figure 3.29 Simulation model and results of reference Antenna 3. 48
Figure 3.30 Current distributions on the surface of Antenna 3 at different frequencies..... 49

Figure 3.31 Simulated S_{11} and peak realized gain of Antenna 3. (a) With different length of the parasitic strip (L2). (b) With different distance between the parasitic strip and the inner edge of the loop (d2)..... 50
Figure 3.32 Configurations of the feed structures for the proposed antenna. (a) With coaxial balun. (b) With the only coaxial cable. 51
Figure 3.33 Simulated S-parameters with different feed structures. 51
Figure 3.34 Simulated results of the proposed antenna. (a) Input impedances of the proposed antenna with and without the shorting sheet. (b)S_{11} and peak realized gain with different height of the shorting sheet. 53
Figure 3.35 Current distribution on the surface of the outer conductors for the proposed crossed coaxial baluns at 4.9 GHz. 53
Figure 3.36 Photograph of the fabricated prototype of the proposed dual-polarized antenna. 54
Figure 3.37 Measured and simulated S-parameters of the proposed dual-polarized antenna. 54
Figure 3.38 Measured and simulated H-plane radiation patterns of the proposed dual-polarized antenna when port 1 is excited. (a) 1.7 GHz. (b) 2.2 GHz. (c) 2.7 GHz. (d) 3.0 GHz..... 55
Figure 3.39 Measured and simulated HPBW and peak realized gain of the proposed dual-polarized antenna when port 1 is excited..... 56
Figure 3.40 The configuration of the proposed antenna. (a) Isometric view of the antenna. (b) Bottom layer of the antenna substrate. (c) Top layer of the antenna substrate. (d) Side view of the antenna..... 58
Figure 3.41 Equivalent circuit of the proposed antenna for one polarization. 60
Figure 3.42 (a) Input impedance of Z_{in} for equation (3). (b) Simulated input impedance of antenna port 1..... 61
Figure 3.43 Design flow of the proposed dual-polarized antenna..... 61
Figure 3.44 Simulated S_{11} for the evolution antennas. 62
Figure 3.45 Prototype of the fabricated dual-polarized antenna. (a) Photograph of the proposed antenna. (b) Antenna under measurement in the anechoic chamber..... 62
Figure 3.46 Measured and simulated (a) VSWR and (b) isolation of the proposed antenna. 63
Figure 3.47 Measured and simulated normalized radiation patterns of the proposed antenna. (a) 1.7 GHz. (b) 2.7 GHz. (c) 3.6 GHz..... 63

Figure 3.48 Measured and simulated antenna gain and HPBW. 64
Figure 3.49 Configuration of the proposed antenna. 66
Figure 3.50 Coupling structure of the proposed antenna. 67
Figure 3.51 Current distribution on the surface of the resonators. 68
Figure 3.52 (a) Filtering response for the proposed coupling structure. (b) Filtering response with varying cross coupling coefficient. 69
Figure 3.53 Simulated realized gain varies (a) with and without the short slot, (b) with different L2. 70
Figure 3.54 Comparison of S_{11} and peak realized gain between the reference antenna and the proposed antenna. 71
Figure 3.55 Radiation patterns of the reference antenna and the proposed antenna. (a) Co-polarization. (b) Cross-polarization..... 72
Figure 3.56 Configuration of the proposed antenna array. (a) Radiating patch. (b) Ground plane. (c) Feed network. 73
Figure 3.57 S-parameters of the simulated unequal feed network. (b). Radiation patterns of calculated and simulated results..... 74
Figure 3.58 Fabricated antenna element. (a) Top view. (b) Back view. 75
Figure 3.59 Simulated and measured results of S_{11} and peak realized gain for the proposed antenna element..... 75
Figure 3.60 Fabricated antenna array. (a) Top view. (b) Back view. 76
Figure 3.61 Simulated and measured results of S_{11} and peak realized gain for the proposed antenna array. 76
Figure 3.62 Simulated and measured antenna array radiation patterns at 5 GHz. (a) E-plane. (b) H-plane..... 77
Figure 4.1 Configuration of the proposed differentially fed dual-polarized antenna. 80
Figure 4.2 Equivalent circuit of the proposed antenna. 81
Figure 4.3 Current distribution of the proposed antenna at 2.2 GHz when the differential port d1 is excited. 82
Figure 4.4 Simulation model of the six-port power divider. 83
Figure 4.5 Simulated S-parameters of the extracted six-port splitter. (a) Magnitude. (b) Phase..... 83
Figure 4.6 Transmission line equivalent circuit of the six-port power divider. 84

Figure 4.7 Even mode analysis of the transmission line equivalent circuit for the six-port power divider when port 1 is excited. (a) Symmetric forms of port 1 and port 2. (b) Simplified even mode excited equivalent circuit. 85
Figure 4.8 Odd mode analysis of the transmission line equivalent circuit for the six-port power divider when port 1 is excited. (a) Symmetric forms of port 1 and port 2. (b) Simplified odd mode excited equivalent circuit. 86
Figure 4.9 Current distributions on surface of the six-port power divider. (a) Odd mode excitation at port 1. (b) Even mode excitation at port 1. 87
Figure 4.10 Simulated differentially driven and commonly driven S-parameters of the antenna. 87
Figure 4.11 Photograph of the fabricated prototype of the proposed differentially driven dual-polarized antenna. 88
Figure 4.12 Measured and simulated S-parameters of the fabricated differentially driven dual-polarized antenna. 89
Figure 4.13 Measured and simulated H-plane radiation patterns of the fabricated antenna when differentially driven port d1 is excited at different frequencies. (a) 1.7 GHz. (b) 2.2 GHz. (c) 2.7 GHz. (d) 3.0 GHz. 90
Figure 4.14 Measured and simulated peak realized gains and HPBWs of the fabricated antenna. 90
Figure 4.15 Configuration of the proposed dual-polarized antenna. 93
Figure 4.16 Evolution process of the proposed differentially fed dual-polarized antenna. (a) Ant. 1. (b) Ant. 2. (c) Proposed antenna. 94
Figure 4.17 Simulated results of the antennas in the evolution process. (a) Radiation patterns at 2.2 GHz in V-plane. (b) S-parameters. 94
Figure 4.18 Simulated reflection coefficient of the simplified reference antenna (Ant. 3). 95
Figure 4.19 Current distributions of Ant. 3 at different resonant frequencies of the reference antenna. (a) 2.68 GHz. (b) 2.18 GHz. (c) 1.72 GHz. 96
Figure 4.20 Parameters study of the different resonances of the reference antenna. 97
Figure 4.21 Study of the effect of the shorted microstrip lines on the performance of the impedance bandwidth for Ant. 3. 98
Figure 4.22 Configuration of the stepped impedance resonator based lowpass filter. 99
Figure 4.23 Filter response of the stepped impedance resonator based lowpass filter. 99
Figure 4.24 Simulated reflection coefficients and peak realized gains of the proposed antenna and Ant. 3. 100

Figure 4.25 Measured and simulated S-parameters of the proposed differentially fed dual-polarized antenna. 101
Figure 4.26 Measured and simulated normalized radiation patterns of the proposed antenna in H-plane when differential port d1 is excited. 101
Figure 4.27 Measured and simulated HPBW and peak realized gain of the proposed differentially fed dual-polarized antenna. 101
Figure 4.28 Configuration of the proposed dual-polarized antenna. 104
Figure 4.29 Coupling structure of the proposed antenna for one polarization. 105
Figure 4.30 Double loaded open loop resonator for one polarization. 106
Figure 4.31 Surface current distribution on the open loop resonators. 106
Figure 4.32 Simulated S-parameters between the single-ended and differentially driven dual-polarized antenna. 107
Figure 4.33 Simulated normalized H-plane radiation patterns for the single-ended and differentially driven dual-polarized antenna. 107
Figure 4.34 Comparison between the traditional capacitively coupled antenna and the proposed antenna. 108
Figure 4.35 (a) Configuration of the dual-polarized antenna array for base station ±45° polarizations. (b) The simulated reflection coefficients before and after optimization. 109
Figure 4.36 Photographs of the fabricated dual-polarized antenna prototype. (a) Top view. (b) Inside view of the intersected open loop resonators. 110
Figure 4.37 Measured and simulated S-parameters of the fabricated antenna element.... 110
Figure 4.38 Simulated and measured H-plane radiation patterns when differential port d1 is excited. (a) 3.2 GHz. (b) 3.7 GHz. 110
Figure 4.39 Photographs of (a) the fabricated 1×4 antenna array, (b) the fabricated out-of-phase power divider, and (c) the hardware platform for beam scanning performance. 111
Figure 4.40 Measured S-parameters of the four antenna elements in the fabricated 1×4 antenna array. 111
Figure 4.41 Simulated and measured radiation patterns when the differential port d1 is excited for the fabricated antenna array. (a) 3.3 GHz. (b) 3.6 GHz. 112
Figure 4.42 Measured radiation patterns with the scan angles of -20°, 0°, and +20°. (a) 3.3 GHz. (b) 3.6 GHz. 113

Figure 5.1 Configuration of the proposed four closely spaced, orthogonal arranged crossed open slot-pairs. 117
Figure 5.2 Simulated near-field distribution of the antenna when the slot-pair of slot 1 and slot 3 is excited. 118
Figure 5.3 Active input impedance of the crossed slot-pairs excited with equal magnitude and quadrature phase signals varies with different (a) Ws0 and (b) Lf0. 119
Figure 5.4 Configuration of the proposed half-power phase shifter. 120
Figure 5.5 Equivalent circuit of the proposed half-power phase shifter. 120
Figure 5.6 Calculated frequency response of the equivalent circuit for the proposed phase shifter compared to the traditional microstrip phase delay line. 121
Figure 5.7 (a) EM simulated transmission magnitude and phase of the proposed half-power phase shifter compared to the calculated results. (b) Simulated transmission magnitude and phase of the proposed half-power phase shifter vary with different feed positions Lf1. 122
Figure 5.8 Configuration of the proposed differentially fed CP antenna. 123
Figure 5.9 Equivalent circuit of the proposed differentially fed CP antenna. 124
Figure 5.10 Evolution of the proposed CP antenna. 125
Figure 5.11 (a) Input impedances of Antenna 1 and Antenna 2. (b) Input impedances of Antenna 3 and the proposed antenna. (c) S-parameters and axial ratios of Antenna 3 and the proposed antenna. 126
Figure 5.12 Comparison to the traditionally designed CP counterpart (Antenna 4). 127
Figure 5.13 Photographs of (a) the fabricated prototype of the proposed differentially fed CP antenna and (b) the prototype under radiation pattern test. 128
Figure 5.14 Measured and simulated S-parameters and axial ratios of the proposed differentially fed CP antenna. 129
Figure 5.15 Measured and simulated peak realized gain of the proposed differentially fed CP antenna. 129
Figure 5.16 Measured and simulated normalized radiation patterns of the proposed CP antenna in xz-plane and yz-plane at (a) 2 GHz, (b) 2.7 GHz, and (c) 3.4 GHz. 130
Figure 5.17 Detailed configuration of the proposed DCP antenna. 134
Figure 5.18 Equivalent circuit of the proposed DCP antenna. (PSs: phase shifters) 134
Figure 5.19 Surface current distributions of the proposed antenna at different times of the oscillation period when (a) port 1 is excited and (b) port 2 is excited. 135

Figure 5.20 (a) Simulation model of the OPD. (b) Current distribution on the surface of the OPD when port 1 is excited. (c) Equivalent circuit of the OPD. (d) Simplified equivalent circuit of the OPD when port 1 is excited. 136
Figure 5.21 Simulated results of the OPD. (a) Simulated S-parameters. (b) Transmission phase from port 1. (c) Transmission phase from port 2. 138
Figure 5.22 (a) T-type RH-TL unit cell and T-type LH-TL unit cell. (b) Phase response of the two unit cells. (c) Phase difference between the two unit cells..... 139
Figure 5.23 The integrated feed network incorporating with OPD and ±45° phase shifters. 140
Figure 5.24 Photographs of the fabricated prototype of the proposed DCP antenna. (a) 3D view. (b) Top view. 142
Figure 5.25 Measured and simulated S-parameters of the proposed DCP antenna..... 142
Figure 5.26 Measured and simulated (a) axial ratio, peak realized gain, and (b) radiation efficiency of the fabricated prototype when RHCP radiation (port 1) is excited. 143
Figure 5.27 Measured and simulated normalized radiation patterns at (a) 1.1 GHz and (b) 1.7 GHz when RHCP radiation (port 1) is excited. LHCP radiation is the cross-polarization. 144

List of Tables

Table 2.1 Comparisons of the patch antennas 10
Table 2.2 Comparisons of the slot antennas 11
Table 2.3 Comparisons of the dipole antennas 16
Table 2.4 Performance comparison between the CP patch antennas 18
Table 2.5 Performance comparison between the CP slot antennas. 20
Table 2.6 Performance comparison between the CP dipole antennas. 22
Table 3.1 Comparison of the dual-polarized antennas for base stations 40
Table 3.2 Comparison of the dual-polarized antennas for base stations 56
Table 3.3 Dimensions of the proposed antenna (mm) 59
Table 3.4 Comparison of the dual-polarized antennas for base station applications. 64
Table 3.5 Optimized magnitude distribution for each array element 73
Table 4.1 Comparison of the recently published differentially driven antennas 91
Table 4.2 Comparison of the reference antennas 102
Table 4.3 Comparison of the reference antennas 113
Table 5.1 Comparison of the recently published CP antennas 131
Table 5.2 Comparison of the recently published DCP antennas 145

Chapter 1. Introduction

1.1 Motivation

With the rapid development of wireless communication systems, dual-polarized antennas are widely adopted owing to their advantages of the reduced multi-path fading effect and increased channel capacity [1]-[2]. Dual-polarized antennas have been widely applied in radars, satellites and mobile base station communication systems. These systems usually require dual-polarized antennas with wide impedance bandwidth and high port isolation. Antennas for mobile base station communication systems have other critical specifications, such as the stable antenna gain and half-power beamwidth (HPBW) over a wide frequency band. With the emergence of the newly developed wireless communication systems such as the 5G wireless communication system and others, it is important to investigate novel designs with high-performance antennas, including multi-polarization, wide bandwidth, stable antenna gain, stable HPBW, and compact size [3].

With the development of base station systems, many 5G frequency bands have been licensed in many countries. The possible two sub-6 GHz frequency bands, which are 3.4-3.6 GHz and 4.8-5 GHz, could produce interferences to the current 2G/3G/4G base station systems. Therefore, the newly introduced 5G antennas will lead to the more limited space for base station antennas. So it is necessary to develop compact antennas with high suppression at the interference bands for the current 2G/3G/4G/5G base station applications.

In addition, compared to the dual-polarized antennas, circularly polarized (CP) antennas have also been drawn increasing popularity in wireless communication systems, such as satellites, radars, and global positioning systems. Compared to linearly polarized antennas, CP antennas have the advantages of reduced multipath effect and flexible orientation angle between the receiving and transmitting antennas [4]. In addition to the traditional bandwidth requirements like the linearly polarized antennas, such as the impedance bandwidth, gain, beamwidth, etc., axial ratio is a unique specification for CP antennas, which usually limits the available bandwidth of the CP antennas. Recently, with both right-hand circularly polarized and left-hand circularly polarized radiations, the dual circularly polarized antennas are widely reported owing to the advantages of the polarization diversity and frequency reusability. By using the dual circularly polarized antennas, the channel capacity and receiver sensitivity in the wireless communication systems can be greatly enhanced.

In view of the above advantages of dual-polarized and circularly polarized antennas, this thesis mainly focuses on the novel design methods of realizing dual-polarized and circularly

polarized antennas. Based on the requirements of compact size, wide bandwidth, harmonic suppression, filtering response, and common-mode suppression required in the different wireless communication systems, several novel antennas are presented and developed with different especially accustomed performances.

1.2 Main Contributions

The main contributions in this thesis are listed as follows.

1. Wideband and compact base station antennas.
   - A novel design concept of dual-polarized shared-dipole (DPSD) antenna is presented. The arms of the DPSD antenna are shared for two orthogonal polarizations. This design technique has the advantages of significant size reduction and high isolation compared to the traditional crossed dipole antennas.
   - A compact wideband dual-polarized antenna with enhanced upper out-of-band suppression is presented. This antenna is equivalent as two electric dipoles and two magnetic dipoles with wide impedance bandwidth and compact radiator size. In addition, four parasitic strips and a shorting sheet are introduced to achieve the high upper out-of-band suppression.
   - A novel design method of wideband dual-polarized antenna is presented by using shorted dipoles, integrated baluns, and crossed feed lines. The presented antenna achieves wide impedance bandwidth, high port isolation, stable antenna gain, and stable HPBW with a simple structure and compact size.
   - A fourth-order filtering patch antenna with a novel coupling structure is presented. Two identical slots etched on the ground plane are utilized to excite the radiating patch with reduced cross-polarization level. A short slot etched on the ground is employed for cross coupling, which introduces two controllable radiation nulls with steep roll-off rate.
2. Wideband and low-profile differentially fed antennas
   - A new method to design wideband differentially driven dual-polarized antenna with high common mode suppression and high port isolation is presented. Based on the wideband and high even mode suppressed six-port power divider, a wideband differentially driven dual-polarized antenna is developed with high common mode suppression.

- A wideband differentially fed dual-polarized antenna with wideband harmonic suppression is presented. Eight open slots, stair-shaped strips, and the centre patch are used to produce multi-resonance, symmetrical radiation, and low cross-polarization. Compact stepped impedance resonators are introduced to achieve wideband harmonic suppression.
- A novel differentially driven dual-polarized patch antenna is presented. The antenna is composed of two intersected open loop resonators. With the even and odd mode current distributions on the intersected resonators, high port isolation and low cross-polarization level are obtained.

3. Wideband circularly polarized antennas

- A novel method of designing a wideband series-fed CP differential antenna by using crossed open slot-pairs is presented. A wideband half-power phase shifter using open slot-pair is proposed and utilized to realize CP radiation.
- A wideband DCP antenna is presented. The orthogonal power divider has two orthogonal inputs and four equal magnitude in-phase and out-of-phase outputs. The lumped element based right-hand transmission line unit cell and left-hand transmission line unit cell are elaborately introduced as the ±45° phase shifters to realize quadrature feed network.

1.3 Publications

Journals

1. L. Wen, S. Gao, Q. Luo, W. Hu, and Y. Yin, "Wideband dual circularly polarized antenna for intelligent transport systems," *IEEE Trans. Veh. Technol.*, vol. 69, no. 5, pp. 5193-5202, May 2020.

2. L. Wen, S. Gao, Q. Luo, Q. Yang, W. Hu, Y. Yin, J. Wu, and X. Ren, "A wideband series-fed circularly polarized differential antenna by using crossed open slot-pairs," *IEEE Trans. Antennas Propag.*, vol. 68, no. 4, pp. 2565-2574, April 2020.

3. L. Wen, S. Gao, Q. Luo, W. Hu, Q. Yang, Y. Yin, X. Ren, and J. Wu, "A wideband differentially driven dual-polarized antenna by using integrated six-port power divider," *IEEE Trans. Antennas Propag.*, vol. 67, no. 12, pp. 7252-7260, Dec. 2019.

4. L. Wen, S. Gao, Q. Luo, Q. Yang, W. Hu, Y. Yin, X. Ren, and J. Wu, "A wideband differentially fed dual-polarized antenna with wideband harmonic suppression," *IEEE Trans. Antennas Propag.*, vol. 67, no. 9, pp. 6176-6181, Sept. 2019.

5. L. Wen, S. Gao, Q. Luo, Q. Yang, W. Hu, Y. Yin, X. Ren, and J. Wu, "A compact wideband dual-polarized antenna with enhanced upper out-of-band suppression," *IEEE Trans. Antennas Propag.*, vol. 67, no. 8, pp. 5194-5202, Aug. 2019.

6. L. Wen, S. Gao, Q. Luo, Q. Yang, W. Hu, and Y. Yin, "A low-cost differentially driven dual-polarized patch antenna by using open-loop resonators," *IEEE Trans. Antennas Propag.*, vol. 67, no. 4, pp. 2745-2750, April 2019.

7. L. Wen, S. Gao, Q. Luo, C. Mao, W. Hu, Y. Yin, Y. Zhou, and Q. Wang, "Compact dual-polarized shared-dipole antennas for base station applications," *IEEE Trans. Antennas Propag.*, vol. 66, no. 12, pp. 6826-6834, Dec. 2018.

8. L. Wen, S. Gao, C. Mao, Q. Luo, W. Hu, Y. Yin, and X. Yang, "A balanced feed filtering antenna with novel coupling structure for low-sidelobe radar applications," *IEEE Access*, vol. 6, pp. 77169-77178, 2018.

9. L. Wen, S. Gao, Q. Luo, Z. Tang, W. Hu, Y. Yin, Y. Geng, and Z. Cheng, "A wideband dual-polarized antenna using shorted dipoles," *IEEE Access*, vol. 6, pp. 39725-39733, 2018.

Conferences

1. L. Wen, S. Gao, Q. Yang, Q. Luo, Y. Yin, X. Ren, and J. Wu, "A compact monopole antenna with filtering response for WLAN applications," *2019 International Symposium on Antennas and Propagation (ISAP 2019)*, Xi'an, China, 2019, pp. 1-3. (Best Student Paper Award)

2. L. Wen, S. Gao, Q. Yang, Q. Luo, X. Ren and J. Wu, "A compact dual-polarized patch antenna loaded with metamaterial unit cell for broadband wireless communication," *2019 IEEE MTT-S International Wireless Symposium (IWS 2019)*, Guangzhou, China, 2019, pp. 1-3. (Finalist in the competition of FLASH AWARD)

3. L. Wen, S. Gao, Q. Luo, Q. Yang, and Y. Yin, "A compact and wideband dual-polarized antenna using folded loops," *Loughborough Antennas Propag. Conf. (LAPC 2018)*, Loughborough, 2018, pp. 1-4.

1.4 Outline of the Thesis

This thesis is organized as follows.

Chapter 1 briefly introduces the motivation and the main technical contributions in the PhD research. Then, the relevant publications on these researches are summarized.

Chapter 2 gives a brief introduction of my research background. Then, it is followed by the detailed state-of-art literature review on the wideband dual-polarized antennas and circularly polarized antennas for wireless communication systems. Based on these literature review, different kinds of dual-polarized antennas and circularly polarized antennas are developed. Finally, a summary and the research objectives are given for this thesis.

Chapter 3 presents several designs on the wideband and compact antennas for base station applications, which have different improved performances, such as the compact size, enhanced upper out-of-band suppression, stable beamwidth, filtering property, etc. The detailed design principles and studies are illustrated in this chapter. These antennas were fabricated and measured for the performance verification.

Chapter 4 illustrates three wideband and low-profile differentially fed dual-polarized antennas, which are designed directly for the newly emerged differential circuit systems. The first design has the high common mode suppression by using a high even mode suppressed six-port power divider. The second design features the high harmonic suppression owing to the introduced stepped impedance resonators. The final design is a low-profile patch antenna using crossed open loop resonators.

Chapter 5 presents two wideband circularly polarized antennas. The first one utilizes a wideband half-power phase shifter to realize wideband CP radiation. The second design is a wideband dual circularly polarized antenna. The orthogonal power divider and the lumped element based right-hand transmission line unit cell and left-hand transmission line unit cell are elaborately utilized for the wideband DCP radiation.

Chapter 6 gives the conclusion of this thesis, and discusses the work in future research.

Chapter 2. Literature Review

2.1 Introduction

In this chapter, both dual-polarized antennas and circularly polarized antennas are extensively reviewed. These antennas will be classified into three different types according to the different radiating mechanisms, including the patches, slots, dipoles working as different main radiators. Each type of antennas have different features, and the typical antennas will be illustrated with figures in each section. Comparison tables will also be given for different types of antennas for detailed performance illustration.

Patch antenna can be a good choice for low-profile configuration but with relatively narrow impedance bandwidth due to the high-Q resonance of the patch. One can simply increase the thickness of the substrate, or change the direct probe feed into capacitive feed or aperture feed to broaden the impedance bandwidth. However, this will increase the design complexity and fabrication cost of the antenna. Usually, a single-layer patch antenna has a narrow bandwidth of a few percentages only. It is possible to increase the bandwidth of patch antenna using multiple layers or other techniques, but it is challenging to achieve dual-polarized patch antennas with compact size, high polarization purity, stable radiation patterns and high isolation over a very wide frequency range.

Slot antenna can achieve very wide impedance bandwidth of more than 100% both for dual-polarization or circular polarization owing to the multi-resonance on the slot radiator. However, the slot antenna has the instable radiation characteristic due to the multi-resonance on the slot, which causes different radiation patterns varying with the frequencies. Another unappealing feature is the radiation pattern of the slot antenna is quasi-omnidirectional or bidirectional. To obtain high and unidirectional radiation patterns, the bandwidth will be significantly affected by the backed reflectors or the cavities.

Dipole antenna can be a good compromise between the patch antenna and slot antenna. It can have a stable radiation characteristic over a wide frequency bandwidth. To realize unidirectional radiation, planar reflectors or cavities can be used with the impedance bandwidth of around 50% for both dual-polarized and circularly polarized radiations. Because of the stable radiation characteristic, dipole antennas are always used in the applications such as base stations, satellites, radio frequency identifications, radars, navigations, etc.

These different kinds of antennas for dual-polarized and circularly polarized radiations are intensively discussed and compared according to their different working mechanisms.

Based on these reviewed dual-polarized and circularly polarized antennas, several works of proposed novel dual-polarized antennas and circularly polarized antennas for wireless communication systems will be started in this thesis.

2.2 Wideband Dual-Polarized Antennas

This section will review recent development of wideband dual-polarized unidirectional antennas for wireless communication systems. First, wideband dual-polarized patch antennas are discussed with different feed methods. Then, as a different radiation type, wideband dual-polarized slot antennas are illustrated. Finally, the most widely used wideband dipole antennas are investigated including the printed dipole antennas, folded dipole antennas, magneto-electric dipoles and differentially excited dipoles.

2.2.1 Wideband Dual-Polarized Patch Antennas

Patches are good choices to excite two ideal orthogonal modes to realize dual-polarization. At the beginning of the 2G/3G mobile communication systems, patch antennas play an important role owing to their low profile and low manufacturing cost. By using of different feeding methods and multi-layer technology, patch antennas can be easily designed to apply in base station dual-polarization circumstances.

Patch antennas using direct probes feeding methods [5]-[6] can get wideband operation bandwidth. Fed by two orthogonal meandering probes, the patch antenna in [5] achieves an impedance bandwidth of 26% for VSWR<2 at each input port. By adjusting the meandering probes location appropriately, the antenna has an isolation of more than 25 dB, which can be further enhanced to 30 dB by surrounding the antenna with vertical metallic walls. The meandering probes fed dual-polarized patch antenna in [6] has a low profile with the height of $0.109\lambda_0$. By surrounding the antenna with vertical walls, the antenna can obtain the gain of 9-10 dBi for GSM1800 (1.71-1.88 GHz) and CDMA1900 (1.85-1.99 GHz) base stations.

By using coupling methods, patch antennas can obtain more broadband bandwidth [7-16] compared to the direct probe feed method. Also the coupling method can be multifaceted, it can be realized by proximate coupling L-shaped stubs [7-10], coupling apertures [11-12], or recent popular electromagnetic feed [13-16]. An L-probe coupling antenna [8] is shown in Figure 2.1, which is composed of four quadruple L-probes and a square patch. By means of a pair of novel 180° broadband microstrip baluns, the antenna achieves improved isolation and better cross-polarization suppression over a wider bandwidth. Measured results show

that the impedance bandwidth is from 1.7 GHz to 2.2 GHz for VSWR<2 with its port isolation higher than 30 dB.

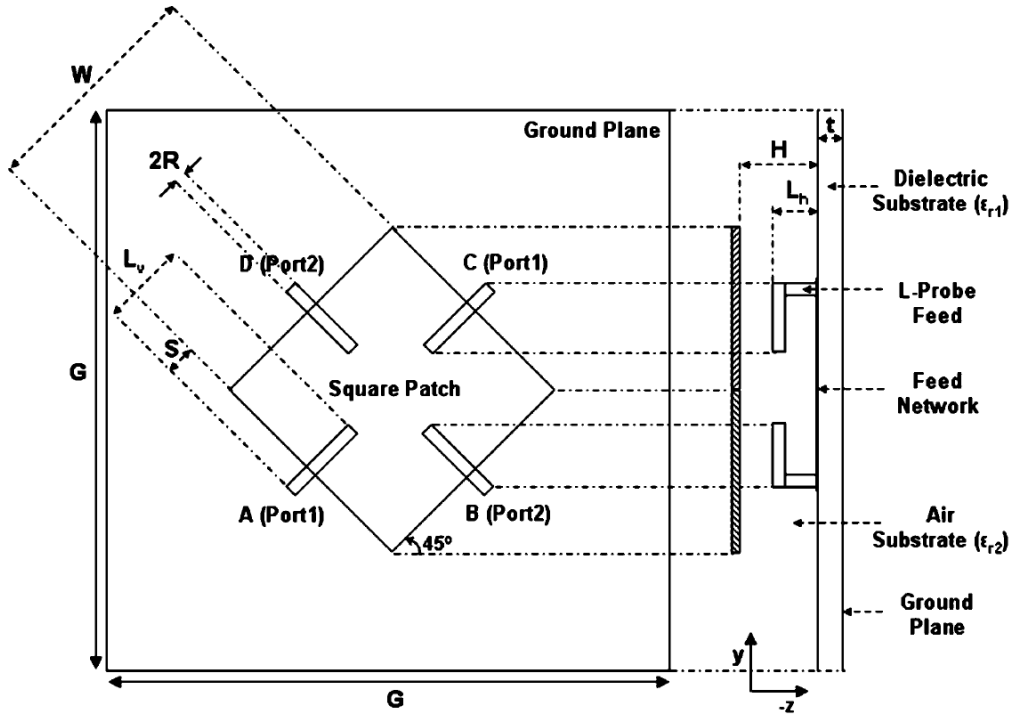

Figure 2.1 Dual-polarized quadruple L-probe single-element square patch antenna [8].

The slot coupled dual-polarized antenna in [11] consists of two printed circuit boards, a copper plate, and 12 copper pillars, which is shown in Figure 2.2. A cross slot is etched on the ground plane to couple the feeding energy to the patch. Two microstrip feeding lines are printed on the top layer of the feeding substrate to achieve the dual-polarized radiation. The measured impedance bandwidth with VSWR<2 is from 1.69 GHz to 2.21 GHz, and ports isolation within the frequency band is higher than 25 dB. The method of adding copper pillars is proposed to mitigate the influence of the ground plane and get the good radiation patterns.

The magnetic loop feeding method was first designed by J.-J. Xie [13], and then it was developed by many researchers [14-16], which is very efficient to enhance the antenna bandwidth and isolation. In [14], the magnetic loop feed method is demonstrated by a single-polarized antenna, as is shown in Figure 2.3, which covers the base station bandwidth (1710-2170 MHz) with S_{11}<-15 dB. Then, a dual-polarized antenna is proposed by placing another magnetic loop to feed the other linear polarization. In Figure 2.4, each polarization has two loops for convenient integration of two orthogonal printed circuit boards. In addition, slight differences between the two boards make them to cross each other and support the radiating

patch. Measured results showed that both ports cover the frequency band of 1700-2200 MHz with reflection loss better than 15 dB and isolation better than 30 dB.

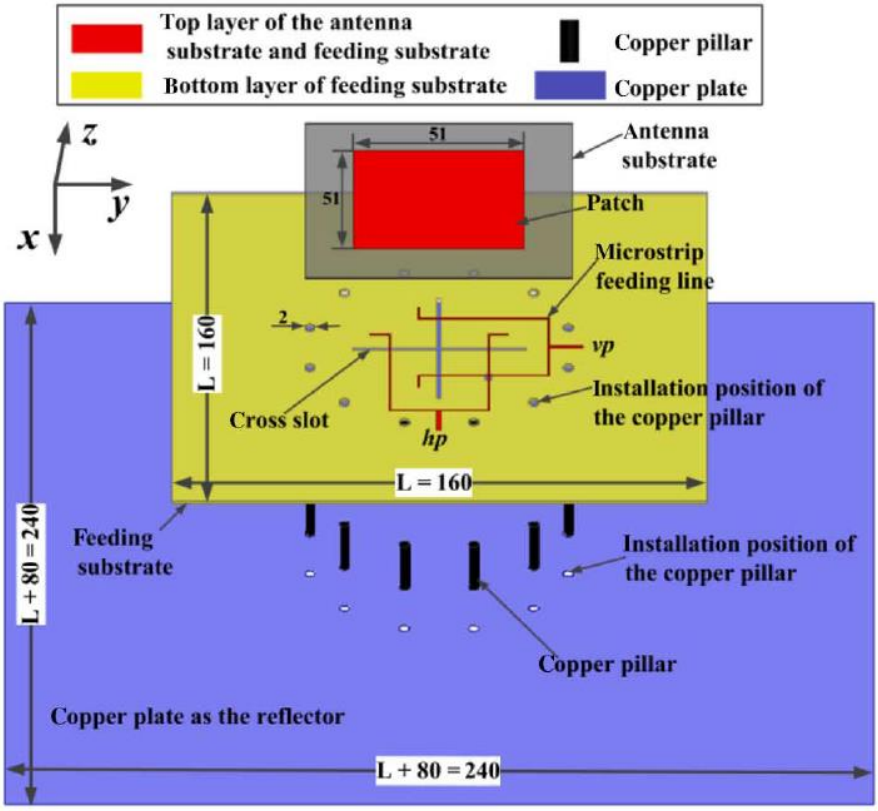

Figure 2.2 Geometry of the antenna element with dimensions in millimetres [11].

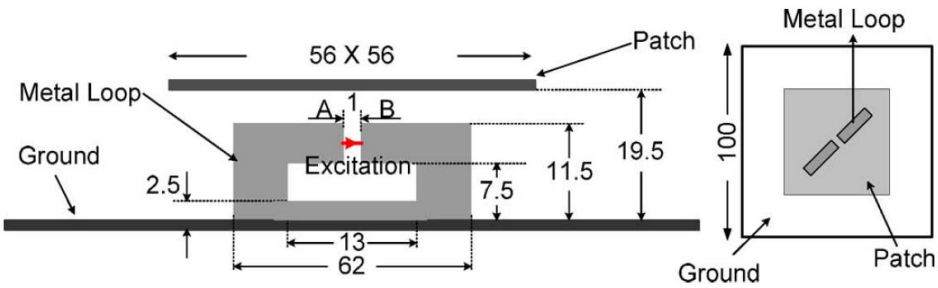

Figure 2.3 Configuration of loop fed patch for single polarization, side view and top view (unit: mm) [14].

There are also mixed feed methods to excite the patch antenna for orthogonal dual linear polarizations [17-18]. Any feeding methods of mentioned above can be utilized to design dual-polarized antennas, like L-stub coupling, direct probe feeding, proximate or aperture coupling methods, etc. However, because of the different feeding mechanisms, different port impedance response characteristics may be obtained. Sometimes, they can get different bandwidths for each polarization, and there will be a trade-off between the bandwidths of two orthogonal ports.

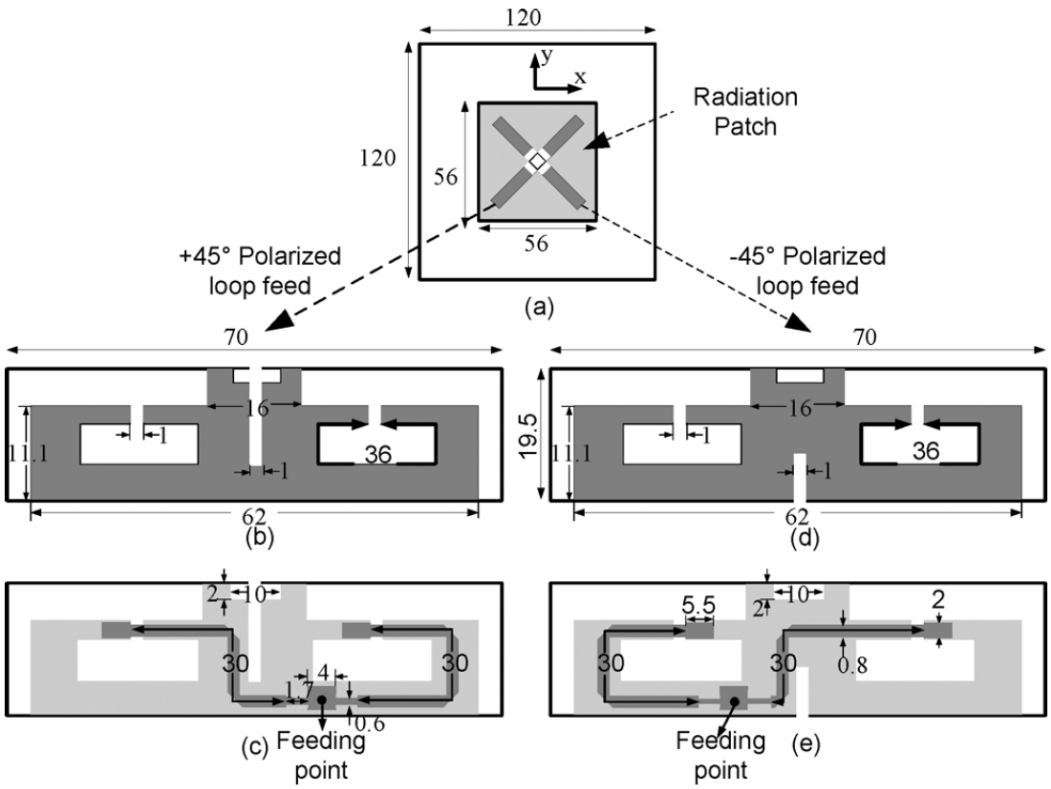

Figure 2.4 Geometry of dual-polarized double tuned antenna. Unit: mm
(a) Top view, (b) loop for +45° polarization, (c) feed line for +45° polarization, (d) loop for -45° polarization, (e) feed line for -45° polarization [14].

Table 2.1 Comparisons of the patch antennas

Patch antennas	Height	RBW	VSWR	Isolation	Feed methods
Ref. [5]	0.11 λ_0	26 %	VSWR<2	>25 dB	Meandering probe
Ref. [8]	0.15 λ_0	25.6 %	VSWR<2	>30 dB	Proximate coupling
Ref. [11]	0.18 λ_0	26.7 %	VSWR<2	>25 dB	Aperture coupling
Ref. [14]	0.13λ_0	25.6 %	VSWR<1.433	>30 dB	Magnetic loop

Key performances of these patch antennas are listed in Table 2.1 as a good comparison. It is known that the impedance bandwidth of a patch antenna will be seriously affected by its height, so the height is important to be listed it in the table, and λ_0 is the wavelength of the central frequency in the operation bandwidth. From Table 2.1, it is can be seen that all these antennas have a relative bandwidth about 26%, however, compared with the VSWR and isolation performances, magnetic loop feeding method in [14] is the most appealing method to excite dual-polarized patch antennas.

2.2.2 Wideband Dual-Polarized Slot Antennas

Compared to the patch antennas, slot antennas are a good choice for its integration with radiators and feeding networks [19-22]. Four-leaf clover slot [19], ring slot along with four

narrow slots [20], bow-tie slot [21], and stepped impedance slot [22] are utilized to realize dual-polarized antennas with wide impedance bandwidth and good radiation performances. These antennas are normally composed of simple structures: a layer of slots, a layer of feedlines, and a reflecting ground plane. To make a good comparison, the performances in these works are listed in Table 2.2.

Table 2.2 Comparisons of the slot antennas

Slot antennas	Height	RBW	VSWR	Isolation
Ref. [19]	0.17 λ_0	10.8 %	<2	>30 dB
Ref. [20]	0.29 λ_0	17.3 %	<2	>22dB
Ref. [21]	0.08 λ_0	18.3 %	<2	>28.5 dB
Ref. [22]	0.15λ_0	31 %	<2	>30 dB

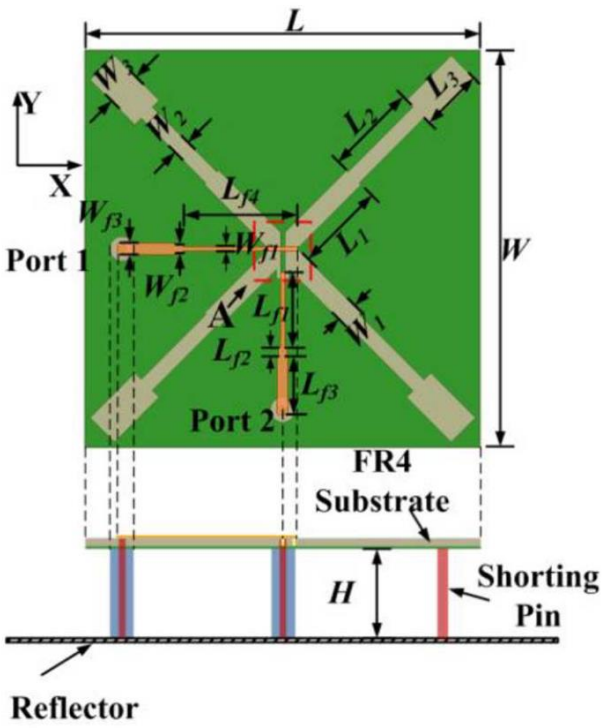

Figure 2.5 Configuration and prototype of the proposed antenna [22].

In [22], two identical pairs of stepped impedance slots and two stepped microstrip feed lines are designed to generated dual-polarization. This antenna is inspired by the previous work in [19], nevertheless, it obtained much wide impedance and isolation bandwidth than that. The configuration of the antenna is shown in Figure 2.5. The structure is very simple with radiators and feedlines on the same board. By combining the multi-resonance stepped impedance slots, the antenna gets broadband characteristic. In addition, good cross-

polarization is achieved by introducing two shorting pins. The slot antenna achieves an overlapped band of 620 MHz ranging from 1680 to 2300 MHz for each port, and its isolation is higher than 30 dB. Base on this slot antenna, four-element dual-polarized antenna array was designed, constructed, and measured. The array prototype achieves a wideband in the range of 1.69-2.5 GHz for 10 dB return loss, and the isolation between the two ports is higher than 35 dB.

In addition, ultra wideband slot-aperture antennas like dual-polarized Vivaldi antennas [23]-[25] and dual-polarized horn antennas [26]-[28] can have a very wide impedance bandwidth covering up to 10:1 frequency band ratio. By inserting two orthogonal Vivaldi antennas in a cross-shaped form [24], the presented dual-polarized antenna has a 10 dB impedance bandwidth from 0.7 to 7.3 GHz (166%), and the isolation between the antenna input ports is better than 30 dB. Broadband horn antenna in [26] utilizes the crossed exponential-shaped ridges and the quadruple-ridge waveguide transition to improve the return loss performance. The measured results of this antenna prove that the impedance bandwidth can cover the frequency band of 2-26.5 GHz. However, the radiation patterns and gains of these antennas are always unstable as the increase of frequency due to innate radiation characteristic of the slot-aperture. Moreover, large profiles are required to ensure the wide impedance bandwidth.

2.2.3 Wideband Dual-Polarized Dipole Antennas

Among all the other types of dual-polarized antenna, dipoles are the most commonly used types for dual-polarization [29-62]. Due to their orthogonal configurations and simple constructions, dipole antennas are widely used in the area of base station communications. Dual-polarized dipole antennas can be designed by using low cost metals, like copper, or aluminium, or printed circuit boards [29-42]. They can have different working mechanisms, like folded dipoles [43-47], magneto-electronic dipoles [48-58] or differential feeding dipoles [59-62]. In this section, an extensive discussion will be developed on these topics, and at the same time, some comparisons also will be made to show their different features in impedance bandwidth and radiation characteristics.

Loop radiating dipoles etched on the printed circuit boards are developed to realize dual polarization. Figure 2.6 shows a broadband ±45° dual-polarized base station antenna [36]. The proposed antenna has two Y-shaped feeding lines, two pairs of loop radiator dipoles, and a rectangular box-shaped reflector. Both the loop radiator dipoles and the Y-shaped feeding lines are printed on the horizontally placed FR4 substrate. The radiators have the

shape of an octagonal loop, and they are placed orthogonally in cross-pairs to get a dual-polarization radiation characteristic. Measured results showed that the antenna's impedance bandwidth is 45% for VSWR<1.5 from 1.7 to 2.7 GHz at both ports, and the port-to-port isolation is better than 25 dB. In addition, a five-element antenna array was developed and tested. The array has a good impedance matching with SWR<1.5, a stable gain of 14.8±1.4 dBi at port 1 and 14.5±1.4 dBi at port 2, and very stable radiation patterns with 3-dB beamwidth at H-plane of 66.56°±2.22° at port 1 and 64.85°±4.96° at port2 from 1.7 to 2.7 GHz. When the degree of electrical down tilt of the antenna beam is increased, the radiation patterns at H-plane are still very stable.

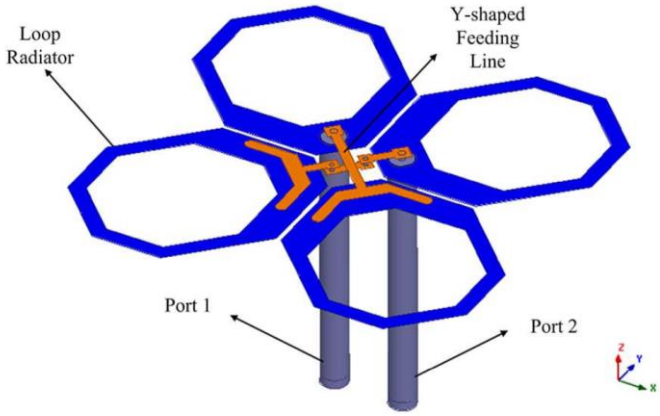

(a)

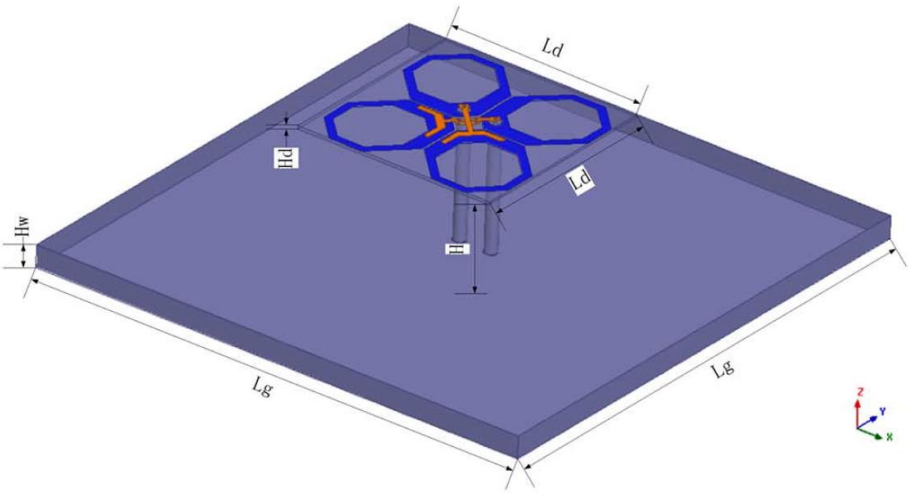

(b)

Figure 2.6 Geometry of the proposed dual-polarized antenna element.
(a) Perspective view of the antenna element. (b) Three-dimensional view [36].

Apart from simply feed method by using coaxial cables, Dipoles can be fed by the integrated baluns [38]. As shown in Figure 2.7, four horizontal triangular patches formed two dipoles in two orthogonal polarizations, and two integrated baluns connected with 50 Ω

SMA launchers are used to excite the dipole antenna. These configurations make the antenna achieving a wideband impedance and isolation bandwidth. The measured VSWR for both ports is less than 1.5, ranging from 1.7 GHz to 2.7 GHz, and the measured port isolation is higher than 35 dB.

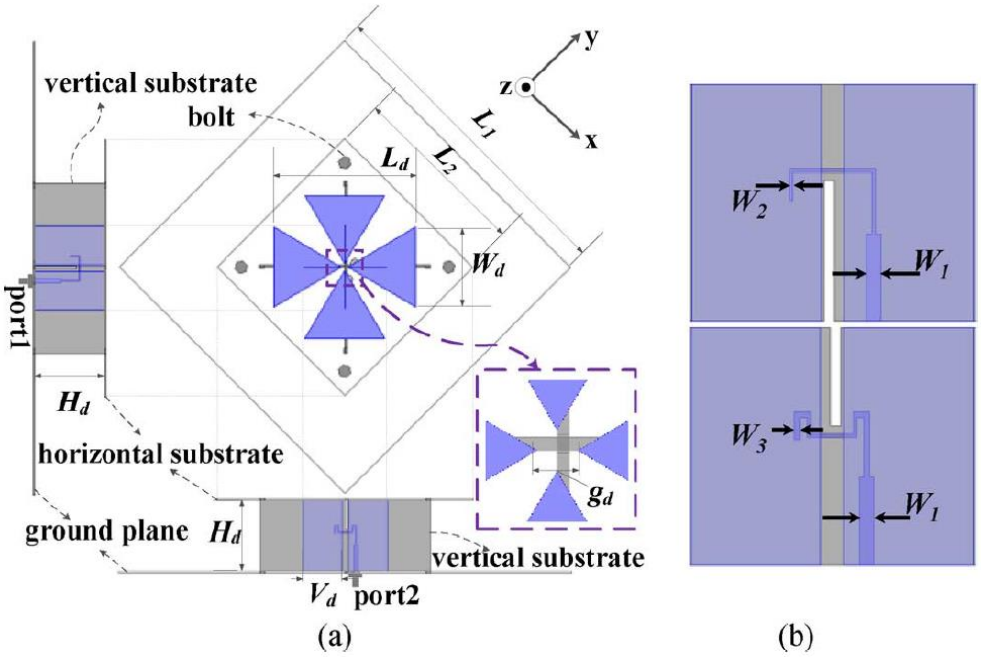

Figure 2.7 (a) Geometry of antenna. (b) Baluns for different ports [38].

As an important part of dual-polarized antenna, magneto-electric dipoles are welcomed by many researchers [48-58]. First reported by Kwai-Man Luk [48], various types of low profile magneto-electric dipoles and reconfigurable dipoles [54, 58] are designed. The magneto-electric dipoles can be simply fed by Γ-shaped strips [49, 50, 53], open-ended slot [56] and other methods. A classic dual-polarized magneto-electric dipole [49] is shown in Figure 2.8. The antenna is composed of electric dipoles, vertically oriented shorted patches, and Γ-shaped feeding strips. The measured results show that the common bandwidth of the two ports is 65.9 % (VSWR<2), ranging from 1.72 to 3.4 GHz. Over the whole operating frequency band, the isolation between two input ports is more than 36 dB, which satisfied the designed requirement for commercial base station antennas.

Differential signals are more preferable in the wireless communication systems due to their superior advantages of noise immunity, mode current elimination, and fundamental harmonic rejections. In consequence, more and more researches are performed on the differential dual-polarized antennas [59-62]. A differential-driven dual-polarized magneto-electric dipole antenna [59] was first proposed with excellent performance. Because of the ideally symmetrical antenna configuration and differential driven methods, the antenna's

port-to-port isolation is theoretically infinite. Therefore, there is no need to worry much about the isolation in designing the differential dual-polarized antennas. Afterwards, more and more differentially fed dipoles were presented [60-62].

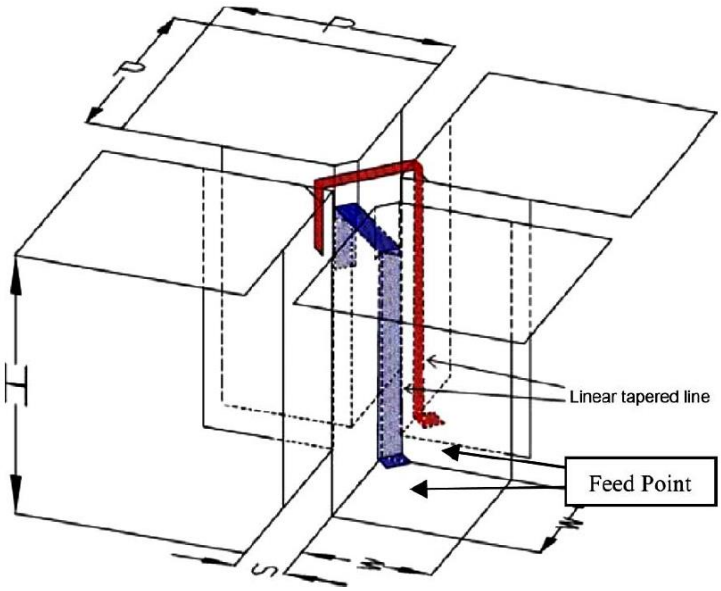

Figure 2.8 Geometry of the proposed antenna [49].

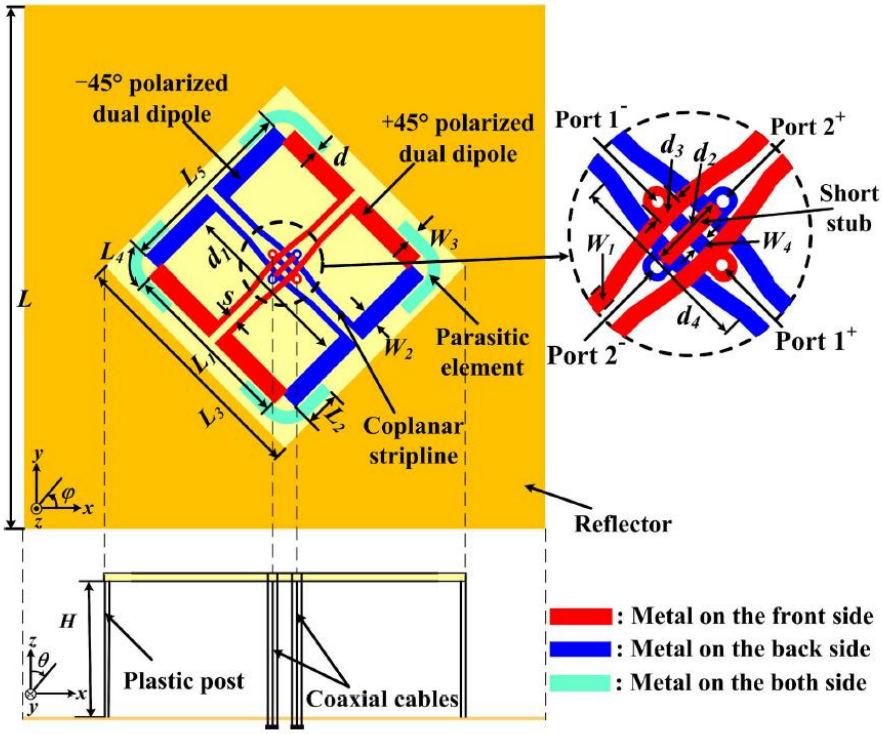

Figure 2.9 Configuration of the proposed differentially fed dual-polarized antenna [62].

In Figure 2.9, a novel broadband differentially fed dual-polarized planar antenna [62] is proposed with simple configuration. The antenna is composed of two dual-dipole elements,

each of which is differentially fed by two coaxial cables through a short stub. Four pairs of parasitic elements are introduced to enhance the bandwidth. Both the dual-dipole elements and the parasitic elements are etched on the same substrate. The prototype measured results show the antenna have a very good performance. Its 15dB differential impedance bandwidth is 45% (1.7-2.75 GHz), and the isolation is better than 45 dB. In addition, the antenna gain is about 9 dBi and the HPBWs are within 65±8° in the whole bandwidth.

Table 2.3 gives the detailed comparisons of the abovementioned dual-polarized dipole antennas. In the table, it can be seen that different types of antennas have the different performances. For base station applications, the height is often set as 0.25 λ_0. The impedance bandwidth is 45% for VSWR<1.5, and isolation better than 30 dB, which is enough to cover the high band (1.7-2.7 GHz) for 2G/3G/4G base station applications.

Table 2.3 Comparisons of the dipole antennas

Dipole antennas	Height	Relative bandwidth	VSWR	Isolation	HPBW	Gain
Ref. [36]	0.25 λ_0	45 %	VSWR<1. 5	>25 dB	65°±5°	8.2±0.6 dBi
Ref. [38]	0.25 λ_0	52 %	VSWR<1. 5	>35 dB	NG	7 ~ 8.6 dBi
Ref. [40]	0.31 λ_0	49 %	VSWR<1. 433	>30 dB	65°±10°	~ 8.5 dBi
Ref. [45]	0.21 λ_0	47 %	VSWR<1. 925	>38 dB	NG	>9.3 dBi
Ref. [49]	0.24 λ_0	65.9 %	VSWR<2	>36 dB	NG	Max: 9.5 dBi
Ref. [57]	0.34 λ_0	56 %	VSWR<1.5	>30 dB	NG	5.8 ~8.9 dBi
Ref. [62]	0.29 λ_0	45 %	VSWR<1. 433	>45 dB	65°±8°	~ 9dBi

2.3 Wideband Circularly Polarized Antennas

In this section, wideband circularly polarized antennas are reviewed. First, different kinds of patch antennas for CP radiation are discussed. Then are the wideband CP slot antennas radiated with quasi-omnidirectional or bidirectional patterns. Finally, the wideband CP dipole antennas are illustrated with different feed method.

2.3.1 Wideband Circularly Polarized Patch Antennas

It is very convenient to realize CP radiation by using different shaped patches. By using the chamfered patches [63]-[66], protruded stubs [67], or etching different slots [68]-[70], two orthogonal radiating modes with quadrature phase difference are excited by using single-feed method. These patch antennas keep simple configuration and low-profile normally with single layer substrate but with relatively narrower AR bandwidth. To improve

the CP radiation bandwidth and increase the design flexibility of CP antennas, quadrature feed networks [71]-[76] are commonly utilized to realize wideband CP patch antennas. In [71], by introducing the wideband quadrature Wilkinson power divider, a very wide AR bandwidth of 82% is achieved for the four-feed patch antenna. To reduce the size occupied by the Wilkinson power divider, serial feed power divider is utilized in [74] to obtain a compact structure. To further reduce the size of the serial feed network, a square-loop shaped patch is used in the CP antenna design [75]-[76], which is realized for high gain array antennas. In addition, by etching different shaped slots [77]-[80] in the ground plane to excite the CP radiating mode, wideband CP patch antennas are developed. In [80], double Y-shaped slots are etched in the ground plane to realize right-hand CP radiation with the AR bandwidth of 20.4%.

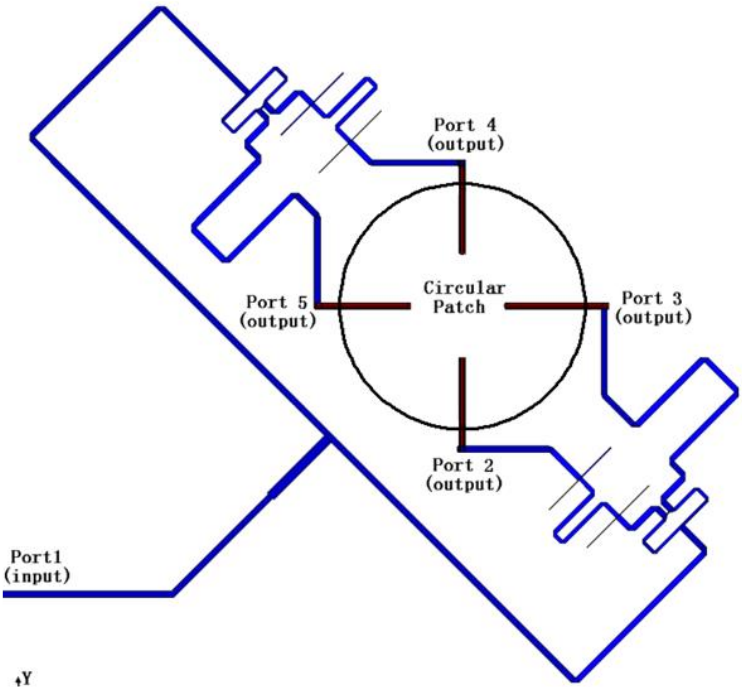

Figure 2.10 Wideband CP patch antenna presented in [71].

In Figure 2.10, a broadband quadrature hybrid feed network is presented to realize wideband CP radiation for the four-feed radiating patch antenna. The broadband quadrature hybrid feed network is composed of a Wilkinson power divider, the shunted open-circuited microstrip lines and shunted short-circuited microstrip lines. The feed network achieves a consistent quadrature phase within ±3° variance over a wide bandwidth of 75%, and the patch antenna achieves a wide CP bandwidth of 82% for AR less than 3 dB. Figure 2.11 shows the configuration of the CP array antenna presented in [75], which is realized for low-profile and high gain radiation. The centre loop feeding structure provides sequential phase

for CP radiation. Four square patches at the outside works as the driven patches, while four chamfered patches works as the parasitic patches. By using the CP mode induced from the centre feed square loop, the AR bandwidth is greatly improved. The CP array antenna features flat antenna gain and a low profile of only $0.028\lambda_0$.

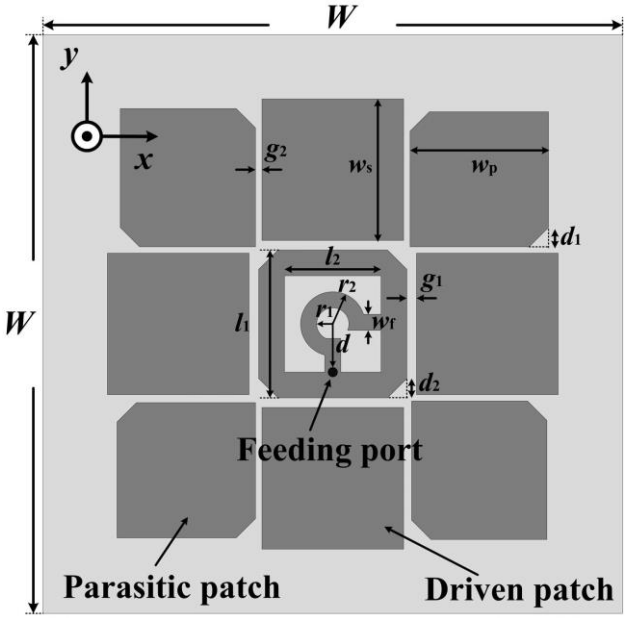

Figure 2.11 Geometry of the proposed CP array antenna in [75].

Table 2.4 compares the performances between the typical above-mentioned CP patch antennas. As can be seen in the table, the single-feed CP antenna using chamfered patch [63] has the narrowest AR bandwidth. By increasing the thickness of the substrate, the AR bandwidth is broadened accordingly. By using wideband quadrature feed network for multi-feed CP antenna, the AR bandwidth can be greatly improved in [71] and [72]. With the help of the loop feeding structure, the array antennas in [75]-[76] have wide AR bandwidth of around 12% with low profile of $0.028\lambda_0$. In addition, high antenna gains are obtained in these two CP antennas.

Table 2.4 Performance comparison between the CP patch antennas

Patch antennas	Height	Impedance bandwidth for VSWR<2	AR bandwidth for AR<3 dB	Peak antenna gain
[63]	$0.05\lambda_0$	15.2 %	3.2%	4.5 dBic
[66]	$0.14\lambda_0$	42.3%	16.8%	6.6 dBic
[71]	$0.157\lambda_0$	79.4%	82%	7.4 dBic
[72]	$0.084\lambda_0$	35%	20.4%	7.5 dBic
[75]	$0.028\lambda_0$	19.5%	12.9%	9.8 dBic
[76]	$0.028\lambda_0$	15.9%	11.8%	12.9 dBic

2.3.2 Wideband Circularly Polarized Slot Antennas

Patch antennas are easy to realize CP radiation with low profile. However, it is difficult to realize very wide AR bandwidth due to the limitation of the relatively high Q patch resonance. To further improve AR bandwidth, low profile slot antennas are developed for low-cost wireless communication systems [81]-[86]. In these CP antenna designs, the ground of the antenna is normally etched with stair-shaped slot, and the feed line in the slot is always designed in L shape or other similar shapes. Figure 2.12 shows the typical CP slot antenna design in [85]. The slot etched in the ground is C-shaped, but with a semi-circle bump protruded at the right edge. The L-shaped strip in the slot works as the radiator. With the combination of the C-shaped slot and the L-shaped radiator, the developed antenna has a wide impedance bandwidth of 124.4% and wide AR bandwidth of 115.2%.

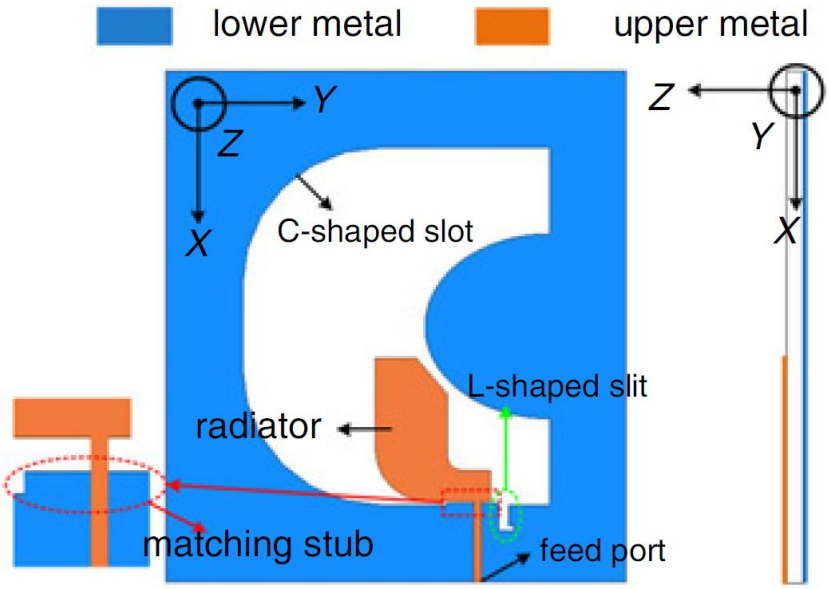

Figure 2.12 Configuration of the CP slot antenna presented in [85].

Table 2.5 compares the performances of these CP slot antennas. The overlapped impedance and AR bandwidth is normally wider than the CP patch antennas shown in Table 1 and with compact size. The radiation patterns are normally quasi-omnidirectional or bidirectional due to the slot configuration. The radiation patterns will be changed as the increase of the frequency due to the different resonances on the slot radiator, and with relatively low antenna gain. Therefore, these antennas are especially useful for the low-cost terminal wireless communication systems, where the radiation pattern and gain are not seriously required to be very stable.

Table 2.5 Performance comparison between the CP slot antennas.

Patch antennas	Height	Impedance bandwidth for VSWR<2	CP bandwidth for AR<3 dB	Peak antenna gain
[81]	0.8mm	132%	32.2%	4.2 dBic
[83]	1mm	60%	40%	2 dBic
[85]	1mm	124.4%	115.2%	4.5 dBic
[86]	1mm	104%	58.6%	3.5 dBic

2.3.3 Wideband Circularly Polarized Dipole Antennas

To obtain a wideband CP antenna with stable radiation pattern, gain, and AR beamwidth, dipoles are always used in these kind of CP antenna designs [87]-[96], and with an reflector for unidirectional radiation. To realize CP radiation, an arc-shaped phase delay line is always integrated into the crossed dipoles for quadrature excitation. Combing with the different parasitic patches, wideband CP bandwidth can be achieved. In designs [87]-[92], crossed line dipoles [87], rectangular dipoles [88], L-shaped dipoles [89]-[90], triangular dipoles [91], and quadrangular dipoles [92] are used for driving element, along with other parasitic elements, wide AR bandwidths are achieved in these antennas.

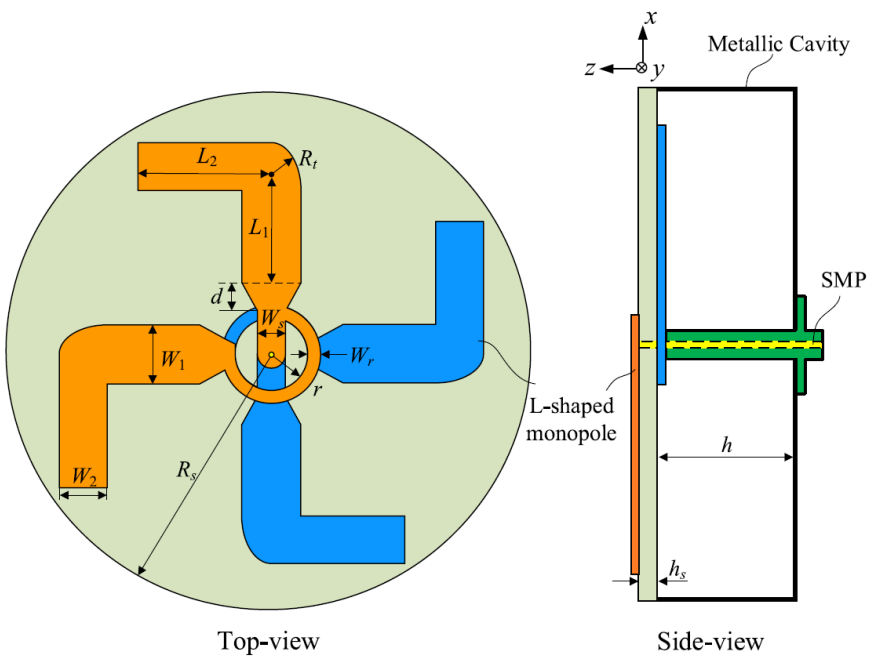

Figure 2.13 Configuration of the CP dipole antenna presented in [90].

Figure 2.13 shows a wideband CP dipole antenna presented in [90]. The antenna has a simple configuration of circular phase delay line for quadrature excitation, crossed L-shaped

dipoles for radiation, a circular cavity for unidirectional radiation. This antenna has a wide impedance bandwidth of 92.8% and a wide AR bandwidth of 62.3%. The backed circular cavity in the figure is also utilized to achieve stable and wide AR beamwidth, which is very useful for radiation pattern requirements in the navigation antenna design.

In addition to the phase delay line integrated in the crossed dipoles, the self-phased method by using combination of long and short dipoles is also utilized to design wideband CP antennas [93]-[96]. In these antennas, the short dipole works as the capacitive loading while the long dipole works as the inductive loading. Therefore, internal quadrature phase delay can be obtained at the input port or the feed line between the long dipole and the short dipole. The self-phase long and shorted dipoles can be directly connected to the coaxial cable as [93] and [94] for the simple feed method, or can be connected a coplanar stripline working as impedance transformer for further bandwidth enhancement [95]-[96].

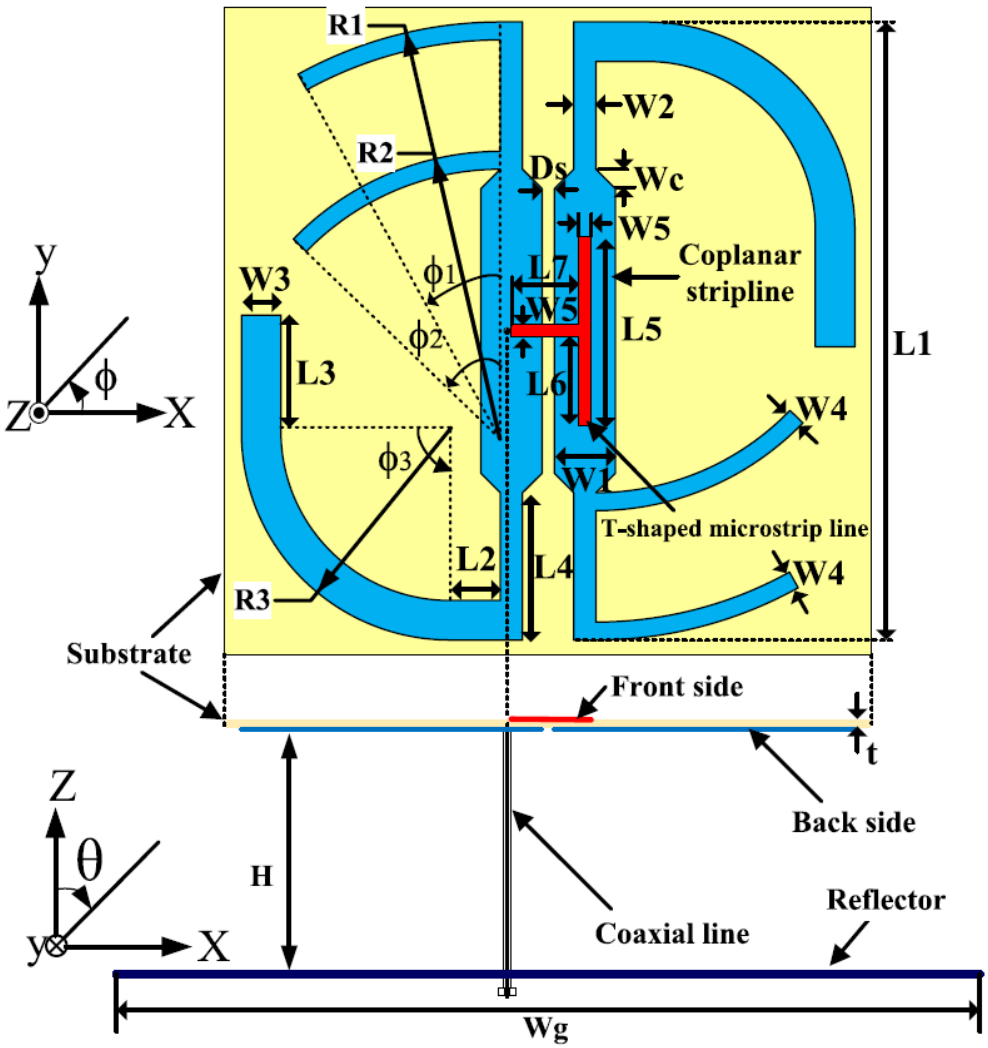

Figure 2.14 Self-phased CP dipole antenna presented in [95].

Figure 2.14 shows the configuration of a self-phased CP dipole antenna presented in [95]. The antenna is composed of a long wide dipole and two narrow short dipole for internal quadrature phase excitation. The centre coplanar stripline works as impedance inverter for bandwidth improvement. A planar reflector is backed for unidirectional and stable CP radiation. This antenna has a wide AR bandwidth of 55% and a wide impedance bandwidth of 60% while keeps simple configuration.

Table 2.6 compares the performances between these CP dipole antennas. As can be seen in the table, dipole antennas using phase delay lines are more convenient to obtain both wide impedance and AR bandwidths as the antennas in [87], [90], and [91]. However, it will be a little difficult for the CP dipole antennas by using self-phased method [94]-[96] to achieve wider AR bandwidth, due to nonlinear input impedance variance caused by different lengths of the crossed dipoles.

Table 2.6 Performance comparison between the CP dipole antennas.

Dipole antennas	Height	Impedance bandwidth for VSWR<2	AR bandwidth for AR<3 dB	Peak antenna gain
[87]	$0.28\lambda_0$	67.5%	53.4%	10.6 dBic
[90]	$0.23\lambda_0$	98.2%	67.5%	12.4 dBic
[91]	$0.23\lambda_0$	57%	51%	10.7 dBic
[94]	$0.17\lambda_0$	6.7%	6%	11 dBic
[95]	$0.3\lambda_0$	60%	55%	9 dBic
[96]	$0.18\lambda_0$	52.4%	7.55%	8 dBic

2.4 Summary and Objectives

In this chapter, different techniques of realizing wideband dual-polarized and circularly polarized antennas for wireless communication systems are reviewed. Patch antenna can be a good choice for low-profile configuration but with relatively narrow impedance bandwidth due to the high-Q resonance of the patch. Generally, a single-layer patch antenna has a narrow bandwidth of a few percentage only for dual-polarized or circularly polarized antennas. Slot antenna can achieve very wide impedance bandwidth of more than 100% both for dual-polarization or circular polarization, but with relatively unstable radiation characteristics. Dipole antenna can be a good compromise between the patch antenna and slot antenna. It can have a stable radiation characteristic over a wide frequency bandwidth of around 50% for both dual-polarized and circularly polarized radiations.

Based on the above state-of-art review, compact-size and wideband antennas and arrays with different features are developed in this thesis to accommodate different application scenario. The objectives of this thesis include the following different research directions.

- Antennas with the wide bandwidth.

To meet the requirements for 2G/3G/4G/5G base station applications, the base station antennas are required to cover the frequency bandwidths of 1.7-2.7 GHz, 3.3-3.6 GHz, and 4.8-5.0 GHz respectively.

- Antennas with the compact size.

If antennas are designed for array designs, especially for large-angle beam-scanning performance, the element distance is required to be close to $\lambda_0/2$. Therefore, antenna element with the aperture size of less than $\lambda_0/2 \times \lambda_0/2$ is very appealing for array designs.

- Antennas with the enhanced upper out-of-band suppression or high harmonic suppression.

Traditional antennas have undesired harmonic radiations, this will cause serious interference to the nearby wireless communication systems. For the 2G/3G/4G base station systems working at 1.7-2.7 GHz, it will produce the harmonic interference to the current 5G base station systems working at 3.3-3.6 GHz and 4.8-5 GHz. Therefore, it is meaningful to develop base station antennas with enhanced upper out-of-band suppression or high harmonic suppression.

- Antennas with the high common mode suppression.

As one of the important parameters for the differential devices, poor common mode suppression will increase the noise level to the circuit system and cause the circuit system a poor signal-to-noise ratio. Therefore, it is necessary to develop differentially driven antennas with high common mode suppression.

- Antennas with dual orthogonal polarized radiations.

Dual-polarized antennas have the advantages of reduced multi-path fading effect and polarization diversity. Therefore, dual-polarized antennas, including dual linearly polarized antennas and dual circularly polarized antennas, have been drawn increasing popularity in the wireless communication systems.

Chapter 3. Wideband and Compact Base Station Antennas

3.1 Introduction

Compact-size dual-polarized antennas are widely used in many array antenna systems, such as base stations, radars and multiple inputs multiple outputs (MIMO) systems. For an array antenna, if the antenna element is of half-wavelength length, the distance between the antenna elements will become larger than half wavelength, taking consideration of the effects of mutual coupling and isolation. Nevertheless, it is required that the distance between the antenna element should be about a half wavelength in order to avoid the grating lobes when the array antenna performs beam scanning [97]. Thus, it is necessary to investigate new techniques to reduce the size of dual-polarized antennas. Traditionally, the arms of reported crossed dipole antennas [61], [49], and dual-dipole antennas [62], [98] for one polarization are not shared for another polarization, and they are separate and independent with a large radiator size. In [62] and [98], four dipoles with eight dipole arms are used for dual-polarization separately. If dipole arms can be shared by each orthogonal polarization, then the radiator size of the dual-polarized antenna can be reduced.

In addition, to obtain a broad bandwidth, various dual-polarized crossed dipole antennas are reported in recent years. In [45] and [99], fan-shaped dipoles and bowtie-shaped dipoles are proposed with wide bandwidth and high isolation. In [61] and [100], different parasitic elements are used to improve the antenna bandwidth and stabilize the radiation patterns. Also, tuned loop [14] and printed integrated baluns [31], [38] are introduced to design dual-polarized antennas. These dual-polarized antennas can normally meet the current requirements for base stations. However, with the development of base station systems [101], 5G frequency bands have already been licensed in China. Two sub-6GHz frequency bands, which are 3.4-3.6 GHz and 4.8-5 GHz, could have produced interferences to the current 2G/3G/4G base station systems. In addition, the newly introduced 5G antennas will lead to the more limited space for base station antennas. So it is necessary to develop compact antennas with high suppression at the 5G bands or filtering property for the current 2G/3G/4G base stations.

Recently, metamaterial-inspired, near-field resonant parasitic, Huygens source antennas are reported to realize electrically small antennas [102]-[104]. By using near-field resonant parasitic elements, both electric and magnetic dipoles are integrated to achieve Huygens

source radiation with very compact configurations. However, the bandwidth of these proposed antennas is normally not wide enough to cover base station requirement, and these antennas are mainly focused on the single-polarized antennas or circularly polarized antennas. Dual-polarized magneto-electric dipole antennas in [49], [57], and [59] have achieved wide impedance bandwidth, but large spaces are occupied compared to the Huygens source antennas.

3.2 Compact Dual-Polarized Shared-Dipole Antennas

In this section, a novel design concept of using shared-dipole to design compact dual-polarized antenna is presented. Four dipole arms of the presented antennas are shared for two orthogonal polarizations. Thanks to the shared-dipole configuration, the overall size of the radiator can be theoretically reduced by 50% compared to the traditional dual-polarized CD antennas. Furthermore, the presented dual-polarized shared-dipole (DPSD) antennas have a wideband impedance bandwidth and high isolation which is comparable to the existing designs including the traditional differentially driven dual-polarized CD antennas.

To validate the design concept, two prototypes are designed, fabricated and measured. One is the four-port DPSD antenna for conceptual verification, and the other is the highly integrated DPSD antenna for low-cost design. Both antennas achieve significant size reductions compared to the CD antennas popularly used for base stations. Furthermore, the operation principle of the proposed DPSD antennas is analyzed and discussed. Both the four-port DPSD antenna and the highly integrated DPSD antenna meet the requirements for the base station systems (1.7 GHz to 2.7 GHz with VSWR< 1.5 and isolation> 35 dB) with stable gain and half-power beamwidth (HPBW).

3.2.1 Operation Principle

The operation principle of the DPSD antenna is analyzed and discussed. Firstly, the configuration of the DPSD antenna is described and compared to the traditional CD antennas. Then the isolation and S-parameters for the DPSD antenna are illustrated. Verification of the operation principle of the DPSD antenna and CD antenna is also investigated.

Figure 3.1(a) and (b) shows the configurations of the proposed DPSD antennas, which are compared to the traditional CD antennas (Figure 3.1(c) and (d)). A dual-polarized antenna is composed of four arms (Arm1, Arm2, Arm3, and Arm4), and it can be designed as the horizontal, vertical polarizations or the ±45° polarizations. In Figure 3.1(a), dipole pair of Arm1 and Arm4 and dipole pair of Arm2 and Arm3 are excited for horizontal polarization

with equal magnitude and co-phase excitation, and dipole pair of Arm1 and Arm2 and dipole pair of Arm3 and Arm4 are excited for vertical polarization. In Figure 3.1(b), a similar method can be applied for ±45° polarizations.

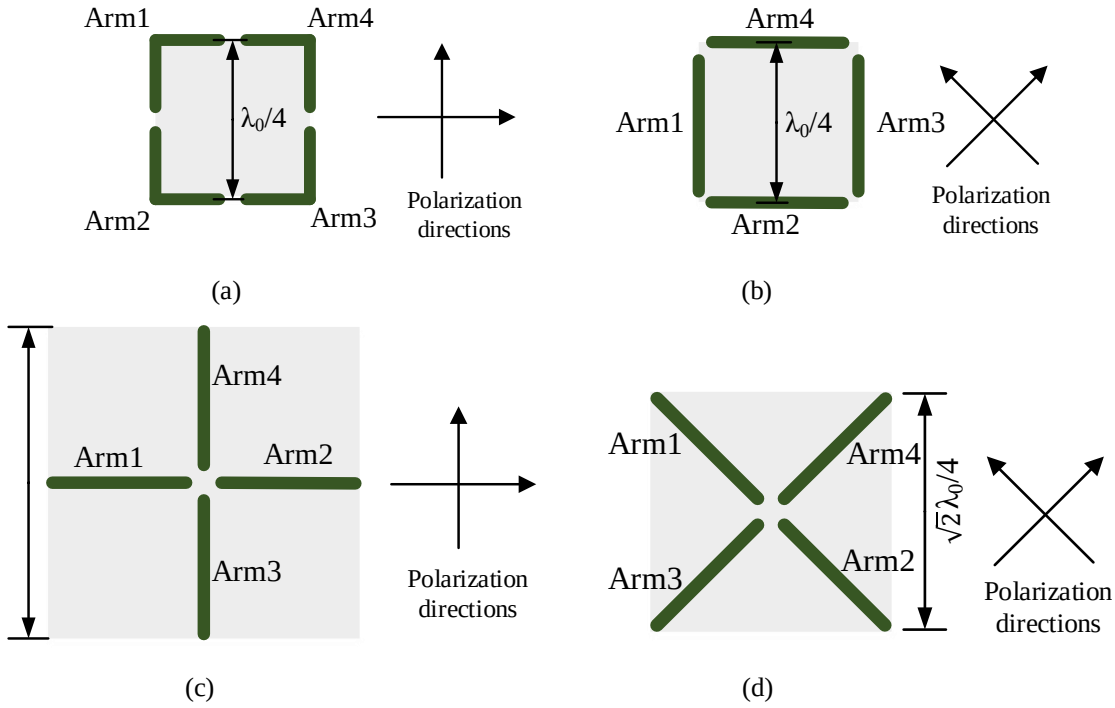

Figure 3.1 Different configurations for dual-polarized antenna.
(a) ±45° polarized DPSD antenna. (b) Horizontal and vertical polarized DPSD antenna. (c) Horizontal and vertical polarized CD antenna. (d) ±45° polarized CD antenna.

For a dual-polarized antenna, the length of each dipole arm is about $\lambda_0/4$. Different antenna configurations lead to different aperture size. The ratios of these different aperture sizes are $S_c{:}S_a = 4{:}1$ and $S_d{:}S_b = 2{:}1$, where S_a, S_b, S_c, and S_d represent the aperture size of the antenna shown in Figure 3.1 (a)-(d), respectively. Therefore, DPSD antenna can effectively reduce the size of the antenna aperture compared to the traditional CD antenna. Theoretically, DPSD antenna can save 50% of the antenna occupied area compared to a dual-polarized wired CD antenna.

To explain how the high isolation of the DPSD antenna is achieved, the equivalent circuit for the DPSD antenna is shown in Figure 3.2. Assume that the port 1 and port 3 are excited with RF signals with voltage V_{p_1} and V_{p_3}, where

$$\begin{aligned} V_{p_1} &= +\mathrm{v}_1 - (-\mathrm{v}_1) = 2\mathrm{v}_1 \\ V_{p_3} &= +\mathrm{v}_3 - (-\mathrm{v}_3) = 2\mathrm{v}_3 \end{aligned} \tag{3.1}$$

At the terminal of Arm1, Arm4, Arm2 and Arm3, the voltage values are $\alpha \mathrm{v}_1 e^{j\theta}$, $-\alpha \mathrm{v}_1 e^{j\theta}$, $\beta \mathrm{v}_3 e^{j\gamma}$, and $-\beta \mathrm{v}_3 e^{j\gamma}$ respectively, where α and β are coefficients of the magnitude, and θ and γ are the corresponding delayed phases. So the voltage values at port 2 and port 4 are

$$V_{p_2} = \alpha v_1 e^{j\theta} - \beta v_3 e^{j\gamma}$$
$$V_{p_4} = -\alpha v_1 e^{j\theta} - (-\beta v_3 e^{j\gamma}) \tag{3.2}$$

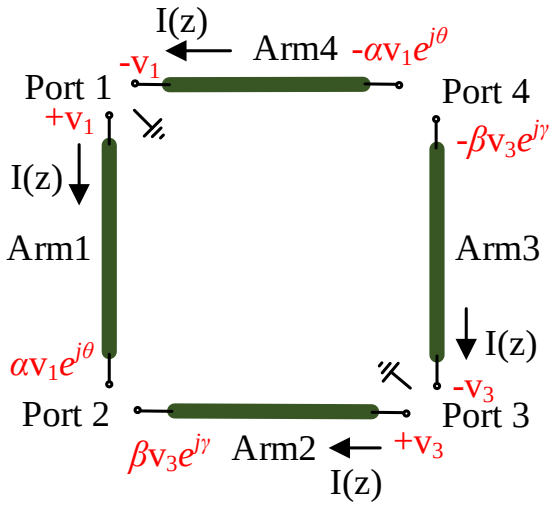

Figure 3.2 Equivalent circuit for the DPSD antenna.

For a symmetrical DPSD antenna, the four arms are of the same length. Besides, port 1 and port 3 excited with equal magnitude and co-phase signals. Thus, the following conditions should be satisfied.

$$v_1 = v_3$$
$$\alpha = \beta \tag{3.3}$$
$$\theta = \gamma$$

Then, it can be derived that

$$V_{p_2} = V_{p_4} = 0 \tag{3.4}$$

This means that if port 1 and port 3 are excited with equal magnitude and co-phase signals, the voltage across the other two port (port 2 and port 4) is zero. For the DPSD antenna, the signals transmitted from port 1 and port 3 are cancelled by each other at port 2 and port 4. Therefore, high isolation is obtained for the DPSD antenna.

Each polarization of the DPSD antenna needs two equal magnitude and co-phase excitations, and normally it needs a feed network. To facilitate the evaluation of antenna performance without using feed network, the S-parameters are analyzed by using the principle of four-port microwave network theory [105].

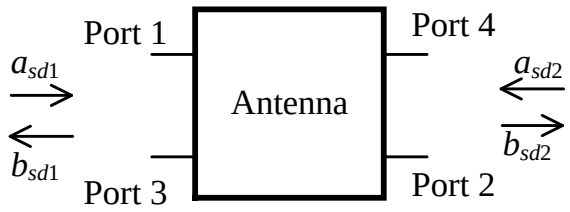

Figure 3.3 Four-port single-ended network with common mode excitation.

Four-port excited DPSD antenna is regarded as a common mode excited four-port network. Figure 3.3 shows the equivalent four-port single-ended network with common mode excitation. Single-ended port 1 and port 3 are together designated as shared-dipole port 1 for one polarization, and single-ended port 2 and port 4 are together defined as shared-dipole port 2 for another polarization. The S-parameters for the DPSD antenna (S_{sd11}, S_{sd22}, S_{sd21}, and S_{sd12}) are derived as

$$S_{sd} = \begin{bmatrix} S_{sd11} & S_{sd12} \\ S_{sd21} & S_{sd22} \end{bmatrix} = \begin{bmatrix} \frac{b_{sd1}}{a_{sd1}} & \frac{b_{sd1}}{a_{sd2}} \\ \frac{b_{sd2}}{a_{sd1}} & \frac{b_{sd2}}{a_{sd2}} \end{bmatrix} = \frac{1}{2}\begin{bmatrix} S_{11}+S_{13}+S_{31}+S_{33} & S_{12}+S_{14}+S_{32}+S_{34} \\ S_{21}+S_{23}+S_{41}+S_{43} & S_{22}+S_{24}+S_{42}+S_{44} \end{bmatrix} \quad 5)$$

As expressed in (3.5), the S-parameters of the DPSD antenna are calculated by taking the mutual couplings into consideration. Thus, the input impedance and VSWR of the DPSD antenna can be calculated as

$$Z_{sd11} = Z_0 \frac{1+S_{sd11}}{1-S_{sd11}} \quad (3.6)$$

$$VSWR_{sd} = \frac{1+|S_{sd11}|}{1-|S_{sd11}|} \quad (3.7)$$

By using (3.5)-(3.7), the actual impedance and isolation bandwidth for the DPSD antenna are derived. This method enables the verification of the S-parameters of the DPSD antenna without using any external power divider network.

To verify the above analysis, both the DPSD antenna and CD antenna are simulated by using ANSYS Electromagnetics Suite 18. Both antennas are arranged for ±45° polarizations. The two antennas are excited with ideal lumped ports. As a general definition in this paper, the yz plane is designated as the horizontal plane (H-plane), and the xz plane is defined as the vertical plane (V-plane).

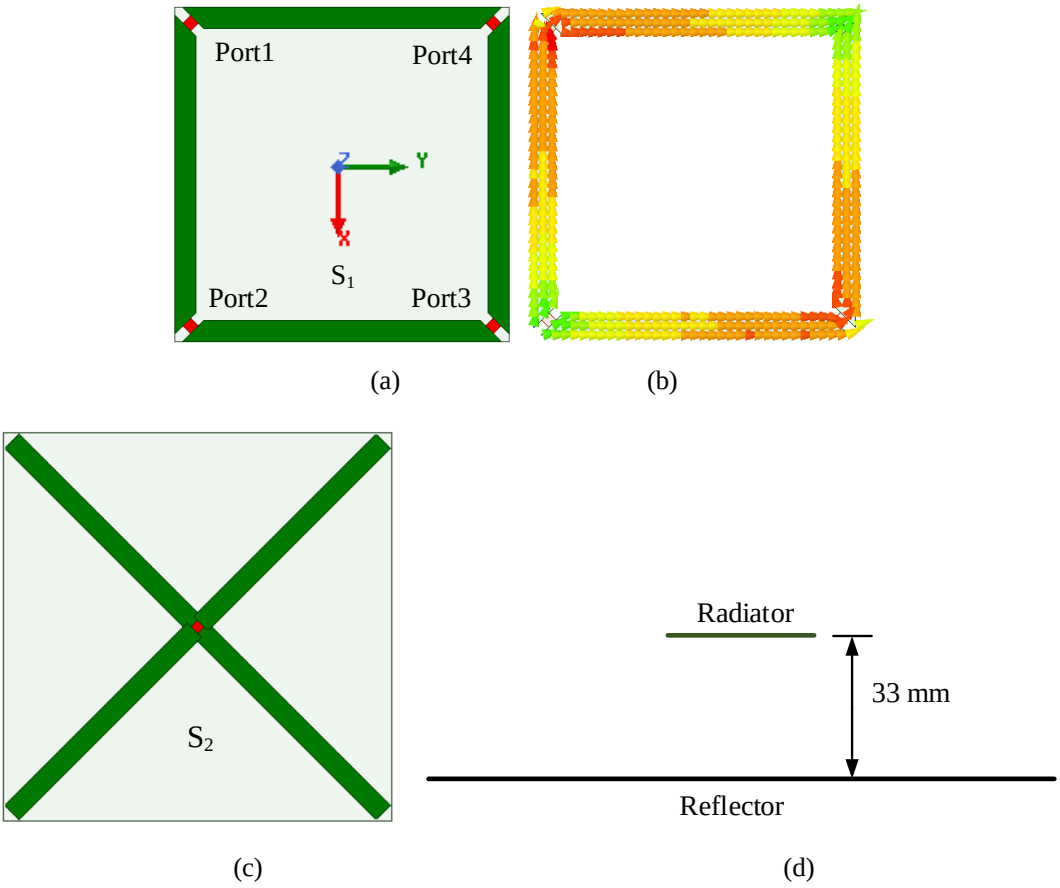

Figure 3.4 Models of simulated DPSD antenna.
(a) DPSD antenna. (b) Surface current distribution of DPSD antenna with port 1 and port 3 excited. (c) CD antenna. (d) Side view of both two simulated antenna models.

As shown in Figure 3.4, the width of the dipole arm for the DPSD and CD antenna is 2 mm. The distance from the radiator to the reflector for both antennas is 33 mm. The two dual-polarized antennas are designed at the resonant frequency of 2.5 GHz. The length of each antenna arm is about a quarter wavelength in free space. Figure 3.4 (b) shows the surface current distribution when port 1 and port 3 are excited with equal magnitude and co-phase signals. As can be seen, the strongest current magnitude is in the centre of the feed point, and the weakest current magnitude is at the end of the dipole arm, which implies good isolation is obtained for another polarization.

Figure 3.5 (a) shows the input impedance of the DPSD antenna (Z_{sd11}) and the CD antenna (Z_{cd11}). The real parts of the input impedance of two antennas are almost the same. Regarding the imaginary part, the DPSD antenna has a flatter variation than that of the CD antenna, which means a wider impedance bandwidth can be achieved for the DPSD antenna. Figure 3.5 (b) compares the simulated normalized H-plane radiation patterns between the DPSD antenna and the CD antenna when port 1 and port 3 are excited with the ideal equal magnitude and co-phase signal. The radiation patterns are almost the same in the range of

±30° around the boresight direction. In the range of ±90°, the DPSD antenna has slightly lower cross polarization discrimination (XPD) than the CD antenna.

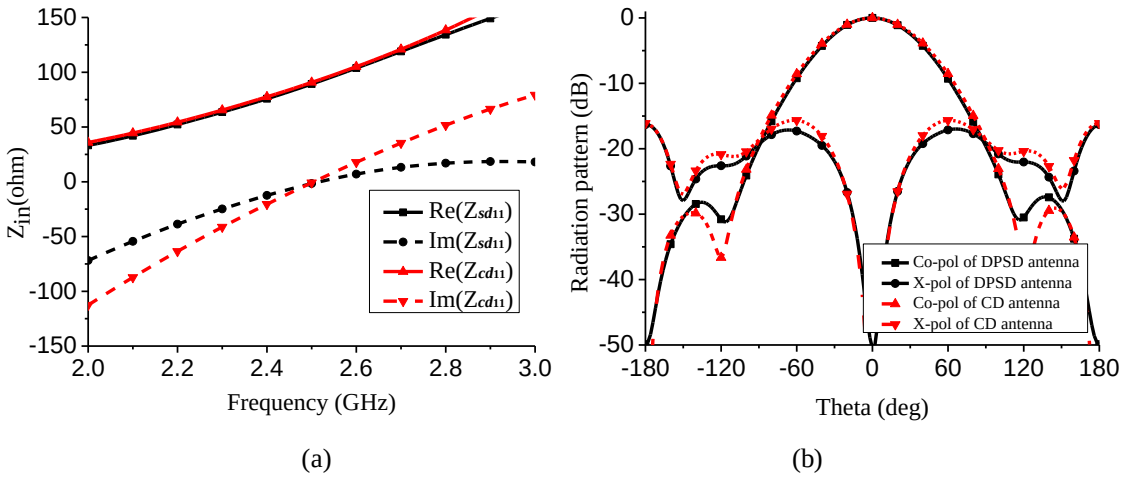

(a) (b)

Figure 3.5 (a) Input impedance of the DPSD antenna and the CD antenna. (b) H-plane radiation patterns of the DPSD antenna and CD antenna.

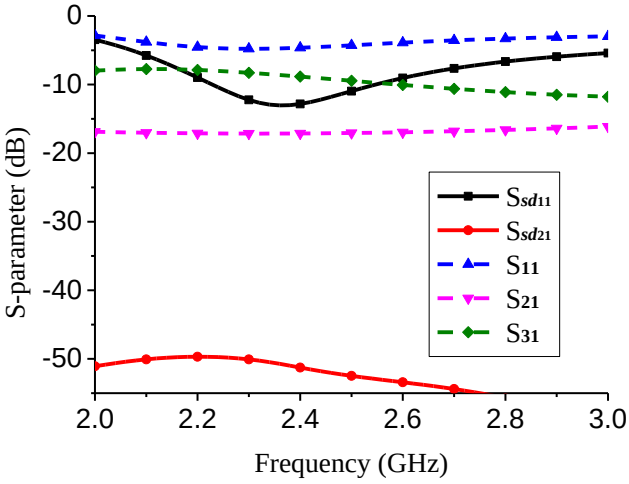

Figure 3.6 Simulated S-parameters of DPSD antenna.

The simulated S-parameters of the four-port DPSD antenna are shown in Figure 3.6. The isolation between port 1 and port 3 (S_{31}) is about -10 dB and the isolation between port 1 and port 2 (S_{21}) is about -17 dB. As discussed in Section II. C, equation (3.5) needs to be used for S-parameters calculation. The calculated results are also shown in Figure 3.6. The best impedance matching frequency for the DPSD antenna is at about 2.4 GHz, and the isolation is better than 50 dB.

3.2.2 Design I: Four-Port DPSD Antenna

In this subsection, the configuration of the four-port DPSD antenna is illustrated. Then, the presented antenna is analyzed and discussed using its equivalent circuit model. After that, the prototype of the four-port DPSD antenna is fabricated and measured by two methods.

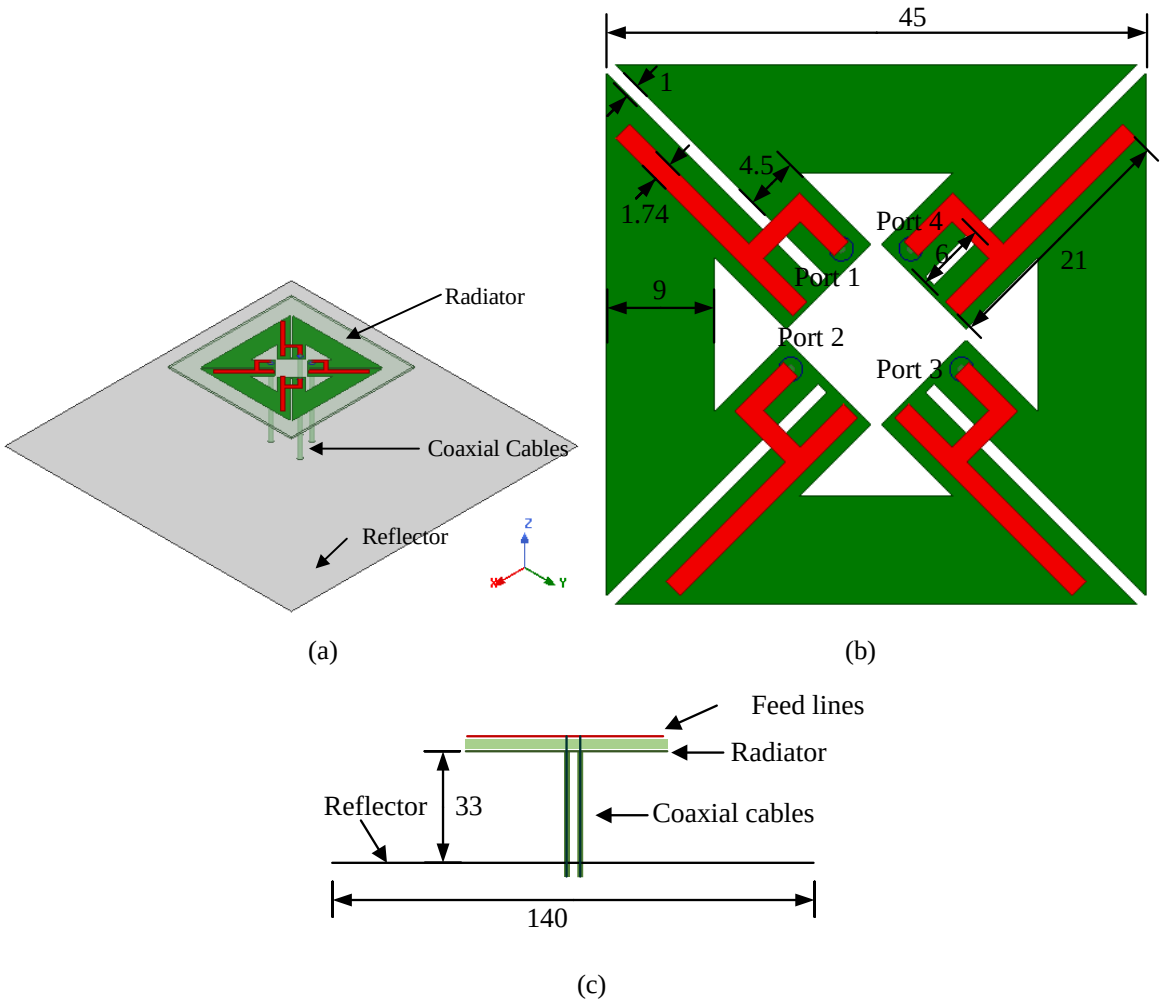

Figure 3.7 Geometry of the four-port DPSD antenna. (a) 3D view. (b) Detailed configuration of radiator. (c) Side view. (Unit: mm)

The configuration of the four-port DPSD antenna is shown in Figure 3.7. The developed antenna is composed of a radiator, four equal-length semi-flexible coaxial cables, and a reflector for unidirectional radiation. Rogers RO4003C substrates with a relative dielectric constant of 3.55 and thickness of 0.813 mm are employed for the antenna design. The bottom layer of the substrate is four symmetrically arranged shared-dipole arms connected by four shorted coplanar striplines (CPSs). The top layer is the four feed lines, which is designed for the antenna impedance matching. The CPS on the bottom layer and the feed line on the top layer together function as a balun, which transforms the unbalanced coaxial line to the balanced CPS. The outer conductor of the coaxial cable is soldered to the bottom layer of

CPS, while the inner conductor of the coaxial cable is soldered to the top layer of the feed line. Figure 3.7 (c) depicts the side view of the four-port DPSD antenna. The distance from the radiator to the reflector is 33 mm, which is about a quarter wavelength at 2.2 GHz in free space. The size of the square reflector is 140 mm × 140 mm.

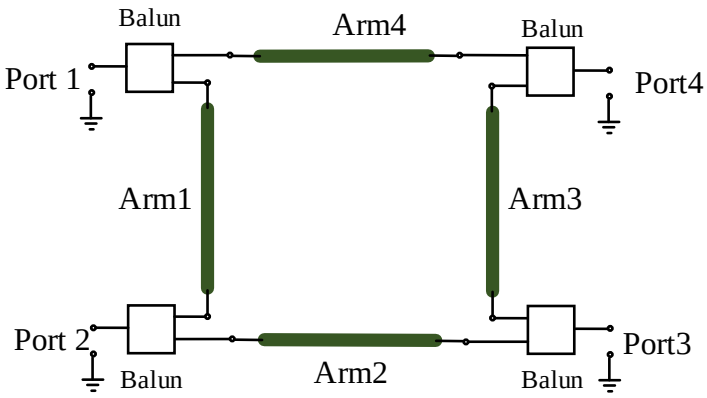

Figure 3.8 Equivalent circuit model of the four-port DPSD Antenna.

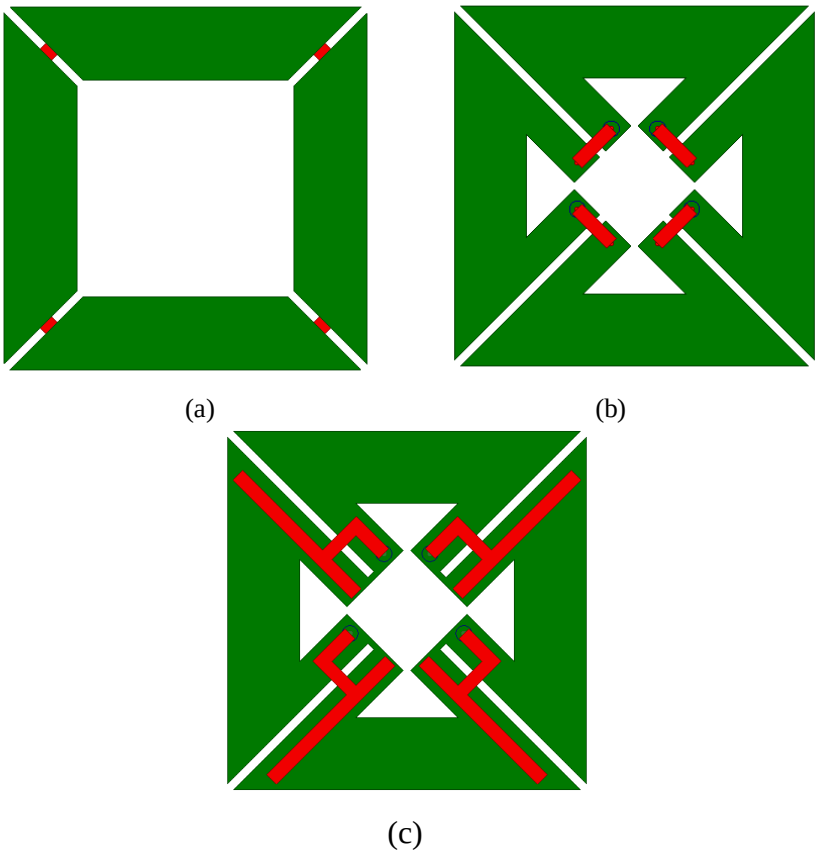

Figure 3.9 Design steps of the four-port DPSD antenna. (a) With ideal lumped port feed. (b) With CPS feed. (c) With balun feed.

Figure 3.8 shows the equivalent circuit model of the four-port DPSD antenna. The single-ended unbalanced coaxial cables are connected to the baluns, then the unbalanced coaxial

cables are transformed into the balanced CPSs. By using the balanced CPSs feed method, four shared-dipole arms are excited for the balanced radiation.

Figure 3.9 illustrates the design steps of the proposed four-port DPSD antenna. The corresponding simulated S-parameters under different design steps are shown in Figure 3.10. First, the four-port DPSD antenna is excited with four ideal 50Ω lumped ports. One resonance can be founded at about 2 GHz, and the isolation is better than 60 dB. When the four-port DPSD antenna is fed by CPS connected by a 50Ω coaxial cable, a better impedance matching is obtained, but the isolation at higher frequency band is deteriorated because of the unbalanced feed coaxial cables. To realize the balanced feed and increase the impedance bandwidth, y-shaped open feed line and shorted CPS are employed to form a balun. As a result, another resonance is obtained and the impedance bandwidth is increased. Moreover, the isolation within the whole frequency band is higher than 48 dB.

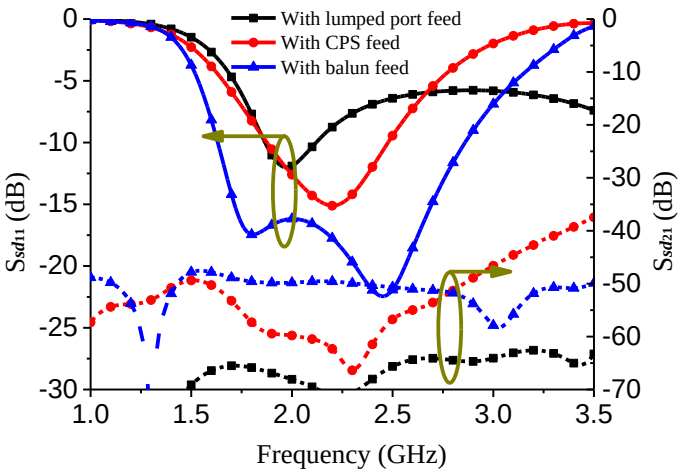

Figure 3.10 Simulated S-parameters of the four-port DPSD antenna with different feed methods.

To validate the operation principle and the analysis of the four-port DPSD antenna, the proposed antenna is verified by two measurement methods, one is measured directly without feed network, and the other is measured with feed network.

1) Without feed network: Figure 3.11 shows the photographs of the fabricated four-port DPSD antenna. The antenna is fed by four semi-flexible coaxial cables. Figure 3.12 shows the simulated and measured four-port single-ended S-parameters. Due to the symmetry of the antenna, only the simulated and measured S_{11}, S_{22}, S_{21}, S_{31}, and S_{41} are given in the figure. The measured S-parameters agree well with the simulated results. The small discrepancy is mainly due to the effect of the extension of the coaxial cables and the fabrication errors of the antenna.

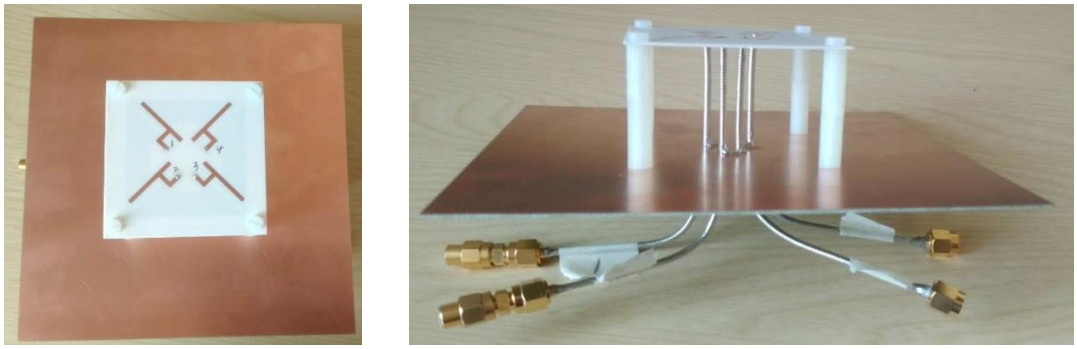

(a) (b)

Figure 3.11 Photographs of the fabricated four-port DPSD antenna without feed network. (a) Top view. (b) Side view.

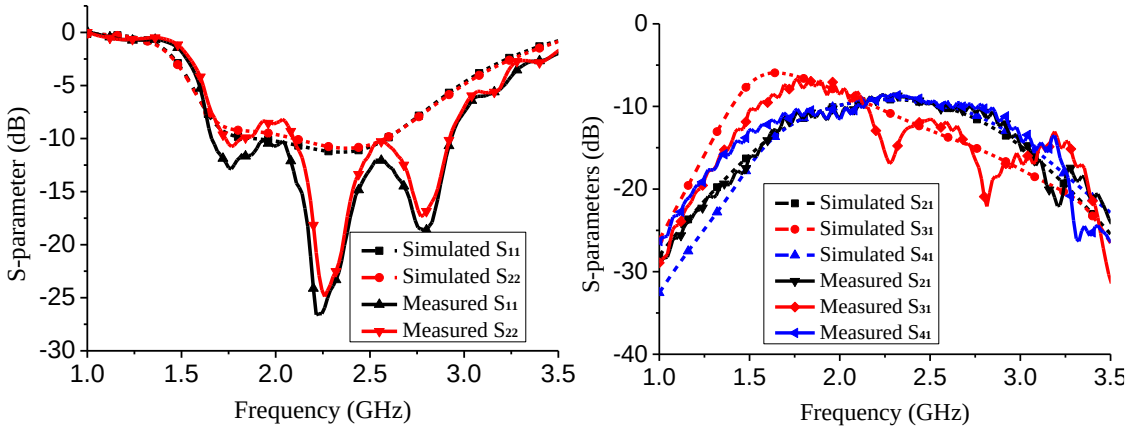

(a) (b)

Figure 3.12 Simulated and measured S-parameters for the four-port DPSD antenna. (a) $\boldsymbol{S_{11}}$ and $\boldsymbol{S_{22}}$. (b) $\boldsymbol{S_{21}}$, $\boldsymbol{S_{31}}$ and $\boldsymbol{S_{41}}$.

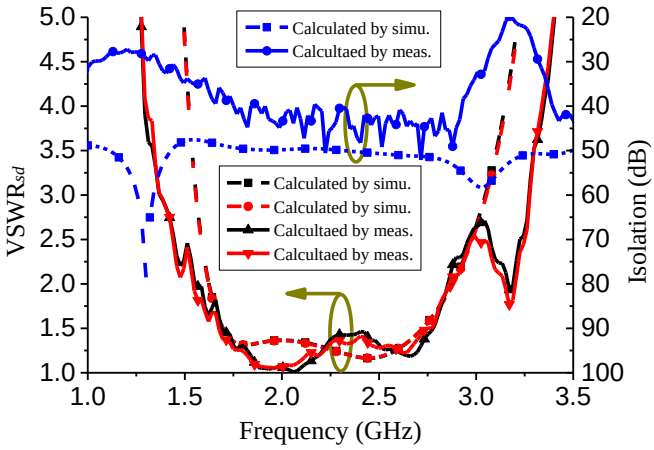

Figure 3.13 The calculated VSWR and isolation by the simulated and measured results for the four-port DPSD antenna without feed network.

To illustrate the true impedance characteristic of the DPSD antenna, by using (5)-(7), the calculated VSWR and isolation from the simulated and measured four-port S-parameters are shown in Figure 3.13. The calculated overlapped impedance bandwidth for VSWR<1.5 of the dual-polarization is from 1.69 GHz to 2.77 GHz. Although the measured isolation is

slightly lower than the simulated isolation, it is still better than 37 dB within the impedance bandwidth.

2) With feed network: As discussed in Section II, the four-port DPSD antenna needs equal magnitude and co-phase excitation. Therefore, a feed network is designed to feed the four-port DPSD antenna. The photograph of the four-port DPSD antenna with the feed network is shown in Figure 3.14. The reflector of the antenna is replaced by a PCB with one layer of copper functioned as a reflector and the other layer composed of the antenna feed network. The four output ports of the power dividers are connected to the four input ports of the antenna radiator by four semi-flexible coaxial cables with equal length and phase. Each input port of the power divider is connected by an SMA connector for each polarization.

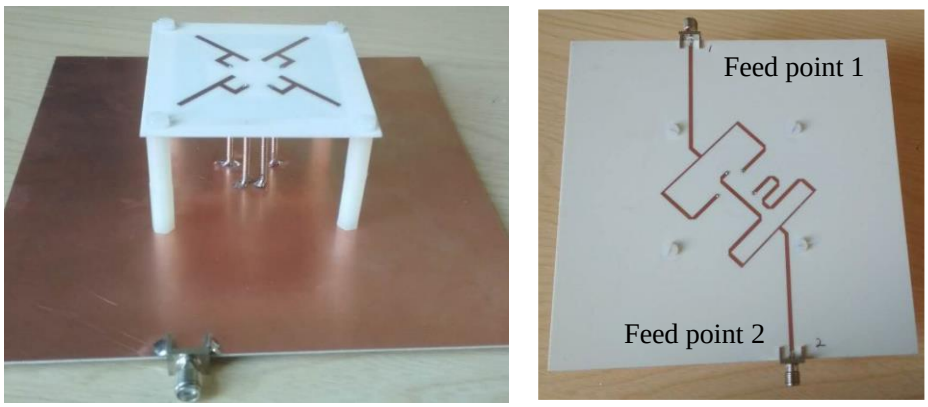

(a) (b)

Figure 3.14 Photographs of the fabricated four-port DPSD antenna with the feed network.
(a) Antenna radiator and reflector. (b) The feed network on the bottom layer of the reflector.

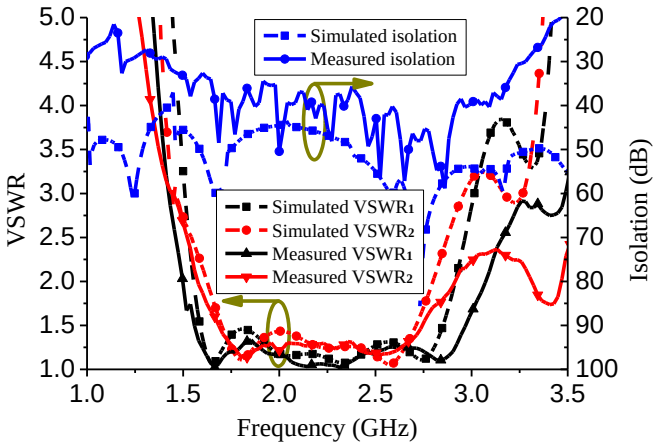

Figure 3.15 Simulated and measured results for the four-port DPSD antenna with the feed network.

Figure 3.15 shows the simulated and measured VSWR and isolation at the two ends of the feed network. A good agreement is observed between the simulated and measured results. Due to the effect of the feed network, the impedance bandwidth for port 1 is slightly wider

than port 2. The measured overlapped two port impedance bandwidth for VSWR<1.5 is from 1.68 GHz to 2.74 GHz. The isolation of the impedance bandwidth is better than 35 dB, which is close to the calculated isolation of the four-port DPSD antenna using (3.5)-(3.7).

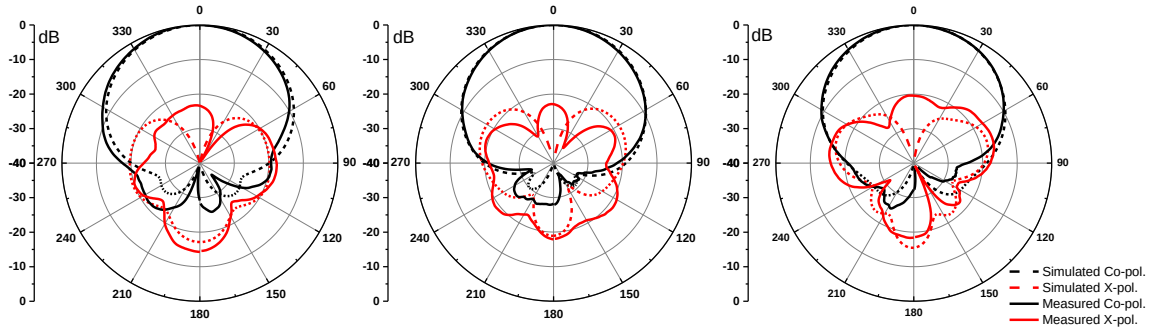

(a) (b) (c)

Figure 3.16 Simulated and measured radiation patterns of the four-port DPSD antenna with the feed network for the H-plane when the feed point 1 excited. (a) 1.7 GHz. (b) 2.2 GHz. (c) 2.7 GHz.

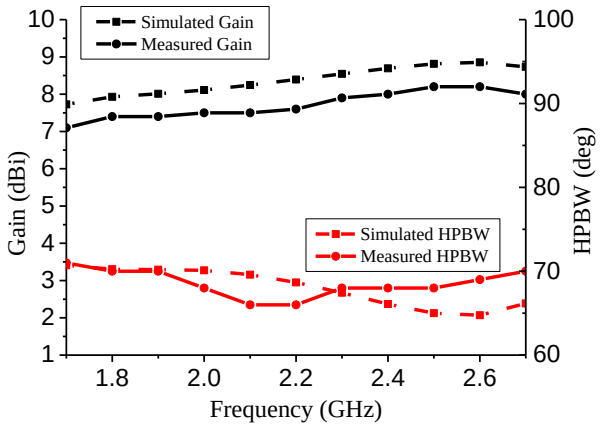

Figure 3.17 Simulated and measured gain and HPBW for H-plane when the feed point 1 excited.

The measured and simulated H-plane radiation patterns of the four-port DPSD antenna with the feed network when feed point 1 is excited are given in Figure 3.16. Because of the symmetrical configuration, only the radiation patterns at 1.7 GHz, 2.2 GHz, and 2.7 GHz are presented. The measured XPD at boresight direction is better than 20 dB over 1.7 GHz to 2.7 GHz. For the direction over the range of ±30°, the XPD is better than 20 dB. Figure 3.17 shows the simulated and measured gain and HPBW within the bandwidth of the antenna. There is a good agreement between the measured and simulated results, which shows stable gain and HPBW are obtained. The measured gain varies from 7.1 dBi to 8.2 dBi, and the measured HPBW for H-plane varies from 66° to 71°.

3.2.3 Design II: Highly Integrated DPSD Antenna

In this subsection, a highly integrated DPSD antenna, which avoids using the feed network, is put forward with only two single-ended feed coaxial cables. An equivalent circuit of this proposed antenna is illustrated. At last, the proposed highly integrated DPSD antenna is fabricated and measured for verification.

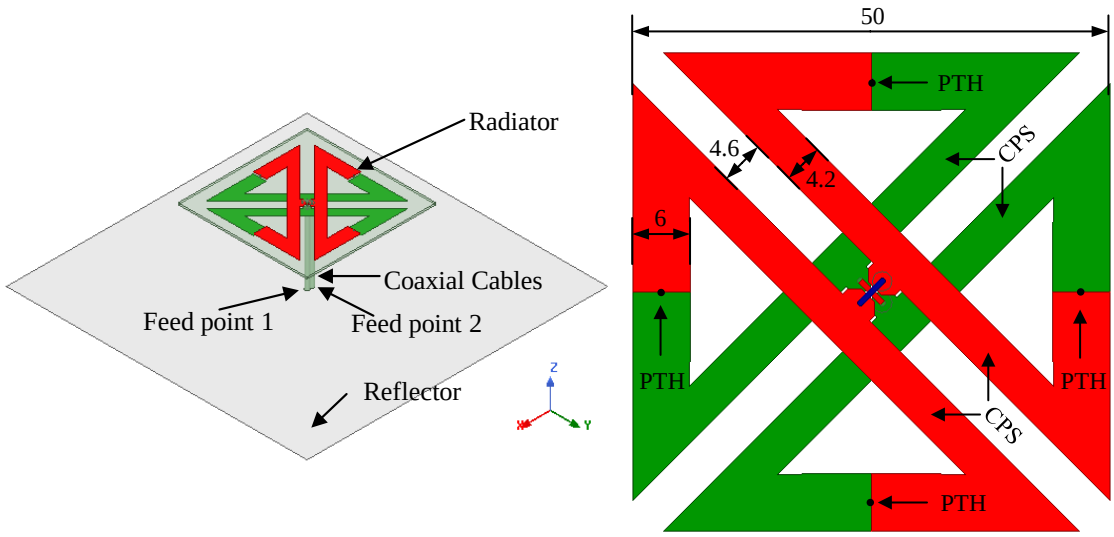

(a) (b)

Figure 3.18 Geometry of the highly integrated DPSD Antenna. (a) 3D view. (b) Top view of the radiator. (Unit: mm)

The configuration of the highly integrated DPSD antenna is shown in Figure 3.18. The proposed antenna consists of three parts, the radiator for dual-polarization, two coaxial cables for direct feed, and a square reflector. Compared to the four-port prototype in Section III, this antenna is integrated with two pairs of CPSs, and two coaxial cables are soldered on each pair of the CPS for each polarization. This direct coax feed method avoids the use of the feed network and thus reduces the design complexity and fabrication cost. The antenna is printed on a substrate of Rogers RO4003C with a relative dielectric constant of 3.55 and thickness of 0.813 mm.

As shown in Figure 3.18 (b), the top layer of the antenna is depicted in red color, while the bottom layer is highlighted in green color. Four plated through holes (PTHs) are inserted into the dipole arms to connect the radiating element. At the centre of the PCB, two coaxial cables are connected to the crossed CPSs for each polarization. Specifically, for the +45° polarization, the outer conductor of one coaxial cable is soldered on the top right side of the CPS, and the inner conductor is soldered on the bottom left side of the CPS. Same feed

method is applied to the -45° polarization. The distance from the radiator to the radiator is 33 mm, and the square reflector size is 140 mm.

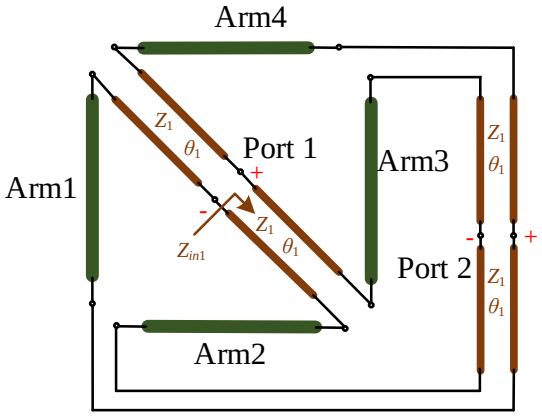

Figure 3.19 Equivalent circuit of highly integrated DPSD antenna.

Figure 3.19 illustrates the equivalent circuit of the highly integrated DPSD antenna. The characteristic impedance of the CPS is Z_1, and its phase length is θ_1. Therefore, the input impedance Z_{in1} is

$$Z_{in1} = Z_1 \frac{2Z_{sd11} + jZ_1 tan\theta_1}{Z_1 + j2Z_{sd11} tan\theta_1} \tag{3.8}$$

Then, the input impedance at port 1 is

$$Z_{in} = \frac{Z_{in1}}{2} = \frac{Z_1}{2} \frac{2Z_{sd11} + jZ_1 tan\theta_1}{Z_1 + j2Z_{sd11} tan\theta_1} \tag{3.9}$$

Therefore, if $\theta_1 = 90°$, the transmission line (Z_1) acts as an impedance transformer. In this condition, it can be derived that

$$Z_{in} = \frac{Z_1^2}{4Z_{sd11}} \tag{3.10}$$

Thus, Equations (3.8)-(3.10) provide a good guidance to design the highly integrated DPSD antenna.

Based on the above analysis, the highly integrated DPSD antenna is fabricated and measured. Figure 3.20 shows the photograph of the highly integrated DPSD antenna. Figure 3.21 shows the simulated and measured VSWR and isolation for the highly integrated DPSD antenna. The measured overlapped impedance bandwidth for VSWR<1.5 is from 1.69 GHz to 2.82 GHz, and the corresponding isolation is better than 36 dB. Both the simulated and measured radiation patterns at 1.7 GHz, 2.2 GHz, and 2.7 GHz are shown in Figure 3.22 for comparison. The measured XPD is over 23 dB at the boresight direction, and better than 22

dB over the range of ±30° direction. In Figure 3.23, the measured average gain is about 8.2 dBi (7.7 dBi to 8.7 dBi) and the HPBW is about 68° (65° to 72°) for the base station frequency band.

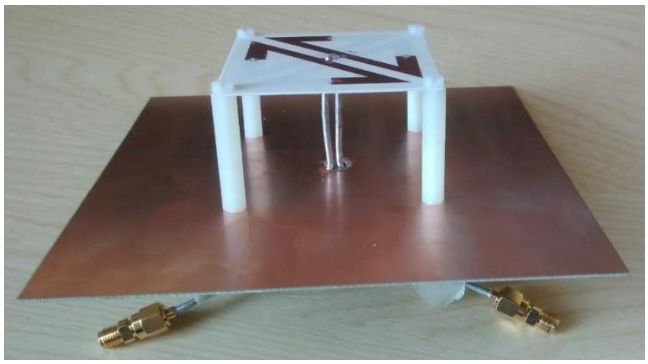

Figure 3.20 Photograph of the fabricated highly integrated DPSD antenna.

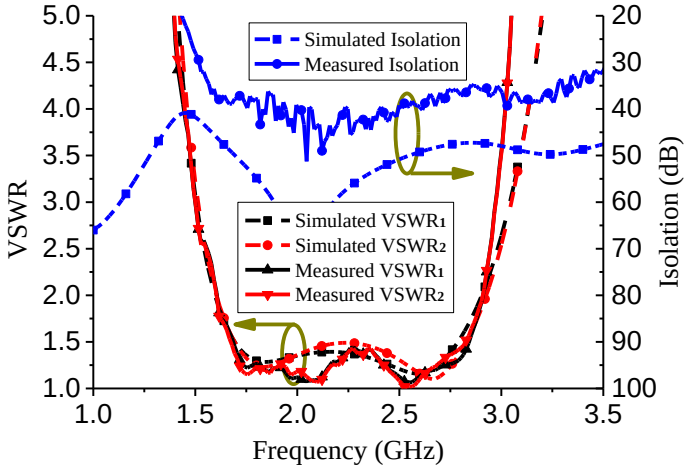

Figure 3.21 Simulated and measured results for the highly integrated DPSD antenna.

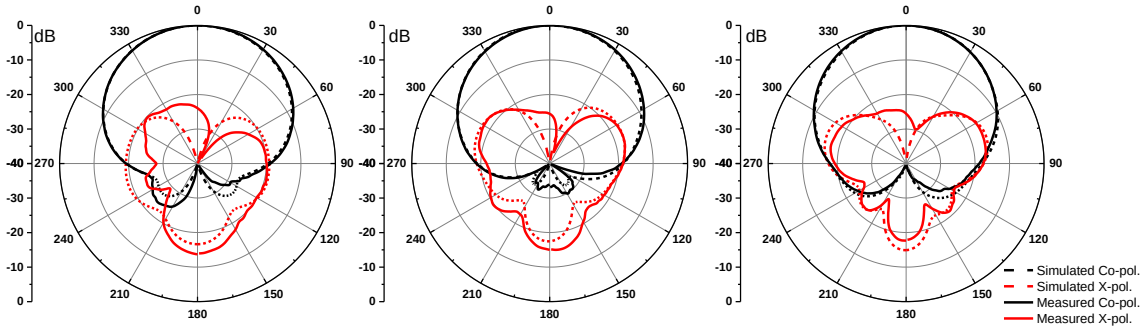

(a) (b) (c)

Figure 3.22 Simulated and measured radiation patterns of the highly integrated DPSD antenna for the H-plane with the feed point 1 excited. (a) 1.7 GHz. (b) 2.2 GHz. (c) 2.7 GHz.

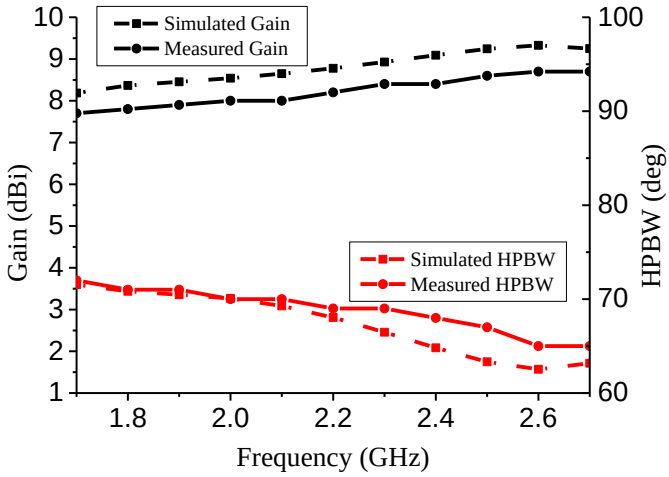

Figure 3.23 Simulated and measured gain and HPBW of the highly integrated DPSD antenna for H-plane with the feed point 1 excited.

Compared to the four-port DPSD antenna, the XPD and gain of the integrated DPSD antenna are a little bit higher, while the impedance characteristic and isolation are almost the same. Furthermore, the proposed highly integrated DPSD antenna only needs two single-ended coaxial cables for dual-polarization as the traditional dual-polarized antenna. It reduces the manufacturing cost with the integrated feed CPSs on the radiating element. With a simple configuration and good radiation performances, it is suitable for the low-cost base station applications.

Table 3.1 Comparison of the dual-polarized antennas for base stations

Antennas	Radiator size (mm×mm)	Height (mm)	VSWR / RL for base station	Isolation (dB)
[41]	140×140	41	VSWR<1.5	>25
[57]	61.6×61.6	45.7	VSWR<1.5	>30
[60]	109.8×109.8	55	VSWR<1.5	>39
[61]	68.5×68.5	34	VSWR<1.5	>26
[98]	68×68	42	RL>15 dB	>30
[113]	70.4×70.4	27	RL>15 dB	>28
Antenna 1	45×45	33	VSWR<1.5	>35
Antenna 2	50×50	33	VSWR<1.5	>36

Table 3.1 compares the developed antennas with the CD antennas reported in recently published papers that can operate from 1.7 GHz to 2.7 GHz for base station applications. Antenna 1 is the prototype DPSD antenna with the feed network, and antenna 2 is the highly integrated DPSD antenna. Antennas in [41], [57], [98], and [113] are the traditional CD

antennas. In [41], four parasitic elements are inserted beside the crossed dipoles to enhance the XPD of the dual-polarized antenna, however, this method increases the overall size of the antenna. It should be noted that antennas in [60] and [61] are the typical differentially driven dual-polarized CD antennas, which is known for their ideal high isolation. The proposed DPSD antennas are of the similar high isolation as the differentially driven antennas but with more compact size. Compared to these antennas, the proposed DPSD antennas have the most compact size with very high isolation.

3.3 Dual-Polarized Antenna With Enhanced Upper Out-of-Band Suppression

In this section, a novel dual-polarized antenna with electric and magnetic resonances is proposed with wide impedance bandwidth and compact radiator size. Figure 3.24 compares the proposed equivalent electric dipole and magnetic dipole configuration with the Huygens source antenna [102] and the magneto-electric dipole antenna [49]. Huygens source antennas feature electrically small configuration owing to the incorporation of both an electric dipole and a magnetic dipole. Magneto-electric dipole antennas are a combination of resonating dipole mode and patch mode. The equivalent electric dipole and magnetic dipole configuration for our proposed antenna is shown in Figure 3.24(c), which is different from these two types, and composed of two electric dipoles and two magnetic dipoles. The proposed antenna can also be seen as a new type of the printed biquad antennas [106]-[109]. However, the traditional biquad antennas are normally realized for single-polarization, and radiate as the electric dipoles.

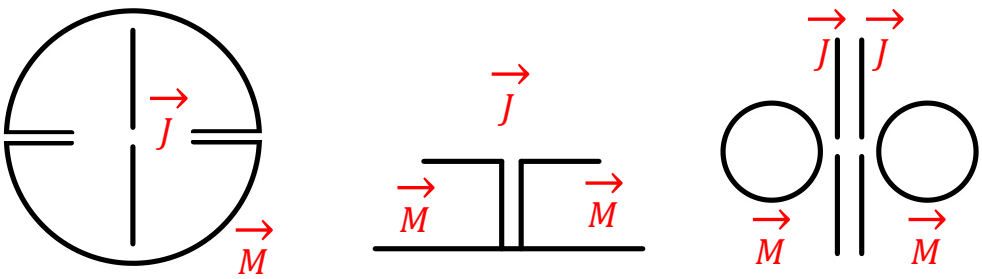

(a) (b) (c)

Figure 3.24 Equivalent electric dipole and magnetic dipole configurations. (a) Reference [102]. (b) Reference [49]. (c) Proposed antenna.

The equivalent electric dipoles and magnetic dipoles are developed by the crossed shunt loops, which make the proposed antenna achieve wider impedance bandwidth and more compact size. Compared to the first matching frequency of the single-polarized shunt loop

antenna, the first matching frequency of the dual-polarized crossed shunt loop antenna is only 1/3 of its counterpart. This means large antenna size can be reduced owing to the introduction of electric dipoles and magnetic dipoles. Furthermore, four parasitic strips are introduced near the inner edge of the loops, which not only help to enlarge the antenna impedance bandwidth, but also improve the antenna selectivity and produce the first suppression at 3.5 GHz. In addition, crossed coaxial baluns are used to feed the proposed antenna with the newly introduced shorting sheet, which is utilized to create the second suppression at 4.9 GHz. Therefore, two radiation nulls are achieved at the centre of two 5G base stations bands.

To validate the design concept, the proposed dual-polarized antenna is designed, fabricated, and measured. The measured results show that the proposed antenna has a wide impedance bandwidth of 1.625-3.05 GHz (61%) for S_{11}<-14 dB and high isolation of 38.3 dB with a compact radiator size. Furthermore, enhanced upper out-of-band suppression from 3.35 GHz to 5.25 GHz with S_{11}>-2 dB is achieved with two radiation nulls at the desired frequency of 3.5 GHz and 4.9 GHz. Stable antenna gain and beamwidth are also achieved for base station applications.

3.3.1 Antenna Configuration

The configuration of the proposed dual-polarized antenna is shown in Figure 3.25. This antenna is composed of a square antenna reflector, two crossed coaxial baluns, and the antenna radiator. The antenna is designed of ±45º polarizations for base station applications. The square reflector is made up of a square copper sheet with the length of 140 mm, which is designed for the unidirectional radiation and low back radiation. The antenna radiator is printed on both sides of a Rogers 4003C substrate with the dielectric constant of 3.55 and the thickness of 0.813 mm. Two crossed coaxial baluns are used to feed the top radiator with balanced excitation magnitude and phase, which are of great importance to improve the antenna isolation.

Figure 3.25 (b) shows the detailed configuration of the antenna radiator. It consists of two pairs of crossed shunt loops. Note that one pair is printed on the top layer of the substrate, which is realized for -45º polarization. Another pair is printed on the bottom layer and realized for +45º polarization. These two pairs of shunt loops are of the same size and symmetrical to each other with the stepped line width of w1 and w3. The distance between the edges of two crossed loops is d1. These three parameters are important to the improvement of antenna input impedance. By using the crossed shunt loops, electric and

magnetic resonance characteristic is introduced with the compact radiator size. Four parasitic strips are located near the inner edge of the loops, and they can further broaden the antenna impedance bandwidth and introduce the first suppression at 3.5 GHz. In the figure, the copper on the top layer of the substrate is depicted in red color, and the copper on the bottom layer is depicted in green color.

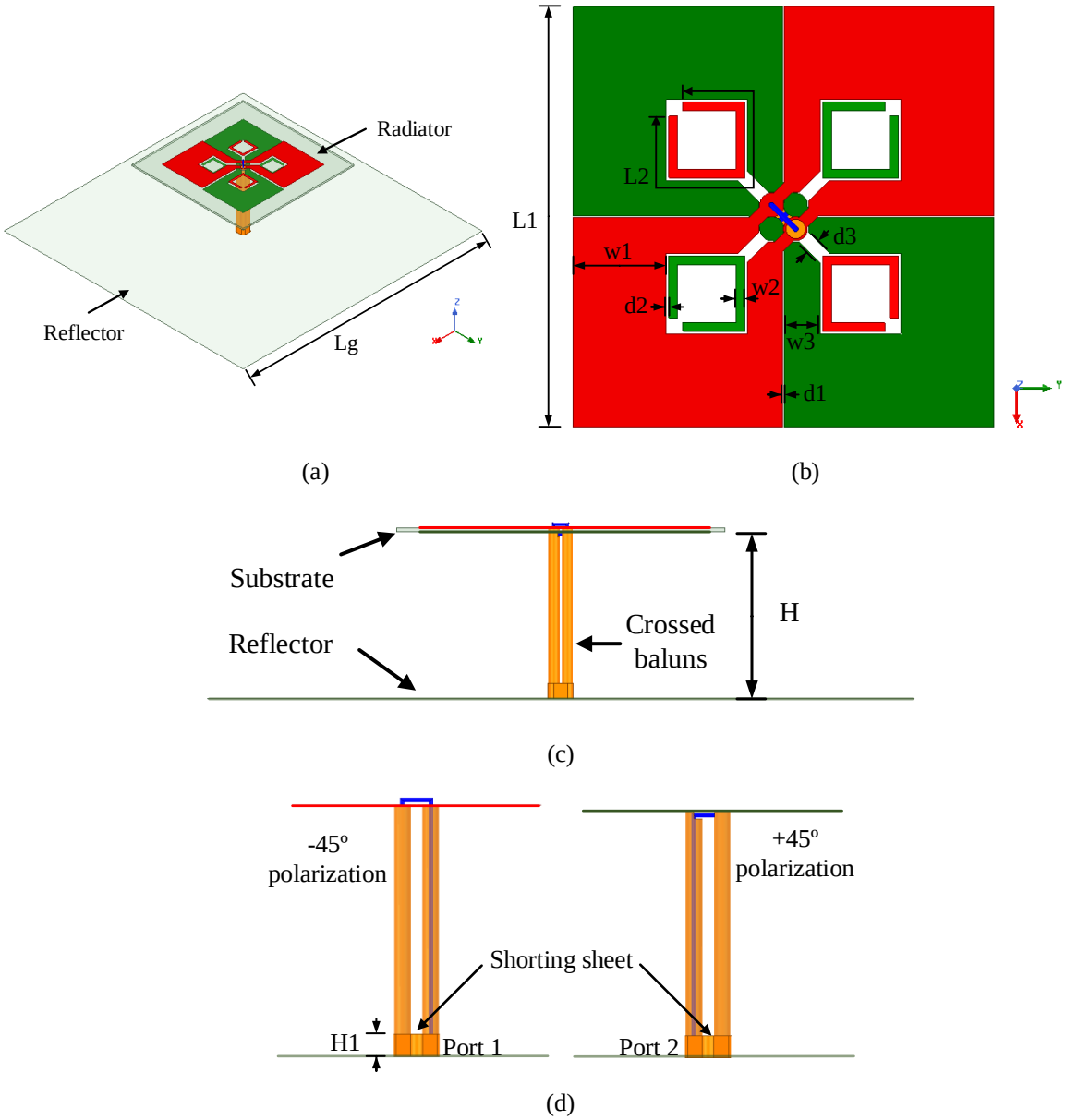

Figure 3.25 Configuration of the proposed dual-polarized antenna.
(a) 3D view. (b) Top view of the antenna radiator. (c) Side view. (d) Details of the crossed coaxial baluns. (Detailed parameters of the proposed dual-polarized antenna. Lg=140 mm, L1=47.5 mm, L2=27.5 mm, w1=10.5 mm, w2=1 mm, w3=4 mm, d1=0.2 mm, d2=0.3 mm, d3=1.5 mm, H=33 mm, H1=3 mm)

Figure 3.25 (c) shows the side view of the dual-polarized antenna. The distance from the top radiator to the antenna reflector is designed as 33 mm to obtain stable unidirectional radiation for base station applications. To realize high port isolation, crossed coaxial baluns

are used to feed the proposed dual-polarized antenna. The detailed side view of the crossed coaxial baluns is shown in Figure 3.25 (d). For the -45° polarization, the outer conductors of the two coaxial cables are connected to both sides of the shunt loops, while the inner conductor of one coaxial cable is penetrated through one shunt arm, and connected to the other shunt arm on the top layer. For the +45° polarized shunt loops, the outer conductors of the coaxial cables are also soldered to the two centre strips of loops, while the inner conductor of one cable is soldered to the outer conductor of the other cable. In addition, a shorting sheet is added at the end of the crossed baluns, which is used to introduce the second upper suppression at 4.9 GHz. All the simulation works in this paper are with the help of Ansys HFSS 18.0. The details of the optimized parameters for the dual-polarized antenna are shown in the caption of Figure 3.25.

3.3.2 Working Principle

The proposed antenna can be equivalent as a combination of electric dipoles and magnetic dipoles. Therefore, electric and magnetic resonances are developed by using the crossed shunt loops. Two simplified antenna models are used to illustrate the different resonance characteristics of electric and magnetic dipoles, and they are shown in Figure 3.26. In this figure, Antenna 1 is the simplified antenna for dual-polarization by using crossed shunt loops, which is excited by the ideal lump ports. Antenna 2 is the single-polarized counterpart with only one shunt loops. Both two reference antennas are simulated with the same antenna reflectors, and the reflectors are also of the same size as the proposed antenna in Figure 3.25.

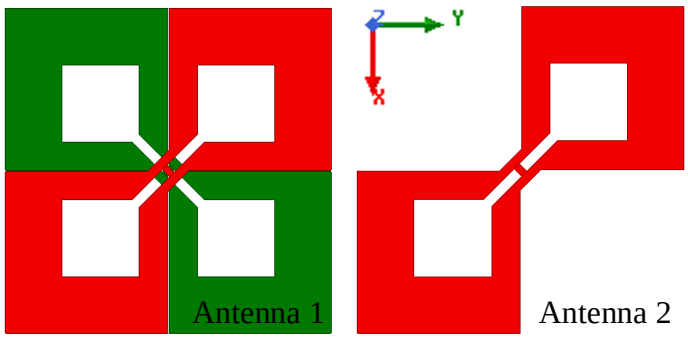

(a) (b)

Figure 3.26 Simulation models of the dual-polarized antenna and single-polarized antenna. (a) Antenna 1. (b) Antenna 2.

Figure 3.27 (a) shows the simulated S-parameters of the two reference antennas. The impedance bandwidth of Antenna 1 for S_{11}<-15 dB is from 1.65 GHz to 2.6 GHz, and two reflection zeroes are observed at 1.74 GHz and 2.36 GHz. Whereas the Antenna 2 has only

one reflection zeroes, which is observed at 5.24 GHz. Although the two antennas have the same radiator configuration for one polarization, different resonant frequencies are observed in the figure. With the combination of electric and magnetic resonances, the ratio of the first reflection zeroes between the Antenna 1 and Antenna 2 is about 1/3, which denotes that a significant size reduction can be achieved by using the proposed structure of Antenna 1.

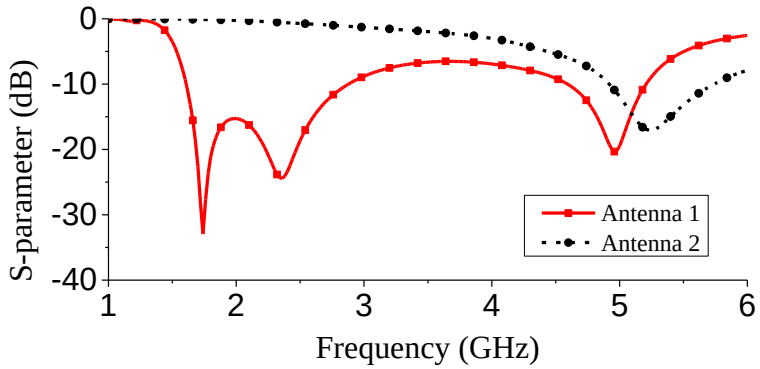

(a)

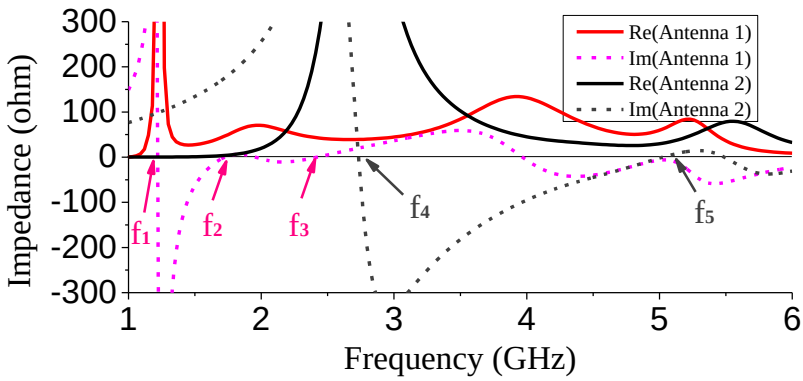

(b)

Figure 3.27 Simulated results of the reference Antenna 1 and Antenna 2. (a) S-parameters. (b) Input impedances.

To clearly illustrate the inner resonance characteristics of the two antennas, the simulated input impedances of the two antennas are shown in Figure 3.27 (b). According to the definition given in [110]-[111], the natural resonance and anti-resonance can be indicated by the input impedance of the antenna. The input impedance $Z_{in}(\omega)$ of the antenna can be defined as

$$Z_{in}(\omega) = R_{in}(\omega) + jX_{in}(\omega) \tag{3.11}$$

where the real part $R_{in}(\omega)$ is the input resistance of the antenna, and the imaginary part $X_{in}(\omega)$ is the input reactance. If $X_{in}(\omega_0) = 0$ and $X'_{in}(\omega_0) > 0$, the frequency ω_0 is defined as the resonance frequency. Contrarily, if $X_{in}(\omega_0) = 0$ and $X'_{in}(\omega_0) < 0$, the frequency ω_0 is defined as the anti-resonance frequency.

As shown in this figure, the first anti-resonance frequency (f_4) of the single-polarized shunt loop Antenna 2 is found at 2.7 GHz with high resistance and fast variated reactance. The first resonance frequency (f_5) is observed at around 5.1 GHz, which is the second order resonance of the shunt loop antenna, and produces a reflection zero at 5.24 GHz. Whereas the first anti-resonance frequency (f_1) of crossed shunt loop Antenna 1 is observed at 1.2 GHz, which is very lower than the first anti-resonance frequency of the single polarized Antenna 2. Two resonance (f_2 and f_3) are observed within the bandwidth at around 1.74 GHz and 2.36 GHz. Considering the values of f_1, f_2, and f_3, it can be inferred that f_3 is the second order of f_1, and f_2 is produced by the incorporation of the other pair of the crossed shunt loops. Therefore, with these two resonances, wide impedance bandwidth can be achieved for Antenna 1.

Figure 3.28 shows the current distributions on the surface of the two antennas. The two reference antennas are excited for +45º polarization, and auxiliary arrows are added to help to illustrate the different resonance characteristics. As shown in Figure 3.28 (a), Antenna 1 can be equivalent as a combination of two electric dipoles (in φ= 45º plane) and two magnetic dipoles (in φ= -45º plane) at the centre frequency of 2.2 GHz. Two electric dipoles are of the same direction, whereas the magnetic dipoles are of the reverse direction. This can be further validated by the H-field and E-field distributions in φ= -45º plane and φ= 45º plane, respectively. As shown in Figure 3.28 (c) and (d), the directions of H-field in the φ= -45º plane of the two magnetic dipoles are reverse, while the directions of the E-field in the φ= 45º plane are same.

Therefore, the resonance characteristics of the two reference antennas are totally different. Antenna 1 is a combination of electric dipoles and magnetic dipoles, and the excited shunt loops are the magnetic dipoles. However, for the excited single-polarized antenna in Figure 3.28 (b), it is equivalent only as four electric dipoles and excited for +45º polarization at the first resonant frequency. Owing to the introduction of magnetic dipoles, the first impedance matching frequency moves to the much lower frequency with the dual-resonance characteristic.

Figure 3.28 (e) and (f) show the current distributions of the Antenna 1 at two reflection zero frequencies of 1.74 GHz and 2.36 GHz. Two different resonances of magnetic resonance and electric resonance can be characterized. It can be seen that, when +45º polarization is excited at the first resonance of 1.74 GHz, strong current distributions are mainly distributed on the top right and bottom left loops of the antenna and form two current loops. Therefore, Antenna 1 can be equivalent as two magnetic dipoles at 1.74 GHz. While

at the second resonance of 2.36 GHz, strong current distributions are mainly concentrated on the top left and bottom right loops, and flow with the same direction. So Antenna 1 can be equivalent as two electric dipoles at 2.36 GHz.

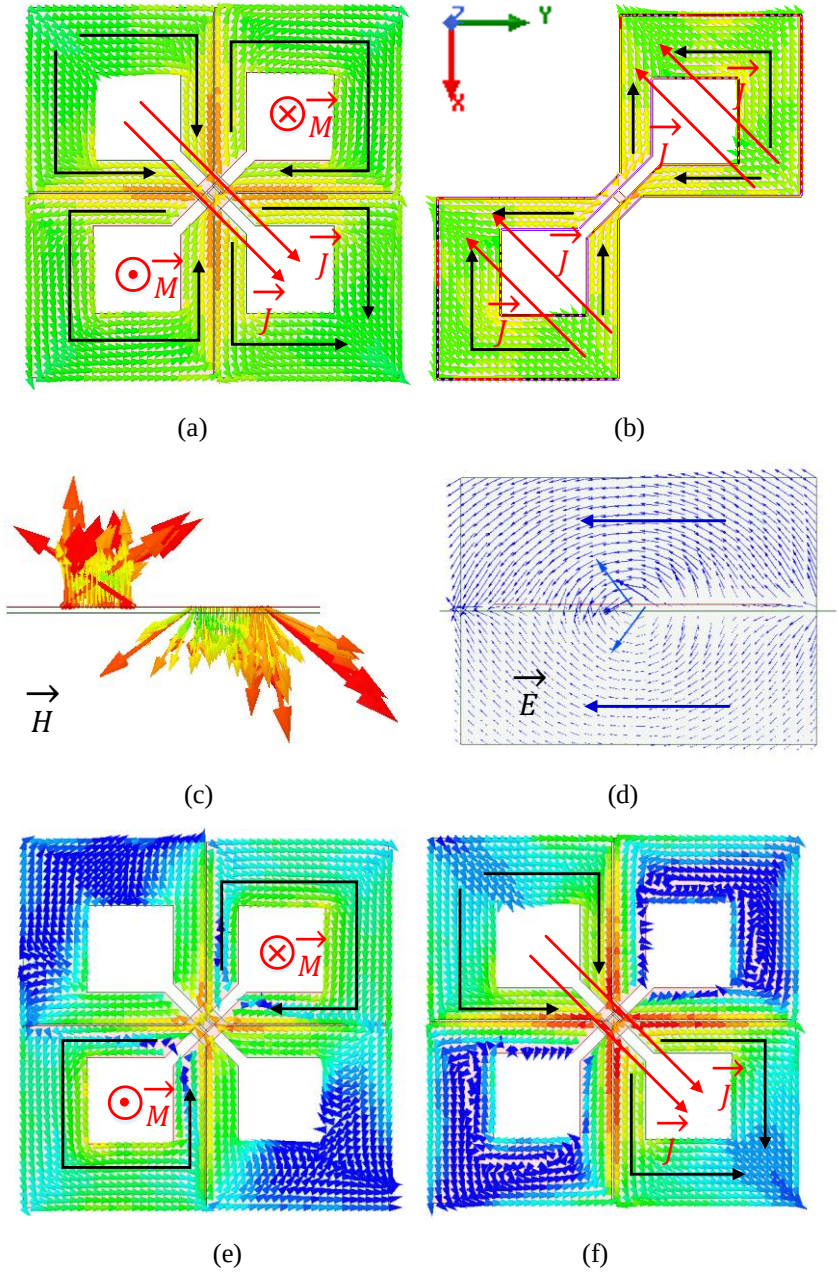

Figure 3.28 Current distributions on the surface of the two antennas:
(a) Antenna 1 at 2.2 GHz. (b) Antenna 2 at 5.24 GHz. H-field and E-field distributions of the reference Antenna 1 at 2.2 GHz: (c) H-field distribution in φ=-45° plane. (d) E-field distribution in φ=45° plane. (e) Current distribution of Antenna 1 at 1.74 GHz. (f) Current distribution of Antenna 1 at 2.36 GHz.

With both the electric and magnetic resonances, wide impedance bandwidth of 1.7-2.6 GHz for S_{11}<-15 dB is achieved for Antenna 1. However, two obvious problems can be seen from Figure 3.29. The first is that the impedance bandwidth is not wide enough to cover the full communication band for current 2G/3G/4G base stations. In addition, the suppression

at the upper band is not very good. The simulated S_{11} from 3.4 GHz to 5 GHz is below -5 dB, and a parasitic resonance can be observed at about 5 GHz. This will bring certain interferences or blockages to the current base station systems if unwanted signals appear at these frequency bands.

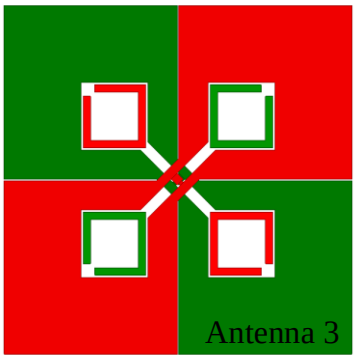

(a)

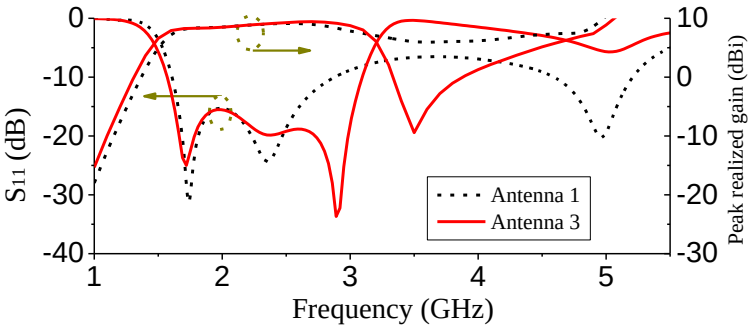

(b)

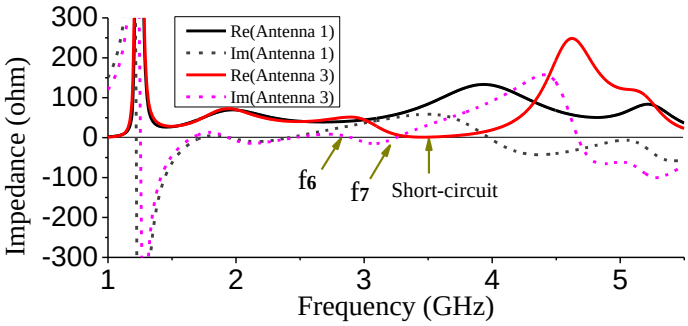

(c)

Figure 3.29 Simulation model and results of reference Antenna 3.
(a) Simulation model. (b) $\boldsymbol{S_{11}}$ and peak realized gain of the reference Antenna 1 and Antenna 3. (c) Input impedances of the reference Antenna 1 and Antenna 3.

To overcome these problems, four parasitic strips are introduced, and they are printed near the inner edge of the loops. The performance of the newly introduced four parasitic strips is illustrated by Antennas 3, and the simulation model is shown in Figure 3.29 (a). The only difference between Antenna 3 and Antenna 1 is the introduction of the four parasitic

strips. As shown in Figure 3.29 (b), the first and second reflection zeroes of Antenna 3 are observed at 1.7 GHz and 2.35 GHz, which are almost the same resonant frequencies as the reference Antenna 1. However, different from Antenna 1, a third reflection zero appears at 2.9 GHz, and a steep roll-off rate is found at the upper band edge for Antenna 3. Another should be noted that a radiation null is observed at 3.5 GHz. Accordingly, a maximum reflection is also found at 3.5 GHz. The newly introduced third reflection zero at 2.9 GHz and the first suppression at 3.5 GHz can also be illustrated by the input impedances of these two antennas, as shown in Figure 3.29 (c). As shown in the figure, when the parasitic strips are added into the Antenna 3, one pair of anti-resonance (f_6) and resonance (f_7) is introduced into the frequency band of interest, which produces the third reflection zero at 2.9 GHz. Moreover, very low resistance is found at 3.5 GHz with the value close to zero, which means the antenna is short-circuited at this frequency. Therefore, strong reflection is found at this frequency, and the radiation at this frequency is highly suppressed.

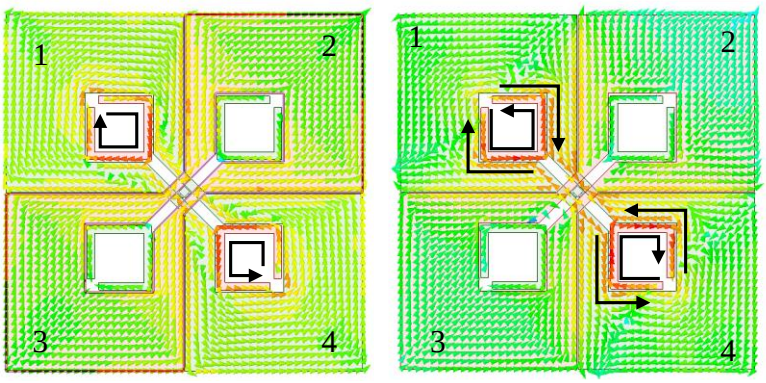

(a) (b)

Figure 3.30 Current distributions on the surface of Antenna 3 at different frequencies.
(a) 2.9 GHz. (b) 3.5 GHz.

To further illustrate new resonance and suppression introduced by the parasitic strips, current distributions of the reference Antenna 3 at the new reflection zero at 2.9 GHz and the first suppression at 3.5 GHz are shown in Figure 3.30. In Figure 3.30 (a), strong current distributions are found on the surface of the two parasitic strips at 2.9 GHz. The strong current distribution on these two strips denotes that the third reflection zero is produced by the resonances of the two parasitic strips. As shown in Figure 3.30 (b) at 3.5 GHz, strong current distributions are distributed not only on the surface of two strips, but also on the inner edge of the two loops. However, the current distributions on the strip and inner edge are opposite, and they cancel each other's radiation in the far field. In addition, the combination of the strip and inner edge works as a quarter wavelength open-circuited

transmission line. Therefore, short-circuit is observed at the antenna input port and high suppression is achieved at 3.5 GHz.

To investigate the effect of the parasitic strips on the reflection coefficient and the realized gain for the proposed antenna, the length of the parasitic strips (L2) and the distance between the parasitic strip and the inner edge of the loop (d2) are studied. Figure 3.31 (a) shows the simulated S_{11} and peak realized gain vary with the different length of the parasitic strips. It can be seen that, as the increase of the length, the third resonance frequency shifts to the lower frequency, and the suppression frequency also moves to the lower frequency. Whereas the first and second resonant frequencies are almost unchanged with the variance of the length of the parasitic strips. This shows that the newly introduced third resonance and the first suppression have nearly no effect on the first and second resonance.

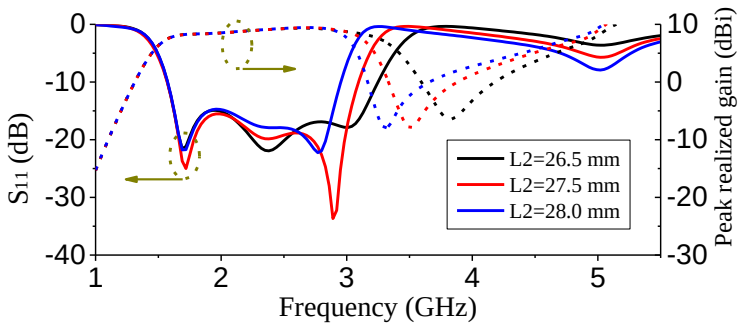

(a)

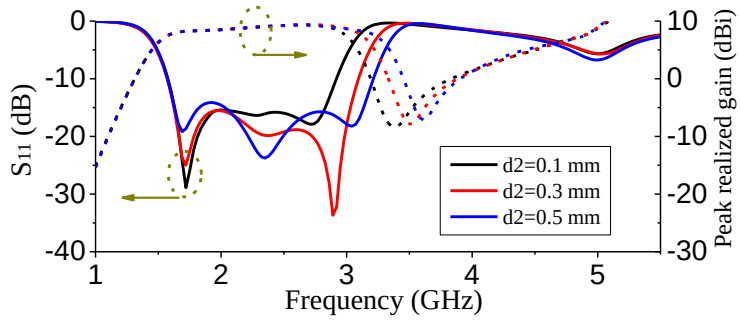

(b)

Figure 3.31 Simulated S_{11} and peak realized gain of Antenna 3. (a) With different length of the parasitic strip (L2). (b) With different distance between the parasitic strip and the inner edge of the loop (d2).

In Figure 3.31(b), as the increase of d2, the first two resonances are almost unchanged. However, with the increase of d2, the capacitance between the parasitic strip and the inner edge of the loop is decreased. Therefore, less energy is coupled from the radiating loops to the parasitic strips, which causes the third resonance and the first suppression to be shifted to higher frequencies. It should be noted that both L2 and d2 can affect the introduced resonance and suppression, but with little effect on the first two resonances. These two

parameters provide much more freedom to adjust the newly introduced resonance and suppression to the desired frequencies.

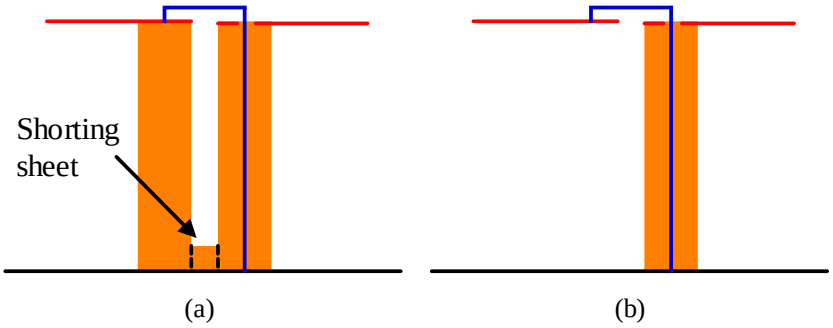

Figure 3.32 Configurations of the feed structures for the proposed antenna. (a) With coaxial balun. (b) With the only coaxial cable.

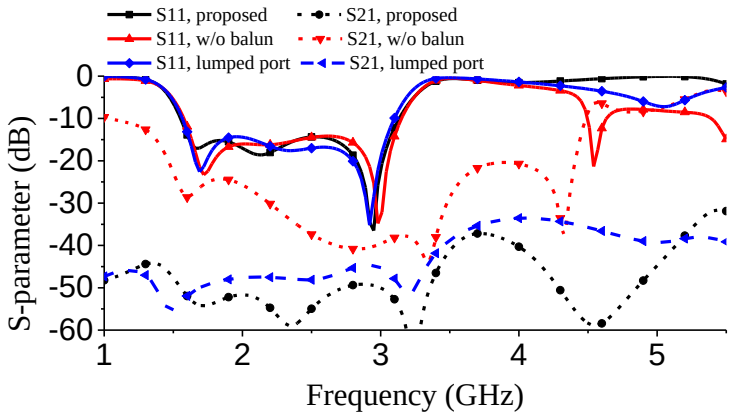

Figure 3.33 Simulated S-parameters with different feed structures.

Crossed coaxial baluns are used to feed the proposed antenna with enhanced port isolation. Furthermore, a second suppression at the desired frequency of 4.9 GHz is achieved by using a shorting sheet at the end of the crossed coaxial baluns. To illustrate the working principle of the baluns, Figure 3.32 compares the different feed configurations for the proposed antenna with the coaxial balun and with the unbalanced coaxial cable. Figure 3.32 (a) shows the side view the proposed antenna fed by the coaxial balun. The outer conductors of the two cables are soldered to two arms of the antenna, while only one inner conductor of the cable is penetrated through one arm and soldered to the other arm of the antenna. Figure 3.32 (b) shows the proposed antenna fed by ordinary unbalanced coaxial cable. The outer conductor is connected to one arm, while the inner conductor is connected to the other antenna arm.

Different impedance performances will be achieved by using two different feed structures. Figure 3.33 compares the simulated S-parameters with different feed structures. In the figure, the simulated results depicted in blue colour is driven by the ideal balanced lumped port,

and the simulated isolation is higher than 45 dB within the bandwidth. With the crossed baluns and the shorting sheet, the simulated isolation is better than 49 dB, which is as good as the ideal balanced lumped port driven antenna. The simulated antenna without baluns shows the worst port isolation, and the simulated isolation is only higher than 24.4 dB. Three simulated antennas show almost the same reflection coefficients within the bandwidth. Furthermore, different suppression levels are observed for the upper out-of-band. The second suppression frequency is observed at about 4.9 GHz for the proposed antenna, and the simulated reflection from 3.4 GHz to 5.4 GHz is higher than -1.7 dB. Whereas the simulated antenna without crossed baluns shows the worst suppression at around 5 GHz with two parasitic resonances. Poor suppression is also observed for the ideal lumped port driven antenna with one out-of-band parasitic resonance.

With the newly introduced shorting sheet at the end of baluns, the second suppression can be adjusted by changing the height of shorting sheet. Figure 3.34 (a) shows the simulated input impedance of the antenna with and without the shorting sheet. It can be observed that, the shorting sheet has little effect on both the antenna input impedance within the bandwidth and the first suppression at 3.5 GHz. However, it can affect the second short-circuit frequency. As shown in the figure, when there is no shorting sheet soldered on the crossed coaxial baluns, the second short-circuit frequency with nearly zero resistance is observed at about 4.5 GHz. After the shorting sheet is introduced with the height of 3 mm, this short-circuit frequency shifts to the desired suppression frequency of 4.9 GHz. Therefore, high suppression is achieved at this frequency.

To further research the working principle of the introduced suppression, the height of the shorting sheet (H1) is studied. As shown in Figure 3.34 (b), with the increase of the height of the shorting sheet, the second suppression frequency moves to the higher frequency. Whereas the in-band impedance matching is almost unchanged. Three resonances within the band are shown with little variance, and the reflection coefficient within the bandwidth is well below -15 dB. The first suppression at 3.5 GHz is also not affected as the variance of H1. It should be noted that, H1=0 mm also denotes that the shorting sheet is not introduced to the crossed coaxial baluns. Observing from the simulated results, H1=3 mm is selected as the height of the introduced shorting sheet.

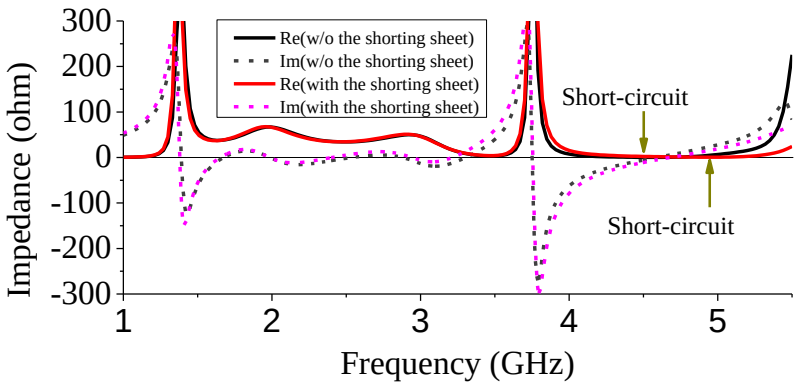

(a)

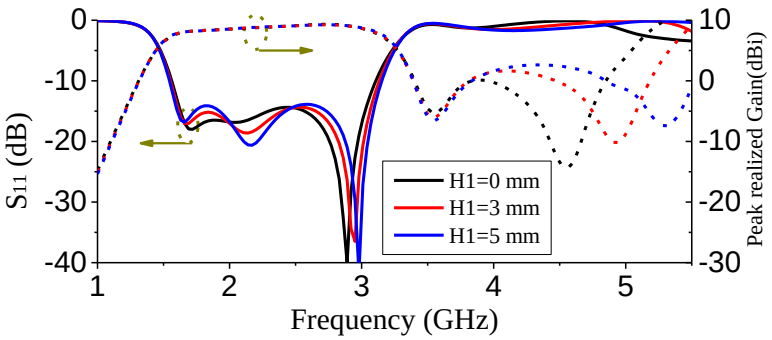

(b)

Figure 3.34 Simulated results of the proposed antenna. (a) Input impedances of the proposed antenna with and without the shorting sheet. (b)S_{11} and peak realized gain with different height of the shorting sheet.

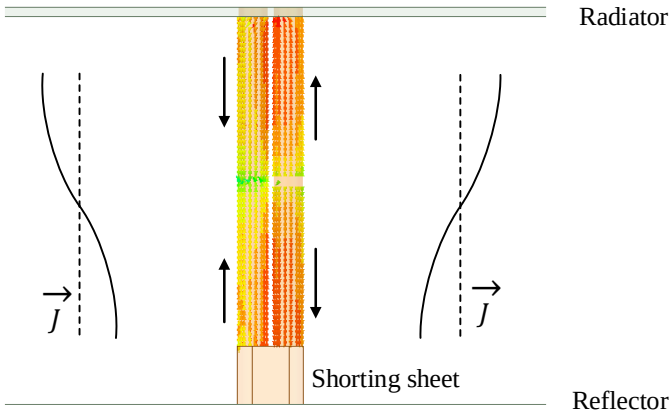

Figure 3.35 Current distribution on the surface of the outer conductors for the proposed crossed coaxial baluns at 4.9 GHz.

Figure 3.35 shows the simulated current distribution on the surface of the crossed coaxial baluns at the second suppression frequency of 4.9 GHz when port 1 is excited, which can help to understand the principle of the second suppression. It can be seen that balanced current distribution is realized on the surface of the crossed coaxial baluns. Maximum current magnitude is observed at the position of both the antenna radiator feed point and the end of the shorting point. At the centre of the balun, there is a current zero. 180 degree

current phase is found at both ends of the balun, and the phases on the two coaxial cables are out-of-phase. At this frequency, the equivalent electric length of the balun is half the guided wavelength. So the feed point at the antenna radiator is short-circuited, and the input impedance will be equal to zero at 4.9 GHz. Therefore, another suppression can be achieved by adjusting the height of the shorting sheet.

3.3.3 Results and Discussion

To validate the antenna design concept, the proposed antenna was designed, fabricated and measured. Figure 3.36 shows the photograph of the fabricated prototype of the proposed dual-polarized antenna. The antenna was measured by Anritsu 37397C vector network analyzer and ASYSOL far field antenna measurement system.

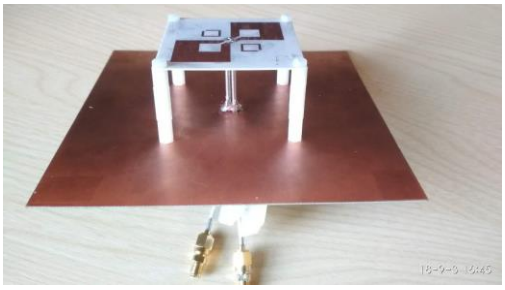

Figure 3.36 Photograph of the fabricated prototype of the proposed dual-polarized antenna.

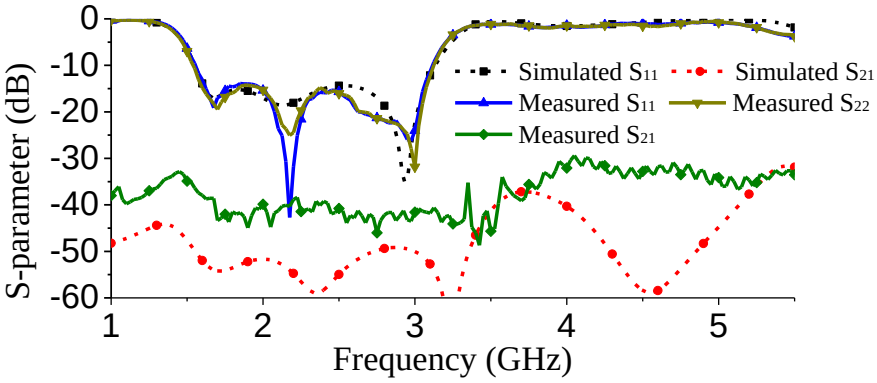

Figure 3.37 Measured and simulated S-parameters of the proposed dual-polarized antenna.

Figure 3.37 compares the measured and simulated S-parameters of the proposed dual-polarized antenna. As shown in the figure, three reflection zeroes can be observed for the reflection coefficients of the two antenna ports, which agree well with the simulated reflection coefficient. The measured overlapped impedance bandwidth for S_{11}/S_{22}<-14 dB is from 1.625 GHz to 3.05 GHz (FBW=61%). In addition, maximum reflection can be seen at 3.5 GHz and 4.9 GHz. Flat upper out-of-band suppression is also observed form 3.35 GHz to 5.25 GHz, with the minimum reflection coefficient higher than -2 dB. The isolation within the bandwidth is better than 38.3 dB. Compared with the simulated isolation, due to the

fabrication and assembly errors, the measured isolation is not better than the simulated isolation. However, owing to the balanced balun feed method, it is better than the reported traditional single-ended coaxial feed dual-polarized antennas.

The measured and simulated radiation patterns are shown in Figure 3.38. Because of the symmetry of the proposed dual-polarized antenna, only H-plane radiation patterns excited by the antenna port 1 are given in the figure. Good agreement can be observed between the simulated and measured radiation patterns. Stable radiation patterns are also achieved within the impedance bandwidth. In addition, very low cross-polarization level can be observed in the broadside direction, which is lower than -28 dB. Owing to the antenna reflector, the measured front to back ratio of the radiation patterns is higher than 17 dB.

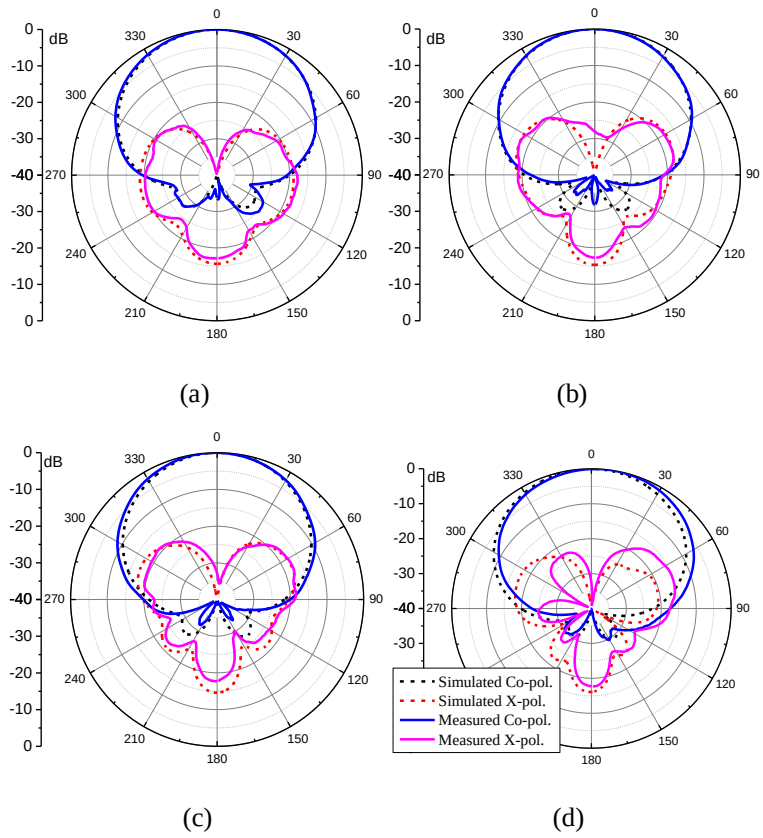

Figure 3.38 Measured and simulated H-plane radiation patterns of the proposed dual-polarized antenna when port 1 is excited. (a) 1.7 GHz. (b) 2.2 GHz. (c) 2.7 GHz. (d) 3.0 GHz.

The measured and simulated half power beamwidth (HPBW) and peak realized gain are shown in Figure 3.39. Good agreement can be observed between the simulated and measured results. The measured HPBW from 1.7 GHz to 3 GHz is 67±5°, and stable HPBW of 67±4° is achieved for the base station band. The deviation of between the simulated and the measured the HPBWs is mainly caused by the fabrication errors from the antenna radiator

and reflector. Regarding the measured HPBW, it is a reasonable result for base station applications [61]. Flat antenna gain of 8.2±0.4 dBi is achieved within the impedance bandwidth. In addition, two deep antenna gain zeroes are observed at 3.5 GHz and 4.9 GHz, which are 18.1 dB and 20.6 dB lower than the maximum antenna gain, respectively.

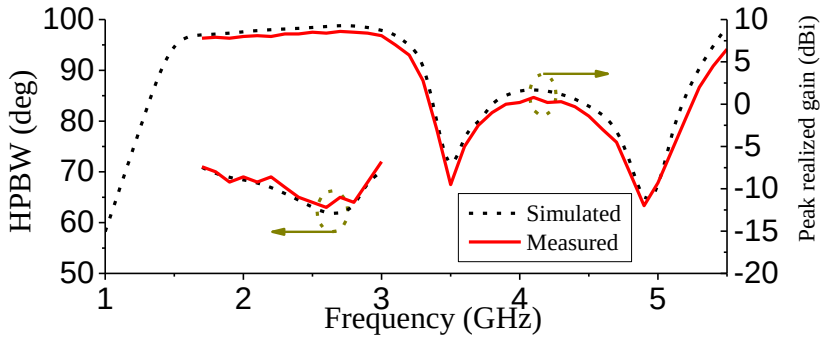

Figure 3.39 Measured and simulated HPBW and peak realized gain of the proposed dual-polarized antenna when port 1 is excited.

Table 3.2 Comparison of the dual-polarized antennas for base stations

Ref.	BW (GHz)	S_{21} (dB)	Radiator Size (mm)	Height (mm)	Suppression at 5G bands
[22]	1.69-2.5 (38.9%) RL>14 dB	-35	69	22	NG
[31]	1.68-2.74 (48%) RL>14 dB	-22	60	31.5	NG
[61]	1.7-2.9 (52.2%) RL>14 dB	-26	63.5	34.8	NG
[99]	1.7-2.2 (25.6%) RL>15 dB	-32	54	38	NG
[114]	1.66-2.75 (49.4%) RL>15 dB	-37	63	35	NG
[115]	1.68-2.74 (48%) RL>14 dB	-35	56	33	NG
This work	1.625-3.05 (61%) RL>14 dB	-38.3	47.5	33	Yes

In recent years, large amounts of dual-polarized antennas are reported for base station applications. However, to the best knowledge of the authors, little of these concerns about the out-of-band suppression. As the development of 5G communication systems, this will definitely bring new inferences to the current 2G/3G/4G base station systems. Therefore, it is necessary to investigate antennas with nature suppression at 5G frequency bands for current base stations. In addition, most of these reported antennas for base stations are

crossed dipoles, which cover 1.7-2.7 GHz. A second-order harmonic resonance band will be normally found at about 3.4-5.4 GHz for crossed dipole antennas. Undesired harmonic radiation from 2G/3G/4G antennas will also produce interference to the 5G base station systems. Fortunately, as shown in Table 3.2, our proposed antenna are demonstrated that two radiation nulls are achieved at 3.5 GHz and 4.9 GHz, and wide upper out-of-band suppression is realized from 3.35 GHz to 5.25 GHz with S_{11}>-2 dB.

Another feature of our proposed antenna is the compact size and high isolation. The length of the square radiator size of the recently reported antennas are around 60 mm. With the incorporation of electric resonance and magnetic resonance, smallest radiator size and widest bandwidth are achieved as compared to the reference antennas shown in the Table 3.2. In addition, by using the integrated coaxial baluns, high port isolation of 38.3 dB is also obtained for base station applications.

3.4 Wideband Dual-Polarized Antenna Using Shorted Dipoles

In this section, a novel wideband ±45° dual-polarized antenna using four printed shorted dipoles is proposed. The four printed dipoles are symmetrically shorted in the centre of the PCB and excited by two crossed feed lines. Compared to the traditional dual-polarized antennas, the proposed antenna has the three important advantages by using the baluns and shorted dipoles. Firstly, thanks to the integrated baluns, the proposed antenna achieves an improved impedance bandwidth of 74.5% (1.69-3.7 GHz) for VSWR<1.5. Secondly, the isolation of two ports is higher than 30 dB over the whole antenna impedance bandwidth because of crossed feed configuration. Thirdly, with the configuration of two pairs of parallel shorted dipoles, a stable gain of 8.0-8.7 dBi and a stable HPBW of 65-70° for 2G/3G/4G base stations are obtained without using any parasitic elements and modifying the reflector. In addition, the proposed antenna has a simple structure and compact size. Because of the wideband impedance bandwidth and good unidirectional radiation property, the proposed antenna is potentially useful for future 5G base stations, radars, satellites and other wireless systems.

3.4.1 Antenna Configuration

The configuration of the antenna is shown in Figure 3.40. As shown in Figure 3.40 (a), the antenna is composed of a PCB etched with the radiator and the feed lines, two 50 Ω RF coaxial cables, and a square reflector. On the bottom layer of the PCB, two pairs of shorted dipoles and four central shorted coplanar strip lines which operate as the baluns are printed.

The top layer consists of two crossed feed lines, which are used to feed the power from the baluns to the radiator. The radiator and feed lines are printed on a low-cost substrate of Rogers 4003C, with ε_r of 3.55 and thickness of 0.813 mm.

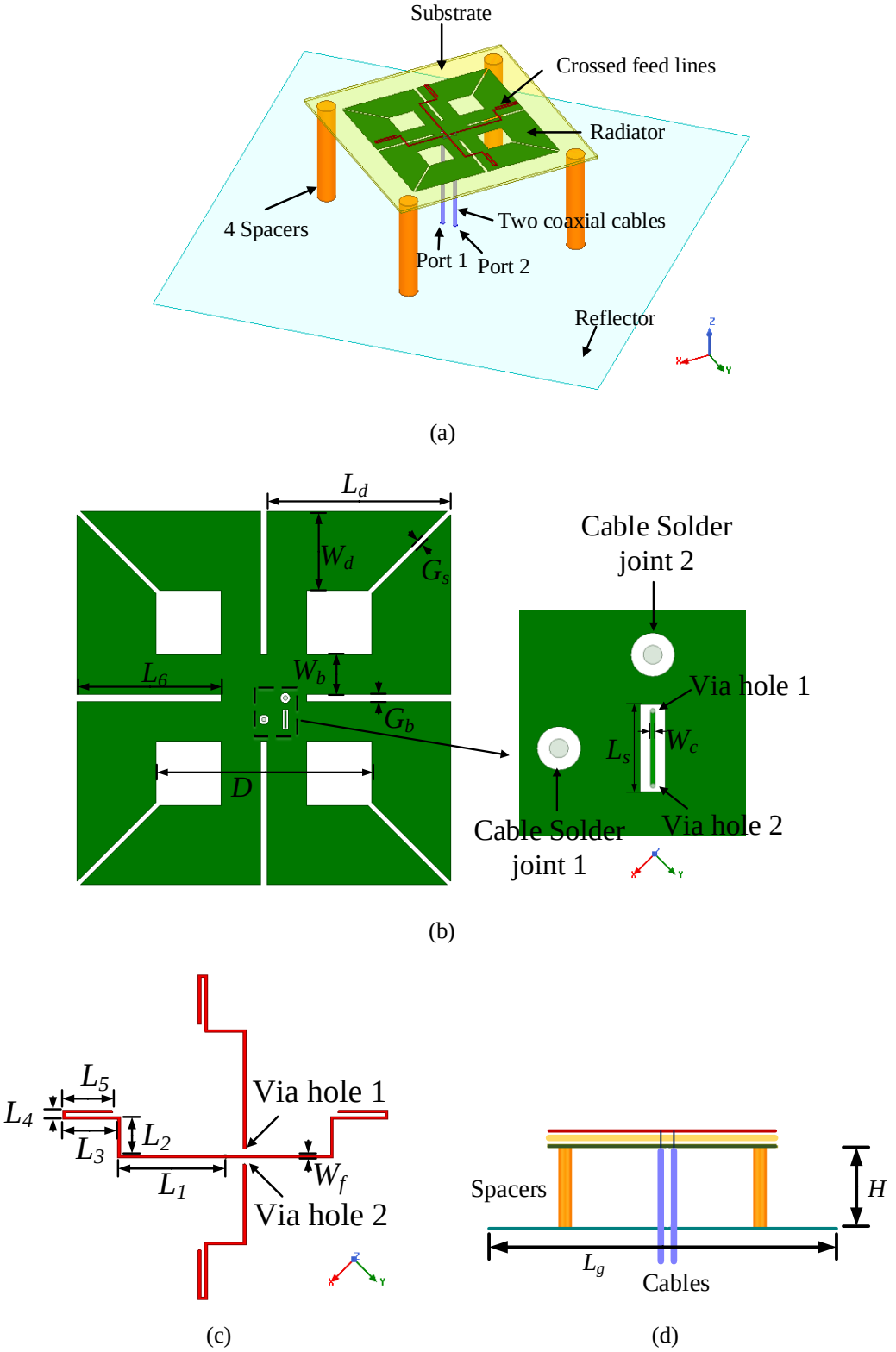

Figure 3.40 The configuration of the proposed antenna. (a) Isometric view of the antenna. (b) Bottom layer of the antenna substrate. (c) Top layer of the antenna substrate. (d) Side view of the antenna.

The geometry parameters of the bottom layer radiator and top layer feed lines are shown in Figure 3.40 (b) and Figure 3.40 (c). The detailed dimensions are listed in Table 3.3. There are two circular slots around the centre of the radiator on the bottom layer, which are used to solder the outer conductor of the two 50 Ω coaxial cables. Two crossed feed lines on the top layer are soldered to the inner conductor of the coaxial cables. There is a rectangular slot close to the two circular slots, which is utilized to avoid the intersection of two crossed feed lines. It should be noted that the vertical feed line is connected by two via holes and a narrow feed line on the bottom layer. Its detailed configuration is zoomed in the right of Figure 3.40 (b). Figure 3.40 (d) shows the side view of the proposed antenna. The height of the radiator to the reflector is selected to 35 mm, which is about $\lambda_0/4$, where λ_0 is the free space wavelength at 2.2 GHz. The proposed antenna is designed for ±45° polarization as shown in the reference coordinate system in Figure 3.40.

Table 3.3 Dimensions of the proposed antenna (mm)

W_b	W_c	W_d	W_f	L_s	L_1	L_2	L_3	L_4
5.5	0.15	11	0.4	2.8	16.5	6	8.5	1
L_5	L_6	L_d	G_b	G_s	D	L_g	H	
7.5	20	25	1	0.7	30	150	35	

3.4.2 Working Principle

To investigate the wideband characteristic of the proposed antenna, the equivalent circuit of the antenna is shown in Figure 3.41. Due to the symmetry of the antenna structure, only one polarization is analyzed. As shown in the figure, port 1 is connected by a coaxial cable with the characteristic impedance of $Z_0 = 50\ \Omega$. Then it is connected by two identical baluns, which transform the input impedance of dipoles (Z_A) to the characteristic impedance of the microstrip feed lines (Z_1). For the design of the balun, the characteristic impedance of the crossed feed line (Z_1) is designed as 100 Ω to match the high impedance of the coplanar strip line (Z_s). In addition, the parallel configuration of two 100 Ω feed lines is also designed to match the 50 Ω coaxial cable. The characteristic impedance and the length of the shorted coplanar strip line are Z_s and L_6. The characteristic impedance of the open stub is Z_1, with the length of $L_o = L_2/2 + L_3 + L_4 + L_5$.

According to the equivalent circuit in Figure 3.41, the input impedance of the wideband balun Z_{in} can be expressed as [112]

$$Z_{in} = -jZ_1 cot\theta_1 + jZ_s tan\theta_s \,||\, Z_A \tag{3.12}$$

where θ_1 is the electrical length of open stub, and θ_s is the electrical length of the shorted coplanar strip line. When the input impedance (Z_{in}) equals the characteristic impedance (Z_1), the proposed antenna obtains impedance matching. Assuming $Z_A = Z_s$, the equation (3.12) can be simplified to:

$$Z_{in} = Z_s sin^2\theta_s + jZ_s sin\theta_s cos\theta_s - jZ_1 cot\theta_1 \tag{3.13}$$

Assuming that the electrical length of open microstrip stub equals the electrical length of coplanar strip line:

$$\theta_s = \theta_1 = \theta \tag{3.14}$$

Then, considering the configuration of the proposed antenna, the conditions for equation (3.12) are: $Z_s = Z_A = 120\ \Omega$, and $Z_1 = 100\ \Omega$. Then the solutions for θ are

$$\begin{cases} \theta_0 = 90° \\ \theta_1 = 65.91° \\ \theta_2 = 114.09° \end{cases} \tag{3.15}$$

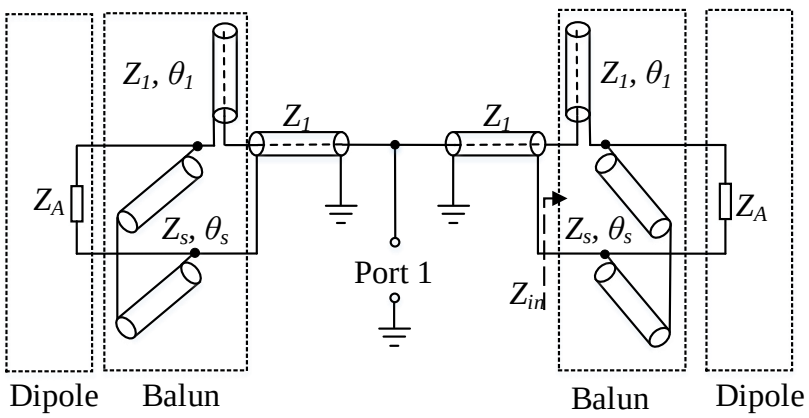

Figure 3.41 Equivalent circuit of the proposed antenna for one polarization.

The curves of the input impedance Zin for the above conditions are shown in Figure 3.42 (a). It is observed that when θ_0=90°, Z_{in}=120 Ω, and when θ_1=65.91° and θ_2=114.09°, Z_{in}=100 Ω, the balun transforms the antenna input impedance Z_A (120 Ω) to Z_1 (100 Ω). The image part has three zeroes, and θ_1 and θ_2 are symmetrical to θ_0.

Therefore, a wide impedance bandwidth can be obtained for the proposed antenna by integrating the shorted dipoles and baluns. Figure 3.42 (b) shows the simulated input impedance from the antenna port 1. All the simulation works in the thesis are obtained by 3D electromagnetic simulation software, ANSYS HFSS 2017. It is can be seen that the proposed antenna has multi-resonance characteristic. Within the interested frequency band from 1.5 GHz to 4 GHz, the imaginary part of the input impedance has six zeroes, and the real part maintains stable around 50 Ω.

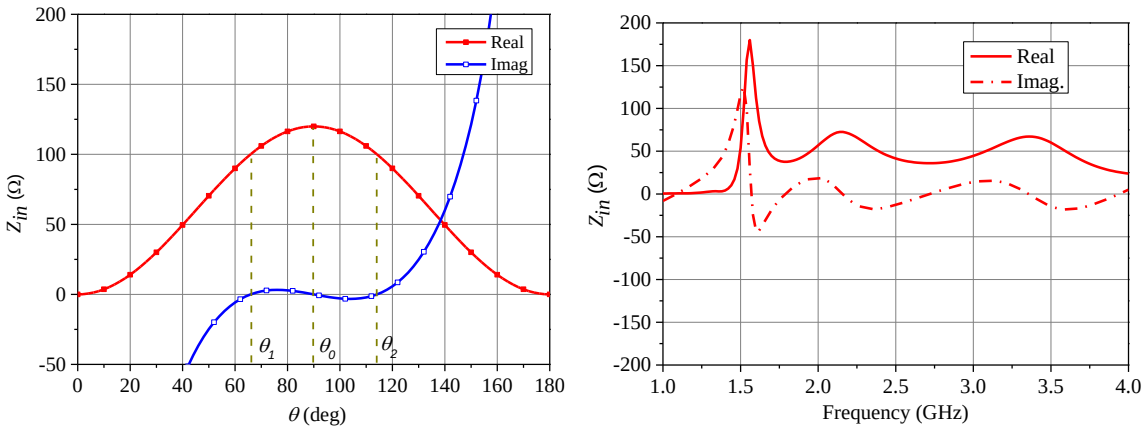

Figure 3.42 (a) Input impedance of Z_{in} for equation (3). (b) Simulated input impedance of antenna port 1.

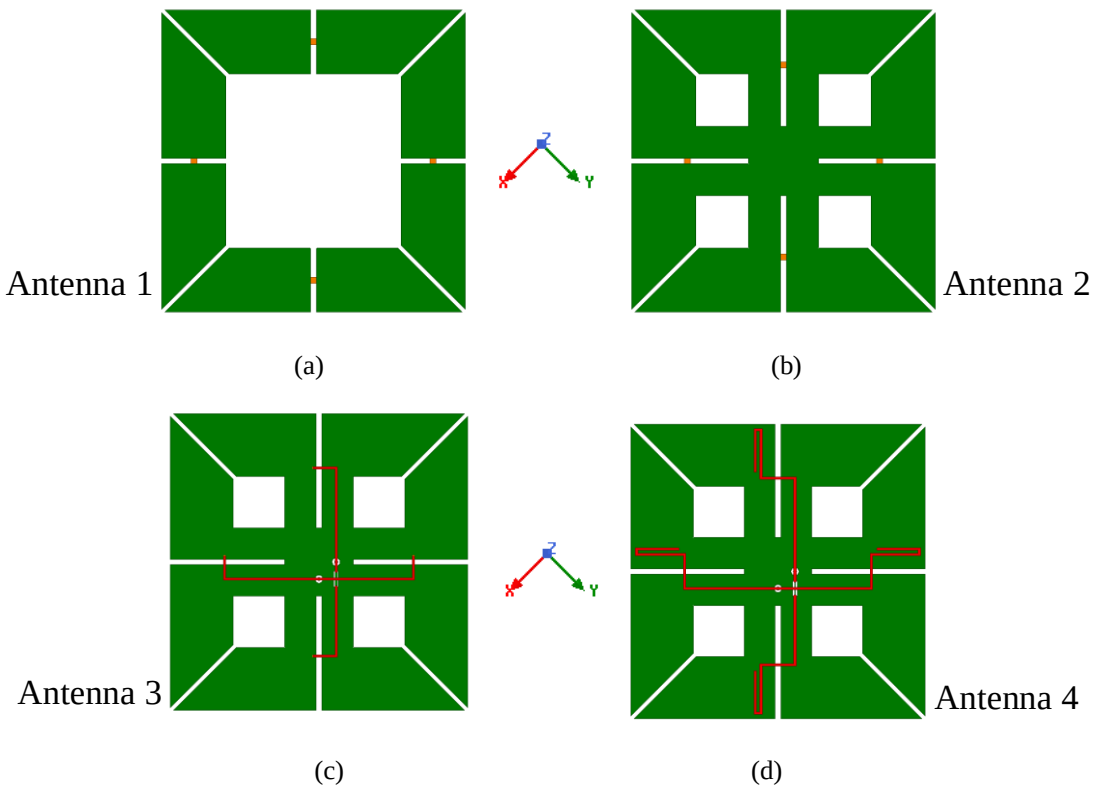

Figure 3.43 Design flow of the proposed dual-polarized antenna.
(a) Antenna 1 (Four printed dipoles excited with same magnitude and phase for each polarization). (b) Antenna 2 (Four printed dipoles shorted in the centre by coplanar strip lines). (c) Antenna 3 (The proposed antenna without the open stub). (d) Antenna 4 (The proposed wideband dual-polarized antenna).

To explain the design approach better, the design flow of the proposed dual-polarized antenna is illustrated in Figure 3.43. Antenna 1 is the simple four printed dipoles, two parallel dipoles are excited with same magnitude and phase for each polarization respectively. Antenna 2 is the four dipoles shorted in the centre by coplanar strip lines. Both Antenna 1 and Antenna 2 are excited with ideal lumped ports in the simulation. Antenna 3

is the proposed antenna without the open stub. Instead, four conducting via holes are inserted to feed the four dipole pairs. Antenna 4 is the proposed wideband dual-polarized antenna.

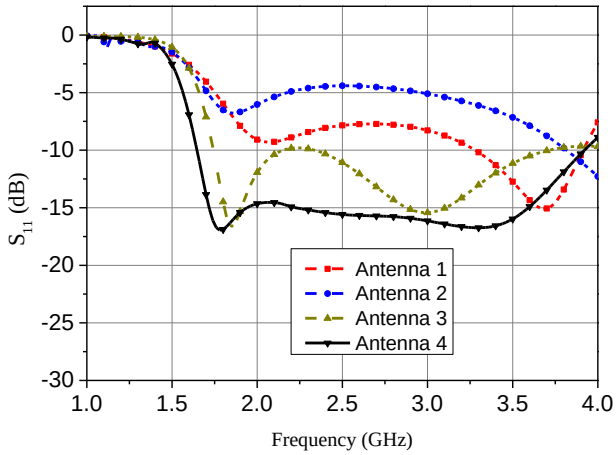

Figure 3.44 Simulated S_{11} for the evolution antennas.

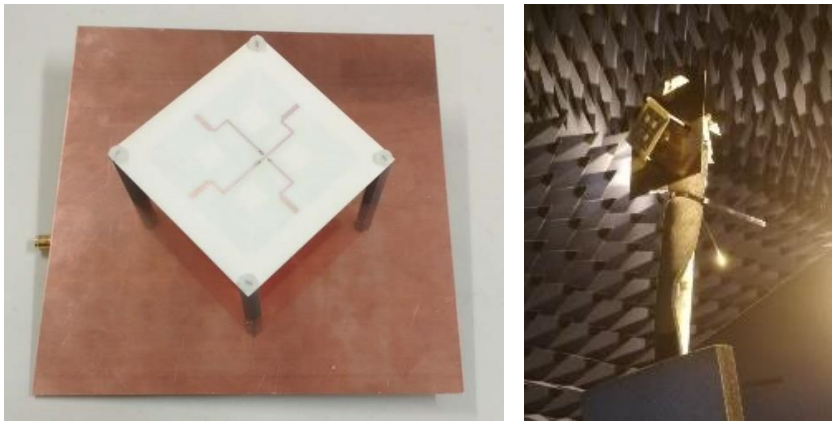

(a) (b)

Figure 3.45 Prototype of the fabricated dual-polarized antenna. (a) Photograph of the proposed antenna. (b) Antenna under measurement in the anechoic chamber.

The simulated reflection coefficients of the four antennas are shown in Figure 3.44. As can be seen, Antenna 1 shows a poor reflection coefficient. After incorporating the shorted strip lines, the reflection coefficient for Antenna 2 is even worse. However, the first reflection zero shifts to the lower frequency compared to Antenna 1. As the crossed feed lines are inserted into Antenna 3, the reflection coefficient gets much better and becomes lower than -10 dB. This improvement is mainly attributed to the contribution of the baluns, even if without the open stub. With the open stubs incorporated into the baluns for the proposed design (Antenna 4), the first reflection zero moves to even lower frequency, and the third reflection zero appears in the frequency band of interest. The simulated impedance bandwidth for S_{11} lower than -14 dB is increased from 1.7 GHz to 3.6 GHz.

3.4.3 Results and Discussion

A prototype of proposed antenna was fabricated and measured. The photographs of the fabricated antenna and its measurement in the anechoic chamber are shown in Figure 3.45. The antenna was measured at University of Kent, UK. Both the simulated and measured VSWR and isolation are provided in Figure 3.46 for comparison. The overlapped impedance bandwidth for both ports is 74.5% (from 1.69 GHz to 3.7 GHz) for VSWR<1.5, which is slightly wider than the simulated results, which is caused by the fabrication tolerance. The VSWR of port 2 is slightly worse than port 1. This is due to the via hole configuration which is used to avoid the intersection, but the VSWR is still good below 1.5. The measured isolation between the two ports is higher than 30 dB over the whole impedance bandwidth, which agrees well with the simulated result.

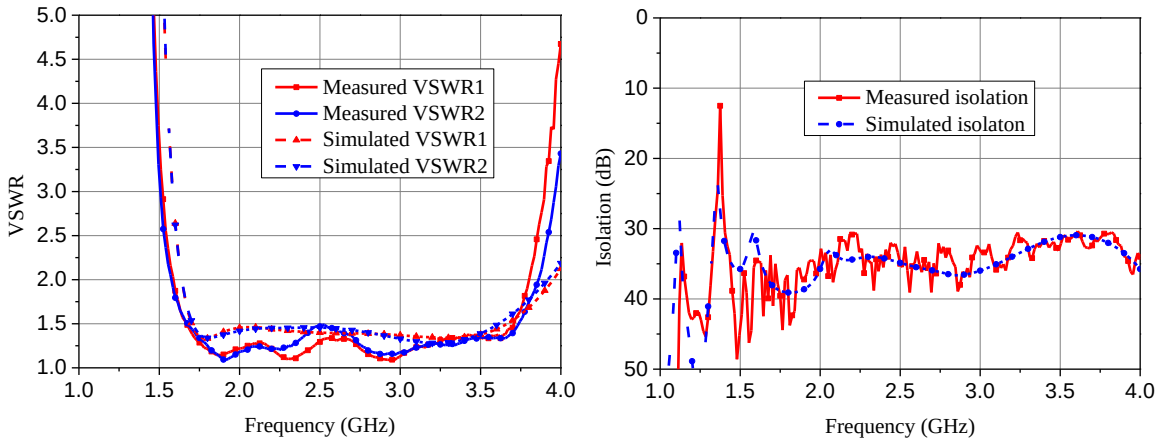

(a) (b)

Figure 3.46 Measured and simulated (a) VSWR and (b) isolation of the proposed antenna.

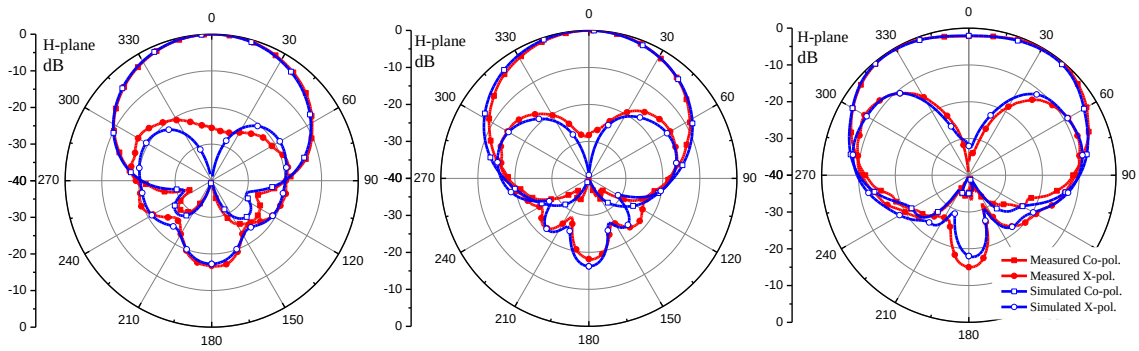

(a) (b) (c)

Figure 3.47 Measured and simulated normalized radiation patterns of the proposed antenna. (a) 1.7 GHz. (b) 2.7 GHz. (c) 3.6 GHz.

To illustrate the radiation patterns, the xz plane is defined as the H-plane (Horizontal plane) and yz plane is defined as the V-plane (Vertical plane). Radiation patterns in the H-plane are given in Figure 3.47. It is can be seen that the measured radiation patterns agree well

with the simulated results. The measured XPD at the boresight direction is higher than 25 dB for base station communication frequency band (1.7 GHz ~ 2.7 GHz), and the XPD is even better at the remains upper frequency band. Figure 3.48 shows the measured and simulated gain and HPBW. The measured HPBW is between 65° and 70° from 1.7 GHz to 2.7 GHz, while the gain is from 8 dBi to 8.7 dBi. The HPBW increases to 117°and the gain decreased to 5.4 dBi at 3.6 GHz.

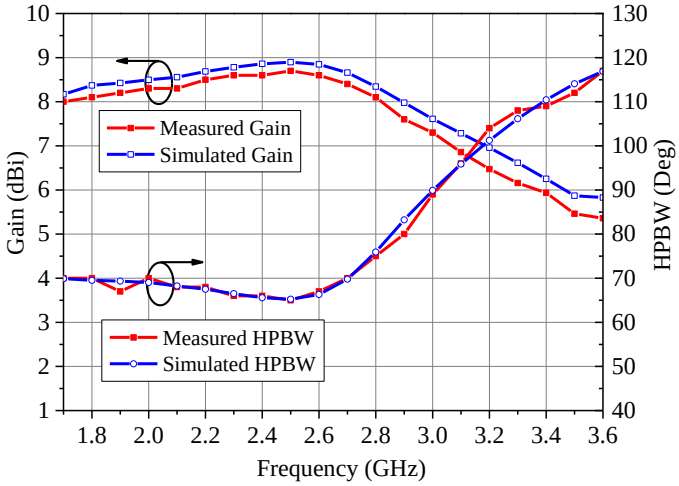

Figure 3.48 Measured and simulated antenna gain and HPBW.

Table 3.4 Comparison of the dual-polarized antennas for base station applications.

Antennas	Size (mm×mm×mm)	Bandwidth	Isolation (dB)	Radiation for base stations		Modification to the reflector
				Gain (dBi)	HPBW (deg)	
[24]	300×145×34.7	1.63 -2.95 GHz VSWR<1.5	>31	8.2-8.8	Not Given	Yes
[29]	200×134×36	1.7 -2.7 GHz RL>15 dB	>30	About 8.5	Around 65	Yes
[36]	140×140×34	1.7-2.7 GHz VSWR<1.5	>25	7.6-8.8	66-70	Yes
[38]	150×150×32.5	1.7-2.9 GHz VSWR<1.5	>35	7-8.6	Not Given	No
[45]	160×160×28	1.7 -2.73 GHz RL>10 dB	>38	>9.3	Not Given	No
[61]	140×140×34	1.7 -2.9 GHz VSWR<1.5	>26	About 8.5	63-69	Yes
[62]	160×160×40	1.7 -2.75 GHz RL>15 dB	>45	About 9	57-73	No
This work	150×150×35	1.7 -3.7 GHz VSWR<1.5	>30	8-8.7	65-70	No

Table 3.4 compares the proposed antenna with other recently reported dual-polarized antennas that operate at the similar frequency band. It is found that with a relatively compact size, the impedance bandwidth of the proposed antenna is wider than these reported designs due to the multi-resonance characteristic and the wideband baluns employed in the design. Furthermore, the proposed antenna has very stable radiation characteristic for base station applications. Therefore, there is no need to modify the reflector to stabilize the radiation property, which can decrease the design complexity and cost of the antenna.

3.5 Filtering Array Antenna With Low Sidelobes

In this section, a steep roll-off rate filtering patch antenna with a fourth-order coupling structure is presented. Inspired by the previous research works in [116] and [117], split ring resonators and hairpin resonators are used to excite the antenna radiating patch with improved impedance bandwidth. However, different from these works, by using the proposed novel coupling structure, balanced coupling feed method is used to reduce the cross-polarization of the antenna, which overcomes the problem of the cross-polarization deterioration due to the resonators and slots loading effects. Furthermore, a short slot etched on the ground plane is introduced to further enhance the antenna frequency selectivity. By using the cross coupling between the split ring resonator and patch, two controllable radiation nulls are obtained. Therefore, low cross-polarization lever (<-31 dB) and high out-of-band suppression (>31 dB) with two radiation nulls and fourth-order filtering response are achieved. Detailed analysis of antenna working principles, including the antenna coupling structure, controllable radiation nulls, and reduced cross-polarization, are illustrated and discussed in this paper. Using the developed antenna element, a low-sidelobe filtering antenna array optimized by differential evolution algorithm is also designed for low interference applications. Both of the filtering antenna element and the antenna array are designed, fabricated, and measured to validate the antenna design concept.

3.5.1 Antenna Element Design

The configuration of the proposed antenna element is shown in Figure 3.49. The antenna element is composed of three copper layers. The top layer is the radiating patch, the centre layer is the ground plane etched with coupling slots, and the bottom layer is the feed resonators. In Figure 3.49 (a), the length of the square patch is about 0.5 λ_g, where λ_g is the guided wavelength at the centre frequency. Three slots are etched on the ground plane, as shown in Figure 3.49 (b). The two long slots have the same length and width, and they are

utilized to couple energy to the patch with equal magnitude and co-phase excitation. Whereas the short slot is the weak cross coupling slot, which plays an important role on the improvement of the antenna frequency selectivity.

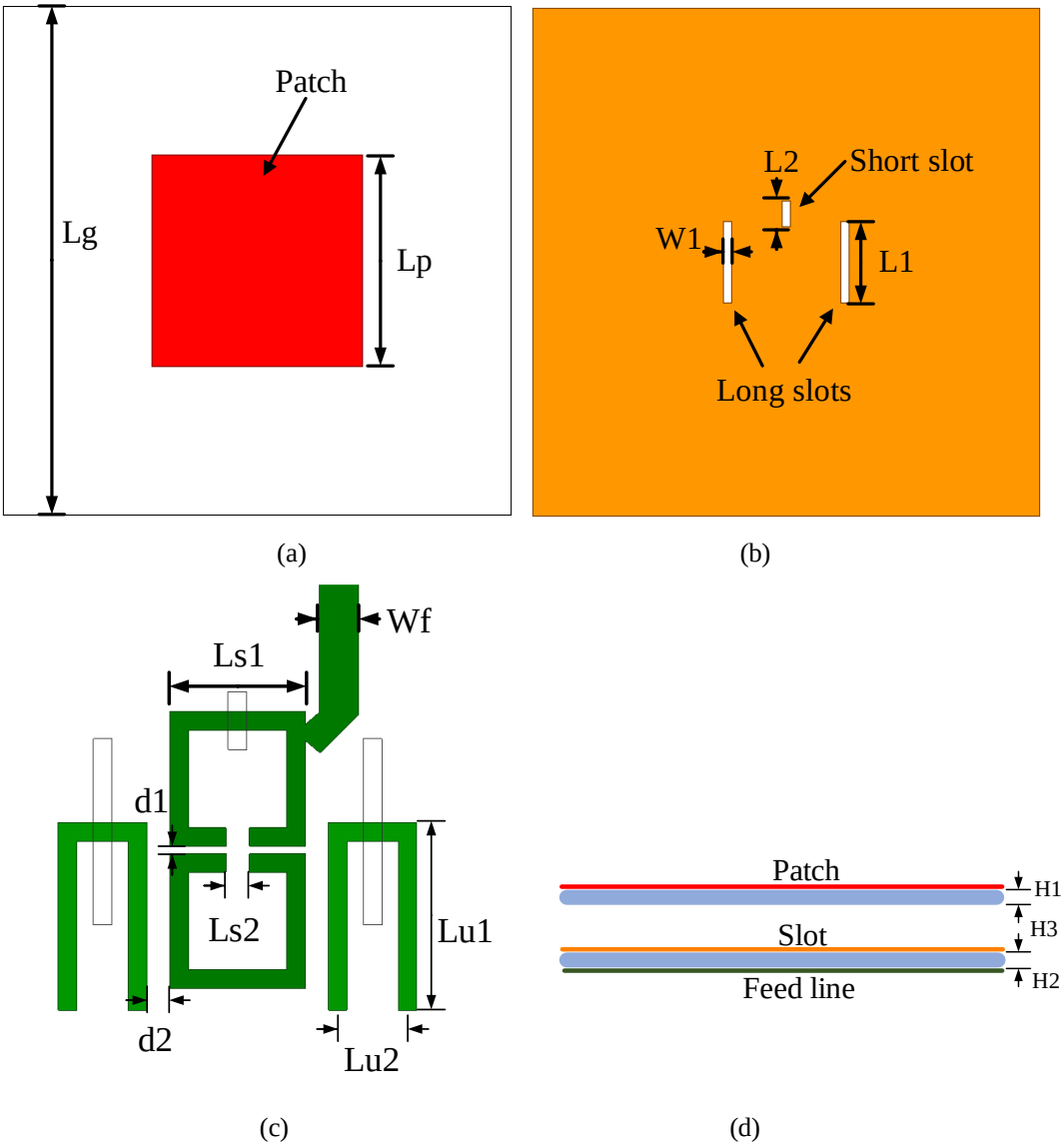

Figure 3.49 Configuration of the proposed antenna.
(a) Square patch. (b) Ground plane with slots. (c) Resonators. (d) Side view. Detailed antenna design parameters: Lp= 20.2 mm, Lg= 50 mm, W1= 0.8 mm, L1= 8 mm, L2= 2.5 mm, Wf= 1.7 mm, Lu1= 7.3 mm, Lu2= 3 mm, Ls1= 5 mm, Ls2= 1 mm, d1= 0.3 mm, d2= 0.9 mm, H1= H2= 0.813 mm, H3= 2 mm.

Four resonators including two square split ring resonators and two hairpin resonators are used to excite the top patch, as shown in Figure 3.49 (c). All of these resonators have the length of about half guided wavelength at the centre frequency, and operate at the same resonant frequency. The energy from the 50 Ω microstrip feed line flows to the split ring resonators. Then, the energy is divided into two balanced parts by two hairpin resonators. After that, it is coupled to the top patch by the two identical and symmetrical slots with the

equal magnitude and co-phase feed. It should be noted that the short slot etched on the ground plane is introduced to produce two controllable radiation nulls. The coupling energy here is weak compared to the long slots. The short slot is designed as the cross coupling in the coupling structure. The detailed working principles of the proposed antenna, including the balanced coupling structure and realization of two controllable radiation nulls, are illustrated in the following paragraphs.

The antenna element consists of two Rogers 4003C substrate layers, with the dielectric permittivity of 3.55, and thickness of 0.813 mm. The two substrates are separated by four nylon spacers with the height of 2 mm. The side view of the proposed antenna is shown in Figure 3.49 (d). Detailed antenna design parameters are listed in the figure caption.

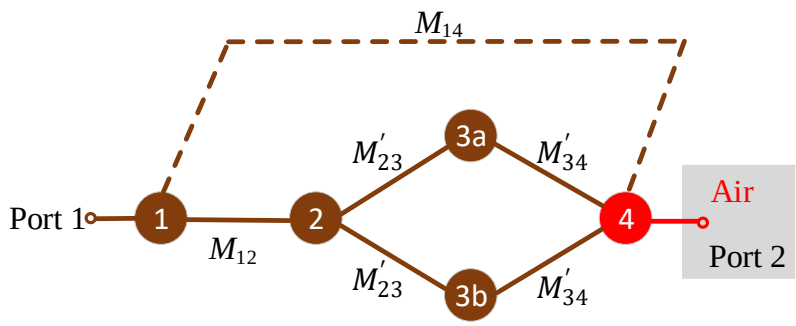

Figure 3.50 Coupling structure of the proposed antenna.

The proposed antenna has a multi-resonance filtering characteristic owing to the loading of split ring resonators and hairpin resonators. Moreover, by using a short slot etched on the ground, the weak cross coupling is utilized to realize two controllable radiation nulls with skirt roll-off rate. To illustrate the antenna working principles, the coupling structure of the antenna is shown in Figure 3.50. In this figure, resonators 1 and 2 are the split ring resonators. Resonators 3a and 3b are the hairpin resonators, which are used to excite the antenna with balanced coupling feed. Resonator 4 is the top radiating patch. The solid lines between each resonator or the antenna patch represent the strong couplings, and the corresponding coupling coefficients are denoted as M_{12}, M'_{23} and M'_{34}. The dash line between the first split ring resonator and the antenna patch represents the weak cross coupling, and the coupling coefficient is expressed as M_{14}. It should be noted that the coupling for M'_{34} is realized by the two long slot underneath the patch, whereas the cross coupling for M_{14} is obtained by the short slots. Both of the desired coupling strength for M'_{34} and M_{14} can be achieved by controlling the length and the width of the long slots and short slots.

Using the coupling structure, if we put a port at the end of the patch, as shown in Figure 3.50, the corresponding S-parameters for the fourth-order filter can be expressed as [118]

$$S_{21} = 2[A]_{41}^{-1}/\sqrt{q_{e1}q_{e4}} \tag{3.16}$$

$$S_{11} = \pm(1 - 2[A]_{11}^{-1}/q_{e1}) \tag{3.17}$$

$$[A] = [q] + p[U] - j[m] \tag{3.18}$$

where $[U]$ is the 4×4 unit matrix, $[q]$ is an 4×4 matrix with all entries of zeroes, except for $q_{11} = 1/q_{e1}$ and $q_{44} = 1/q_{e4}$, and $[m]$ is the normalized 4×4 coupling matrix. These entries for the matrix $[m]$ are needed to be determined to guide the design of the proposed filtering antenna.

In the filter design, different coupling types, including magnetic and electric coupling, are essential to realize different filtering performances, such as the in-band selection and the out-of-band suppression characteristics. Therefore, the first step is to determine which types of coupling can be used to realize filter response. Figure 3.51 shows the current distribution on the surface of the resonators simulated by using ANSYS HFSS. As shown in the figure, strong current distribution is observed on the centre of hairpin resonators and split ring resonators. The current on the two hairpin resonators flows with the same direction below the coupling slots. All the resonators are designed to operate at the same frequency. Therefore, if the coupling coefficient of the magnetic coupling is defined as positive, then, the coupling coefficient of electric coupling is negative. According to the current distribution, the conditions for the normalized coupling coefficients can be derived

$$\begin{aligned} &m_{12} < 0 \\ &m_{23}, m_{34}, m_{14} > 0 \end{aligned} \tag{3.19}$$

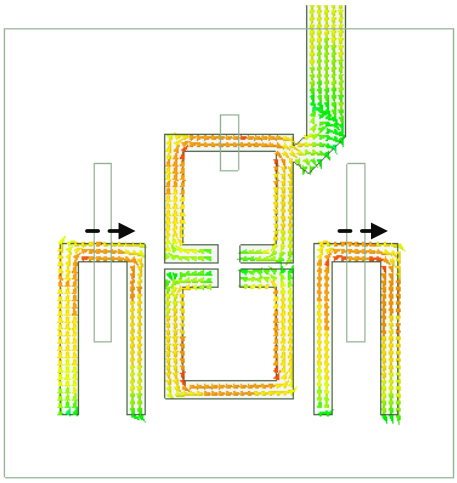

Figure 3.51 Current distribution on the surface of the resonators.

After determining the different coupling types for the proposed antenna, another step is to determine the relations between m_{23}, m_{34}, m'_{23}, andm'_{34}. Owing to the symmetry of the

coupling structure, the entries of m_{23} and m_{34} have the following relations with the balanced coupling coefficients m'_{23} and m'_{34}.

$$m_{23} = \sqrt{2}\, m'_{23}$$
$$m_{34} = \sqrt{2}\, m'_{34} \tag{3.20}$$

Therefore, to realize a filtering response with S_{11}< -20 dB and FBW=0.1, the synthesized result for $Q_e = q_e/FBW$ is 9.68, and the synthesized result for synchronously tuned coupling matrix $[M] = [m] \times FBW$ is

$$[M] = \begin{bmatrix} 0 & -0.0867 & 0 & 0.0143 \\ -0.0867 & 0 & 0.0803 & 0 \\ 0 & 0.0803 & 0 & 0.0936 \\ 0.0143 & 0 & 0.0936 & 0 \end{bmatrix} \tag{3.21}$$

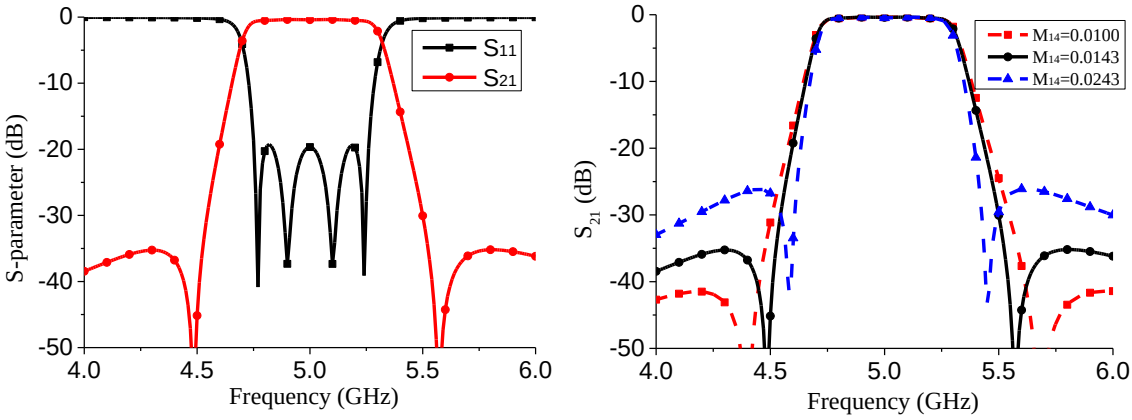

(a) (b)

Figure 3.52 (a) Filtering response for the proposed coupling structure. (b) Filtering response with varying cross coupling coefficient.

Based on the above calculations, the filtering response of the proposed coupling structure is shown in Figure 3.52 (a). The synthesized S_{11} is lower than -20 dB within the bandwidth, and two transmission zeros are observed at about 4.5 GHz and 5.6 GHz. In addition, by controlling the cross coupling strength (M_{14}), two controllable transmission zeroes are obtained, which is shown in Figure 3.52 (b). When the cross coupling becomes stronger, the two transmission zeroes move closer to each other. This implies that it will be possible to obtain two controllable radiation nulls by adjusting the dimensions of the cross coupling slot.

To verify the consistency of the proposed coupling structure and the desired filtering response, the filtering antenna is designed based on the calculated coupling matrix in (3.21). The coupling coefficients and external quality factors are extracted by using the methods presented in [116] and [118]. According to the synthesized filtering response, the proposed antenna will radiate with two radiation nulls. This is demonstrated by the simulated peak realized gain with and without the cross coupling slot. As shown in Figure 3.53 (a), when

the centre short slot is removed out of the ground plane, two radiation nulls are disappeared from the curve of the antenna peak realized gain, and the out-of-band suppression is deteriorated with flatter roll-off rate. When the short slot is introduced on the ground plane, two radiation nulls are produced with skirt roll-off rate and increased out-of-band suppression.

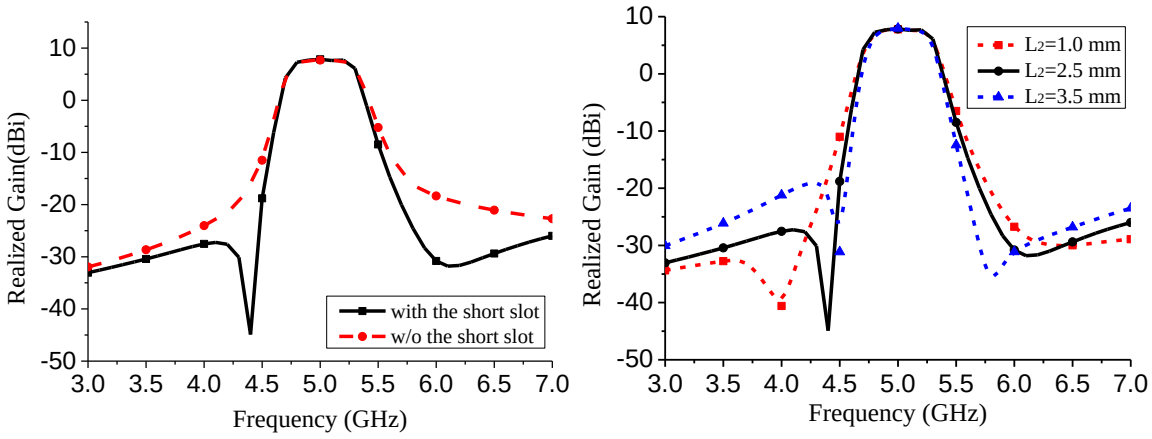

(a) (b)

Figure 3.53 Simulated realized gain varies (a) with and without the short slot, (b) with different L2.

To demonstrate the controllability of the two radiation nulls, as indicated by the filtering response in Figure 3.52 (b), the length of the short slot (L2) are parametrically studied. As shown in Figure 3.53 (b), when L2 is increased from 1.0 mm to 3.5 mm, both radiation nulls move closely to the centre frequency. One should be noted that there is a little different for the two sides of the out-of-band. In the parametric study, the lower out-of-band suppression is a little higher than the upper out-of-band suppression when L2=1 mm. The roll-off rate for the lower band edge is steeper than the upper band edge when L2=3.5 mm. To get a similar rejection level beside the operation band, L2=2.5 mm is selected in this design. The simulated overlapped rejection level for the upper and lower out-of-bands is higher than 32 dB.

By integrating the resonators into the antenna, another benefit is the enhancement of the impedance bandwidth. Figure 3.54 compares the S_{11} between the reference antenna and the proposed antenna. The reference antenna shown in Figure 3.54 has the same configuration as the proposed antenna, including the same substrate and the same air gap between the two substrates, except that it has a simple aperture feed configuration. It should be noted that the reference antenna has been optimized to obtain the largest possible impedance bandwidth.

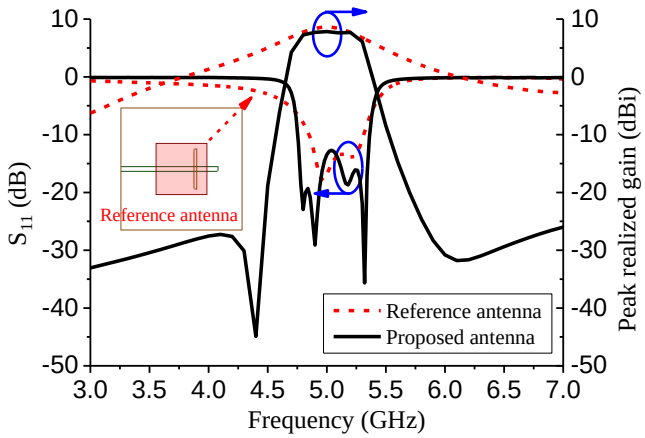

Figure 3.54 Comparison of S_{11} and peak realized gain between the reference antenna and the proposed antenna.

As shown in Figure 3.54, the proposed antenna has a wider bandwidth than the reference antenna. The simulated results show that impedance bandwidth ($S_{11} < -10\ dB$) for the reference antenna is 4.86-5.3 GHz (8.6%), while the impedance bandwidth for the proposed antenna is 4.7-5.3 GHz (12%). Thanks to the loading of the resonators, four reflection zeros are observed for the proposed antenna. In addition, steep roll-off rate is observed at the band edges of both S_{11} and the peak realized gain. More importantly, two radiation nulls are observed for the peak realized gain. Compared to the referenced antenna, the out-of-band suppression is improved by more than 23 dB. Although the simulated peak realized gain for the proposed antenna within bandwidth is about 0.6 dB lower than the reference antenna, its filtering response is more appealing with flatter in-band antenna gain and higher out-of-band suppression.

Owing to the balanced dual-slot coupling feed, the proposed antenna radiates with low cross-polarization. Figure 3.55 compares the normalized radiation patterns between the proposed antenna and the reference antenna. Both the simulated E-plane and H-plane radiation patterns are shown in the figure. In Figure 3.55 (a), the patterns in the broadside direction are almost the same, and this means the proposed antenna has the same unidirectional radiation characteristic as the reference antenna. Regarding the cross-polarizations shown in Figure 3.55 (b), the reference antenna has a higher cross-polarization in the H-plane than the proposed antenna due to the unbalanced single slot excitation. Within the half-power beamwidth, cross-polarization level is enhanced by 10.4 dB as compared to the reference antenna. It also should be noted that the reference antenna has a different cross-polarization level in the E-plane and H-plane, which limits its use in low cross-polarization

applications. In contrast, the proposed antenna has a low cross-polarization level in both planes owing to the balanced dual-slot coupling feed.

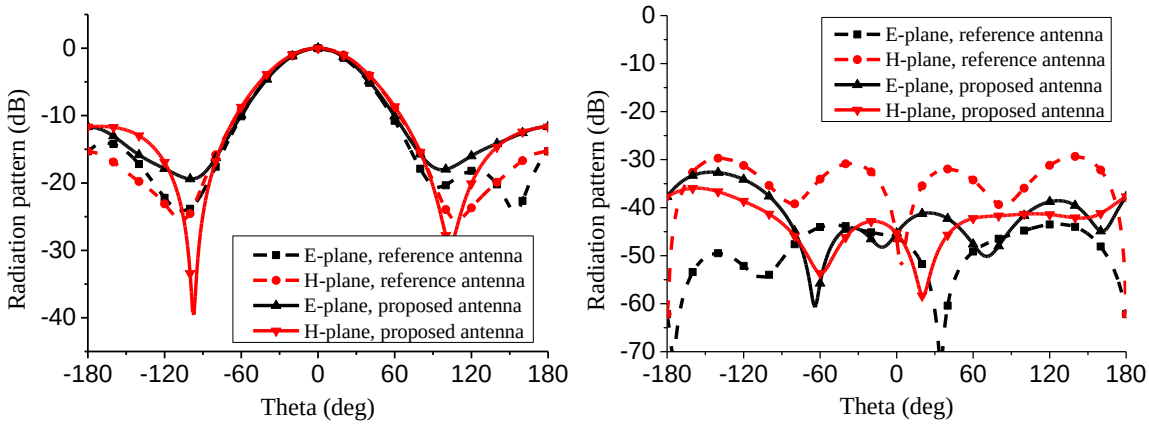

(a) (b)

Figure 3.55 Radiation patterns of the reference antenna and the proposed antenna. (a) Co-polarization. (b) Cross-polarization.

3.5.2 Array Design

With the improved impedance bandwidth, skirt frequency selectivity, and low cross-polarization level, the proposed antenna is used to design a low-sidelobe antenna array for C-band radar applications. The configuration of the 1×8 antenna array is shown in Figure 3.56. The antenna array is realized for vertical polarization. The distance between each element is 40 mm, which is about 0.64 λ_0, where λ_0 is the free space wavelength at the centre frequency. To facilitate the design of the feed network for the antenna array, the even number feed slots and resonators are mirrored and symmetrical to their odd number counterparts. Unequal T-junction power dividers are used to get the required power distribution, which is utilized to obtain low-sidelobe radiation pattern.

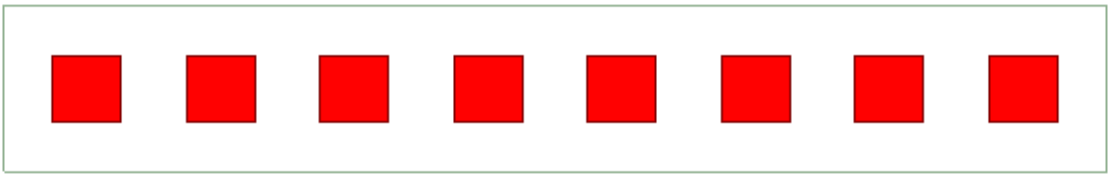

(a)

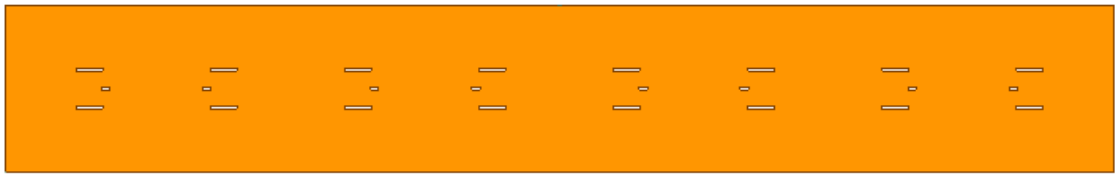

(b)

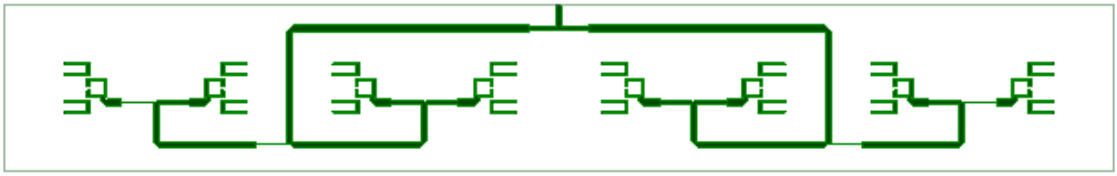

(c)

Figure 3.56 Configuration of the proposed antenna array. (a) Radiating patch. (b) Ground plane. (c) Feed network.

Table 3.5 Optimized magnitude distribution for each array element

Element	1	2	3	4	5	6	7	8
Magnitude	0.25	0.521	0.808	1	1	0.808	0.521	0.25
dB	-18.03	-11.66	-7.84	-5.99	-5.99	-7.84	-11.66	-18.03

Traditional radiation pattern synthesis methods, such as the Dolph-Tschebyscheff and the Taylor synthesis methods, have the problems of the undesired low-Q distribution with decreased array gain or the sampling errors with deteriorated sidelobe level, especially for the ultra-low sidelobe synthesis. To realize the low-sidelobe and overcome the above mentioned problems, differential evolution (DE) algorithm is used to optimize the magnitude distribution of the eight antenna elements [119]-[122]. DE algorithm is a population-based stochastic global optimization algorithm, which is a simple, highly efficient, and robust evolution algorithm. The classical DE strategy is used to optimize the side lobes of the antenna array. The array factor for this eight element linear array is expressed as

$$AF(I_n, \varphi_n, z_n) = \sum_{n=1}^{8} I_n \exp(jk(z_n - z_1)cos\theta + j\varphi_n) \tag{3.22}$$

where $I_n, \varphi_n,$ and z_n are the magnitude, phase, and position of each antenna element.

From this equation, one can obtain the directivity (Dir), sidelobe level (SLL), and the radiation pattern of the array. The objective function for this application is defined as

$$F = \alpha\,|DesSLL - \max(SLL)| - \beta Dir \tag{3.23}$$

where α and β are the weight factors of the best optimization results. To ensure that the optimized array has a high directivity, directivity is included in the objective function. DesSLL is the desired sidelobe level. In this design, the DesSLL is designed as -30 dB.

Using the DE algorithm and objective function in (3.23), the optimized magnitude distribution is shown in Table 3.5. Based on these values, the feed network for the low-sidelobe array is designed by controlling the characteristic impedances of the unequal T-

junction power dividers, which is shown in Figure 3.56 (c). The simulated S-parameters of the feed network are shown in Figure 3.57 (a). It should be noted that, port 1 is the input port of the feed network. Port 2, 3, 4, and 5 are the antenna input ports for array elements 1, 2, 3, and 4. Because of the symmetry of the feed network, only half of the S-parameters are shown in the figure. The variance of the simulated power transmission by the feed network with the calculated results is less than 0.22 dB within the impedance bandwidth. The simulated S_{11} is below -20 dB from 4.8 GHz to 5.2 GHz.

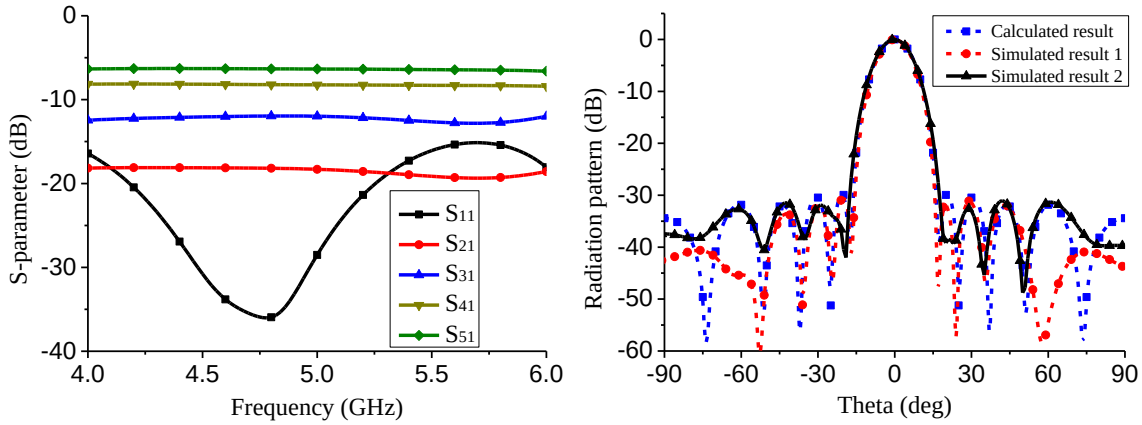

(a) (b)

Figure 3.57 S-parameters of the simulated unequal feed network. (b). Radiation patterns of calculated and simulated results.

Radiation patterns of both the calculated result and the simulated results are shown in Figure 3.57 (b). The calculated result is obtained by calculating the array factor using isotropic element. The simulated result 1 is achieved by using HFSS with ideal port excitation. The simulated result 2 is obtained by simulating the array antenna with the feed network shown in Figure 3.56 (c). As can be seen, the calculated radiation pattern has the sidelobes lower than -30 dB. The simulated result 1 is consistent with the calculated result, especially for the sidelobes beside the main beam. Whereas the simulated result 2 shows a little bit variance for the first sidelobe because of magnitude and phase errors caused by the designed feed network. However, the sidelobes for the antenna array are still lower than -30 dB.

3.5.3 Results and Discussion

The proposed antenna element is fabricated and measured to validate the design concept. Figure 3.58 shows the top view and back view of the fabricated antenna prototype. All the antennas were measured by using Anritsu 37397C vector network analyzer and ASYSOL far field antenna measurement system.

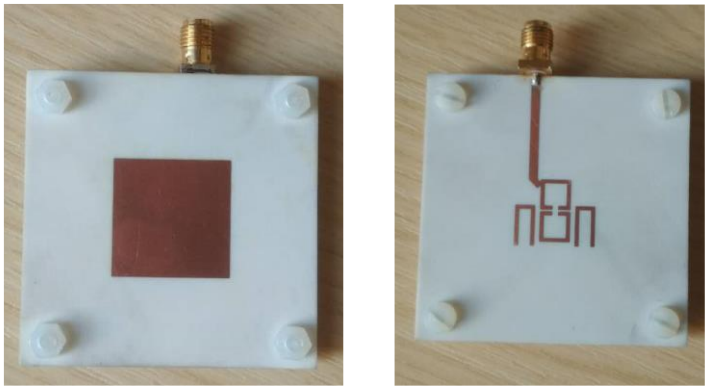

(a) (b)

Figure 3.58 Fabricated antenna element. (a) Top view. (b) Back view.

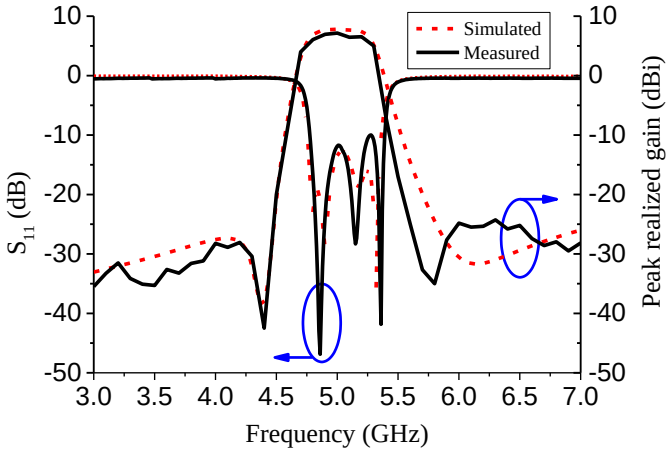

Figure 3.59 Simulated and measured results of S_{11} and peak realized gain for the proposed antenna element.

Figure 3.59 shows the simulated and measured S_{11} and peak realized gain of the proposed antenna element. The measured impedance bandwidth is from 4.78 GHz to 5.39 GHz (FBW = 12%), which agrees well with the simulated S_{11}. The measured in-band peak realized gain is about 6.6 dBi, which is about 1 dB lower than the simulated realized gain. For the out-of-band suppression, it is 35 dB lower than the maximum in-band gain at the lower band, and 31 dB lower than the maximum in-band gain at the upper band. Two deep radiation nulls are obtained near the band edges at 4.4 GHz and 5.8 GHz. As for the two sides of the out-of-band suppression, the measured lower band suppression agrees well with the simulated result. While the upper radiation null moves to lower frequency compared to the simulated result, which is probably caused by the PCB fabrication and the assembly errors.

The fabricated prototype of low-sidelobe antenna array is shown in Figure 3.60. The simulated and measured S_{11} and peak realized gain are shown in Figure 3.61 for good comparison. The measured impedance bandwidth for S_{11}<-10 dB is 4.78-5.39 GHz. Within the impedance bandwidth, the measured realized gain is about 13.2 dBi, while the simulated peak realized gain is about 14.1 dBi. The gain loss of the low-sidelow array is mainly caused

by the non-uniform excitations for the array elements, dielectric loss of the substrates and the mutual coupling between antenna elements. Because of the couplings between the antenna elements, both the simulated and measured out-of-band suppressions show more fluctuations compared to the antenna element. However, the simulated peak realized gain shows good agreement with the measured peak realized gain. Radiation nulls are measured at both sides of the band edges. The out-of-band rejection at lower out-of-band is 27 dB lower than the maximum realized gain, and 25 dB lower than the maximum gain at the upper out-of-band.

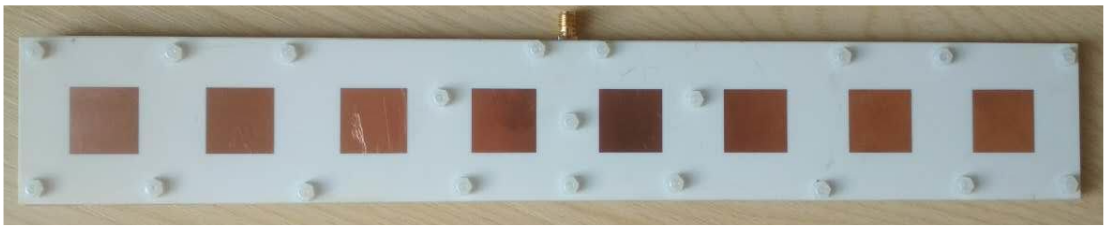

(a)

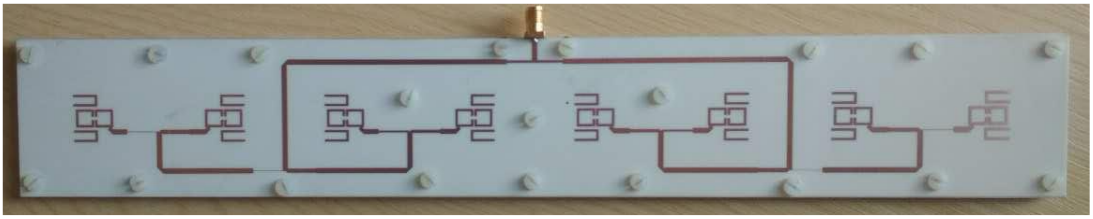

(b)

Figure 3.60 Fabricated antenna array. (a) Top view. (b) Back view.

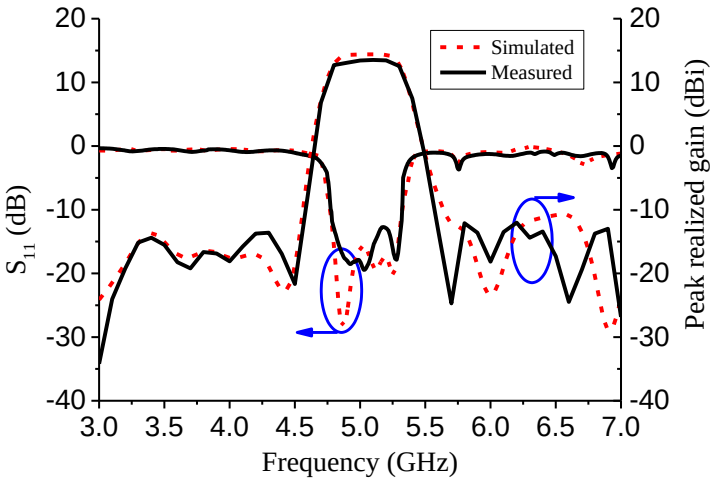

Figure 3.61 Simulated and measured results of S_{11} and peak realized gain for the proposed antenna array.

Figure 3.62 shows the simulated and measured radiation patterns for the low-sidelobe antenna array at 5 GHz. The antenna array shows a good unidirectional radiation at the broadside direction. As shown in the figure, a narrow beam is measured in the E-plane with half power beamwidth of about 12°. Whereas in the H-plane, it is a wide beam with half

power beamwidth of about 60°. In the E-plane, the measured first sidelobe is lower than -28.7 dB, which is slightly higher than the simulated sidelobe. For the cross-polarization, the measured level is lower than -35.5 dB and -34 dB in E-plane and H-plane in the range of half-power beamwidth. Compared to the simulated radiation patterns, the discrepancies for the sidelobes and cross-polarization are mainly due to the fabrication and assembly errors of the antenna array.

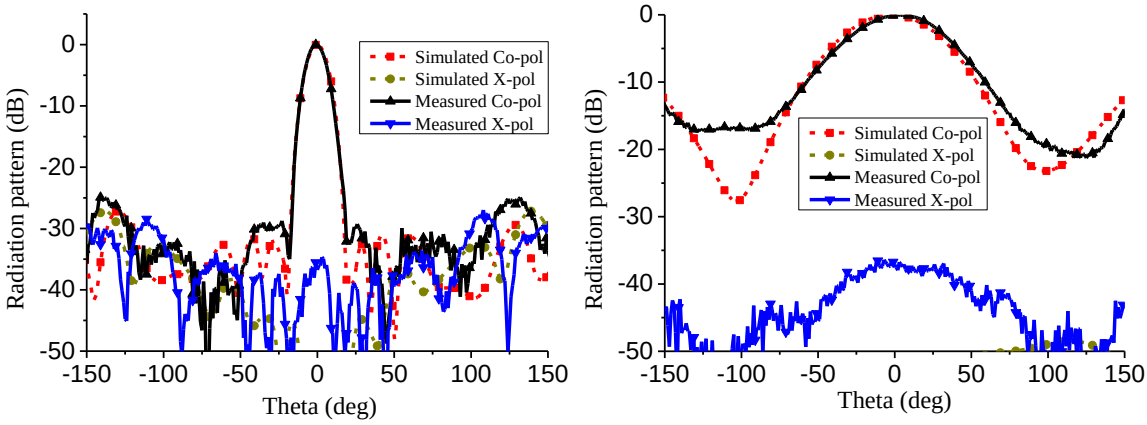

(a) (b)

Figure 3.62 Simulated and measured antenna array radiation patterns at 5 GHz. (a) E-plane. (b) H-plane.

3.6 Summary

In this chapter, wideband and compact base station antennas are presented. First, a compact dual-polarized antenna based on the sharped-dipoles is illustrated, which features the compact radiator size and wide impedance bandwidth. The second design is a compact dual-polarized antenna based on the crossed shunt loops, which not only has the wide impedance bandwidth covering 1.6-3.0 GHz, but also has high upper out-of-band suppression over 3.35-5.25 GHz. The third design is a dual-polarized antenna with very wide impedance bandwidth. This antenna is designed by using shorted dipoles, and has a wide impedance bandwidth of 74.5% (from 1.69 GHz to 3.7 GHz) for VSWR<1.5 at both ports. The last design is a filtering array antenna, which is realized by using a novel balanced coupling structure. The array antenna features low cross-polarization level, two radiation nulls, low sidelobe level, and high out-of-band suppression. Both of these presented antennas were designed, fabricated, and measured for the performance verification.

Chapter 4. Wideband and Low-Profile Differentially Fed Antennas

4.1 Introduction

With the development of the differential microwave circuit system, differentially driven antennas are needed to directly connect to these circuit systems. Otherwise, additional baluns or out-of-phase power dividers will be inserted between the differential circuit systems and the traditional single-ended antennas, and this will cause the undesired insertion loss and mismatching between the two different interfaces. Therefore, wideband differentially driven dual-polarized antennas are developed recently [101], [124].

Owing to the symmetrical differentially driven method, these antennas can have high port isolation. With the help of the high profile crown-shaped multi-dipole configuration, the differentially driven antenna [60] obtains the stable beamwidth for base station applications. By using parasitic patch and slot excitation, the differentially driven antenna in [101] achieves wide differential impedance bandwidth. However, little of these differentially driven antennas are considered about the common mode suppression for these antennas. As one of the important parameters for the differential devices, poor common mode suppression will lead the undesired noises to the circuit system and cause the circuit system a poor signal-to-noise ratio [123].

To obtain wideband impedance bandwidth, many different techniques are utilized to design differentially fed patch antennas [125]-[126]. However, due to the low profile and planar configuration, patch antennas normally face the problem of limited bandwidth, which is difficult to meet the bandwidth requirement for base stations. Because of the wideband requirement for 2G/3G/4G base stations (1.7-2.7 GHz), dipoles are normally utilized to design wideband dual-polarized antennas [115], [127].

These antennas normally can meet the bandwidth requirement for base stations, including the low cross-polarization, stable gain and beamwidth. However, few of them consider the harmonic suppression of the base station antennas, which can reduce the efficiency of the power amplifiers in the transmitter, and cause serious electromagnetic interferences to the other wireless systems [128]. In addition, the undesired harmonic radiations can be received by the receiver, reduce the sensitivity of the receiver, and even congest the receiver with strong magnitude [129]. Therefore, it is necessary to develop wideband base station antennas with harmonic suppression characteristic.

4.2 Wideband Antenna With High Common Mode Suppression

In this section, a novel design method of a wideband differentially driven dual-polarized antenna with high common mode suppression is presented. The presented high common mode suppressed antenna is realized by using an integrated wideband high common mode suppressed power divider. The integrated power divider can be equivalent as a six-port feed network with two orthogonal input ports and four equal magnitude output ports. Detailed working principles of the six-port power divider, including the wideband characteristic and the even-odd mode analysis, are illustrated. Based on the design method, the presented antenna was designed, fabricated, and measured for verification. The measured results show that the impedance bandwidth of the two differentially driven ports is 1.64-3.0 GHz (58.6%) for S_{dd11} and S_{dd22}<-15 dB. Moreover, very high common mode suppression is achieved at the two differentially driven ports with the measured S_{cc11} and S_{cc22} higher than -0.87 dB over the impedance bandwidth.

4.2.1 Antenna Configuration

The detailed configuration of the presented differentially driven dual-polarized antenna is shown in Figure 4.1. The antenna is composed of a square copper sheet as the reflector and a square substrate with both the top and bottom layers printed with the antenna radiator. The antenna is fed by four equal length coaxial cables, which work as the differential feed ports.

In Figure 4.1 (a), the differential port pair of port 1 and port 2 is designated as the differential port d1 for -45º polarization. While the differential port pair of port 3 and port 4 is designated as the differential port d2 for +45º polarization. To facilitate the analysis of the differentially driven dual-polarized antenna, the differentially and commonly driven S-parameters of the antenna can be expressed as [123]

$$S_{dd11} = (S_{11} + S_{22} - S_{12} - S_{21})/2 \tag{4.1}$$

$$S_{dd22} = (S_{33} + S_{44} - S_{34} - S_{43})/2 \tag{4.2}$$

$$S_{dd21} = (S_{31} + S_{42} - S_{32} - S_{41})/2 \tag{4.3}$$

$$S_{cc11} = (S_{11} + S_{22} + S_{12} + S_{21})/2 \tag{4.4}$$

$$S_{cc22} = (S_{33} + S_{44} + S_{34} + S_{43})/2 \tag{4.5}$$

where S_{ij} $(i = 1, 2, 3, 4;\ j = 1, 2, 3, 4)$ are the single-ended S-parameters, which can be obtained from the simulated or measured results. By using (4.1)-(4.5), the differentially and commonly driven S-parameters can be directly obtained by using the simulated or measured single-ended S-parameters.

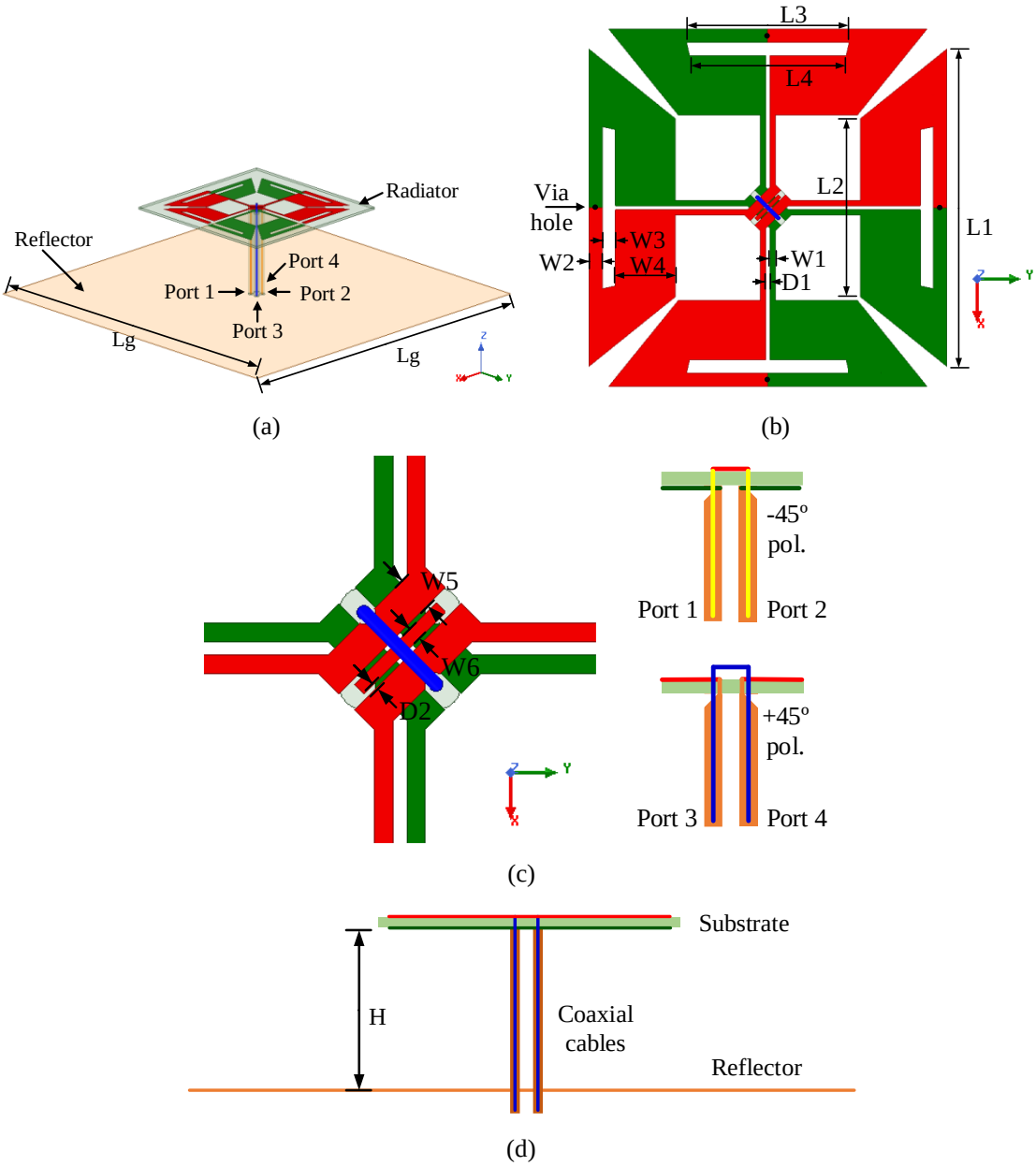

Figure 4.1 Configuration of the proposed differentially fed dual-polarized antenna.
(a) 3D view. (b). Detailed view of the antenna radiator. (c). Detailed view of the inner six-port power divider. (d). Side view of the antenna. (Detailed parameters of the antenna. Lg=140 mm, L1=48 mm, L2=27 mm, L3=24.5 mm, L4=23.5 mm, W1=0.8 mm, W2=2 mm, W3=2 mm, W4=9 mm, W5=1.5 mm, W6=0.6 mm, D1=0.6 mm, D2=0.2 mm.)

The antenna radiator is printed on a substrate of Rogers 4003C, with the relative dielectric permittivity of 3.55 and the thickness of 0.813 mm. As shown in Figure 4.1 (b), the top layer of the substrate is depicted in red color, and the bottom layer is depicted in green color. The main radiating structures of the antenna are four symmetrically arranged folded dipoles. Four via holes are used to connect the top and bottom dipole arms and form four folded dipoles. The four folded dipoles at the periphery are connected to a symmetrical six-port power divider. The detailed configuration of the six-port power divider is shown in Figure

4.1 (c). The power divider has two differential input ports for two orthogonal polarizations, and four output ports connected to the peripheral four folded dipoles. Detailed working principles of the six-port power divider will be illustrated in the following sections. The connection method of the feeding coaxial cables to the power divider are also shown in Figure 4.1 (c). The outer conductors of the cables are soldered to the two inner arms of the power divider, whereas the inner conductors are connected to each other by themselves or by the top layer strip to avoid feed intersection.

Figure 4.1 (d) shows the side view of the antenna. The distance from the top radiator to the bottom reflector is 35 mm, and the size of the square reflector is 140 mm×140 mm. Note that the presented antenna is designed for ±45º polarizations. As a general definition for the ±45º polarized radiation patterns, the xz plane in this paper is defined as the horizontal plane (H-plane), and the yz plane is defined as the vertical plane (V-plane). All the simulation results in this work are obtained by using the electromagnetic simulation software ANSYS HFSS. The detailed parameters of the presented antenna are shown in the caption of Figure 4.1.

4.2.2 Working Principle

The presented dual-polarized antenna can be equivalent as a combination of a six-port divider and four folded dipoles for dual-polarization. The equivalent circuit of the proposed antenna is shown in Figure 4.2. In the figure, port P1 can be regarded as the differential port d1, which is realized for the -45º polarization. Port P2 can be regarded as the differential port d2, which is realized for the +45º polarization. Whereas the ports of P3, P4, P5, and P6 are utilized to drive the four folded dipoles for the operation of the two orthogonal polarizations.

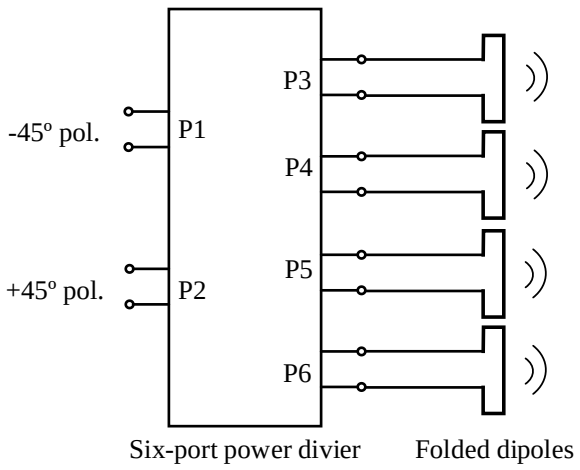

Figure 4.2 Equivalent circuit of the proposed antenna.

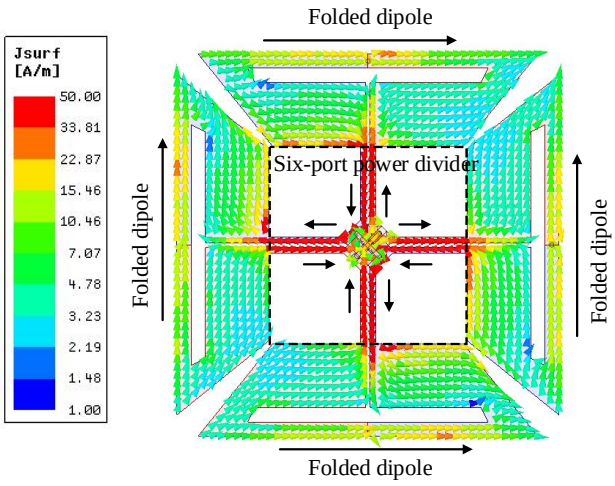

Figure 4.3 Current distribution of the proposed antenna at 2.2 GHz when the differential port d1 is excited.

Figure 4.3 shows the current distribution of the proposed antenna at 2.2 GHz when differential port d1 is excited for -45º polarization. Auxiliary arrows are added to illustrate the current direction on the antenna surface. Compared to the current magnitude on the four folded dipoles, strong current intensity can be found on the centre of the crossed narrow transmission lines. The input power is transmitted to the four folded dipoles by the transmission lines. The four crossed narrow transmission lines in the centre work as a six-port power divider with two orthogonal input ports and four equal magnitude output ports. It should be noted that the transmission lines look similar as the traditional parallel transmission lines. However, different from the traditional parallel transmission line, the symmetrical lines (or the centre lines) of the two parallel lines are not coincided, and the distance between the two inner edges of the parallel lines is 0.6 mm for the presented antenna. To facilitate the analysis of antenna, this type of the parallel transmission line is designated as the offset parallel transmission line in this work. Detailed working principles about the centre six-port power divider, including the wideband characteristic and the even-odd mode analysis, will be illustrated in the following sections.

To illustrate the working principle of the six-port power divider, the power divider is extracted out of the presented antenna, and modelled in Figure 4.4. In the centre of the figure, two lumped ports (P1 and P2) are located at the centre with the reference impedance of 50 ohm, which are used to excite the power divider as the input ports. Four wave ports (P3, P4, P5, and P6) at the end of the offset parallel transmission lines are defined as the output ports. Note that the two ends of the port P1 are connected to the bottom strips in green colour, and the two ends of port P2 are connected to the top strips in red colour. Four wave ports are

connected at the end of strips with the reference driven direction from the bottom centre strips to the top centre strips.

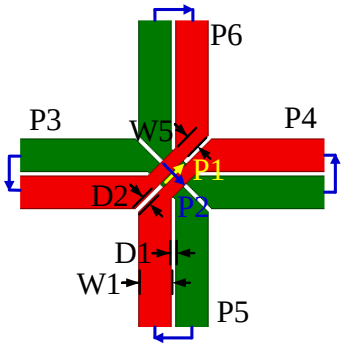

Figure 4.4 Simulation model of the six-port power divider.
(Detailed parameters of the simulation model. W1=4 mm, D1=-0.8 mm. D2=0.6 mm, W5=1.7 mm.)

Figure 4.5 shows the simulated S-parameters of the six-port power divider based on the model shown in Figure 4.4. With the parameters provided in the caption of Figure 4.4, the characteristic impedance of the offset parallel line is equal to 50 ohm. Owing to the symmetry of the power divider, the magnitudes of the S_{11} and S_{22} are almost same, the magnitudes of the S_{33}, S_{44}, S_{55}, and S_{66} are almost same, and the magnitudes of the S_{31}, S_{41}, S_{51}, S_{61}, S_{32}, S_{42}, S_{52}, S_{62} are also almost same. Therefore, only the magnitudes of S_{11}, S_{33}, S_{21}, S_{31} are given in the figure for clarity.

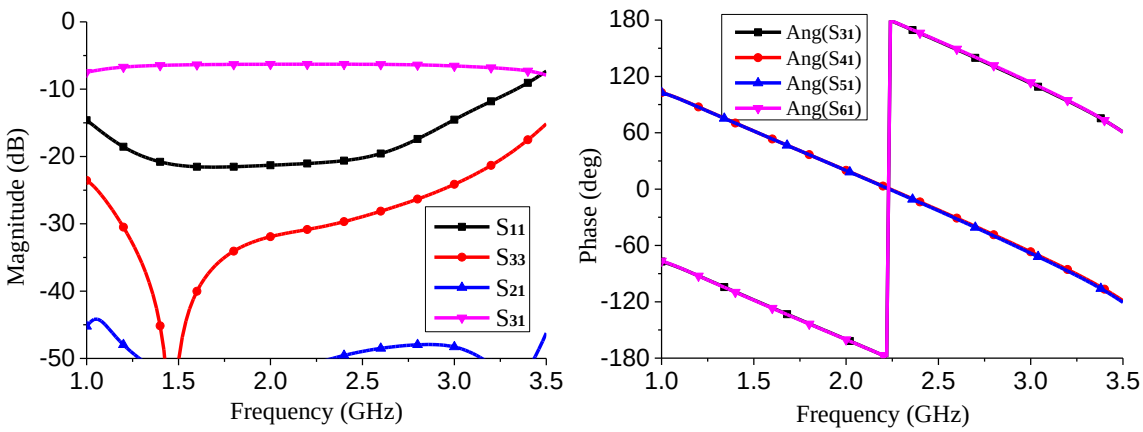

(a) (b)

Figure 4.5 Simulated S-parameters of the extracted six-port splitter. (a) Magnitude. (b) Phase.

It can be seen that a wide impedance bandwidth is realized for all the six ports. The simulated overlapped relative bandwidth for all the six ports of the power divider is 100% for the reflection coefficients lower than -15 dB, which covers from 1 GHz to 3 GHz. Stable transmission is obtained from the input port to the four output ports, which is close to the ideal -6 dB. Very high isolation is achieved between the two orthogonal input ports of P1

and P2, which can be utilized to excite the dual-polarized antenna with high isolation. In Figure 4.5 (b), out-of-phase is observed for the opposite ports, such as phase (S_{31}) and phase (S_{41}). In addition, in-phase is observed for the adjacent ports, such as phase (S_{31}) and phase (S_{51}). Based on these magnitude and phase characteristics, the six-port power divider can be used to excite the four folded dipoles for the two orthogonal polarizations.

According to the simulated magnitude and phase characteristics, the scattering matrix for this six-port power divider can be concluded as

$$[S] = \begin{bmatrix} 0 & 0 & -0.5 & 0.5 & 0.5 & -0.5 \\ 0 & 0 & -0.5 & 0.5 & -0.5 & 0.5 \\ -0.5 & -0.5 & 0 & 0 & 0.5 & 0.5 \\ 0.5 & 0.5 & 0 & 0 & 0.5 & 0.5 \\ 0.5 & -0.5 & 0.5 & 0.5 & 0 & 0 \\ -0.5 & 0.5 & 0.5 & 0.5 & 0 & 0 \end{bmatrix} \tag{4.6}$$

Observing from the matrix, it is can be found that all the input and output ports are well matched. Good isolation can be obtained between the two orthogonal input ports. Four output ports have the same output power with the in-phase or out-of-phase characteristics. A dual-polarized antenna can be realized by using these input and output characteristics. It can be calculated that the scattering matrix also meets the following conditions

$$[S] = [S]^t \tag{4.7}$$

$$[S]^t[S]^* = [U] \tag{4.8}$$

where $[S]^t$ is the symmetric matrix of $[S]$, $[S]^*$ is the conjugate matrix of $[S]$, and $[U]$ is the unitary matrix. Therefore, matrix $[S]$ is a symmetric and unitary matrix, and the six-port power divider is a reciprocal and lossless feed network.

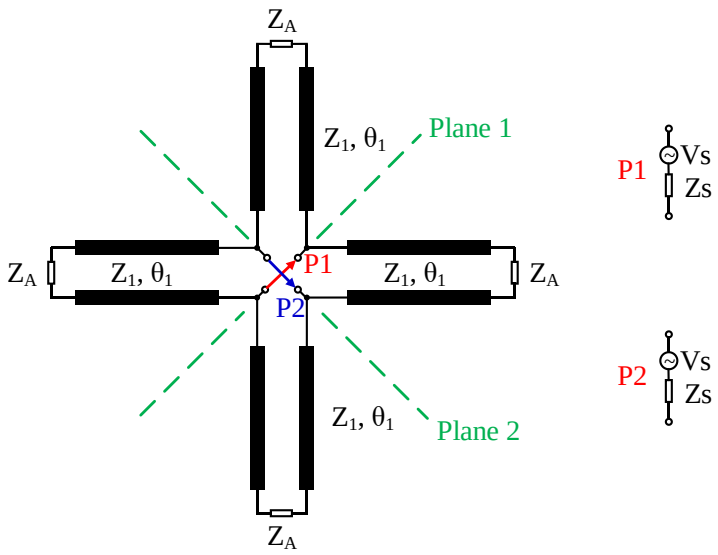

Figure 4.6 Transmission line equivalent circuit of the six-port power divider.

The six-port power divider can be further analyzed by using the equivalent transmission line circuit to get the even-odd mode characteristics. As shown in Figure 4.6, the input impedance of the folded dipoles are Z_A, the voltage and impedance of the driven sources of P1 and P2 are Vs and Zs, the characteristic impedance and electric length of the offset parallel lines are Z_1 and θ_1. Two symmetrical planes, Plane 1 and Plane 2, can be found for the presented six-port power divider. Because of the symmetry of the power divider, important impedance characteristics, including the common mode suppression and impedance matching, can be analyzed by using the even-odd mode analysis.

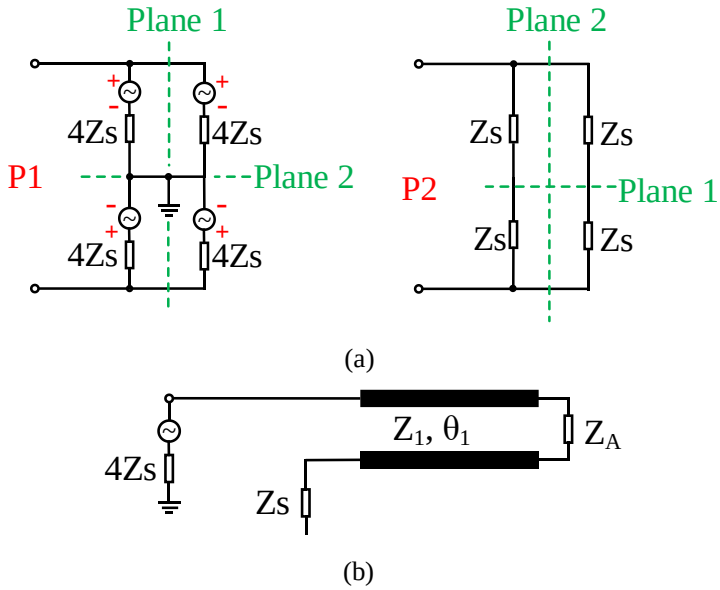

Figure 4.7 Even mode analysis of the transmission line equivalent circuit for the six-port power divider when port 1 is excited. (a) Symmetric forms of port 1 and port 2. (b) Simplified even mode excited equivalent circuit.

Figure 4.7 shows the transmission line equivalent circuit when P1 is driven by the even mode signal. As shown in Figure 4.7 (a), because of the even mode excitation at P1, Plane 1 and Plane 2 are equivalent to the open-circuited planes. The load at P2 will be open-circuited with regard to both two symmetrical planes. Therefore, as shown in Figure 4.7 (b), the simplified even mode excited equivalent circuit is driven with a source impedance of $4Z_s$ at P1. The current flowing through this circuit cannot form a loop because of the equivalent open-circuit at P2. This means that it will be totally mismatched for the even mode signal. Therefore, high common mode suppression can be obtained owing to the even mode driven symmetrical six-port power divider, and the reflection coefficient under even mode excitation can be expressed as

$$\Gamma_{1,even} = \infty \tag{4.9}$$

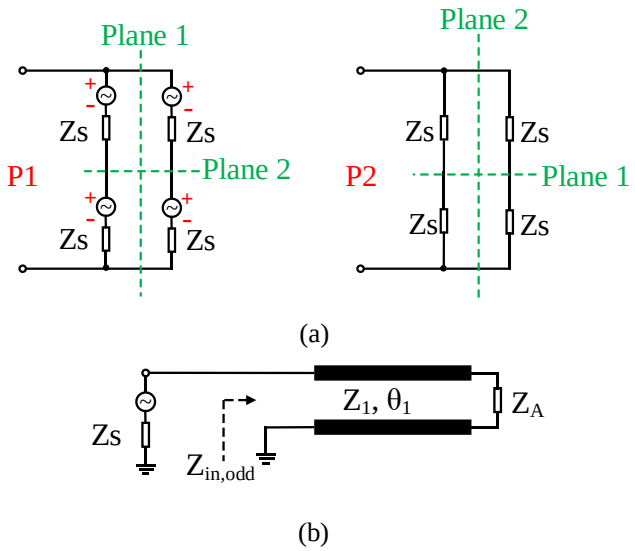

Figure 4.8 Odd mode analysis of the transmission line equivalent circuit for the six-port power divider when port 1 is excited. (a) Symmetric forms of port 1 and port 2. (b) Simplified odd mode excited equivalent circuit.

Figure 4.8 shows the transmission line equivalent circuit when P1 is driven by the odd mode signal. As shown in Figure 4.8 (a), because of the odd mode excitation at P1, Plane 1 is equivalent as the open-circuited plane, and Plane 2 is equivalent as the short-circuited plane. The load at P2 will be directly shorted to the ground because of the equivalent short-circuit with regard to Plane 2. Therefore, as shown in Figure 4.8 (b), the simplified equivalent circuit under odd mode excitation is driven with a source impedance of Z_s, and the current loop is formed because of the equivalent short-circuit at P2. As shown in the figure, the input impedance Z_{in} under odd mode excitation can be expressed as

$$Z_{in,odd} = Z_1 \frac{Z_A + jZ_1 tan\theta_1}{Z_1 + jZ_A tan\theta_1} \tag{4.10}$$

So the reflection coefficient for P1 can be expressed as

$$\Gamma_{1,odd} = \frac{Z_{in,odd} - Z_s}{Z_{in,odd} + Z_s} \tag{4.11}$$

As a special case, when $Zs=Z_1=Z_A=50$ ohm,

$$\Gamma_{1,odd} = 0 \tag{4.12}$$

This means that the transmission line equivalent circuit will be well matched when it is excited by the odd mode signal. This is also verified by the simulated results in Figure 4.5.

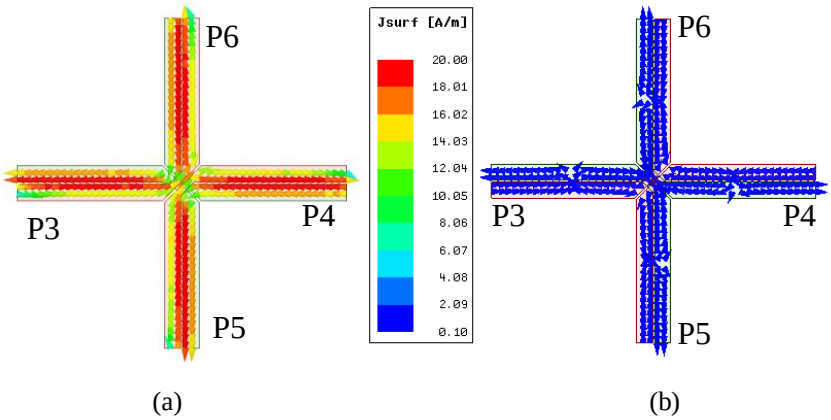

Figure 4.9 Current distributions on surface of the six-port power divider. (a) Odd mode excitation at port 1. (b) Even mode excitation at port 1.

To further illustrate the good transmission under odd mode excitation and high reflection under even mode excitation, Figure 4.9 shows the current distributions on the surface of the six-port power divider under even-odd mode excitations. It should be noted that Z_1 and Z_A are designed as 50 ohm based on the above analysis. The current distributions in the figure are shown with the same scale to illustrate the current magnitude. As shown in the figure, when odd mode is excited at P1, transmission mode is excited and the input power is transmitted to the four output ports with the very strong magnitude. Whereas when the even mode is excited at P1, very weak magnitude are excited on the surface of the six-port power divider. The current magnitude ratio between the odd mode and the even mode excitation can reach up to almost 200 times. Comparing the two different current distributions, it can be concluded that a good common mode suppression can be obtained by using the proposed six-port power divider.

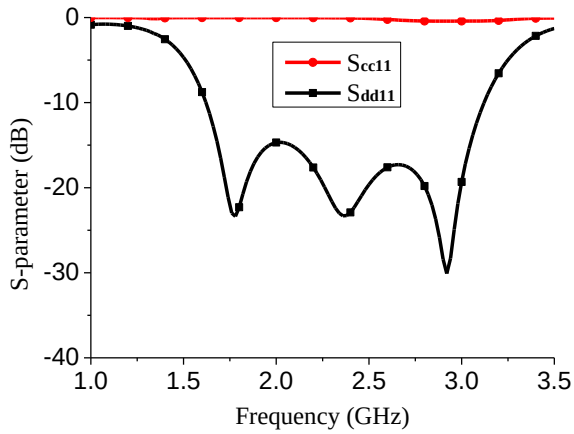

Figure 4.10 Simulated differentially driven and commonly driven S-parameters of the antenna.

Combining with the wide impedance bandwidth and the innate even mode suppression of the six-port power divider, wide impedance bandwidth and high common mode suppression

can be achieved for the proposed antenna. Figure 4.10 shows the simulated differentially driven and commonly driven S-parameters of the antenna. It can be seen that three reflection zeros are achieved on the differentially driven reflection coefficient curve with the wide impedance bandwidth from 1.68 GHz to 3.02 GHz for S_{dd11}<-15 dB. Furthermore, very flat and high suppression is observed over the entire bandwidth with the simulated lowest reflection coefficient higher than -0.42 dB.

The proposed differentially driven dual-polarized antenna is designed based on the above discussed design method. However, it is should be noted that the input impedance of the folded dipole cannot always designed as 50 ohm. Therefore, the offset parallel lines can also function as the impedance transformer. As illustrated by (4.10), when the electric length of the offset parallel line (θ_1) is equal to 90 degree, the input impedance of the proposed antenna can be expressed as

$$Z_{in} = \frac{Z_1^2}{Z_A} \tag{4.13}$$

As shown in the configuration of the proposed antenna, when the width of the offset parallel line is changed, its characteristic impedance will be changed as well. The length of the offset parallel line in the design is approximately a quarter of the guided wavelength. Thus, the function of impedance transformer is realized by adjusting the characteristic impedance of the offset parallel lines.

4.2.3 Results and Discussion

To validate the above design method, the proposed differentially driven dual-polarized antenna was designed, fabricated, and measured. Figure 4.11 shows the photograph of the fabricated prototype. The antenna was measured by using the Anritsu 37397C vector network analyzer and ASYSOL far field antenna measurement system at University of Kent.

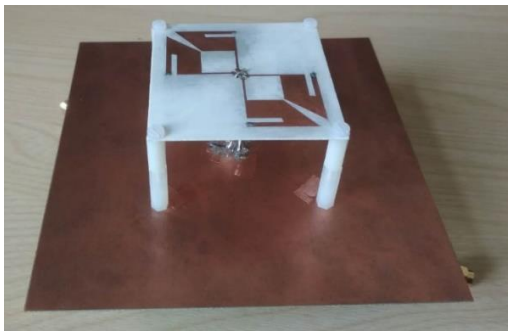

Figure 4.11 Photograph of the fabricated prototype of the proposed differentially driven dual-polarized antenna.

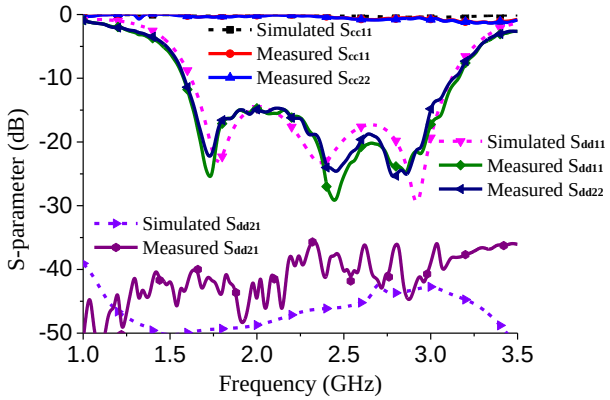

Figure 4.12 Measured and simulated S-parameters of the fabricated differentially driven dual-polarized antenna.

Figure 4.12 shows the measured and simulated S-parameters of the proposed antenna, including the differentially driven and commonly driven S-parameters. It can be seen that a good accordance can be obtained between the simulated results and the measured results. Owing to the symmetry of the antenna, the simulated S_{dd11} and S_{dd22}, and simulated S_{cc11} and S_{cc22} are almost the same as each other. Therefore, only simulated S_{dd11} and S_{cc11} are given in the figure for comparison. The measured overlapped impedance bandwidth for both S_{dd11} and S_{dd22} lower than -15 dB is from 1.64 to 3.0 GHz. Owing to the symmetrical differentially driven method, the measured isolation is higher than 35.4 dB within the bandwidth. Meanwhile, by using the integrated six-port power divider, very high common mode suppression is achieved with the measured S_{cc11} and S_{cc22} higher than -0.87 dB over the whole impedance bandwidth.

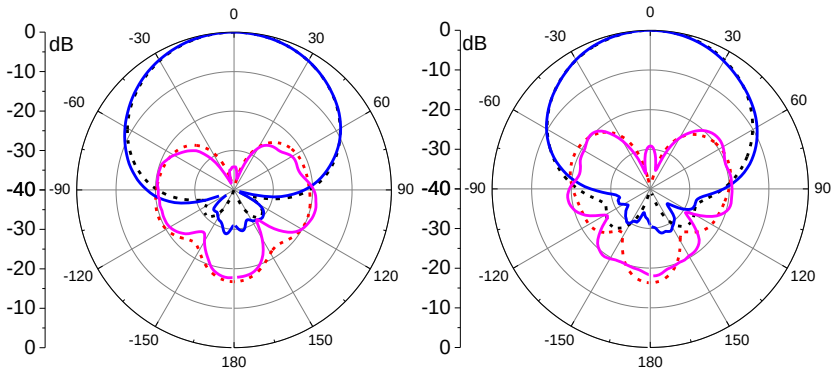

(a) (b)

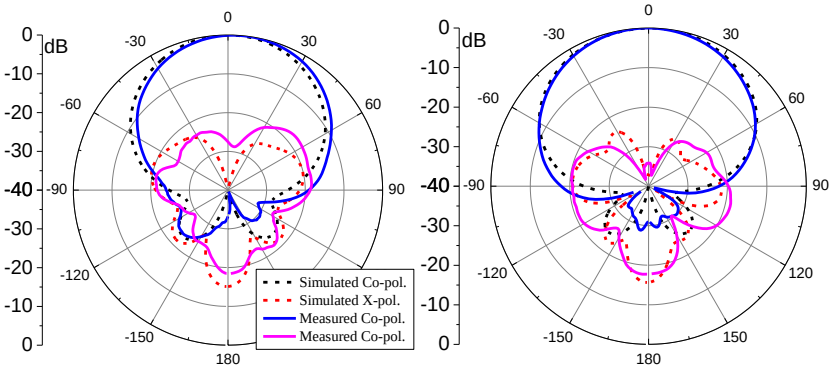

(c) (d)

Figure 4.13 Measured and simulated H-plane radiation patterns of the fabricated antenna when differentially driven port d1 is excited at different frequencies. (a) 1.7 GHz. (b) 2.2 GHz. (c) 2.7 GHz. (d) 3.0 GHz.

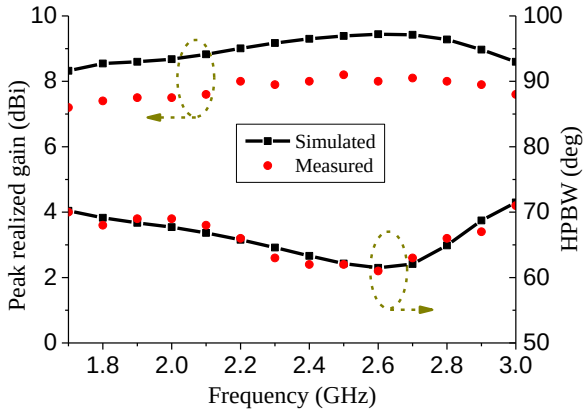

Figure 4.14 Measured and simulated peak realized gains and HPBWs of the fabricated antenna.

The measured and simulated normalized radiation patterns are shown in Figure 4.13. Because of the symmetry of the antenna, only H-plane radiation patterns excited by differential port d1 are given in the figure. Good agreement can be observed between the simulated and measured radiation patterns. The measured cross-polarization level is 27 dB lower than co-polarized radiation patterns in the broadside direction, and 20 dB lower than the co-polarization radiation patterns within ±30º beamwidth. The measured front to back ratio is higher than 17 dB within the bandwidth. Figure 4.14 shows the measured and simulated peak realized gain and half power beamwidth (HPBW) of the antenna. Stable antenna gain and HPBW are achieved within the bandwidth. The measured peak realized gain varies from 7.2 to 8.2 dBi, and the measured half power beamwidth is 66±5º form 1.7 GHz to 3.0 GHz.

By using the integrated high common mode suppressed six-port power divider, wide impedance bandwidth and high common mode suppression are achieved for the presented differentially driven antenna. Table 4.1 compares the recently published differentially driven

antennas with the presented antenna. Antennas in [60]-[62], [100], and [124] are the differentially driven dual-polarized antennas for base station applications. Owing to the symmetrical differentially driven method, normally high isolation (>35 dB) can be achieved. However, few differentially driven antennas are concerned about the common mode suppression. Whereas the common mode signals would introduce serious noise interference to the circuit systems, and deteriorate the signal-to-noise ratio of the circuit systems. With the help of the additional introduced crossed baluns, high common mode suppression is achieved for the antenna in [124]. However, this can introduce undesired insertion loss and increase the antenna design complexity and fabrication cost. Antenna in [130] is a differentially driven circularly polarized antenna, and the antenna was measured with high common mode suppression. However, its working principle is not clearly illustrated. Compared to these two antennas, the presented antenna keeps simple configuration, but still has much higher suppression and wider impedance bandwidth.

Table 4.1 Comparison of the recently published differentially driven antennas

Ref.	Overlapped BW (GHz)	RL (dB)	Height (mm)	S_{21} (dB)	CM reflection coefficient (dB)	Pol.
[60]	1.7-2.7 (45.4%)	>14	71.2	<-39	NG	DP
[61]	1.7-2.9 (52%)	>14	34	<-26.3	NG	DP
[62]	1.7-2.75 (48%)	>15	40	<-38	NG	DP
[100]	1.66-2.75 (49.4%)	>15	35	<-37	NG	DP
[124]	1.66-2.8 (51%)	>15	30	<-38	>-1.32	DP
[130]	1.7-2.38 (31%)	>10	35	/	>-1.5	CP
This work	1.64-3.0 (58.6%)	>15	35	<-35.4	>-0.87	DP

BW: Bandwidth. CM: Common Mode. NG: Not Given. DP: Dual-Polarization. CP: Circular Polarization.

4.3 Wideband Antenna With High Harmonic Suppression

In this section, a wideband differentially fed dual-polarized antenna by using open slots, monopoles, and a square patch is presented with wideband harmonic suppression. Symmetrical eight open slots are etched on the four corners of the centre square patch to realize symmetrical and low cross-polarized radiation. Stair-shaped strips are used to excite the open slots and also radiate as the monopoles. The centre square patch not only introduces the patch resonance, but also leaves space for the newly incorporated function of harmonic suppression. Shorted microstrip lines are introduced to match these three different resonances with wide impedance bandwidth. To get wideband suppression to the harmonic

radiation from the antenna, compact stepped impedance resonators are elaborately introduced on the top of the patch without any increase of the footprint of the antenna. The proposed antenna was finally designed, fabricated, and measured. Both the measured and simulated results prove that the proposed antenna has the impedance bandwidth of 1.70-2.81 GHz with very high isolation of 39 dB. Moreover, compared to the traditional designed base station antennas, wideband harmonic suppression from 3 GHz to 9 GHz is measured with the reflection coefficient higher than -2.2 dB and related undesired harmonic gain lower than -5.3 dBi. In addition, stable antenna gain and radiation patterns are achieved for base station applications.

4.3.1 Antenna Configuration

The configuration of the proposed dual-polarized antenna is shown in Figure 4.15, which is composed of a square substrate printed with antenna radiator, four coaxial cables as the antenna differential feeds, and a square copper sheet as the antenna reflector. A low-cost substrate of Rogers 4003C with the relative dielectric permittivity of 3.55 and the thickness of 0.813 mm is used to fabricate the antenna. The length of the square reflector is 140 mm. Differential pairs of port 1, port 2, port 3, and port 4 are used to excite the dual-polarized antenna for ±45° polarizations. To facilitate the calculation of the differentially driven antenna, the pair of single-ended port 1 and port 2 is defined as the differential port d1, and the pair of single-ended port 3 and port 4 is defined as the differential port d2. Accordingly, the S-parameters of the differentially driven antenna can be obtained by using the single-ended four-port S-parameters [124]. In addition, because the antenna is designed for base station applications, to analyze the radiation patterns for ±45° polarizations, the xz plane in the figure is defined as the horizontal plane (H-plane), and the yz plane is defined as the vertical plane (V-plane).

Figure 4.15 (b) shows the details of the antenna radiator on the top and bottom layers of the substrate. In the figure, the top layer is depicted in red color, and the bottom layer is depicted in green color. On the top layer, there are eight stair-shaped narrow strips, four narrow shorted strips, and four stepped impedance resonators. While on the bottom layer, there is a square patch connected by four T-shaped stubs. With the proposed configuration, three different resonances are developed. First, eight open slots formed by the T-shaped strips and the square patch are excited and radiate as the slot resonance. Then, stair-shaped narrow strips are utilized to feed the open slots and also radiate as the monopoles. In addition, the square patch at the centre of the bottom layer is also resonated and radiated. To get the

wide impedance bandwidth, four shorted microstrip lines are introduced to match the three different resonances to the feed coaxial cables. Furthermore, to suppress the harmonic radiations of the antenna, four compact stepped impedance resonators are elaborately integrated onto the top of the patch to achieve wideband harmonic suppression without any increase of the antenna footprint. Detailed working principles of the antenna will be discussed in the following sections.

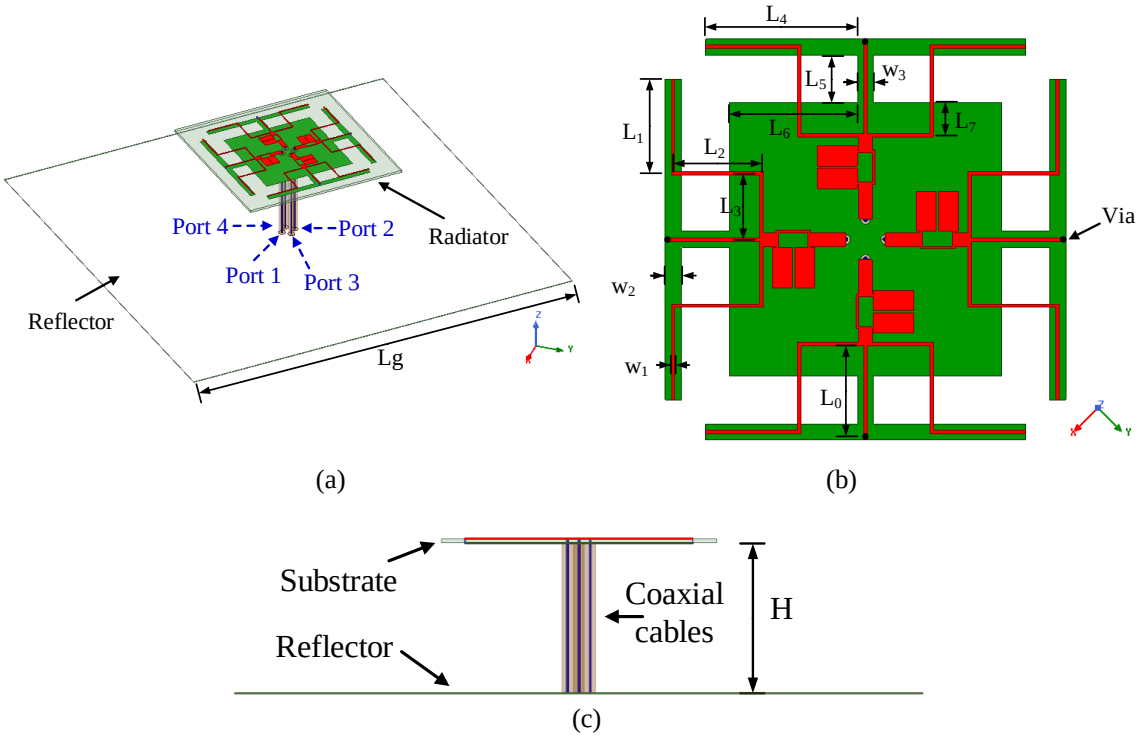

Figure 4.15 Configuration of the proposed dual-polarized antenna.
(a) Isometric view. (b) Top view of the antenna radiator. (c) Side view. (Detailed parameters of the proposed dual-polarized antenna: Lg=140 mm, L_0=11.5 mm, L_1=11.75 mm, L_2=11 mm, L_3=8.25 mm, L_4=20 mm, L_5=6 mm, L_6=16 mm, L_7=4 mm, w_1=0.4 mm, w_2=2 mm, w_3=2 mm, H=33 mm.)

Figure 4.15 (c) shows the side view of the differentially fed antenna. Four coaxial cables are used to feed the antenna. Note that the outer conductors of the cables are soldered to the bottom square patch, while the inner conductors are soldered to the top feed microstrip lines. The height from the radiator to the reflector is 33 mm. All the simulation in this work are obtained from the 3D electromagnetic simulation software ANSYS HFSS. The detailed optimized parameters of the antenna are listed in caption of Figure 4.15.

4.3.2 Working Principle

It is normally difficult to realize symmetrical radiation for dual-polarization by using single open slot. Therefore, eight symmetrical open slots are etched on the four corners of a square patch to obtain symmetrical radiation pattern and also low cross-polarization. To

illustrate the evolution process of the presented antenna, reference antennas in the evolution are shown in Figure 4.16. In the figure, Ant. 1 in Figure 4.16 (a) has two open slots, which are etched on the two opposite corners of the square patch. Two feed lines are orthogonally arranged for dual-polarization. In Figure 4.16 (b), two more symmetrical open slots are added in Ant. 2. In Figure 4.16 (c), eight open slots are etched on the four corners of the patch to obtain the entire structural symmetry as the proposed antenna, and the antenna is fed by the differential fed ports.

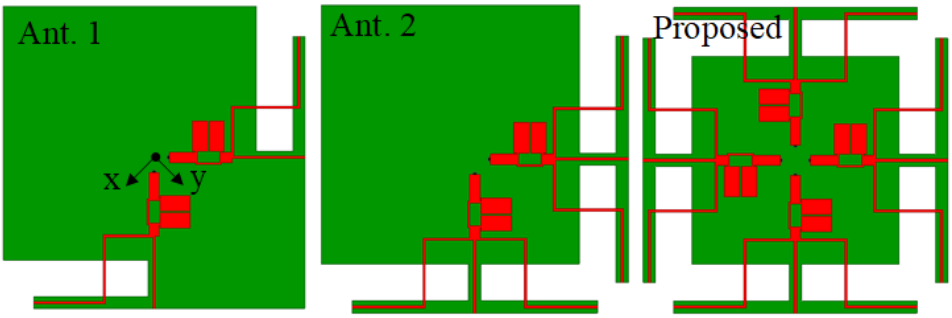

(a) (b) (c)

Figure 4.16 Evolution process of the proposed differentially fed dual-polarized antenna. (a) Ant. 1. (b) Ant. 2. (c) Proposed antenna.

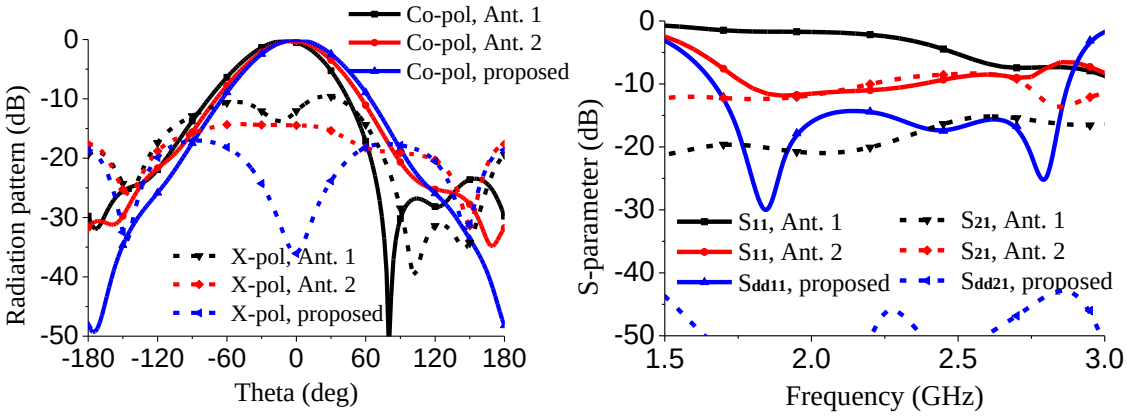

(a) (b)

Figure 4.17 Simulated results of the antennas in the evolution process. (a) Radiation patterns at 2.2 GHz in V-plane. (b) S-parameters.

Figure 4.17 shows the corresponding simulated radiation patterns and the S-parameters of the reference antennas in the evolution process. Although all the reference antennas are symmetrical in V-plane, unsymmetrical radiation patterns are still observed for Ant. 1 and Ant. 2 in V-plane. In Figure 4.17 (a), Ant. 1 has the worst radiation patterns, including the unsymmetrical co-polarization and the poorest cross-polarization level. After incorporating the other two symmetrical slots for Ant. 2, the symmetry of the co-polarized radiation pattern is a little improved and the cross-polarization level is reduced to some extent. However, the radiation patterns of Ant. 1 and Ant. 2 are still worse than the proposed antenna. The main

reason for these results is the strong reflections at the two input ports and the poor isolations between the two input ports for these two reference antennas, and these S-parameters are shown in Figure 4.17 (b). Compared to Ant. 1, worse isolation is observed for Ant. 2. This is caused by the strong coupling between the two radiating slots at the bottom right corner of the square patch. As for the radiation patterns in H-plane, they will be more seriously affected, including the asymmetry of the co-polarized radiation pattern and poor cross-polarization levels, which are caused by the asymmetry of the antenna structure in this plane.

Therefore, to get symmetrical radiation patterns in both H-plane and V-plane, eight open slots are etched symmetrically on the four corners of the patch for the proposed antenna. By using the differentially fed method, orthogonal polarizations are excited with symmetrical radiation patterns and very low cross-polarization level in the broadside direction. Furthermore, the simulated S-parameters in Figure 4.17 (b) also show that the proposed antenna has the high port isolation (>45 dB) and the low reflection coefficient (<-15 dB) with three reflection zeroes within the bandwidth (1.68-2.8 GHz).

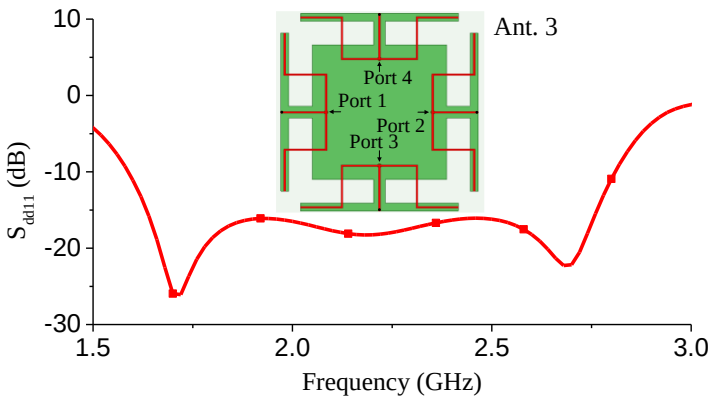

Figure 4.18 Simulated reflection coefficient of the simplified reference antenna (Ant. 3).

The proposed antenna has the multi-resonance characteristic with three different resonances, including the open slot resonance, the monopole resonance, and the patch resonance. In the configuration of the antenna, eight symmetrical open slots are introduced at the four edges of the centre patch. Eight stair-shaped strips working as the monopoles are used to excite the eight open slots. The centre square patch is also elaborately excited by optimizing the parameters of the antenna. To illustrate the working principle of the three different resonances, a simplified reference antenna (Ant. 3) is investigated, and it is inset into Figure 4.18. Different from the proposed antenna, four integrated stepped impedance resonators are removed from the top layer to clearly show the different resonances of the antenna. In addition, the antenna input ports are moved to the feed lines to directly reflect

the input impedance of antenna. Other configuration parameters of Ant. 3 are the same as the proposed antenna. The simulated reflection coefficient of Ant. 3 is shown in Figure 4.18. Three reflection zeroes are clearly observed at 1.72 GHz, 2.18 GHz, and 2.68 GHz, and these different reflection zeroes represent three different resonances.

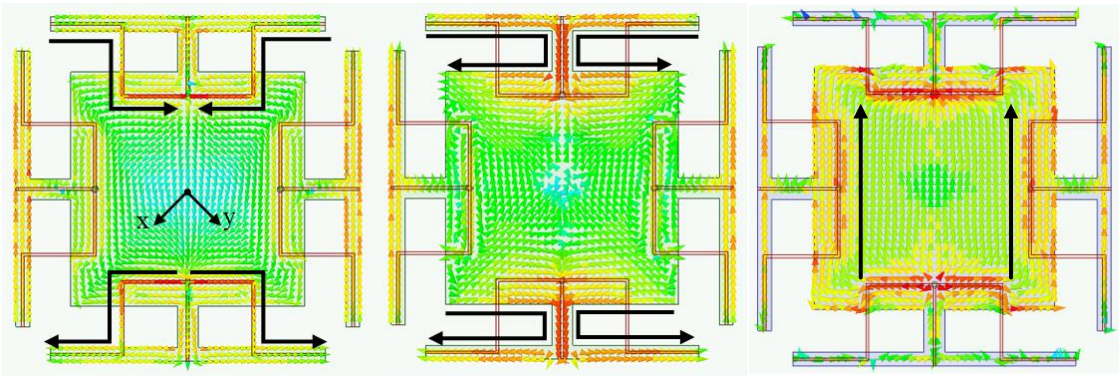

(a) (b) (c)

Figure 4.19 Current distributions of Ant. 3 at different resonant frequencies of the reference antenna. (a) 2.68 GHz. (b) 2.18 GHz. (c) 1.72 GHz.

Figure 4.19 shows the current distributions of Ant. 3 at these different resonant frequencies. In Figure 4.19 (a) at 2.68 GHz, strong current distributions are mainly concentrated on the surfaces of the stair-shaped monopoles, and this means the input energy is mainly radiated into the air by these monopoles. Therefore, the resonant frequency can be estimated by the length of the monopole, that is

$$f_1 \approx \frac{c}{4(L_1 + L_2 + L_3)\sqrt{\varepsilon_{r1}}} \tag{4.14}$$

In Figure 4.19 (b) at 2.18 GHz, strong current distributions are found on the edges of the four open slot. Slot radiation mode is excited at this frequency. So the resonant frequency can be estimated by

$$f_2 \approx \frac{c}{2(L_4 + L_5 + L_6)\sqrt{\varepsilon_{r2}}} \tag{4.15}$$

In Figure 4.19 (c) at 1.72 GHz, strong current distributions are mainly focused on the surface of the square patch. Therefore, patch mode is excited, and the resonance at this frequency is mainly determined by the square patch. The corresponding resonant frequency can be estimated by

$$f_3 \approx \frac{c}{2(2L_6 + w_3)\sqrt{\varepsilon_{r3}}} \tag{4.16}$$

In equations (4.14)-(4.16), c is the light velocity in the free space, and ε_{r1}, ε_{r2}, and ε_{r3} are the effective dielectric permittivities for the monopoles, the slots, and the patch,

respectively. Note that the collective current direction on the stair-shaped monopoles shown in Figure 4.19 (a) and four open slots shown in Figure 4.19 (b) is in the φ=+45° direction, which is realized for the +45° polarization. Whereas in the φ=-45° direction, currents directions are opposite, and radiations from these opposite currents are cancelled in the far-field. Therefore, a low cross-polarization level can be expected for the proposed antenna.

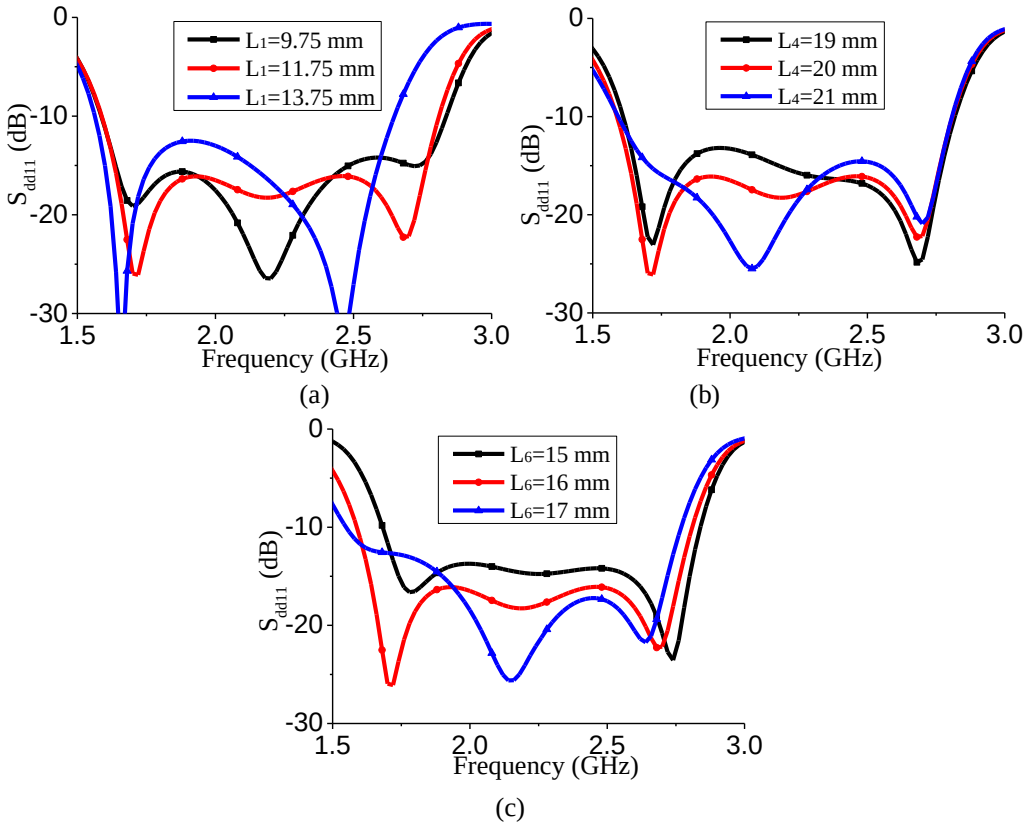

Figure 4.20 Parameters study of the different resonances of the reference antenna.
(a) $\boldsymbol{L_1}$. (b) $\boldsymbol{L_4}$. (c) $\boldsymbol{L_6}$.

To illustrate the effects of the different antenna parameters on the antenna performance of the different resonances, parameters of L_1, L_4, and L_6 are studied in Figure 4.20 according to the equations in (1)-(3). As shown in Figure 4.20 (a), when the length of the monopole L_1 becomes longer, it is can be observed that the monopole resonance at the higher frequency moves to lower frequency, whereas the other resonances almost keep unchanged. In Figure 4.20 (b), when the length of the open slot (L_4) grows longer, the slot mode at the centre frequency also moves to lower frequency. The resonances for the monopole mode and the patch mode are almost unaffected.

When studying the parameter of L_6 for the patch mode in Figure 4.20 (c), the variation of the curves is a little complicated. As the increase of the length of L_6, the lower resonance for the patch mode moves to the lower frequency, while other resonances are affected by the

change of L_6. The centre resonance for the slot mode slightly shifts to the lower frequency due to the increase of the open slot length. The higher resonance for the monopole mode also shifts to the lower frequency due to the increase of the equivalent electric length for L_3, which is printed on the top of the patch. This can also be demonstrated by (1)-(3), when L_6 is changed, both f_2 and f_3 are affected. Therefore, as the change of the patch mode, both the slot mode and the monopole mode will be affected.

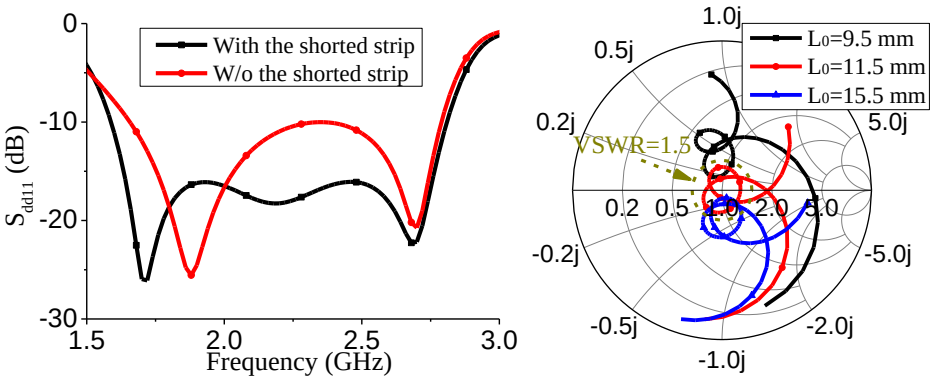

(a) (b)

Figure 4.21 Study of the effect of the shorted microstrip lines on the performance of the impedance bandwidth for Ant. 3.
(a) With and without the shorted microstrip lines. (b) Variation as the length of the shorted microstrip lines.

To match the three different resonances well with characteristic impedance of the differentially fed coaxial cables, shorted microstrip lines are introduced to tune the input impedance of the antenna. Figure 4.21 shows the effect of the shorted microstrip lines on the impedance bandwidth of the antenna. In Figure 4.21 (a), when the shorted microstrip lines are removed from the antenna, it is observed that one reflection zero is disappeared on the curve with narrowed impedance bandwidth due to the mismatching between the antenna radiator and the feeding cables. Furthermore, the first reflection zero shifts to the upper frequency, and the reflection coefficient at the centre band is also affected and deteriorated.

To extensively investigate the variation of the length of the shorted lines, different shorted strip length of L_0 are studied. As shown in the smith chart in Figure 4.21 (b), with the increase of the length, the inductance produced by the shorted microstrip line grows bigger. This means more inductance is shunted to the input port. Therefore, the smith curve is moved to the inverse direction of the inductive region as the increase of the length. As shown in the smith chart, when L_0 is selected as 11.5 mm, a widest impedance bandwidth is obtained for the antenna, and the smith curve of Ant. 3 within the VSWR=1.5 circle is from 1.63GHz to 2.77 GHz.

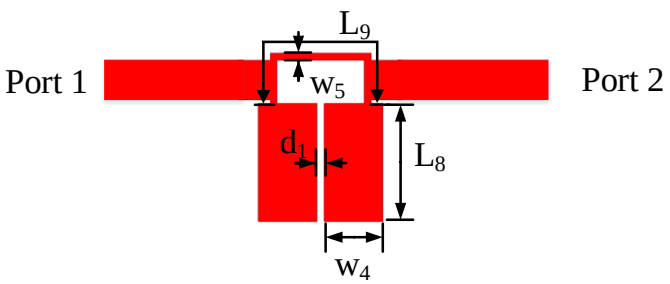

Figure 4.22 Configuration of the stepped impedance resonator based lowpass filter. (Detailed parameters: L_8=5 mm, L_9=8 mm, w_4=2.5 mm, d_1=0.3 mm.)

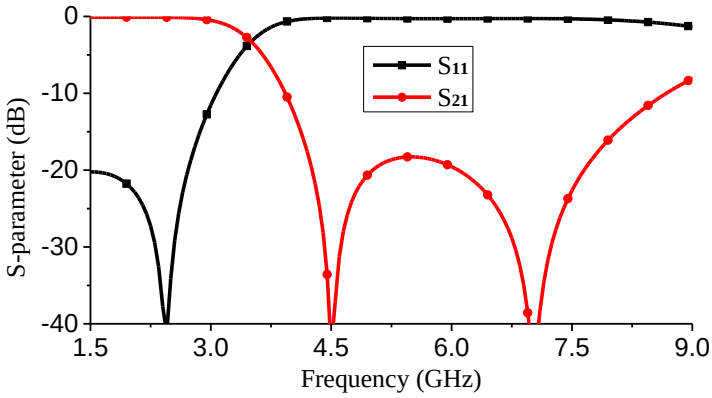

Figure 4.23 Filter response of the stepped impedance resonator based lowpass filter.

Thanks to the centre radiating patch, compact stepped impedance resonators can be elaborately integrated on the top of the patch. Figure 4.22 shows the detailed configuration of the stepped impedance resonator. The stepped impedance resonator is composed of a high impedance microstrip line with the width of w_5 and length of L_9, and a low impedance microstrip line with the width of w_4 and length of L_8. By using the stepped impedance resonator, an elliptic function lowpass filter can be realized with two attenuation poles [131]-[132]. Figure 4.23 shows the filtering response of the integrated lowpass filter. As shown in the figure, the simulated reflection coefficient from 1.7 GHz to 2.7 GHz is lower than -20 dB. Two attenuation poles are obtained at 4.5 GHz and 7 GHz. The simulated suppression for the lowpass filter from 4.1 GHz to 8.1 GHz is higher than 15 dB.

Figure 4.24 compares the simulated S_{dd11} and peak realized gain of the proposed antenna with Ant. 3. As shown in the figure, Ant. 3 has many undesired harmonic resonances and radiations. Harmonic resonances of Ant. 3 can be observed at around 4.1 GHz, 5.5 GHz, 7.15, and 7.6 GHz. Correspondingly, the peak realized gains at these frequencies are found with high values, which are greater than 5 dBi. To reduce the antenna harmonic radiation, compact stepped impedance resonators are elaborately integrated into the proposed antenna without any increase of the antenna footprint. After the stepped impedance resonators are

integrated into the antenna, the higher order harmonic resonances and radiations are greatly suppressed. Referring to the simulated results in Figure 4.23, high suppression can be found at the frequencies of the two deep attenuation poles. Combining with the multi-resonance characteristic of Ant. 3, improved wideband harmonic suppression can be observed in this figure. Strong reflection is achieved from 3 GHz to 9 GHz for the antenna with the simulated S_{dd11}> -1.46 dB. In addition, the gain over the whole harmonic frequency band is lower than -5.1 dBi. Three octave harmonic suppression is achieved by elaborately integrating the stepped impedance resonators into the antenna.

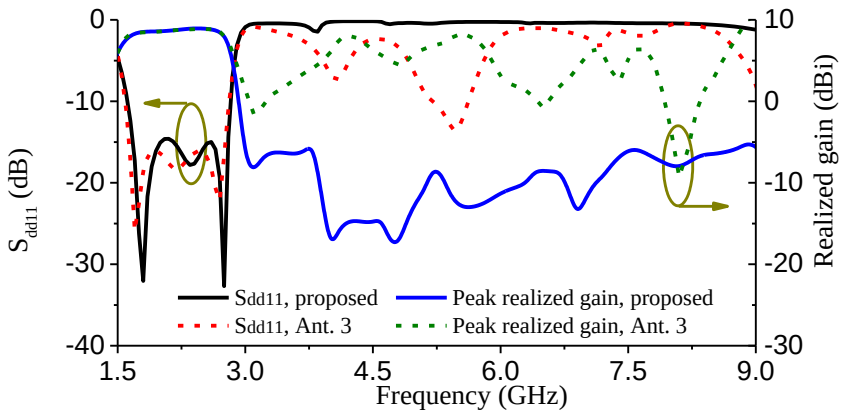

Figure 4.24 Simulated reflection coefficients and peak realized gains of the proposed antenna and Ant. 3.

4.3.3 Results and Discussion

The proposed differentially fed dual-polarized antenna was fabricated and measured at the University of Kent. The photograph of the fabricated prototype of the antenna is inset into the right of the Figure 4.25. In the figure, both the measured and simulated S-parameters of the prototype are shown for a good comparison. The measured impedance bandwidth for S_{dd11} and S_{dd22} lower than -15 dB is from 1.70 GHz to 2.81 GHz. Owing to the symmetry of the antenna, very high isolation is measured within the whole operation band, which is higher than 39 dB. Furthermore, three octave high harmonic suppression is achieved with the measured S_{dd11} and S_{dd22} higher than -2.2 dB from 3 GHz to 9 GHz. Good agreement can be observed between the simulated and measured results. Small differences between the simulated and measured results are mainly caused by the fabrication and solder errors of the feed cables.

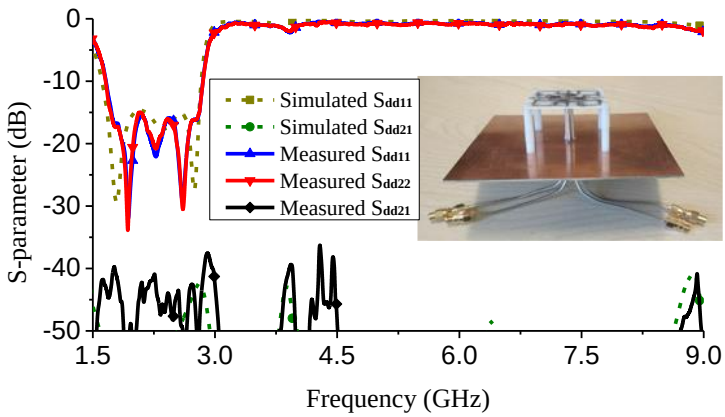

Figure 4.25 Measured and simulated S-parameters of the proposed differentially fed dual-polarized antenna.

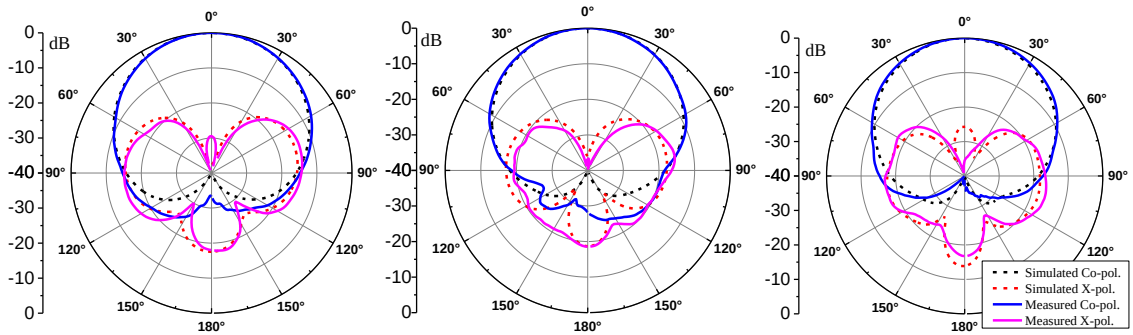

(a) (b) (c)

Figure 4.26 Measured and simulated normalized radiation patterns of the proposed antenna in H-plane when differential port d1 is excited.

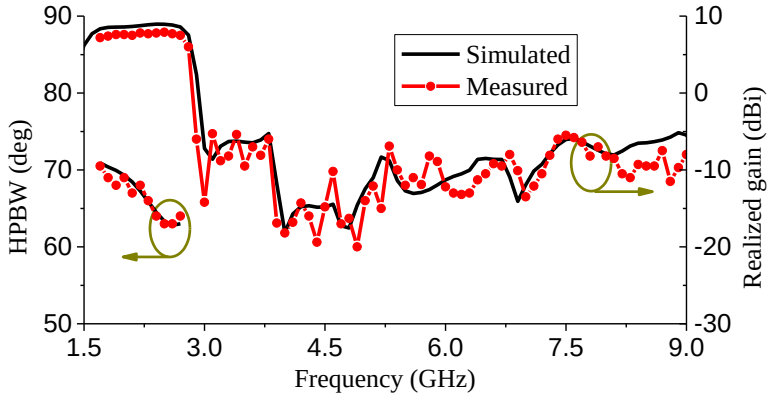

Figure 4.27 Measured and simulated HPBW and peak realized gain of the proposed differentially fed dual-polarized antenna.

Figure 4.26 shows the measured and simulated normalized H-plane radiation patterns when differential port d1 is excited at 1.7 GHz, 2.2 GHz, and 2.7 GHz. Owing to the symmetry of the antenna, only H-plane radiation patterns are given in the figure. As can be seen in the figure, the measured radiation patterns agree well with the simulated radiation patterns. The measured cross-polarization level is 29 dB lower than co-polarization in the broadside direction and 23 dB lower in the ± 30° directions. The measured front to back ratio

is higher than 16 dB. Figure 4.27 shows the measured HPBW and peak realized gain of the antenna. The measured HPBW varies from 63º to 71º within the half-power bandwidth. Stable antenna gain is also achieved within the bandwidth, which varies from 7.2 dBi to 7.9 dBi. Most importantly, wideband harmonic radiations form 3 GHz to 9 GHz are suppressed with the maximum harmonic gain lower than -5.3 dBi.

Table 4.2 Comparison of the reference antennas

Ref.	Bandwidth	Height	Isolation (dB)	S_{11} of the Harmonic	Gain of the Harmonic radiation
[60]	45% 1.71-2.69 GHz	$0.4\lambda_0$	39	N.G.	N.G.
[61]	52% 1.7-2.9 GHz	$0.27\lambda_0$	36.3	N.G.	N.G.
[62]	45% 1.7-2.75 GHz	$0.3\lambda_0$	38	N.G.	N.G.
[133]	7%	0.508 mm	/	>-2.5 dB 3.5-12 GHz	N.G.
[134]	8.42%	0.8 mm	/	>-2.8 dB 3-10 GHz	N.G.
[135]	13.9%	1.8 mm	/	>-4.2 dB 3-9 GHz	N.G.
This work	49% 1.70-2.81 GHz	$0.25\lambda_0$	39	>-2.2 dB 3-9 GHz	<-5.3 dBi 3-9 GHz

Table 4.2 compares the presented antenna with the recently published antennas. In the table, λ_0 is the free space wavelength at the centre operation frequency. Dual-polarized antennas in [60]-[62] are designed for 1.7-2.7 GHz base station applications by using crossed dipoles, dual-dipoles, or the multi-dipoles for wideband operations. Note that the antenna in [62] has the highest port isolation, but its profile is also the largest. As the development of the wireless communication systems, more and more military and commercial wireless devices are increased in the realistic environment. If the harmonic radiations are not considered, serious interferences and congestions will be caused to affect each other's operation. To the authors' knowledge, few of these base station antennas are concerned about the harmonic radiations.

Designs in [133]-[135] are the single-polarized antennas, so there are no port isolations. For the harmonic suppression, normally only reflection coefficients are considered, so the

harmonic radiations are not provided in the references. By introducing a pair of partial ring slots and an open-ended circular stub under the microstrip line [133], wideband harmonic suppression is achieved. However, additional footprint is required for these additional feed network. Designs in [134] are the slot antenna, and the etched slots are employed as the defected ground structures to achieve the wideband harmonic suppression. Regarding the wideband antennas for base station applications, multiple resonances are normally employed to broaden the impedance bandwidth. Therefore, compared to the narrow band antennas in [133]-[135], more complicated harmonic radiations will be appeared at the upper out-of-band, and it is more difficult to realize wideband antennas with wideband harmonic suppression. As for the presented antenna, wide impedance bandwidth of 1.70-2.81 GHz (49%) is achieved for S_{dd11} and S_{dd22} lower than -15 dB with high isolation (>39 dB). Moreover, wideband harmonic suppression from 3 GHz to 9 GHz is obtained with the S_{dd11} and S_{dd22} higher than -2.2 dB. In addition, the corresponding measured harmonic radiation gain is lower than -5.3 dBi.

4.4 Low-Profile Differentially Fed Dual-Polarized Array Antenna

In this section, a novel low-cost differentially driven dual-polarized patch antenna by using the intersected open loop resonators is proposed. By using the electric coupling from the intersected resonators to the top radiating patch, two orthogonal polarizations are realized. With the even and odd mode current distributions on the intersected resonators, high port isolation and low cross-polarization level are achieved. The proposed dual-polarized antenna is further illustrated by the resonator-based filtering antenna design method. The differentially driven resonator can be equivalent as a double loaded resonator, and the external quality factor is extracted based on the double loaded resonator. Compared to the traditional multi-layer patch antennas, the proposed antenna has the advantages of simple configuration with low fabrication cost.

To validate the design method, the proposed antenna and array are designed, fabricated, and measured. For the antenna element, wide impedance bandwidth of 17.2% is measured with the overall thickness of $0.067\lambda_0$ (where λ_0 is the free space wavelength at 3.5 GHz). Furthermore, high isolation (>38.5 dB) and low cross-polarization level (< -33 dB) are achieved. For the dual-polarized 1×4 antenna array, which is designed for 5G base station applications with very low reflection coefficient (<-15 dB). The measured half-power beamwidth within the bandwidth is 66-70º and 20-22º in H-plane and V-plane, respectively. In addition, beam scanning performance is also investigated for base station coverage.

4.4.1 Antenna Element

The configuration of the proposed differentially driven dual-polarized antenna is shown in Figure 4.28. The antenna is composed of three parts, a top square radiating patch, two intersected open loop resonators, and a square ground plane. The top radiating patch operates at the dominant mode (TM_{10} mode) for each polarization. Hence, the length of the square patch is about half guided wavelength at the centre frequency. For the open loop resonators, the total length ((L1+L2+L3)×2) is about half free-space wavelength at the centre frequency.

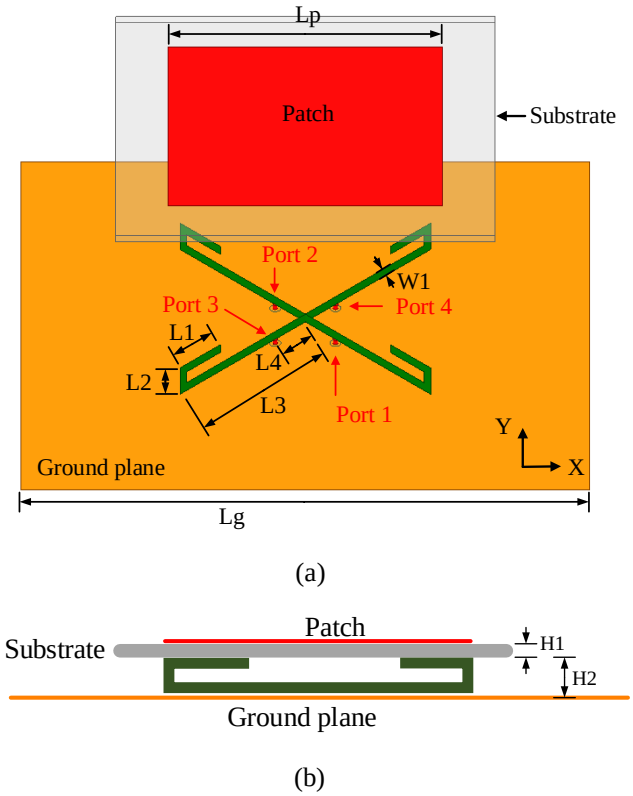

Figure 4.28 Configuration of the proposed dual-polarized antenna.
(a) Exploded view. (b) Side view. (Detailed antenna design parameters: L1 = 6 mm, L2 = 3.4 mm, L3 = 18.7 mm, L4 = 4.5 mm, W1= 1 mm, Lp = 29 mm, Lg= 80 mm, H1 = 0.813 mm, H2 = 5 mm.)

The radiating patch is printed on a substrate of Rogers 4003C, with the relative dielectric permittivity of 3.55 and the thickness of 0.813 mm. The intersected open loop resonators are etched from a copper sheet with the thickness of 0.1 mm. These two open loop resonators are connected to each other at the centre of each resonator, and four feed ports are connected to the intersected resonators with the distance of L4×2. The height from the top substrate to the ground plane is 5 mm. It should be noted that the antenna is designed for ±45° polarizations. Therefore, as a general definition for radiation patterns, the xz-plane in Figure 4.28 is defined as H-plane (horizontal plane), and the yz plane is defined as V-plane (vertical plane). The pair of port 1 and port 2 in the figure is designated as the differential port d1,

while the pair of port 3 and port 4 is designated as the differential port d2. All the simulation results are obtained by using the 3D electromagnetic simulation software ANSYS HFSS. The design parameters of the dual-polarized antenna are given in the caption of Figure 4.28.

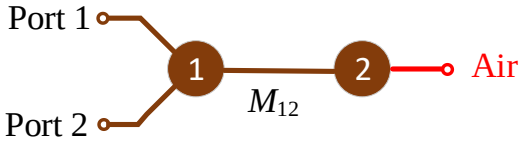

Figure 4.29 Coupling structure of the proposed antenna for one polarization.

To illustrate the working principle of the proposed antenna, the resonator-based coupling structure for the differentially driven antenna is shown in Figure 4.29. Owing to the symmetry of the antenna, only one polarization is illustrated. In the figure, resonator 1 represents the open loop resonator, resonator 2 denotes the top radiating patch. Note that the resonator 1 is driven by the differential pair of port 1 and port 2. The coupling coefficient (M_{12}) and the external quality factor (Q_e) can be synthesized by using the filter and filtering antenna design methods presented in [118]. A filtering response with FBW=15% and S_{11}<-15 dB is used for the initial antenna design, and the synthesized M_{12} and Q_e are 0.215 and 5.565, respectively.

The external quality factor for the differentially driven resonator is different from the traditionally designed singly driven resonator. Because of the loading of the two differential ports, one can get the following relation

$$S_{21} = \frac{1}{1 + jQ_e \Delta\omega/\omega_0} \tag{4.17}$$

then, the external quality factor for the differentially driven antenna can be derived as

$$Q_e = \frac{\omega_0}{\Delta\omega_{3dB}} \tag{4.18}$$

where ω_0 is the resonant frequency, $\Delta\omega_{3dB}$ is the bandwidth at which the attenuation for S_{21} is 3 dB lower than the resonant frequency. Therefore, the relation between the distance of the two differential feed ports ($2 \times$ L4) and the external quality factor (Q_e) can be obtained by using (3)-(4). With the relation of L4 and Q_e, and referring to the initial value of Q_e=5.565, an initial feed position of L4 can be determined for the antenna design.

The symmetrical plane of the excited resonator can be equivalent to a virtual ground plane. As shown in Figure 4.30, TT' plane is a symmetrical plane of the resonator. Because of the differentially driven method, odd mode current is distributed on the φ =45° arranged resonator, and the symmetrical plane (TT') represents the short circuit plane. This will be

further demonstrated by the simulated current distribution on the resonators. Figure 4.31 shows the current distribution on the surface of the open loop resonators at 3.5 GHz. Strong current distribution can be observed on the φ=45° excited resonator with the same current direction, and it is an odd mode current distribution. The strongest magnitude is located at the centre of the resonator, and the weakest current magnitude is distributed on the both ends of the resonator. Therefore, the top radiating patch is excited by the open loop resonator with electric coupling. Whereas the φ=-45° unexcited resonator, reverse current direction (which is the even mode current distribution) is observed with very weak current distribution. The symmetrical TT' plane for this resonator is equivalent to an open circuit plane. By virtue of the short circuit plane and the open circuit plane, there will be no influence on each other's resonance, even though the resonators are connected to each other at the centre. The current distribution on the intersected resonators also reveals that high port isolation and low cross-polarization level can be obtained for the two orthogonal polarizations.

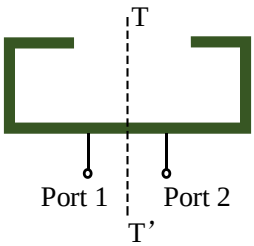

Figure 4.30 Double loaded open loop resonator for one polarization.

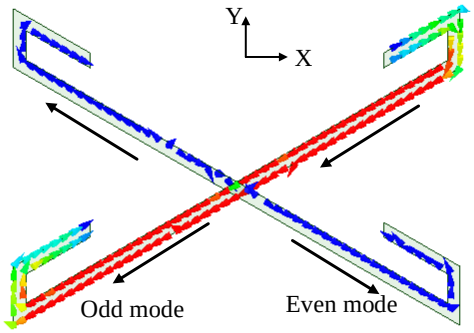

Figure 4.31 Surface current distribution on the open loop resonators.

A single-ended antenna is compared with the proposed differentially driven antenna to illustrate the high isolation and low cross-polarization of the proposed antenna. Both of them are excited by the open loop resonators. The simulation model of the single-ended dual-polarized antenna is inset into the bottom right corner of Figure 4.32. Different from the proposed antenna, the two resonators are crossed but not connected to each other to avoid the mutual influence of the dominant resonant modes on the two open loop resonators. Therefore, there is a crossover bridge at the centre of the φ=-45° arranged resonator. Two

feed ports are connected to the two crossed open loop resonators with the same feed position as the differentially driven antenna in Figure 4.28.

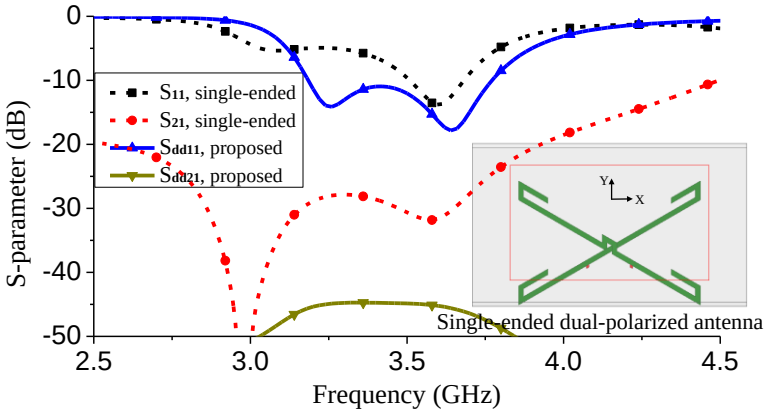

Figure 4.32 Simulated S-parameters between the single-ended and differentially driven dual-polarized antenna.

As shown in Figure 4.32, two obvious differences can be observed. First, the reflection coefficient for the single-ended dual-polarized antenna is deteriorated, which results from different loading effects of external quality factors, as illustrated by (4). The single-ended reference antenna becomes a single loaded dual-polarized antenna. The simulated isolations for two antennas are also different. The simulated isolation for the single-ended dual-polarized antenna is 31 dB within the bandwidth due to the loss of the symmetrical driven ports, while the isolation of the differential driven dual-polarized antenna is higher than 45 dB owing to the symmetrical differentially driven ports.

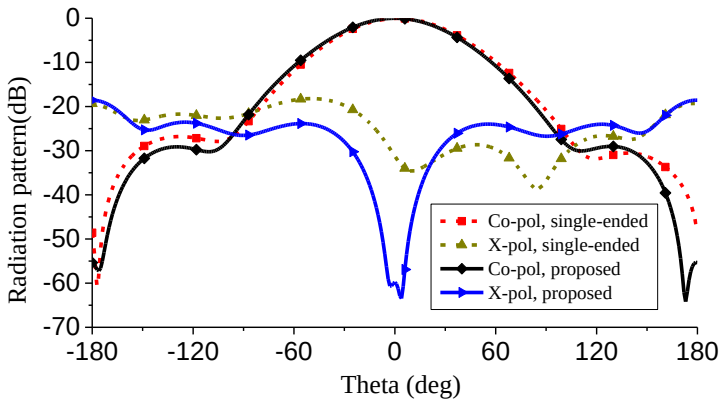

Figure 4.33 Simulated normalized H-plane radiation patterns for the single-ended and differentially driven dual-polarized antenna.

The simulated normalized H-plane radiation patterns for the single-ended and differentially driven dual-polarized antennas are shown in Figure 4.33. The co-polarized radiation patterns are almost the same. However, the simulated cross-polarization of the

single-ended reference antenna is unsymmetrical. Whereas the cross-polarization of the differentially driven antenna is symmetrical, and it is much lower in the broadside direction owing to the symmetrical differential excitation.

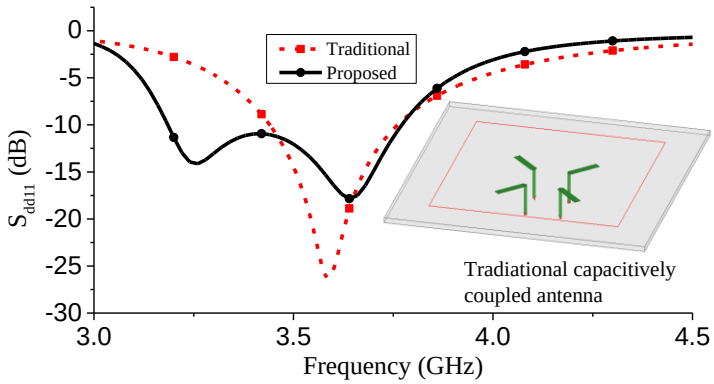

Figure 4.34 Comparison between the traditional capacitively coupled antenna and the proposed antenna.

Owing to the introduction of the intersected open loop resonators, the proposed differentially driven dual-polarized antenna has a wider impedance bandwidth compared to the traditionally designed capacitively coupled antenna. The configuration of the traditionally designed capacitively coupled antenna is inset into the bottom right corner of Figure 4.34. The capacitive coupling is introduced by using the copper strips (in green colour) on the bottom layer of the substrate. The copper strips on the bottom layer can also be regarded as the coupling probes to feed the top radiating patch. It is also designed as a differentially driven antenna for good comparison. Both the capacitively coupled antenna and the proposed antenna have the same height and patch size.

As shown in Figure 4.34, the simulated impedance bandwidth for $S_{11} < -10$ of the capacitively coupled antenna is 3.45-3.76 GHz (FBW= 8.3%) with a deep reflection zero at 3.6 GHz. One resonance is observed, which is from the top radiating patch. The proposed antenna has an impedance bandwidth of 3.16-3.74 GHz (FBW= 16.8%). Two times wider bandwidth is obtained for the proposed dual-polarized antenna with two reflection zeroes at 3.26 GHz and 3.64 GHz. Two resonances are observed, and they are generated from the top radiating patch and the open loop resonator. Because the simulated isolations of these two antennas are higher than 45 dB, they are not included in the figure for comparison.

4.4.2 Array Design

In this section, a 1×4 linear array is designed for base station applications. To meet the requirements for base stations [61], such as the very low reflection coefficient (<-15 dB) and

specific half-power beamwidth (within 60°-70°), the antenna element needs to be further optimized. As shown in Figure 4.35 (a), the optimized total size of the 1×4 antenna array is 235 mm×70 mm, with the element distance of 55 mm. The distance between the elements is $0.64\lambda_0$ (λ_0 is the wavelength in the free space at 3.5 GHz), which is designed to eliminate the possible grating lobes and ensure the beam scanning performance of base stations [106].

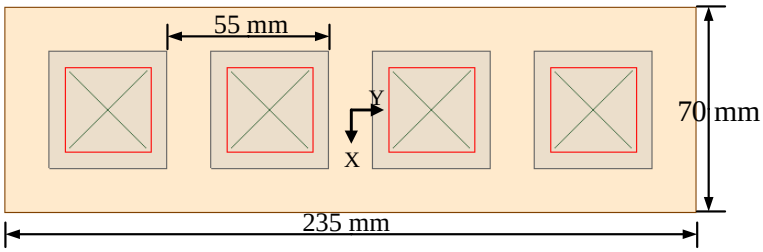

(a)

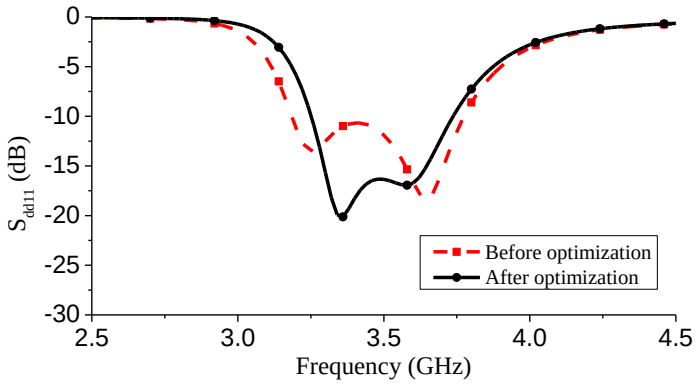

(b)

Figure 4.35 (a) Configuration of the dual-polarized antenna array for base station ±45° polarizations. (b) The simulated reflection coefficients before and after optimization.
(Optimized antenna element parameters: L1=5.8 mm, L2= 3.2 mm, others are unchanged.)

The parameters for the array element are shown in the caption of Figure 4.35, while other parameters are the same as the ones presented in the last section. Figure 4.35 (b) compares the antenna reflection coefficients before and after optimization. After optimization, the simulated bandwidth for $S_{dd11} < -15$ dB is 3.28-3.64 GHz. Because the simulated isolations of both two antennas are higher than 45 dB, they are not included in the figure for comparison.

4.4.3 Results and Discussion

The proposed differentially driven dual-polarized antenna element was fabricated and measured. All the antenna and array were measured by the Rohde & Schwarz ZVL network analyzer and the Asysol far field antenna measurement system at the University of Kent.

The fabricated antenna prototype is shown in Figure 4.36, and the measured S-parameters are shown in Figure 4.37. It can be seen that the measured S-parameters agree well with the simulated results. The measured bandwidth for S_{dd11} and S_{dd22} below -10 dB is 3.17-3.77 GHz, and the isolation between the two differential ports is higher than 38.5 dB. Discrepancies between the simulated and measured results are mainly due to the fabrication and assembly errors.

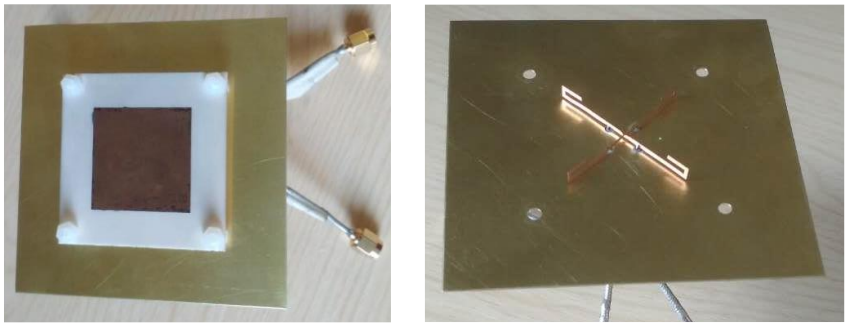

(a) (b)

Figure 4.36 Photographs of the fabricated dual-polarized antenna prototype. (a) Top view. (b) Inside view of the intersected open loop resonators.

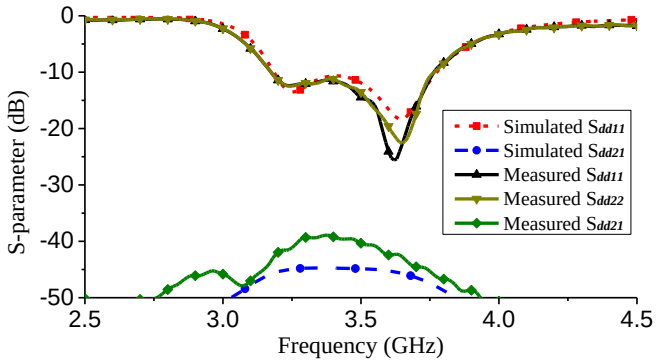

Figure 4.37 Measured and simulated S-parameters of the fabricated antenna element.

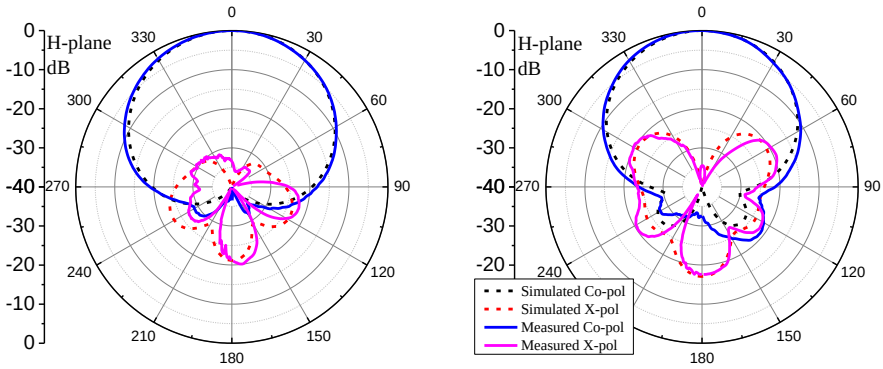

(a) (b)

Figure 4.38 Simulated and measured H-plane radiation patterns when differential port d1 is excited. (a) 3.2 GHz. (b) 3.7 GHz.

Figure 4.38 shows the measured and simulated normalized radiation patterns for the proposed antenna in the H-plane when differential port d1 is driven. Owing to the symmetry

of the antenna, only H-plane radiation patterns are given in the figure. The measured half-power beamwidth in the H-plane is about 65º. The measured cross-polarization level is lower than -33 dB in the broadside direction. Good agreement can be observed between the simulated and measured radiation patterns. The measured peak realized gain is about 8.2 dBi within the bandwidth, which is 1.2 dB lower than the simulated peak realized gain.

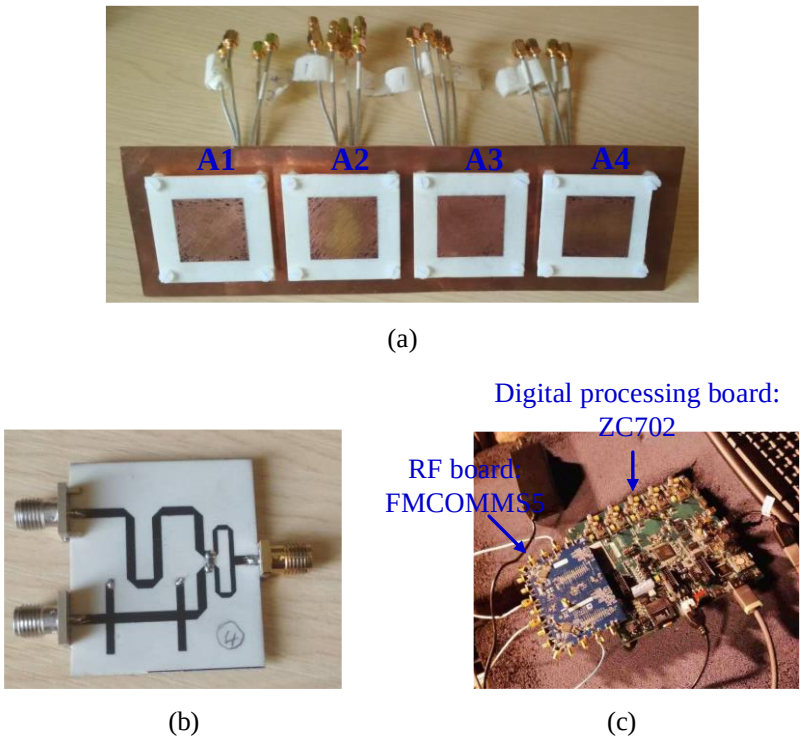

Figure 4.39 Photographs of (a) the fabricated 1×4 antenna array, (b) the fabricated out-of-phase power divider, and (c) the hardware platform for beam scanning performance.

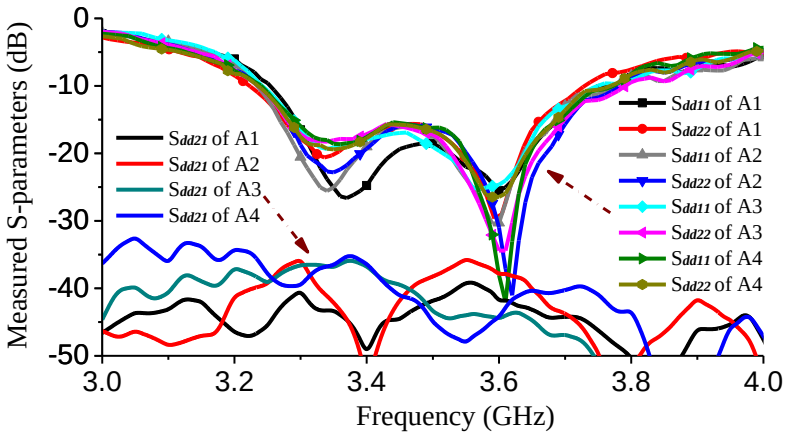

Figure 4.40 Measured S-parameters of the four antenna elements in the fabricated 1×4 antenna array.

Figure 4.39 shows the photographs of the fabricated 1×4 antenna array, an out-of-phase power divider, and a generic hardware platform. The out-of-phase power divider is used to feed differentially driven antenna for radiation patterns measurement. The generic hardware platform, which is composed of a digital processing board ZC702 and a RF board

FMCOMMS5, is used to generate the desired scanning beams. The measured S-parameters of the antenna element in the array are shown in Figure 4.40. The measured overlapped 15 dB return loss bandwidth is from 3.3 GHz to 3.66 GHz. The measured isolation is better than 35 dB. The isolation in the array is a little worse than the antenna element, which is caused by the fabrication errors and the mutual couplings from the other antenna elements.

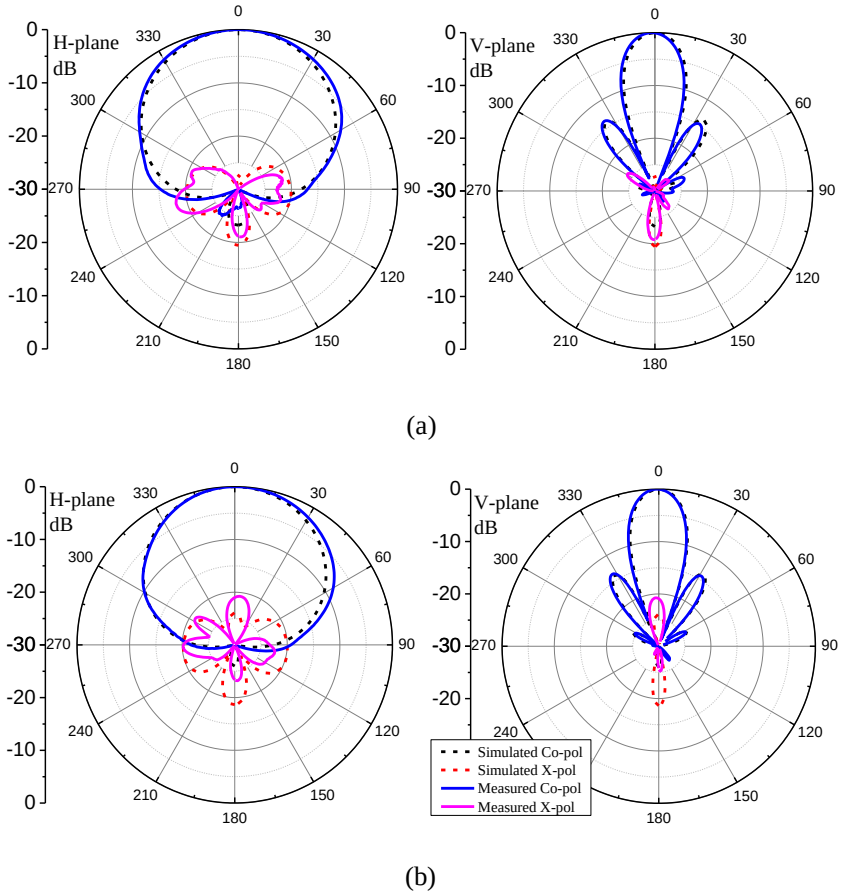

(a)

(b)

Figure 4.41 Simulated and measured radiation patterns when the differential port d1 is excited for the fabricated antenna array. (a) 3.3 GHz. (b) 3.6 GHz.

Figure 4.41 shows the measured and simulated radiation patterns of the antenna array when each antenna element is excited with equal magnitude and co-phase signal at 3.3 GHz and 3.6 GHz. Because of the symmetry of the two polarizations, only radiation patterns excited by the differential port d1 are given in the figure. In the H-plane, the beamwidth is 66-70º within the bandwidth. In the V-plane, the maximum radiation direction is observed in the +z direction, and the beamwidth is 20-22º within the bandwidth. Due to the mutual coupling between the antenna elements, the measured the cross-polarization level is -20.8 dB lower than the co-polarization in the broadside direction. The measured back lobe level

is better than the simulated result, which is probably caused by the blockage of the feeding coaxial cables. The measured realized peak gain of the antenna array is around 13.8 dBi.

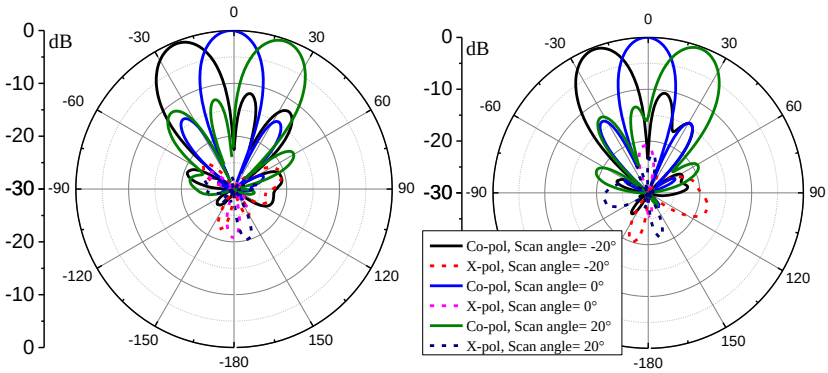

(a) (b)

Figure 4.42 Measured radiation patterns with the scan angles of -20º, 0º, and +20º. (a) 3.3 GHz. (b) 3.6 GHz.

Because the antenna array is measured with the array beamwidth of 20-22º, three beams with the scan angles of -20º, 0º, and +20º are investigated. As shown in Figure 4.42, with the beam scanning performance, the measured overall half-power beamwidth of the three beams can cover 64º and 61º at 3.3 GHz and 3.6 GHz. The measured cross-polarization levels are lower than the broadside beam when the array beam scans at ±20º, which are lower than -24 dB. The measured realized gain at the scan angles of ±20º is about 0.4 dB lower than the broadside beam. Therefore, the beam scanning performance of the proposed antenna array can provide a good coverage for base stations.

Table 4.3 Comparison of the reference antennas

Ref.	FBW	Height	Isolation (dB)	X-pol (dB)	Driven Mode	No. of Substrates	No. of Layers
[11]	26.7%	$0.2\lambda_0$	25	-20	Single	2	3
[136]	3.6%	$0.1\lambda_0$	25	-19.5	Single	2	4
[21]	18.8%	$0.08\lambda_0$	35	-20	Dif.	2	4
[114]	49.4%	$0.27\lambda_0$	37	-21	Dif.	2	3
[137]	2%	$0.025\lambda_0$	62	-50	Dif.	1	2
This work	17.2%	$0.067\lambda_0$	38.5	-33	Dif.	1	1

Table 4.3 compares the performances of the proposed wideband antenna with the recently published dual-polarized patch antennas. In the table, λ_0 is the free space wavelength at the centre operation frequency. Designs in [11] and [136] are the single-ended dual-polarized antennas, and they have the moderate port isolation and cross-polarization level. Antennas

in [21], [114], and [137] are driven by the differential method, and high port isolation is achieved. However, high antenna port isolation does not promise the low cross-polarization level. Although antenna in [114] has the widest impedance bandwidth, its profile is the largest. By using 180º ring hybrid coupler, the dual-polarized antenna in [137] obtains highest port isolation and lowest cross-polarization level. However, additional insertion loss is introduced with a very narrow bandwidth. By using the open loop resonators, our proposed antenna achieves a wide impedance bandwidth, and keeps low profile configuration. Moreover, high isolation (>38.5 dB) and low cross-polarization level (<-33 dB) are also obtained simultaneously. In terms of the fabrication cost, multi-layer PCB technology is normally used to realize wideband patch antennas, which increase the fabrication complexity and cost. Compared to the other reference antennas, the presented design only uses one substrate with one layer to print the radiator. Therefore, our proposed antenna is especially competitive with the simple structure and low fabrication cost.

4.5 Summary

In this chapter, several differentially fed dual-polarized antennas with different features are presented. First, a wideband and high even mode suppressed six-port power divider is utilized to realize a wideband differentially fed dual-polarized with high common mode suppression. The equivalent circuit under even and odd modes excitations are given for detailed illustration. The second design is a wideband differentially fed dual-polarized antenna with wideband harmonic suppression. The radiating structure is designed based on the open slots, stair-shaped strips, and a square patch. To achieve wideband harmonic suppression, compact stepped impedance resonators are elaborately integrated into this antenna. The last design is a low-cost compact differentially fed dual-polarized array patch antenna. The antenna element is driven by intersected open loop resonators, which is features the high isolation and low cross-polarization level. Beam scanning performances are investigated for this presented array antenna.

Chapter 5. Wideband Circularly Polarized Antennas

5.1 Introduction

To improve the bandwidth of CP antennas, dipole antennas [138]-[141] are employed with a ground plane as the reflector for unidirectional radiation. In [138]-[139], by modifying the ground planes or the backed cavities, crossed dipoles are realized for wideband CP radiation. Two pairs of the off-centre-fed dipoles in [95] are used to achieve broadband circular polarization. Crossed dual-dipoles [140]-[141] are presented to realize wideband CP antennas. However, most of these dipole antennas are with relatively large radiator size. In the array design, large radiator size will lead to the large element distance and strong coupling between the antenna elements. Both of these two effects are undesirable for the array design, especially for the array with the requirement of beam scanning performance [106].

Recently, with the development of the differential microwave circuit systems, differentially fed antennas become increasingly popular because they can directly match the balanced differential circuits without the need of additional baluns for signal conversion [100]. Therefore, differentially fed CP antennas [130], [142]-[143] are developed to directly match the differential circuit systems.

In addition, to overcome these problems of multi-path and Faraday rotation effects and ensure high communication quality of the ITS, dual circularly polarized (DCP) antennas, with both right-hand circularly polarized (RHCP) and left-hand circularly polarized (LHCP) radiations, are widely applied into wireless communication systems. Owing to the advantages of the polarization diversity and frequency reuse, the channel capacity and receiver sensitivity in the wireless communication systems can be greatly enhanced by using DCP antennas [144].

By using the vertically coupled resonator-based structure and introducing the neutralization line between two coupling paths, a low profile high isolated DCP patch antenna [145] is realized. Another convenient way to realize DCP antenna is using the series-fed method to excite the patch with one input port for RHCP radiation, and another for LHCP radiation [146]-[147]. However, it is difficult to develop wideband DCP antennas by using patches, especially for the series-fed patch antennas. In addition, with the help of the wideband quadrature couplers, wideband DCP antennas are developed [148]-[149].

However, wideband couplers will introduce additional insertion loss and fabrication cost. The most common wideband low-cost DCP antennas are the monopole antennas and slot antennas [150]-[152]. By using the stepped impedance feed line and U-shaped slot, overlapped impedance and AR bandwidth of 110.5% is achieved in [152]. However, these antennas normally have bidirectional radiations with one direction for RHCP radiation and the other for LHCP radiation. In addition, unstable radiation patterns are observed for these antennas. The maximum radiation direction varies with the working frequency, and the radiation patterns are asymmetrical with regard to the maximum radiation direction.

5.2 Series-Fed Antenna Using Crossed Open Slot-Pairs

In this section, a novel method of designing a wideband series-fed CP differential antenna is presented. The antenna is composed of two crossed open slot-pairs, which can be equivalent as two crossed dipoles based on analysis of the near-field electric and magnetic field distributions. By studying the input impedance of the crossed open slot-pairs, stable radiating resistance and compact radiator size can be realized. To obtain sequential excitation with the equal magnitude and quadrature phase for CP radiation, a wideband half-power phase shifter is realized by loading an open slot under the feed line. Based on the analyses of the crossed slot-pairs and wideband half-power shifter, the presented wideband CP antenna is developed by serially exciting the narrow open slot-pair and the wide open slot-pair.

It is known that the impedance and AR bandwidths of the series-fed CP antennas are always limited by the series-fed method. Whereas in this design, the narrow open slot-pair is serially loaded not only as the radiator, but also to provide wideband equal magnitude and quadrature phase excitation for the last stage wide open slot-pair. Both the proposed wideband half-power phase shifter and the antenna are extensively analyzed and discussed based on the equivalent circuits. To verify the above design concept, the proposed antenna is fabricated and measured. The measured results of S-parameters and radiation patterns agree well with the simulated results. The overlapped bandwidth for AR<3 dB and return loss>10 dB is from 1.95 GHz to 3.45 GHz (55.6%), which is 2.1 times wider than the simulated results of the traditionally designed counterpart.

5.2.1 Design Principle

Before the design of the proposed CP antenna, two important design principles are discussed and elaborated in this section as the basis of the antenna design. The first is the

crossed open slot-pairs as the main radiating structure. Then, it is followed by the half-power phase shifter as both the radiating and feeding structure.

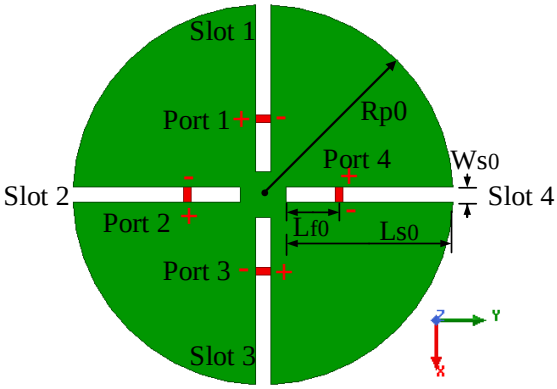

Figure 5.1 Configuration of the proposed four closely spaced, orthogonal arranged crossed open slot-pairs. (Detailed parameters in the configuration: Rp0=54 mm, Ls0=24 mm, Ws0=2 mm, Lf0=6 mm.)

In this design, wideband CP radiation is realized by using two pairs of closely spaced, orthogonal arranged open slot-pairs. The radiation of the closely spaced open slot-pairs can be equivalent as the two crossed dipoles with a stable radiating resistance. Figure 5.1 shows the configuration of the proposed closely spaced open slot-pairs. The radius of the circular patch is Rp. Four symmetrical slots (slot 1, slot 2, slot 3, and slot 4) are arranged closely to each other, and have the same width Ws and length Ls. Four sequential rotated lumped ports (port 1, port 2, port 3, and port 4) are used to excite the open slots with the feed position Lf0. In the figure, the slot-pair of slot 1 and slot 3 can radiate as a dipole located along the y-axis, while the slot-pair of slot 2 and slot 4 can radiate as a dipole located along the x-axis.

Figure 5.2 shows the simulated near-field electric field and magnetic field distributions when the slot-pair of slot 1 and slot 3 is excited with the same current excitation magnitude and direction. As shown in Figure 5.2 (a), the electric fields start from the left part of the patch and end to the right part of the patch. Symmetrical electric field distributions are observed with regard to the x-axis and y-axis in the xy plane. In Figure 5.2 (b), loop-shaped magnetic field distributions are observed around the radiating patch in the xz plane. Also, symmetric magnetic field distributions are observed with regard to the x-axis and z-axis in the xz plane. Therefore, the excited slot-pair of slot 1 and slot 3 can be equivalent as a dipole placed along the y-axis, and the equivalent Dipole-y is shown in Figure 5.2 (c).

Similarly, owing to the symmetry of the four open slots, same near-field distributions can be observed when the slot-pair of slot 2 and slot 4 is excited with the same excitation current magnitude and direction. The radiated electric field and magnetic field can be equivalent as the Dipole-x placed along the x-axis, which is also shown in Figure 5.2 (c). When the

equivalent Dipole-x and Dipole-y are excited with equal magnitude and quadrature phase signals, CP radiation will be achieved. Therefore, by exciting the crossed open slot-pairs with equal magnitude and sequential quadrature phase difference signals, ideal dipole like CP radiation patterns can be achieved.

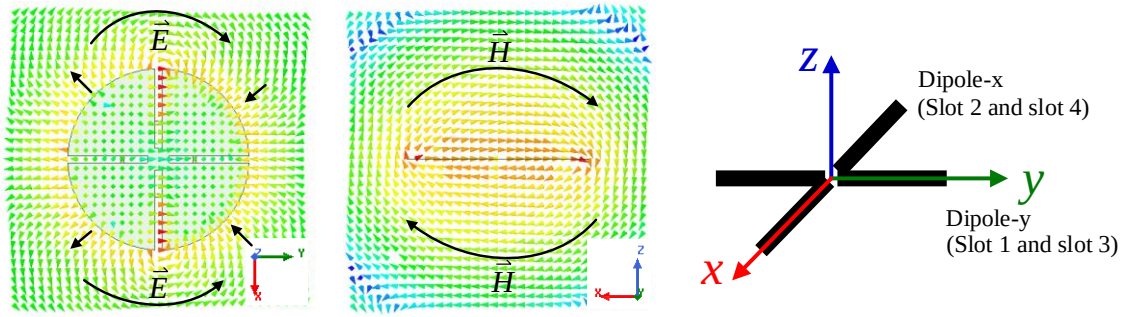

(a) (b) (c)

Figure 5.2 Simulated near-field distribution of the antenna when the slot-pair of slot 1 and slot 3 is excited. (a) Electric field distribution. (b) Magnetic field distribution. (c) Equivalent crossed dipoles for the excited crossed slot-pairs.

The crossed open slot-pairs also show the stable radiating resistance and compact size when the slot width becomes wider. To facilitate the analysis of the input impedance of crossed slot-pairs for circular polarization, active S-parameters are used to evaluate the impedance characteristic of the slot-pairs, which take the consideration of the contributions of all the closely spaced open slot-pairs excited with equal magnitude and sequential quadrature phase signals. According to the definition in [153], the active reflection coefficient of the N-port antenna or array can be expressed as

$$Active\ \mathrm{S}_{11} = \sum_{i=1}^{N} \frac{a_i}{a_1} S_{1i} \tag{5.1}$$

where a_i is the excitation voltage of the ith driven source. Therefore, the active reflection coefficient for the sequentially excited crossed open slot-pairs in Figure 5.2 can be expressed as

$$Active\ S_{11}^{sq} = S_{11} - S_{13} \tag{5.2}$$

and the active input impedance is

$$Active\ Z_{11}^{sq} = Z_0 \frac{1 + Active\ S_{11}^{sq}}{1 - Active\ S_{11}^{sq}} \tag{5.3}$$

where Z_0 is the impedance of the driven source.

Figure 5.3 (a) shows the active input impedance of the slot-pairs varies with different widths of the slot. As shown in the figure, when the width of the slot Ws0 increases to 3 mm, the slop of the input resistance becomes moderate and stable to 50 ohm from 2 GHz to 3

GHz. This means that a stable radiating resistance and an effective radiation can be achieved when the width of the slot becomes wider. However, as the increase of Ws0, higher input inductance is observed. This will affect the impedance matching for the practical antenna design. Another important fact is that both the input resistance and reactance curves of the slot-pairs will shift to the lower frequency as the increase of Ws0. These two facts denote that, by increasing the width of the slots, a stable radiating resistance and a compact radiator size can be realized.

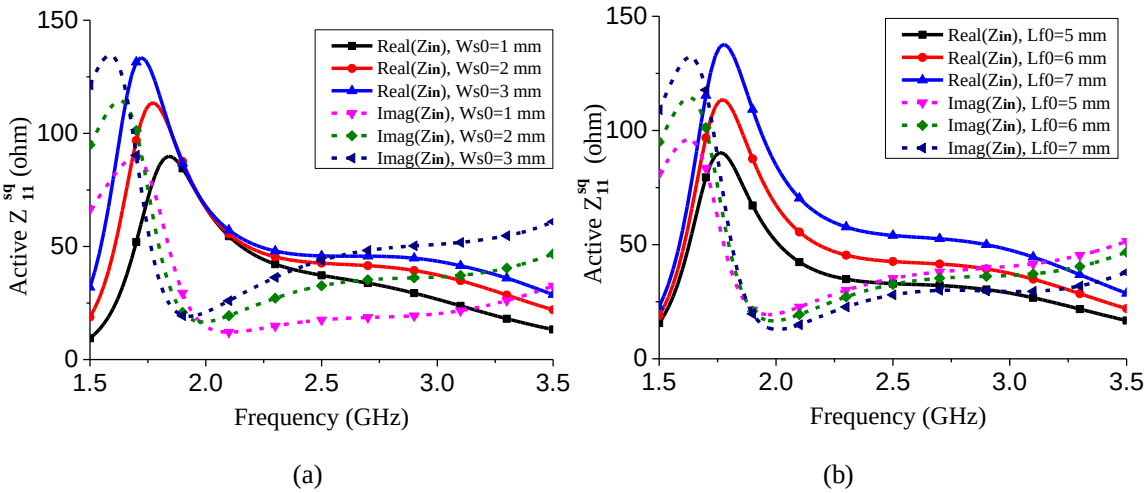

(a) (b)

Figure 5.3 Active input impedance of the crossed slot-pairs excited with equal magnitude and quadrature phase signals varies with different (a) Ws0 and (b) Lf0.

Figure 5.3 (b) shows the input impedance of the antenna varies with different feed position Lf0. It can be seen that, as the feed position away from the centre of the circular patch, the value of the input resistance increases dramatically compared to the input reactance. Therefore, by changing this parameter, the input resistance can be easily adjusted to a desired value, which can be the characteristic impedance of a coaxial cable or the other input port. In addition, both two figures in Figure 5.3 (a) and Figure 5.3 (b) show that the input impedance of the open slot-pairs is inductive, and the inductance increases as the frequency increases. Therefore, capacitive open-circuited stubs will be needed to compensate the inductive component of the input impedance for the practical antenna design.

The open slot can be utilized to design a wideband half-power phase shifter, which is especially designed to achieve wideband half-power output and quadrature phase shift for the serially fed load. Figure 5.4 (a) shows the configuration of the proposed half-power phase shifter. The commercially available Rogers 4003C substrate with the relative dielectric permittivity of 3.55 and thickness of 0.813 mm is used for the half-power phase shifter design. In the figure, a short microstrip line depicted in red colour is printed on the top layer

of the substrate, and a square patch with the length of 40 mm is used as the reference ground and depicted in the green colour. A narrow slot with the width Ws1 and length Ls1 is etched on the bottom layer of the substrate. Details of other parameters are shown in the caption of Figure 5.4. As a good performance comparison, a traditionally designed microstrip phase delay line without the slot loading is shown in Figure 5.4 (b).

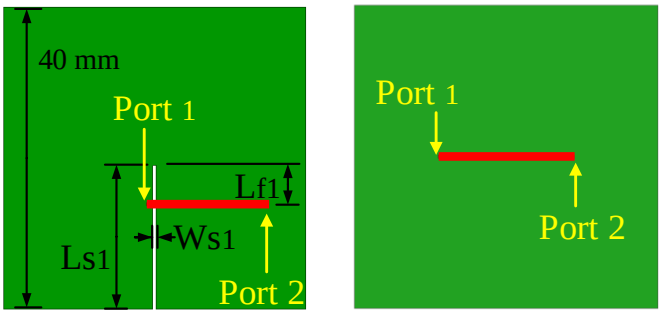

(a) (b)

Figure 5.4 Configuration of the proposed half-power phase shifter.
Detailed parameters: Ls1=19 mm, Ws1= 0.5 mm, Lf1= 5.9 mm. (b) The traditional microstrip phase delay line.

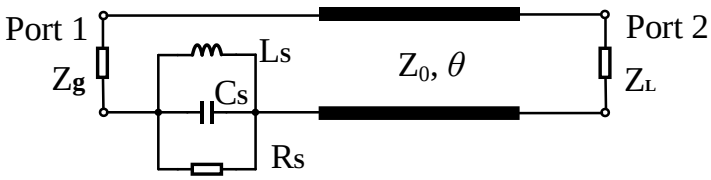

Figure 5.5 Equivalent circuit of the proposed half-power phase shifter.

The equivalent circuit of the proposed half-power phase shifter is shown in Figure 5.5. The loaded open slot can be equivalent as a parallel RLC resonator with the shunt inductor L_S, capacitor C_S, and radiating resistor R_S. The resonator is serially connected to a transmission line with the characteristic impedance Z_0 and the phase θ. The impedance of generator at port 1 is Z_g, and the impedance of load at port 2 is Z_L. Based on the equivalent circuit, the ABCD matrix of this two-port network can be calculated as

$$\begin{bmatrix} A & B \\ C & D \end{bmatrix} = \begin{bmatrix} 1 & Z_S \\ 0 & 1 \end{bmatrix} \begin{bmatrix} cos\theta & jZ_0 sin\theta \\ jsin\theta/Z_0 & cos\theta \end{bmatrix} \tag{5.4}$$

where $Z_s = \frac{1}{\frac{1}{j\omega L_S} + j\omega C_S + \frac{1}{R_S}}$.

By converting the ABCD matrix (5.4) into S matrix, the reflection coefficient (S_{11}) and transmission coefficient (S_{21}) of the two-port network for the proposed half-power phase shifter with the generator impedance Z_g and load impedance Z_L can be calculated as

$$S_{11} = \frac{AZ_L + B - CZ_g^* Z_L - DZ_g^*}{AZ_L + B + CZ_g Z_L + DZ_g} \tag{5.5}$$

$$S_{21} = \frac{2\sqrt{R_g R_L}}{AZ_L + B + CZ_g Z_L + DZ_g} \tag{5.6}$$

As a special case in this design, suppose that Z_L=Z_0=R_s=50 ohm, Z_L=100 ohm, the parallel RLC is resonated at 2.5 GHz, and θ equals 90º at 2.5 GHz, the frequency responses of the equivalent circuit can be then calculated by using (5)-(6). The calculated S-parameters are shown in Figure 5.6. The delayed phase of the traditional microstrip line without the loading of parallel RLC is also shown in the figure for comparison.

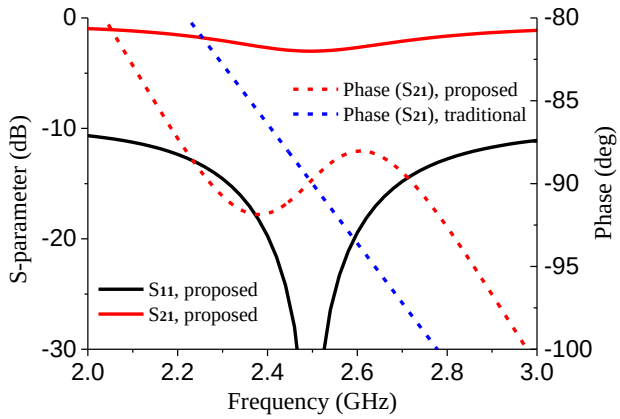

Figure 5.6 Calculated frequency response of the equivalent circuit for the proposed phase shifter compared to the traditional microstrip phase delay line.

As shown Figure 5.6, a wide bandwidth of half-power output and quadrature phase is observed for the proposed phase shifter with one phase peak and one phase valley, and the bandwidth for 90±5º variance is greatly improved, which covers from 2.15 GHz to 2.86 GHz (28%). Whereas the delayed phase of the traditional microstrip line varies linearly as the frequency, and the bandwidth for 90±5º variance is very narrow, which covers only 2.36-2.64 GHz (11%). The phase bandwidth of the proposed phase shifter is 2.5 times wider than the traditional phase shifter. One should be noted is the output magnitude of this phase shifter. Half power is dissipated by the open slot, and half power is transmitted to the output port. Therefore, if another radiator is serially connected to the output port and orthogonally placed to the loaded open slot, CP radiation can be expected owing to phase and magnitude characteristics of this phase shifter.

Normally, to ensure good CP radiation, the magnitude excitations are required to be within ±0.5 dB variance, and the quadrature phase differences are required to be within ±5° variance [152]. Therefore, to achieve wider bandwidth for CP radiation, the highest insertion loss in this design can be increased to 3.5 dB, and the overlapped bandwidth for magnitude

and phase will be further increased. Figure 5.7 (a) shows the EM simulated transmission magnitude and phase of the proposed half-power phase shifter. By adjusting the maximum insertion loss to 3.5 dB, the magnitude bandwidth for -3±0.5 dB is increased, as compared to the calculated result in Figure 5.6. Additionally, the phase bandwidth for 90±5° is slightly increased. The overlapped simulated bandwidth for required magnitude and phase variance is 2.29-2.95 GHz (25%), which is 2.3 times wider than the traditional microstrip phase delay line.

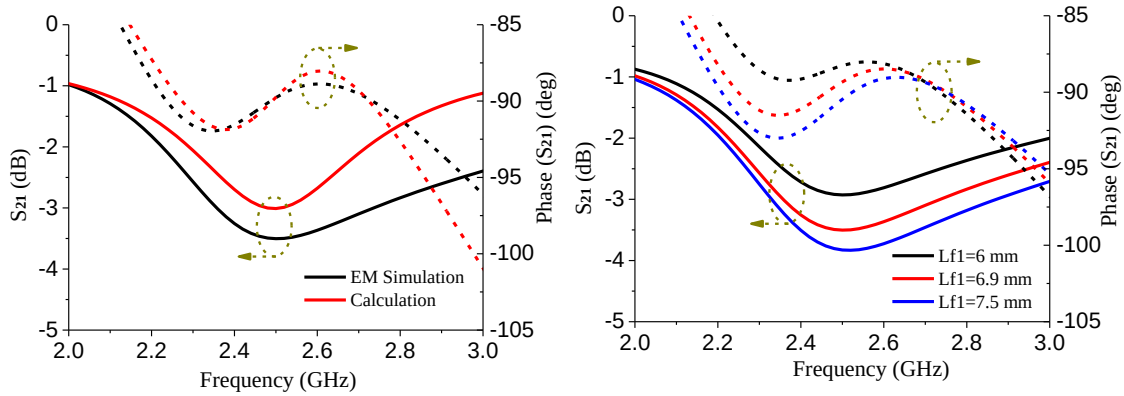

Figure 5.7 (a) EM simulated transmission magnitude and phase of the proposed half-power phase shifter compared to the calculated results. (b) Simulated transmission magnitude and phase of the proposed half-power phase shifter vary with different feed positions Lf1.

In this design, the loaded open slot will be not only used to broaden the phase shift bandwidth, but also elaborately utilized for CP radiation. Therefore, it is important to control both the transmission coefficient and phase of the proposed half-power phase shifter. As shown in Figure 5.7 (b), the transmission magnitude (S_{21}) is mainly determined by the feed position Lf1. As the increase of Lf1, the transmission magnitude will be decreased. This means that more energy will be radiated by the open slot, and less energy is transmitted to output port. By changing the value of this parameter, the delayed phase is nearly unaffected. The phase bandwidth varying from -85° to -95° becomes slightly wider as Lf1 increases to 7.5 mm, but the output magnitude is decreased to -3.8 dB, which can affect the excitation magnitude of the serially fed load.

5.2.2 Antenna Design

Based on the radiation and impedance characteristics of crossed slot-pairs and the proposed wideband half-power phase shifter, a wideband series-fed CP differential antenna is developed. Figure 5.8 shows the detailed configuration of this antenna. In Figure 5.8 (a), the antenna is composed of an antenna radiator printed on the two sides of the substrate and

a planar square copper sheet as the reflector for the unidirectional radiation. Two equal length coaxial cables are used to feed the radiator and works as the differentially fed port-pair. Port+ and Port- are located at the end of the two coaxial cables to excite the antenna for CP radiation. Because of the differentially fed method, the reflection coefficient for the proposed antenna can be calculated by using the active reflection coefficient defined in (5.1), that is

$$S_{11}^{df} = S_{11} - S_{12} \tag{5.7}$$

where S_{11} and S_{12} are the single-ended S-parameters, which can be obtained from the simulated or the measured results. Then the input impedance of the differentially fed antenna is

$$Z_{11}^{df} = Z_0 \frac{1 + S_{11}^{df}}{1 - S_{11}^{df}} \tag{5.8}$$

where Z_0 is the impedance of the driven source.

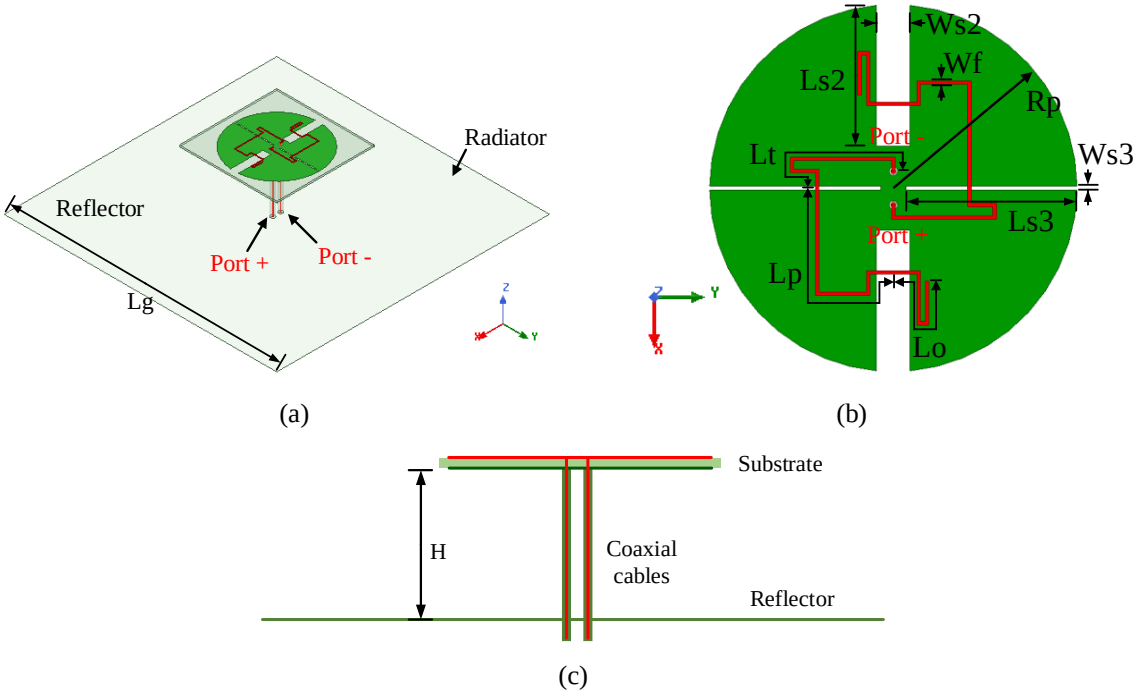

Figure 5.8 Configuration of the proposed differentially fed CP antenna.
(a) 3D view. (b) Detailed view of the antenna radiator. (c) Side view. (Detailed parameters of the antenna. Lg=140 mm, Ws2=4 mm, Ls2=17 mm, Ws3=0.5 mm, Ls3=20.3 mm, Rp=21.75 mm, Wf=0.4 mm, Lo=15 mm, Lp=24 mm, Lt=20 mm, H=30 mm.)

As shown in Figure 5.8 (b), two closely spaced open slot-pairs are etched on the bottom layer of the substrate and depicted in green colour. Two bent microstrip lines are rotationally printed on the top layer of the substrate and depicted in red colour. Note that the widths of crossed open slot-pairs are different, and have different functions in the antenna design. The

wide slot-pair on the bottom layer with the width of Ws2 works as the main radiating structure, and is designed for the wide impedance bandwidth and compact radiator size. Whereas the narrow slot-pair with the width of Ws3 not only works as the radiating structure, but also is elaborately designed for providing the required wideband 90º phase shift to the wide slot-pair. Both of the crossed wide and narrow slot-pairs can radiate as an ideal dipole, as discussed in Section II. A. Whereas the feed lines on the top layer of the substrate, although they have the same width, they perform three totally different functions. The open-circuited stub with the length of Lo compensates the inductive component of the input impedance of the open slots for wide impedance bandwidth. The microstrip line with the length of Lp adjusts the required phase delay for circular polarization. The microstrip line with the length of Lt transforms the input impedance of the antenna into the desired characteristic impedance of the coaxial cables. Details of these working principles will be discussed in the following sections.

Figure 5.8 (c) shows the side view of the antenna. A substrate of commercially available Rogers 4003C with the relative dielectric permittivity of 3.55 and the thickness of 0.813 mm is used in the antenna design. Note that the outer conductors of the cables are soldered to the bottom layer of the patch, while the inner conductors of the cables are soldered to the top layer of the bent feed lines. The distance from the substrate to the reflector is designed as 30 mm for the unidirectional CP radiation. All the simulation results in this work are obtained by using the electromagnetic simulation software ANSYS HFSS. The detailed parameters of the presented antenna are shown in the caption of Figure 5.8.

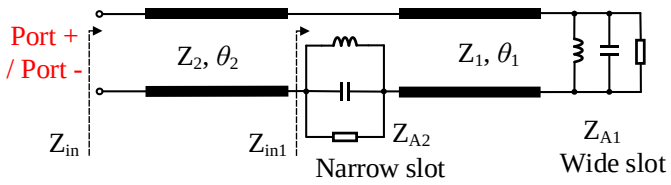

Figure 5.9 Equivalent circuit of the proposed differentially fed CP antenna.

To illustrate the working principle of the proposed antenna, the equivalent circuit of the proposed series-fed CP antenna is shown in Figure 5.9. The wide slot and the narrow slot in the configuration of the antenna can be equivalent as the parallel RLC resonators with the radiating impedance of Z_{A1} and Z_{A2}, respectively. As shown in the figure, the input impedance Z_{in1} at the left of the narrow slot is

$$Z_{in1} = Z_{A2} + Z_1 \frac{Z_{A1} + jZ_1 tan\theta_1}{Z_1 + jZ_{A1} tan\theta_1} \tag{5.9}$$

where Z_1 and θ_1 is the characteristic impedance and electric length of microstrip line Lp. Then, the input impedance Z_{in} at the differential Port+ or Port– can be calculated as

$$Z_{in} = Z_2 \frac{Z_{in1} + jZ_2 tan\theta_2}{Z_2 + jZ_{in1} tan\theta_2} \tag{5.10}$$

where Z_2 and θ_2 is the characteristic impedance and electric length of microstrip line Lt.

In this design, the radiating resistor of the wide slot and narrow slot are design as 100 ohm. Therefore, the characteristic impedance of the microstrip line of Z_1 is designed also as 100 ohm, and θ_1 is required to be 90º for CP radiation. When both the wide slot and narrow slot are resonated at the same frequency, the input impedance of Z_{in1} will be 200 ohm according to (5.9). So an impedance inverter is needed to transform the input impedance Z_{in1} into the characteristic impedance of a coaxial cable. According to (5.10), a transmission line with the impedance of Z_2=100 and electric length of θ_2=90º is needed to transform the input impedance of 200 ohm into the desired 50 ohm. Although Z_1 and Z_2 are of the same values, they perform totally different functions here in the antenna design.

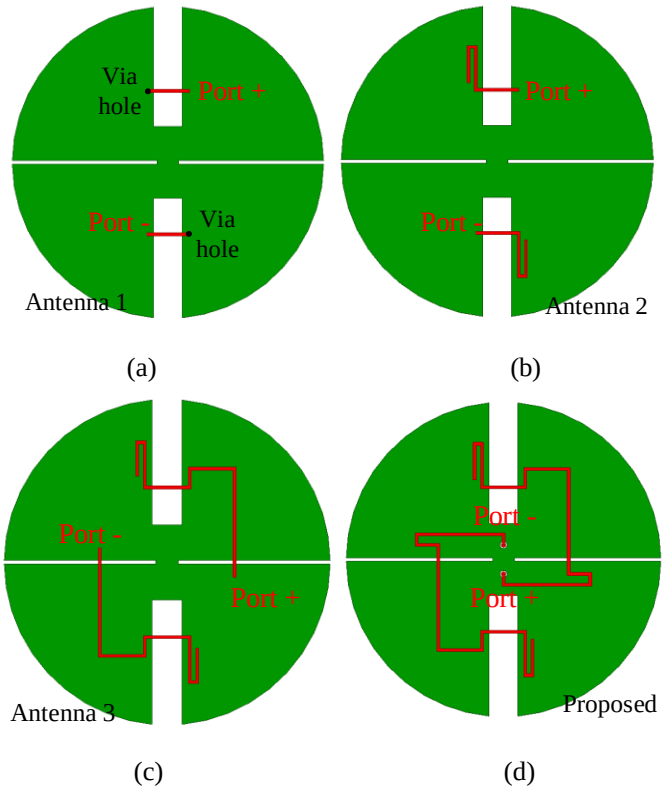

Figure 5.10 Evolution of the proposed CP antenna.
(a) Antenna 1 with the shorting via holes. (b) Antenna 2 with the open-circuited stubs. (c) Antenna 3 loading with the narrow slots, but without the impedance inverter line. (d) The proposed antenna.

To further illustrate the design methods of the antenna, the evolution process of the antenna is shown in Figure 5.10. Four different antennas are included in the figure. Note that all these antennas are differentially fed antennas, and have the same radiating slots at the bottom layer as the proposed antenna. In addition, same substrates and reflectors are included for these antennas in the simulation. The only differences for these antennas are the feed lines on the top layer. As shown in the figure, only wide open slot-pair is excited in Antenna 1, and two via holes are used for the direct excitation. To improve the impedance matching, open-circuited stubs are introduced in Antenna 2. Note that Antenna 1 and Antenna 2 cannot be realized for CP radiation. Therefore, to realize CP radiation, narrow open slot-pair is loaded under the top feed lines in Antenna 3, but without the impedance inverter line. The fourth antenna shown in the bottom right corner of the figure is the proposed antenna with the incorporated impedance inverter line.

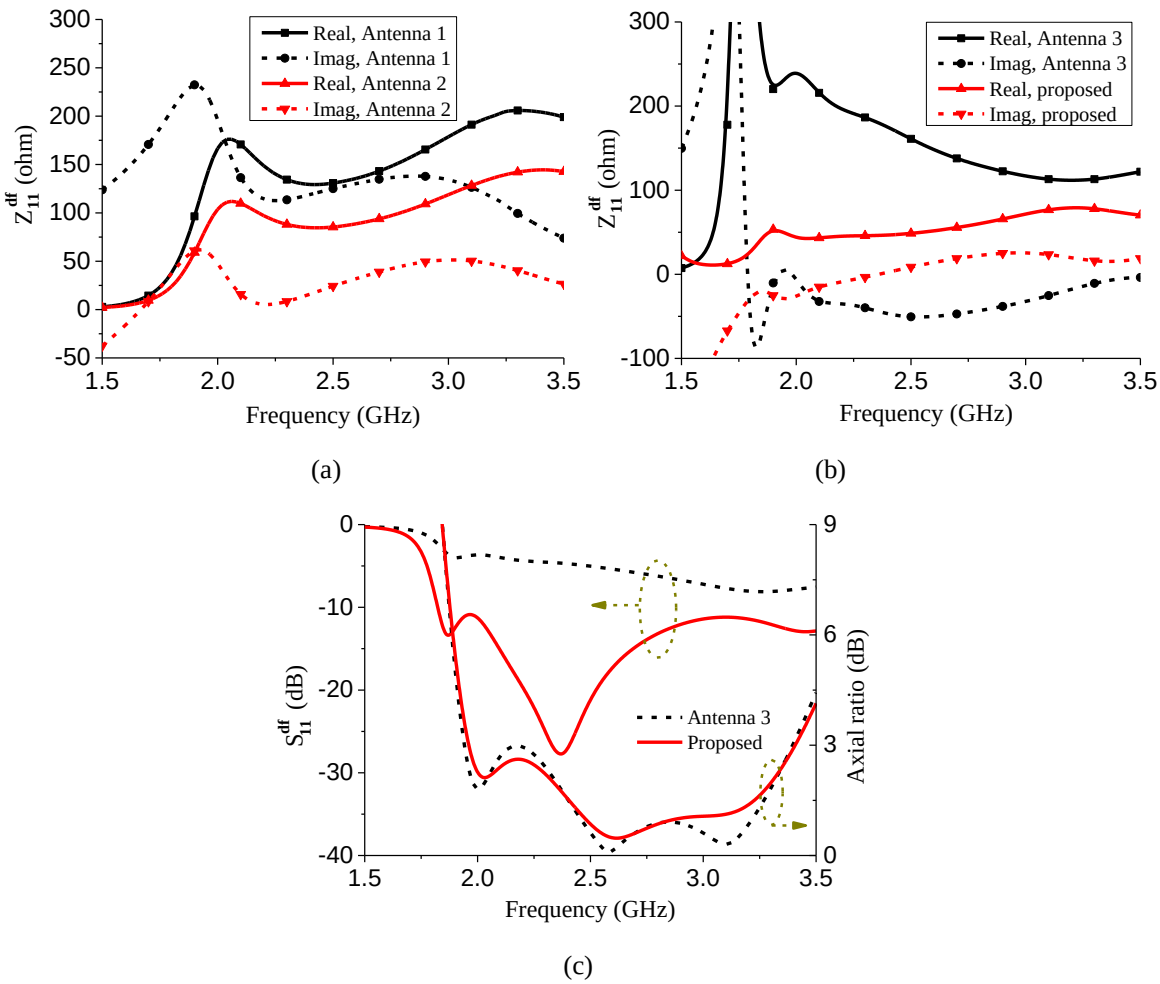

Figure 5.11 (a) Input impedances of Antenna 1 and Antenna 2. (b) Input impedances of Antenna 3 and the proposed antenna. (c) S-parameters and axial ratios of Antenna 3 and the proposed antenna.

Figure 5.11 shows the simulated impedance characteristics of these reference antennas. In Figure 5.11 (a), high inductive component is observed for the direct feed method, and the average inductance is about 100 ohm over the whole band of interest. As discussed in Section II. A, open-circuited stubs should be added to compensate the inductive component. After incorporating the open-circuited stubs into Antenna 2, the reactance of the input impedance is around 0 ohm. In addition, the resistance of the input impedance is also decreased from the average value of 150 ohm to the designed average value of 100 ohm. A wide impedance bandwidth can be ensured by using the open-circuited stubs.

Figure 5.11 compares the simulated input impedances of Antenna 3 and the proposed antenna. As can be seen that the real part of the input impedance of Antenna 3 varies from 250 ohm to 100 ohm from 2 GHz to 3 GHz, while the imaginary part is close to zero. Therefore, an impedance inverter is needed to transform the high input resistance to the desired 50 ohm. After the impedance inverter line with the impedance of 100 ohm is incorporated into the proposed antenna, the real part of the input impedance shifts to the desired value and keeps stable around 50 ohm, while the imaginary part is still close to zero. Figure 5.11 (c) shows the corresponding simulated S-parameters and ARs of the two antennas, both of the two antennas are normalized to 50 ohm. Good impedance matching can be achieved for the proposed antenna with the reflection coefficient lower than -10 dB from 1.82 GHz to 3.5 GHz. Because of the loading of the narrow open slot-pairs, both of the two antennas have almost the same wide axial ratio bandwidth, and the simulated bandwidth of the axial ratio lower than 3 dB for the proposed antenna is from 1.96 GHz to 3.41 GHz (54%).

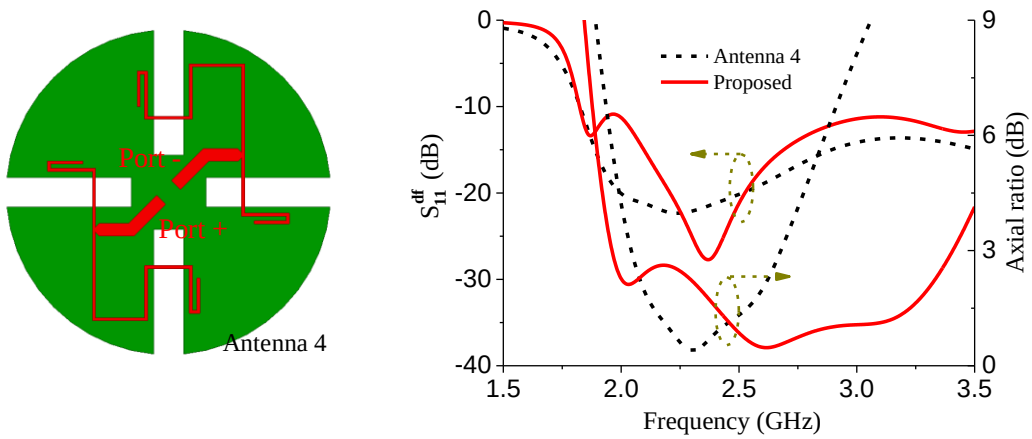

(a) (b)

Figure 5.12 Comparison to the traditionally designed CP counterpart (Antenna 4).
(a) Simulation model of Antenna 4. (b) Simulated results of the two antennas.

The proposed antenna has a wider axial ratio bandwidth than the traditionally designed counterpart. Figure 5.12 (a) shows the configuration of traditional designed Antenna 4, which is also designed as a differentially fed antenna. Different from the proposed antenna, only wide slots are used in Antenna 4. A traditional T-shaped power divider and two bent microstrip lines are used for the required magnitude and phase excitations for CP radiation.

Figure 5.12 (b) shows the simulated S-parameters and axial ratios of these two antennas. As compared to Antenna 4, the reflection coefficient of the proposed CP antenna is slightly higher. However, it is still very good and lower than -10 dB from 1.82 GHz to 3.5 GHz. Most importantly, much wider axial ratio bandwidth is observed for the proposed antenna, which is from 1.96 GHz to 3.41 GHz (54%) for AR<3 dB. Whereas the AR bandwidth for Antenna 4 is quite narrow, which is only from 2.05 GHz to 2.67 GHz (26%). The overlapped bandwidth of impedance and AR limits the application of Antenna 4 for CP radiation. Compared to Antenna 4, 2.1 times wider relative AR bandwidth is achieved for the proposed antenna by using the proposed design method. The simulated AR bandwidth enhancement also agrees well with the simulated magnitude and phase bandwidth enhancement of the proposed half-power phased shifter, as compared to the traditional microstrip phase shift line shown in Figure 5.12.

5.2.3 Results and Discussion

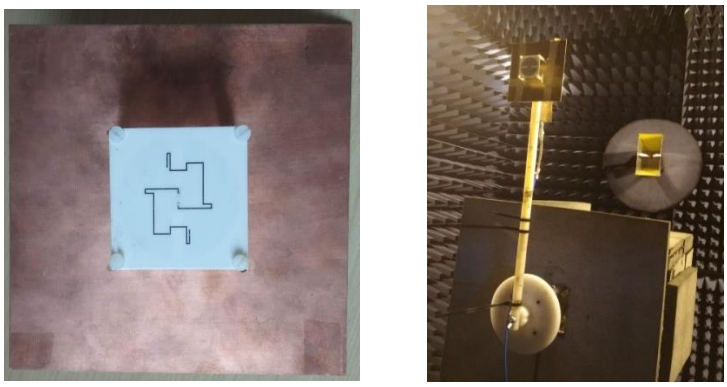

(a) (b)

Figure 5.13 Photographs of (a) the fabricated prototype of the proposed differentially fed CP antenna and (b) the prototype under radiation pattern test.

To validate the antenna design concept, the proposed differentially fed CP antenna was designed, fabricated, and measured. Figure 5.13 shows the photographs of the fabricated prototype and the prototype under test. The antenna was measured by the Anritsu 37397C vector network analyzer and ASYSOL far field antenna measurement system at University of Kent. Figure 5.14 shows the simulated and measured S-parameters and axial ratios of the

proposed differentially fed CP antenna. The measured reflection coefficient from 1.84 GHz to 3.5 GHz is below -10 dB, and the measured AR below 3 dB is from 1.95 GHz to 3.45 GHz. The overlapped relative bandwidth for the reflection coefficient and AR is 55.6%. Both the measured S-parameters and AR agree well with the simulated results. The slight discrepancies between the simulated and measured results are possibly due to the fabrication and solder errors between the radiator and the coaxial cables.

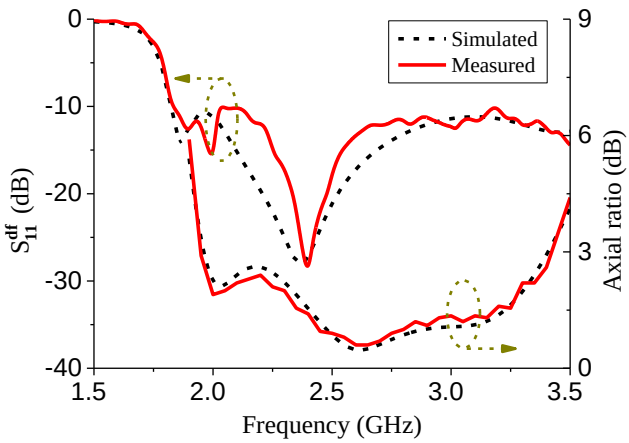

Figure 5.14 Measured and simulated S-parameters and axial ratios of the proposed differentially fed CP antenna.

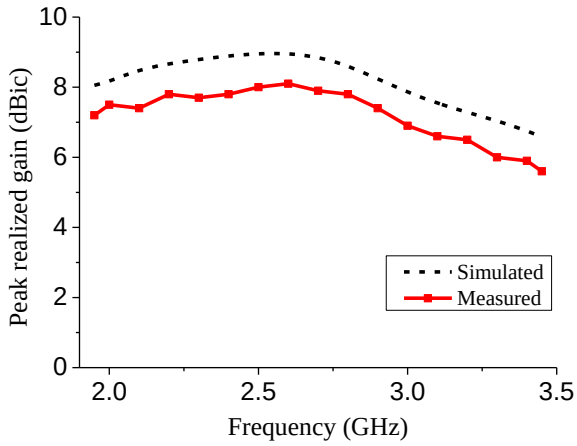

Figure 5.15 Measured and simulated peak realized gain of the proposed differentially fed CP antenna.

The measured peak realized CP radiation gain of the antenna from 1.95 GHz to 3.45 GHz is shown in Figure 5.15, which is compared with the simulated result. Owing to the reflection of the reflector, high antenna gain is achieved. The measured antenna gain is about 0.9 dB lower than the simulated gain, which is probably caused by the simulation and measurement errors. The measured peak realized gain varies from 5.6 dBic to 8.1 dBic within the bandwidth.

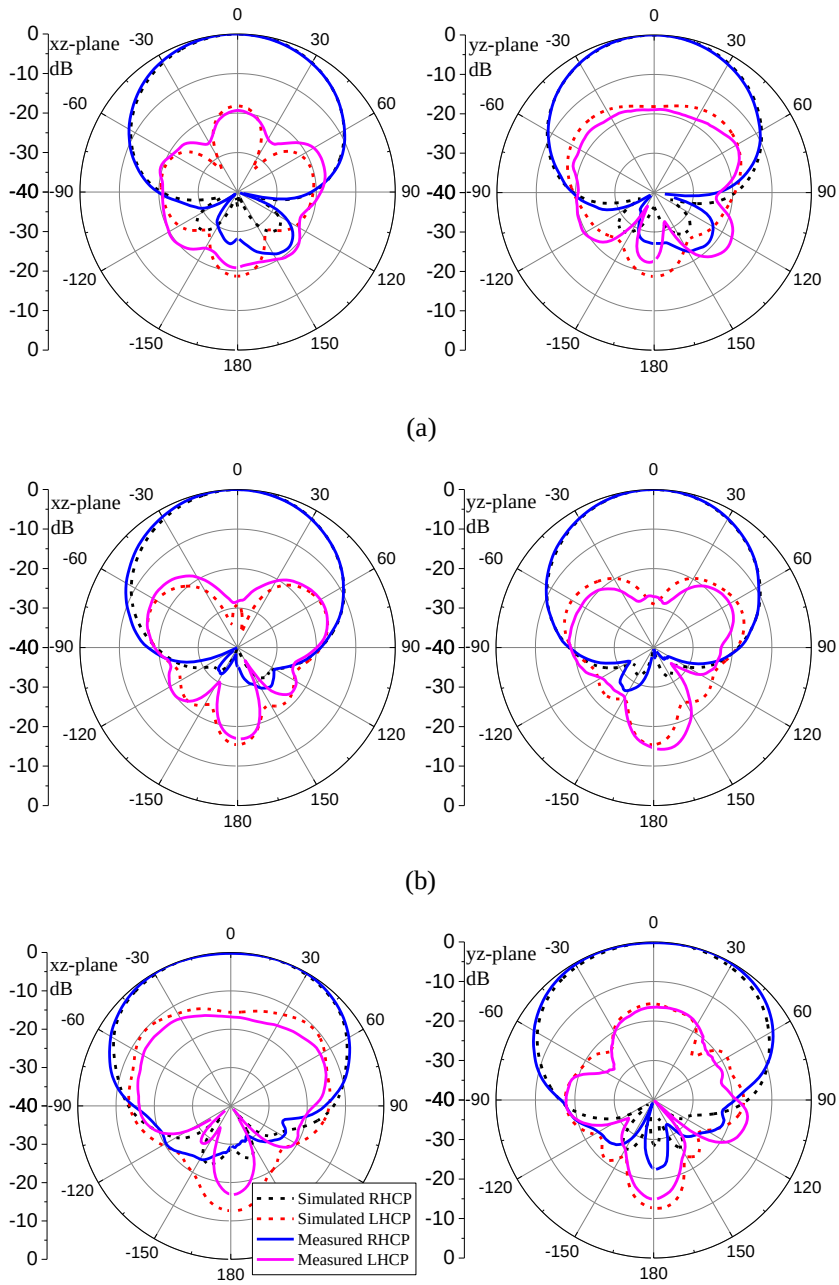

(a)

(b)

(c)

Figure 5.16 Measured and simulated normalized radiation patterns of the proposed CP antenna in xz-plane and yz-plane at (a) 2 GHz, (b) 2.7 GHz, and (c) 3.4 GHz.

Figure 5.16 shows the measured and simulated normalized radiation patterns of the proposed CP antenna in xz-plane and yz-plane at 2 GHz, 2.7 GHz, and 3.4 GHz. As shown in the figure, RHCP radiation is achieved in the broadside direction of the antenna, and the LHCP radiation is the cross-polarization for the antenna. Good accordance is observed between the measured and simulated radiation patterns. The measured half-power beamwidth increases from 70° to 110° in xz-plane, and increases from 68° to 112° in yz-plane. Because of the increase of the beamwidth of the radiation patterns, lower antenna gain

is achieved at the upper band, as compared to the antenna gain at the lower band. Because of the reflection of the reflector, low back-lobe level is achieved, and the measured front-to-back ratio is higher than 14.5 dB with unidirectional radiation patterns. The slight discrepancies between the measured and simulated radiation patterns may be caused by the position errors of the antenna and the blockage of the feeding cables.

Table 5.1 Comparison of the recently published CP antennas

Reference	Overlapped BW (GHz)	f_0 (GHz)	RBW	Radiator Size	Height	Reflector Size	Gain (dBic)
[95]	1.69-3.0	2.35	55%	$0.67\times0.67\lambda_0^2$	$0.32\lambda_0$	$1.59\times1.59\lambda_0^2$	6-9
[130]	1.7-2.38	2.06	31.1%	$0.38\times0.38\lambda_0^2$	$0.25\lambda_0$	$0.95\times0.95\lambda_0^2$	~6.5
[138]	2.0-4.0	3.0	66.7%	$0.86\times0.86\lambda_0^2$	$0.36\lambda_0$	$0.86\times0.86\lambda_0^2$	7.1-9.7
[139]	1-2.87	1.93	96.6%	$0.7\times0.7\lambda_0^2$	$0.35\lambda_0$	$1.5\times1.5\lambda_0^2$	~6
This work	1.95-3.45	2.69	55.6%	$0.38\times0.38\lambda_0^2$	$0.27\lambda_0$	$1.26\times1.26\lambda_0^2$	5.6-8.1

Table 5.1 compares the presented CP antenna with the recently published CP antennas. In the table, λ_0 is the free space wavelength at the centre operation frequency. As can be seen, the height of the proposed antenna is $0.27\lambda_0$, which is a medium height as compared to other reference antennas. A planar square ground plane with a moderate size of $1.26\times 1.26\lambda_0^2$ is designed for unidirectional CP radiation. The antenna reported in [95] have the similar relative bandwidth compared to the presented antenna, but the electric size of the radiator is much larger. The antenna designed in [130] has the same electric size of the radiator as compared to the presented antenna, but its relative bandwidth is much narrower. Antennas in [138]-[139] have much wider overlapped AR and impedance bandwidth than the other antennas. However, all of these antennas have modified ground structures, such as the stair-shaped cavity [138] and the crossed fin-shaped cavity [139], which are bulky and difficult to be extended into the antenna array designs. By using crossed open slot-pairs for CP radiation, a compact radiator size of $0.38\lambda_0\times0.38\lambda_0$ is realized. Owing to the simple and planar reflector, the antenna can be easily extended to large array design. Furthermore, the elaborately introduced narrow slot-pair is not only excited as a radiator, but also elaborately loaded as a wideband half-power phase shifter to provide wideband magnitude and phase excitation to the wide slot-pair. Therefore, wide overlapped bandwidth (55.6%) and compact radiator size is achieved for the presented antenna.

5.3 Wideband Dual Circularly Polarized Antenna

In this section, a wideband DCP antenna is presented with unidirectional and symmetrical radiation patterns for ITS applications, which can be used at the front-end of the receiver in the vehicle or the front-end of the RSU to improve the system sensitivity and communication capacity. In the antenna design, an integrated feed network is elaborately designed to provide two sets of equal magnitude and quadrature phase to the crossed dipoles for DCP radiation. The integrated feed network is composed of an orthogonal power divider (OPD), two +45° phase shifters, and two -45° phase shifters. To realize two sets of wideband quadrature phase excitations for DCP radiation, lumped element based differential left-hand transmission line (LH-TL) unit cell and right-hand transmission line (RH-TL) unit cell are elaborately incorporated into the OPD with ±45° phase shift. Benefiting from the LH-TL and RH-TL unit cells, wide quadrature bandwidth and small phase variance within 6° are obtained from 1 GHz to 2 GHz. Detailed work principle of the integrated feed network for DCP radiation is illustrated by its equivalent circuit analysis. To validate the design method, the presented DCP antenna is designed, fabricated, and measured. Both the measured and simulated results show that the presented antenna has a wide impedance and AR bandwidth of 53.4% (1.07-1.85 GHz) and high port isolation (>15.2 dB). Moreover, low AR (<1.7 dB) and unidirectional symmetrical radiation patterns are achieved for DCP radiation.

5.3.1 Antenna Configuration

The detailed configuration of the proposed DCP antenna is shown in Figure 5.17, which is composed of the antenna radiator printed on the top and bottom layers of the substrate, two coaxial cables used to feed the antenna, and a square copper sheet as the antenna reflector. In Figure 5.17 (a), port 1 is excited for RHCP radiation, while port 2 is excited for LHCP radiation. A commercially available substrate of Rogers 4003C with the relative dielectric permittivity of 3.55 and the thickness of 0.813mm is used for the antenna design.

Figure 5.17 (b) shows the detailed configuration of the antenna radiator. Four crossed dipoles with the same arm length L1 and width W1 are printed at the peripheral of the bottom layer, and are shown in green color. By adjusting L1 and W1, the resonances of the crossed dipoles are changed accordingly. L3 is the feed distance between the two dipole arms, which provides enough space for the centre integrated feed network. L4 is the feed position on the dipole arm, which is normally set as half of the dipole width. The integrated feed network is printed at the centre of the bottom layer, which is composed of an OPD and four lumped

element based phase shifters. The OPD is one of the key components of the integrated feed network for DCP radiation, which is composed of four pairs of coupled coplanar striplines on the bottom layer, and two crossed Y-shaped strips on the top layer for excitation. The coupled coplanar striplines have the width W4, edge distance W5, and length L5. Parameters W4 and W5 determine the characteristic impedance of the coplanar stripline. The crossed Y-shaped strips with the width W2 and length L2 work as the open-circuited stubs, which can provide enough capacitance to couple the balanced energy for four coplanar striplines. The phase shifters are the another key component of the integrated feed network, and realized by the T-type differential RH-TL unit cell and T-type differential LH-TL unit cell for -45° phase shift and +45° phase shift, respectively. The differential RH-TL unit cell consists of four inductors L_R^d and a capacitor C_R^d, and the differential LH-TL unit cell consists of four capacitors C_L^d and an inductor L_L^d. Two different types of RH-TL unit cells and LH-TL unit cells are used in this design to keep the radiator symmetrical and compact. The radiator structure on the bottom layer of the substrate is symmetrical with regard to both the x-axis and y-axis. By exciting different coaxial cables, DCP radiation is realized with the incorporation of the elaborately designed OPD and ±45° phase shifters.

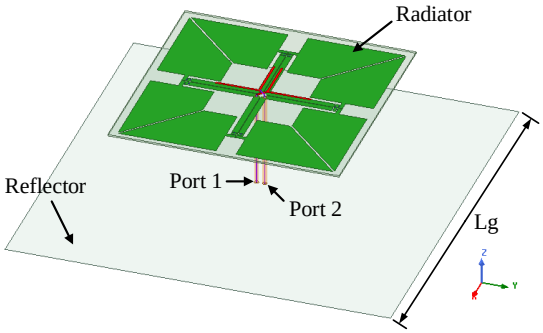

(a)

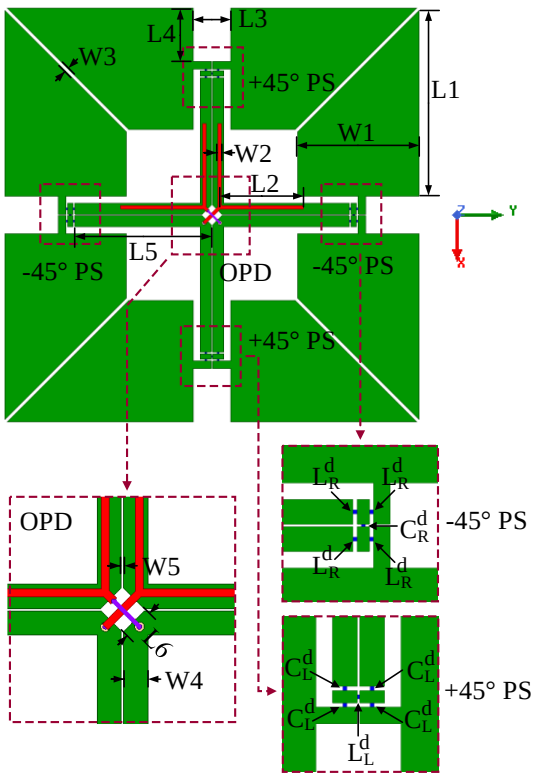

(b)

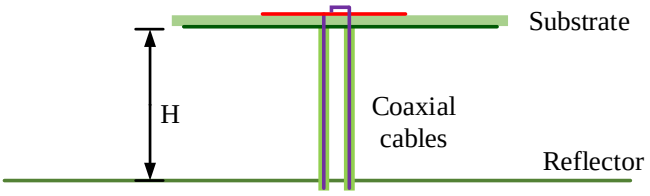

(c)

Figure 5.17 Detailed configuration of the proposed DCP antenna.
(a) 3D view. (b) Detailed view of the antenna radiator. (c) Side view of the antenna. (Detailed parameters of the antenna, Lg=200 mm, L1=50.3 mm, L2=22.6 mm, L3=10.3 mm, L4=14.5 mm, L5=37.2 mm, L6=4 mm, W1=33 mm, W2=1 mm, W3=1 mm, W4=3 mm, W5=0.3 mm, H=50 mm, $\boldsymbol{L_R^d}$=2.5 nH, $\boldsymbol{C_R^d}$=0.2 pF, $\boldsymbol{C_L^d}$=2.5 pF, $\boldsymbol{L_L^d}$=15 nH. PS: Phase shifter.)

Figure 5.17 (c) shows the side view of the proposed DCP antenna. The height between the radiator and the reflector is chosen to be 50 mm for wideband and unidirectional radiation. Note that the inner conductor of the coaxial cable for RHCP radiation is directly soldered to the top feed line, while the inner conductor of the coaxial cable for LHCP radiation is bent across the RHCP feed line to avoid electrical intersection. Then, it is soldered to the crossed feed line for LHCP radiation. The simulation in this work is obtained from the 3D electromagnetic simulation software ANSYS HFSS. All the detailed parameters of the antenna are listed in the caption of Figure 5.17.

5.3.2 Working Principle

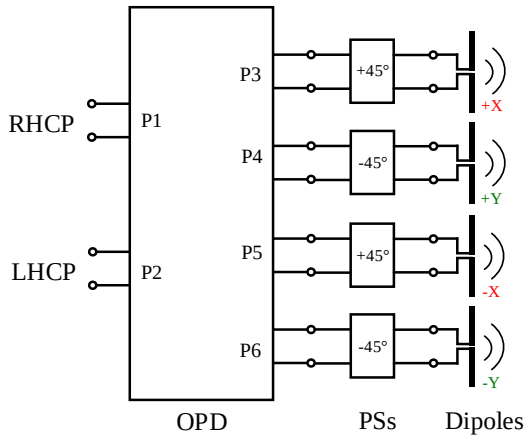

Figure 5.18 Equivalent circuit of the proposed DCP antenna. (PSs: phase shifters)

To illustrate the working principle of the proposed DCP antenna, the equivalent circuit of the antenna is shown in Figure 5.18. The proposed antenna is composed of the integrated feed network (including an OPD and four phase shifters) and four crossed dipoles. The OPD has two orthogonal input ports with high isolation and four output ports with equal magnitude in-phase and out-of-phase output. After cascading two +45° and two -45° phase

shifters, two sets of orthogonal outputs with equal magnitude and quadrature phase are achieved. Therefore, DCP radiation can be achieved by exciting the crossed dipoles located on the ±x and ±y axis, respectively.

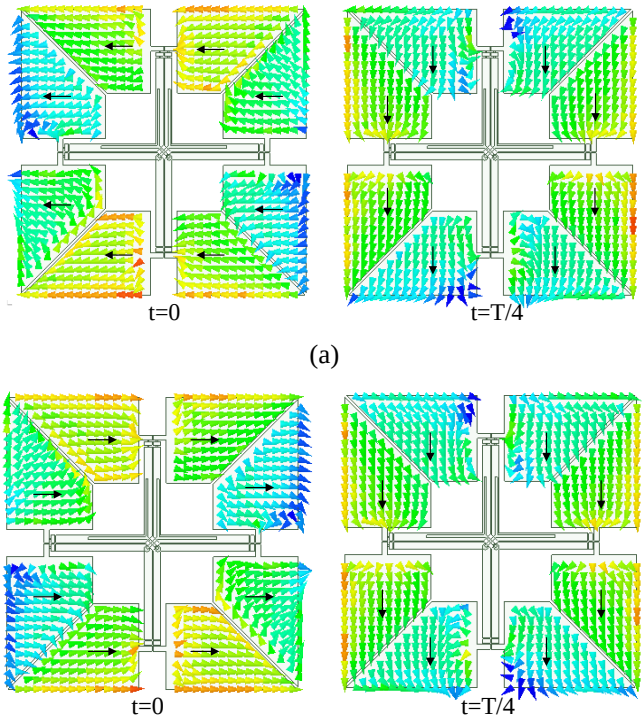

Figure 5.19 Surface current distributions of the proposed antenna at different times of the oscillation period when (a) port 1 is excited and (b) port 2 is excited.

Figure 5.19 shows the surface current distributions on the crossed dipoles at different times of the oscillation period when input port 1 and port 2 are respectively excited. In the figure, T is the oscillation period at the frequency of 1.4 GHz. Auxiliary arrows are added to show the direction of the current. In Figure 5.19 (a), at the time t=0, the top and bottom dipoles are mainly excited with strong current magnitude, whereas the left and right dipoles are shown with relatively weak current magnitude. The collective current direction is to the left. At the time t=T/4, the left and right dipoles are excited with strong current magnitude, and the top and bottom dipoles are shown with relatively weak current magnitude. The collective current direction is from the top to the bottom. Observing from these two figures, the direction of the current rotation is right-handed as the time increases, which stands for the RHCP radiation. Owing to the symmetry of the antenna and the feed ports, almost the same current distributions can also be observed when port 2 is excited, as shown in Figure 5.19 (a) and (b). However, different from Figure 5.19 (a), the direction of the current rotation for the last two figures is left-handed as the time increases, which means LHCP radiation is

realized. From the observation of the current distributions, it can be seen that four crossed dipoles are sequentially excited at different times of the oscillation period, and DCP radiations are realized by exciting different ports.

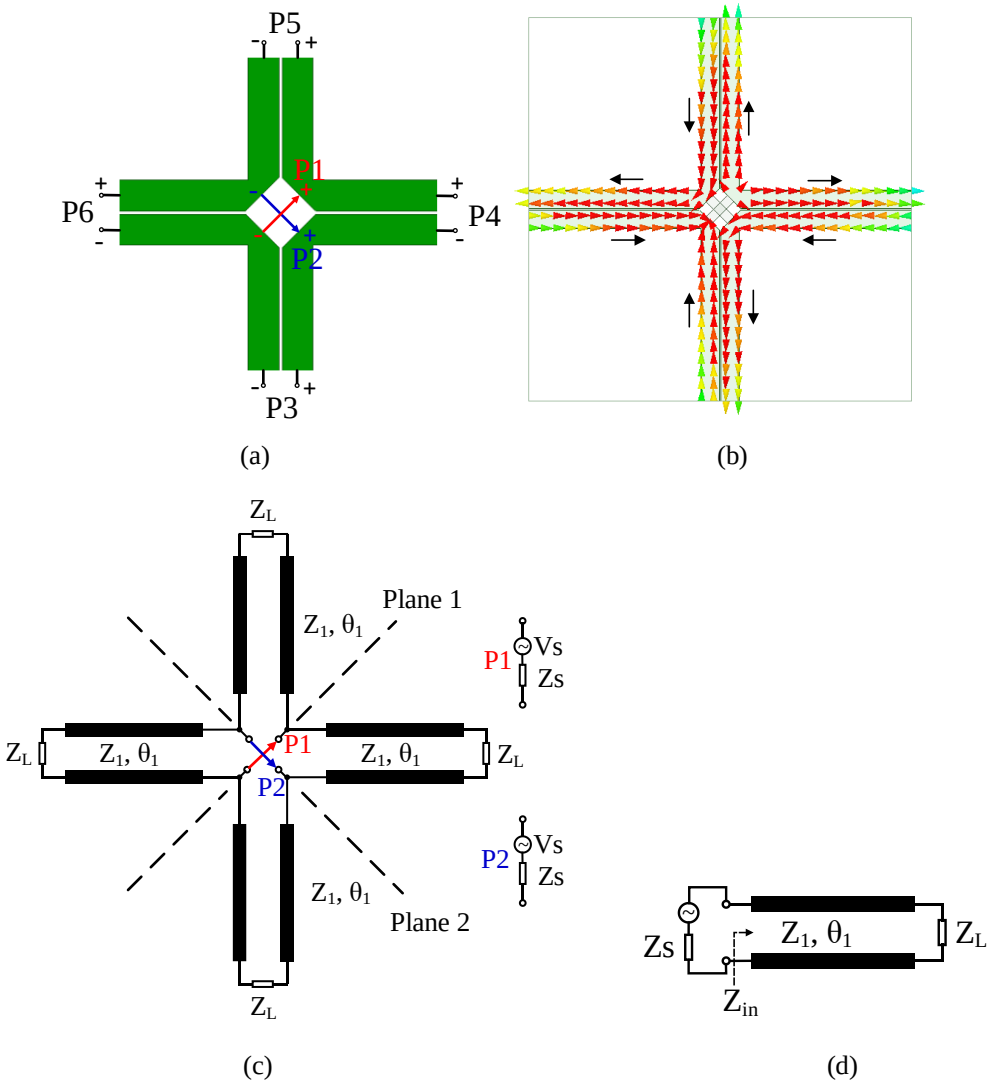

Figure 5.20 (a) Simulation model of the OPD. (b) Current distribution on the surface of the OPD when port 1 is excited. (c) Equivalent circuit of the OPD. (d) Simplified equivalent circuit of the OPD when port 1 is excited.

To illustrate the working principle of the OPD, Figure 5.20 (a) shows the simulation model of OPD extracted from the presented antenna. The OPD is composed of four pairs of coupled coplanar striplines. At the centre of the model, two crossed ideal lumped ports (ports 1 and 2) are inserted to excite the OPD and defined as the input ports. Four wave ports (ports 3, 4, 5, and 6) are located at the peripheral of the model and defined as the output ports. Figure 5.20 (b) shows the current distribution on the surface of the OPD when port 1 is excited. As can be seen that the current directions on the coupled coplanar striplines are opposite. This means that transmission line mode is formed on these coupled coplanar

striplines. Based on this, the equivalent circuit of the OPD is shown in Figure 5.20 (c), which can be equivalent as four cascading transmission lines with the characteristic impedance of Z_1 and electric length of θ_1. The OPD is terminated with the loads of Z_L. Two orthogonal input ports are located at the junction of the cascading points with the source impedance of Z_S. As can be seen that the equivalent circuit has two symmetrical planes (plane 1 and plane 2). Based on the equivalent circuit analysis, when port 1 is excited, the symmetrical plane 1 is equivalent as the open-circuited plane, while the symmetrical plane 2 is equivalent as the short-circuited plane. Therefore, when port 1 is excited, the corresponding simplified equivalent circuit is obtained and shown in Figure 5.20 (d). As can be seen from the simplified equivalent circuit, the input impedance at the input port is

$$Z_{in} = Z_1 \frac{Z_L + jZ_1 tan\theta_1}{Z_1 + jZ_L tan\theta_1} \tag{5.11}$$

and the corresponding reflection coefficient is

$$\Gamma_{in} = \frac{Z_{in} - Z_s}{Z_{in} + Z_s} \tag{5.12}$$

From (5.11)-(5.12), the input impedance and the reflection coefficient at the input port can be adjusted by Z_1 and θ_1. It should be noted that, when $Z_1 = Z_L = Z_S$, the input ports of the OPD will be naturally matched. In addition, if $Z_L \neq Z_S$, the transmission line with the characteristic impedance Z_1 and electric length θ_1 can work as the impedance transformer when θ_1 is designed as 90°. This can provide much flexibility to design the proposed wideband DCP antenna.

Figure 5.21 shows the simulated results of the presented OPD. Owing to the symmetry of the OPD, the simulated magnitudes of S_{11} and S_{22} are almost the same, the simulated magnitudes of S_{31}, S_{41}, S_{51}, S_{61}, S_{32}, S_{42}, S_{52}, and S_{62} are almost same, and the simulated magnitudes of S_{33}, S_{44}, S_{55}, and S_{66} are almost same. Therefore, only S_{11}, S_{31}, and S_{33} are given in Figure 5.21 (a) for brevity. It can be seen that all the input and output ports are well matched, and the two input ports are isolated. Figure 5.21 (b)-(c) show the different transmission phases from different input ports. It can be seen that, when port 1 is excited, all the outputs are in-phase. When port 2 is excited, signals from port 3 and port 5 are in-phase, but out-of-phase as compared to the port 4 and port 6. According to the simulated results in Figure 5.21, the scattering matrix for the OPD can be concluded as

$$[S] = \begin{bmatrix} 0 & 0 & 0.5 & 0.5 & 0.5 & 0.5 \\ 0 & 0 & -0.5 & 0.5 & -0.5 & 0.5 \\ 0.5 & -0.5 & 0 & 0.5 & 0 & -0.5 \\ 0.5 & 0.5 & 0.5 & 0 & -0.5 & 0 \\ 0.5 & -0.5 & 0 & -0.5 & 0 & 0.5 \\ 0.5 & 0.5 & -0.5 & 0 & 0.5 & 0 \end{bmatrix} \tag{5.13}$$

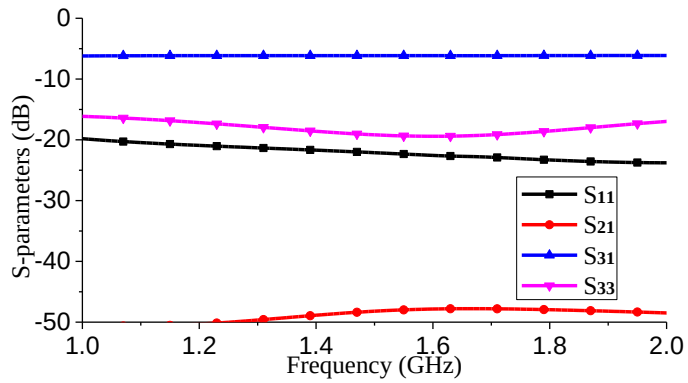

(a)

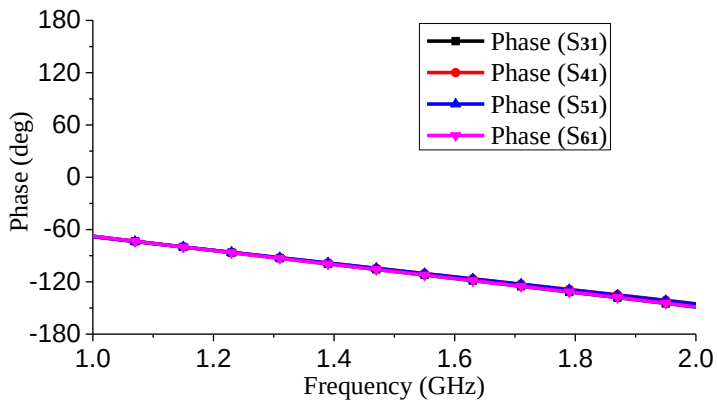

(b)

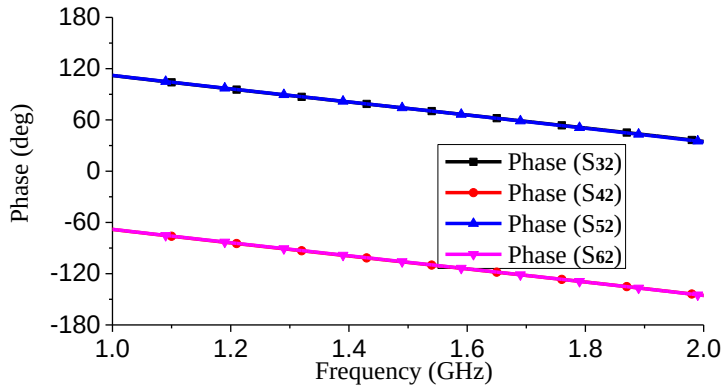

(c)

Figure 5.21 Simulated results of the OPD. (a) Simulated S-parameters. (b) Transmission phase from port 1. (c) Transmission phase from port 2.

Observing from (5.13), because of the transmission phase characteristic at its output ports, it cannot be directly used to design DCP antenna. Therefore, ±45° phase shifters are needed

to elaborately introduced and incorporated at the ends of the OPD to obtain the desired sequential quadrature phase excitations for DCP radiation. Four phase shifters are realized by using the T-type RH-TL unit cells and T-type LH-TL unit cells [154]. Figure 5.22 (a) shows the T-type RH-TL unit cell and LH-TL unit cell. The corresponding phase shifts of these two unit cells are calculated as

$$\phi_R \approx -2\pi f\sqrt{L_{R1}C_{R1}} \tag{5.14}$$

$$\phi_L \approx \sqrt{L_{L1}C_{L1}}\ /(2\pi f) \tag{5.15}$$

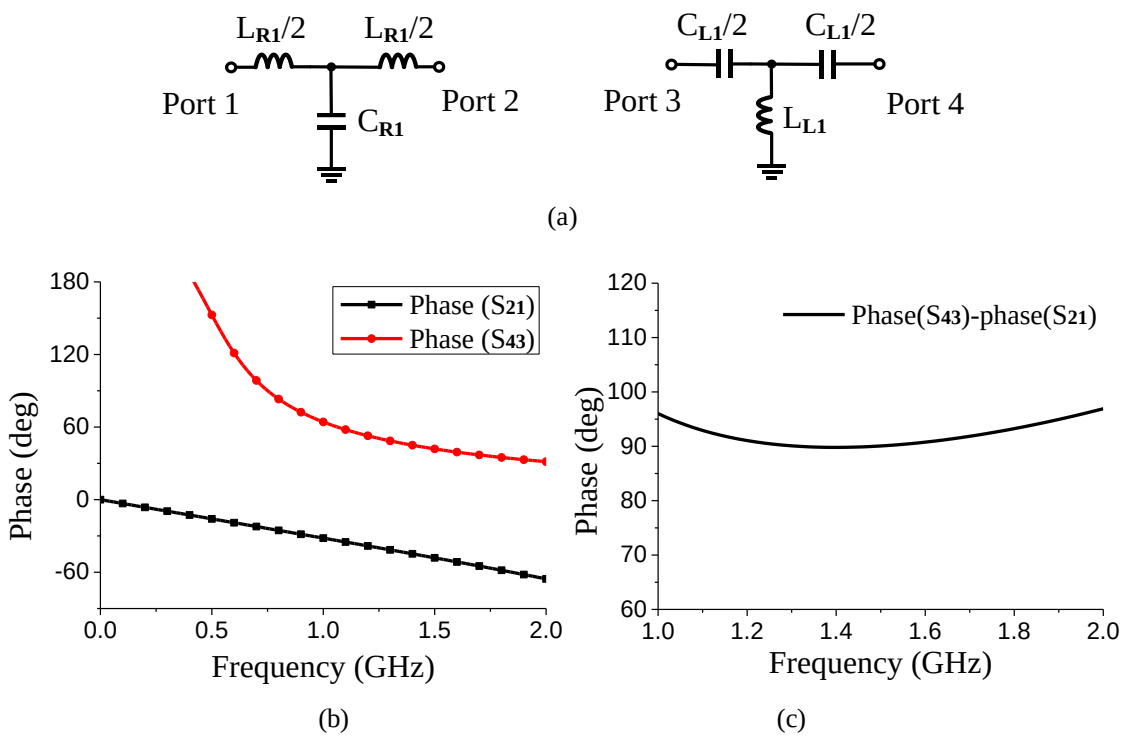

Figure 5.22 (a) T-type RH-TL unit cell and T-type LH-TL unit cell. (b) Phase response of the two unit cells. (c) Phase difference between the two unit cells.

In this design, ϕ_R is designed for -45° phase shift and ϕ_L is designed for +45° phase shift at 1.4 GHz to keep the antenna structure symmetrical for DCP radiation. According to (5.14)-(5.15), values of these lumped elements L_{R1}=2.6 nH, C_{R1}=1.5 pF, L_{L1}=10 nH, and C_{L1}=4.6 pF are obtained. The calculated phase responses of the two unit cells are shown in Figure 5.22 (b)-(c). As shown in the figure, the delayed phase for RH-TL unit cell is -45° at 1.4 GHz, and the delayed phase for LH-TL unit cell is +45° at 1.4 GHz. The phase difference between the two unit cells is 90-96° from 1 GHz to 2 GHz. Wideband quadrature phase and small phase variance are obtained. Therefore, wideband quadrature phase shift and small phase variance can also be expected after incorporating these two types of unit cells into the integrated feed network.

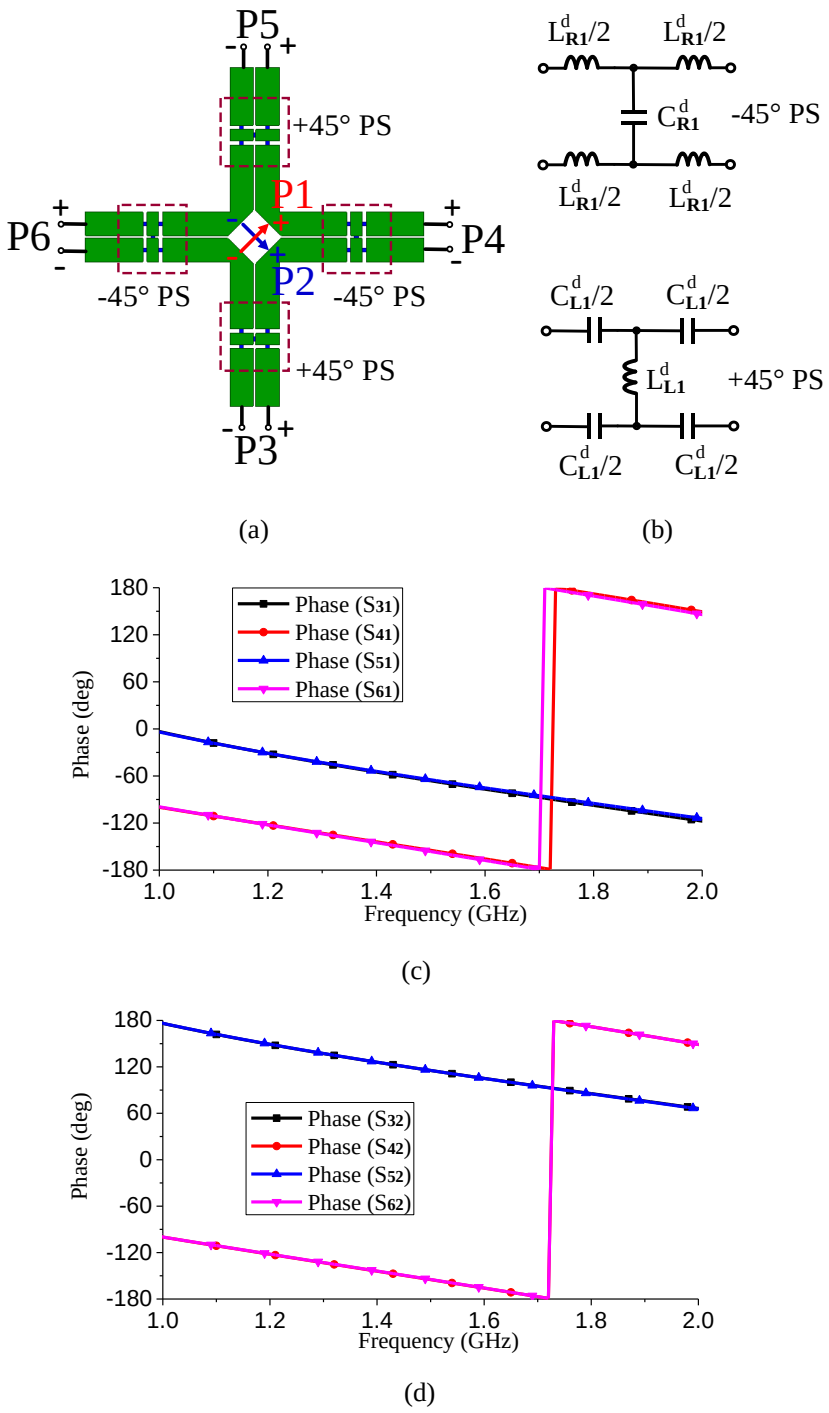

Figure 5.23 The integrated feed network incorporating with OPD and ±45° phase shifters.
(a) Simulation model. (b) Differential RH-TL unit cell and differential LH-TL unit cell (c) Phase responses when port 1 is excited. (d) Phase responses when port 2 is excited.

Figure 5.23 (a) shows the simulation model of the integrated feed network incorporating with the OPD, two RH-TL unit cells for +45° phase shift, and two LH-TL unit cells for -45° phase shift. It should be noted that the unit cells in Figure 5.22 are single-ended circuit. For the proposed integrated feed network, differential RH-TL unit cells and differential LH-TL

unit cell are used, which are shown in Figure 5.23 (b). The component values for the differential unit cells are calculated as

$$\begin{aligned} L_{R1}^{d} &= L_{R1} \\ C_{R1}^{d} &= C_{R1}/2 \\ C_{L1}^{d} &= C_{L1} \\ L_{L1}^{d} &= 2L_{L1} \end{aligned} \tag{5.16}$$

Figure 5.23 (c)-(d) shows the simulated phase responses of the integrated feed network. Two sets of orthogonal quadrature phase responses are achieved when port 1 is excited and port 2 is excited, respectively. As shown in the figure, when port 1 is excited, signals at the port 4 and port 6 are in-phase, but lag -90° behind the port 3 and port 5. Whereas when port 2 is excited, signals at the port 3 and port 5 are also in-phase, but lag -90° behind the port 4 and port 6. Therefore, the scattering matrix for the integrated feed network combining with OPD and phase shifters in Figure 5.23 can be concluded as

$$[S] = \begin{bmatrix} 0 & 0 & 0.5j & 0.5 & 0.5j & 0.5 \\ 0 & 0 & -0.5j & 0.5 & -0.5j & 0.5 \\ 0.5j & -0.5j & 0 & 0.5 & 0 & -0.5 \\ 0.5 & 0.5 & 0.5 & 0 & -0.5 & 0 \\ 0.5j & -0.5j & 0 & -0.5 & 0 & 0.5 \\ 0.5 & 0.5 & -0.5 & 0 & 0.5 & 0 \end{bmatrix} \tag{5.17}$$

Compared to the matrix in (5.13), two sets of orthogonal quadrature signals are achieved at the output ports when the feed network is excited at the different input ports. Therefore, after incorporating four dipoles at the output ports, DCP radiation can be realized.

As discussed above, the component values of the RH-TL unit cell and LH-TL unit cell are important to realize DCP radiation. However, due to the distributed parasitic effects of the parallel transmission lines and the unideal input impedance of the four crossed dipoles, component values of discussed above provide the initial values to design the proposed DCP antenna. The optimal values of these lumped components are given in the caption of Figure 5.17. Therefore, these parameters are studied to provide a guidance to design the proposed DCP antenna.

5.3.3 Results and Discussion

The proposed DCP antenna was designed, fabricated, and measured to validate the above design method. The photographs of the fabricated prototype are shown in Figure 5.24. The S-parameters of the antenna were measured by the Anritsu 37397C vector network analyzer, and the far field radiation patterns were measured by the ASYSOL far field measurement system at University of Kent. Figure 5.25 shows the measured S-parameters of the presented

antenna, which are compared with the simulated results. Good agreement can be observed between the simulated and measured S-parameters. The measured overlapped impedance bandwidth for both two input ports is from 1.07 GHz to 1.85 GHz with the reflection coefficients lower than -10 dB, which is slightly wider than the simulated impedance bandwidth. The corresponding isolation between the two input ports is higher than 15.2 dB within the bandwidth.

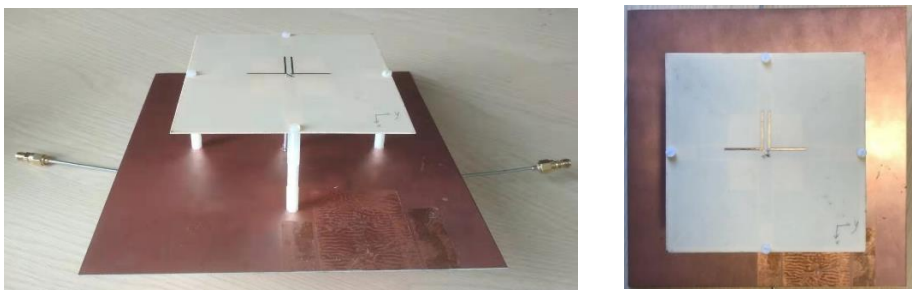

(a) (b)

Figure 5.24 Photographs of the fabricated prototype of the proposed DCP antenna. (a) 3D view. (b) Top view.

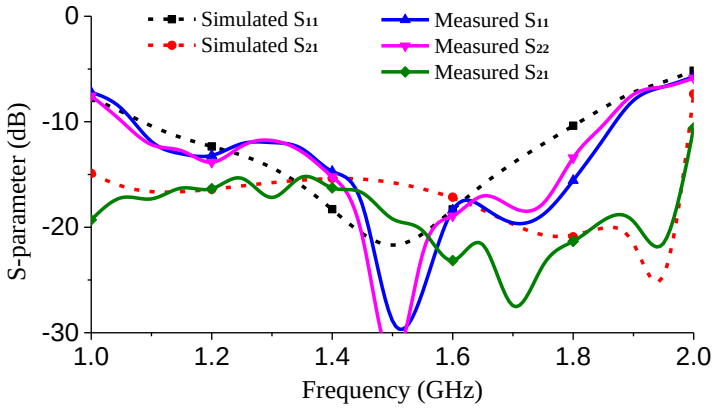

Figure 5.25 Measured and simulated S-parameters of the proposed DCP antenna.

Figure 5.26 shows the measured and simulated AR, peak realized gain, and radiation efficiency of the fabricated antenna prototype when RHCP radiation (port 1) is excited. Owing to the symmetry of the antenna, only RHCP axial ratio and gain are given in the figure. As shown in the figure, the measured AR is less than 1.7 dB from 1.1 GHz to 1.8 GHz within the bandwidth. Stable peak realized gain is achieved, which varies from 7.2-8.8 dBic. In addition, Stable radiation efficiency is achieved for the fabricated antenna. Due to the incorporated lumped element based LH-TL and RH-TL phase shift elements, the measured radiation efficiency is slightly lower than the simulated result. However, it is still very good and high than 87% within the bandwidth.

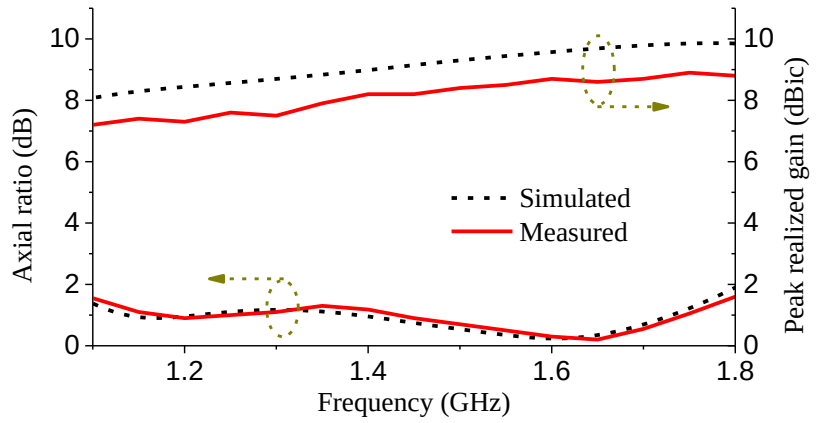

(a)

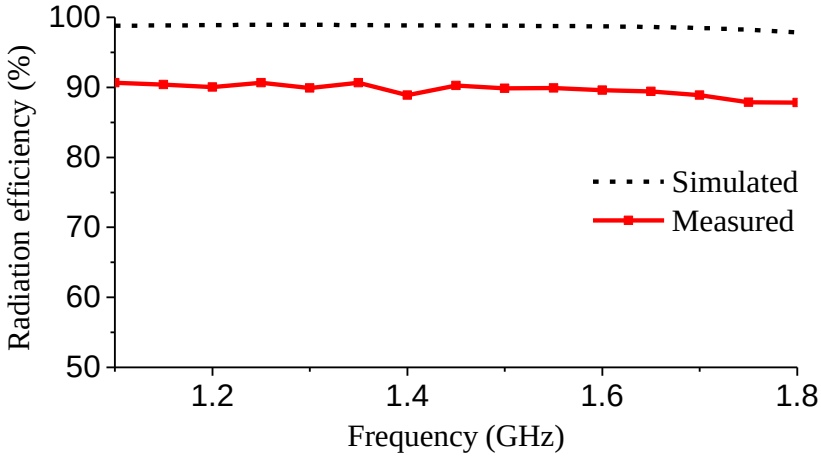

(b)

Figure 5.26 Measured and simulated (a) axial ratio, peak realized gain, and (b) radiation efficiency of the fabricated prototype when RHCP radiation (port 1) is excited.

The measured normalized radiation patterns at the frequency of 1.1 GHz and 1.7 GHz are shown in Figure 5.27, which are compared with the corresponding simulated radiation patterns. As shown in these figures, symmetrical RHCP radiation is achieved when port 1 is excited, and LHCP radiation is the cross-polarization. Good accordance is observed between the simulated and measured radiation patterns. The measured half-power beamwidth is 60-70° in xz-plane, and 60-72° in yz-plane. The beamwidth becomes gradually narrower as the increase of the frequency. Therefore, higher antenna gain is achieved at the upper frequency. Because of the reflection of the antenna reflector, low back-lobe level is achieved with the measured front-to-back ratio higher than 16.4 dB. The slight difference between the measured and simulated results, including the S-parameters and radiation patterns, may be caused by the tolerance of inductors and capacitors, fabrication errors, and position errors in the anechoic chamber.

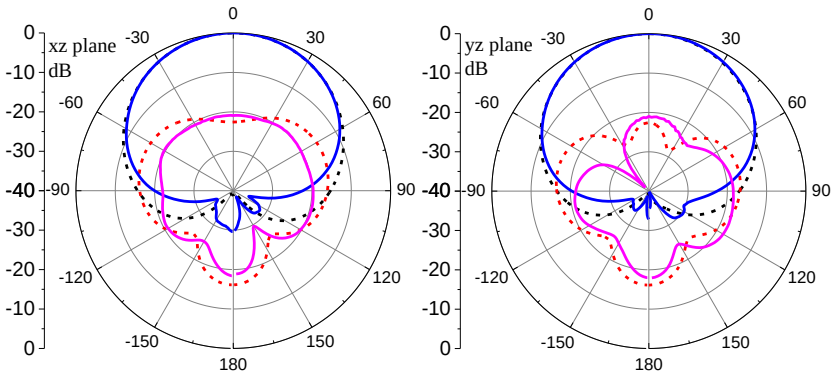

(a)

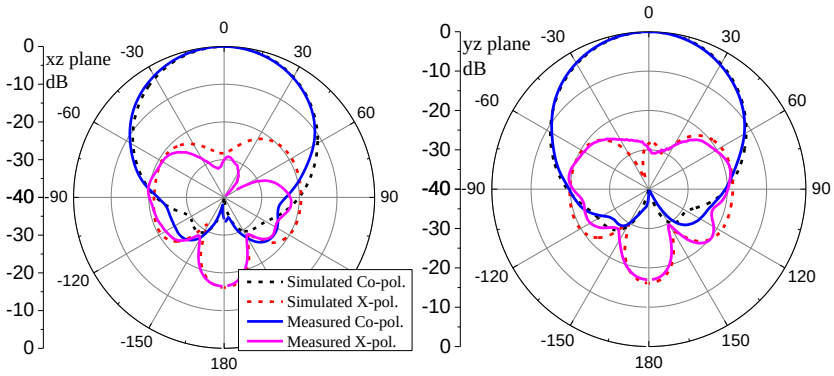

(b)

Figure 5.27 Measured and simulated normalized radiation patterns at (a) 1.1 GHz and (b) 1.7 GHz when RHCP radiation (port 1) is excited. LHCP radiation is the cross-polarization.

Table 5.2 compares the recently published DCP antennas with the presented antenna. DCP radiation can be realized by using patch antennas [145]-[148] with unidirectional and symmetrical radiation patterns. With the help of multi-coupling slots [145], series-fed method [146], or the additionally introduced branchline coupler [148], medium overlapped bandwidth for both impedance and AR is achieved. However, the bandwidth is still limited for the increasingly wider bandwidth required wireless communication systems. Monopole antennas [150] and slot antennas [151]-[152] provide ways to realize very wider bandwidth for DCP radiation. However, these antennas normally have bidirectional and asymmetrical radiation patterns. In addition, it is observed that the radiation patterns of these antennas are unstable, and the maximum radiation direction varies with the frequency. Obviously, it is difficult to use these antennas for array designs.

Backed by reflectors, dipoles antenna in [149] has much wide bandwidth for DCP radiation with unidirectional and symmetrical radiation patterns. However, additional wideband quadrature coupler with four branchlines are utilized to provide required quadrature signals for DCP radiation. This will undoubtedly cause undesired insertion loss

and increase the design cost. In this work, by using the integrated orthogonal feed network, the presented DCP antenna has the overlapped bandwidth of 53.4% for both impedance and AR requirements, which can provide enough operation bandwidth for ITS applications. Moreover, much lower AR (<1.7 dB) and unidirectional and symmetrical radiation patterns are achieved within the bandwidth.

Table 5.2 Comparison of the recently published DCP antennas

Ref.	Overlapped BW (GHz)	AR (dB)	S_{21} (dB)	Radiation	Pattern	Feed network	Radiator
[145]	4.9-5.95 (19.4%)	<3	<-16	UD	Sym.	Integrated	Patch
[146]	9.4-11.0 (15.7%)	<3	<-15	UD	Sym.	Integrated	Patch
[148]	0.8-0.97 (19%)	<3	<-15	UD	Sym.	Additional	Patch
[149]	1.3-3 (79%)	<3	/	UD	Sym.	Additional	Dipole
[150]	3.74-8.8 (80.7%)	<3	<-20	BD	Asym.	No	Monopole
[151]	2-3.7 (60%)	<3	<-15	BD	Asym.	No	Slot
[152]	1.83-6.35 (110.5%)	<3	<-10	BD	Asym.	No	Slot
This work	1.07-1.85 (53.4%)	<1.7	<-15.2	UD	Sym.	Integrated	Dipole

BW: Bandwidth. UD: Unidirectional. BD: Bidirectional. Sym.: Symmetrical. Asym.: Asymmetrical.

5.4 Summary

In this chapter, two wideband circularly polarized antennas are presented. The first one is a wideband series-feed circularly polarized differential antenna, which is designed by using crossed open slot-pairs. This CP antenna is composed of a wide slot-pair and a narrow slot-pair. In the antenna design, the narrow slot-pair is not only excited as a radiator, but also elaborately loaded to provide wideband half-power output and quadrature phase excitation to the wide slot-pair. Both the proposed half-power phase shifter and CP antenna are illustrated by the corresponding equivalent circuits. The second design is a wideband DCP antenna, which is composed of an OPD with orthogonal input ports, four phase shifters for

±45° phase shift, and four crossed dipoles for DCP radiation. In the integrated feed network, the OPD is formed by the coupled coplanar striplines, and can provide equal magnitude in-phase and out-of-phase outputs. Whereas the ±45° phase shifters are designed by using the lumped element based differential LH-TL unit cell and RH-TL unit cell. Both two CP antennas was design, fabricated, and measured for verification.

Chapter 6. Conclusion and Future Work

6.1 Conclusion

In this thesis, several novel designed compact-size wideband antennas and arrays are presented for wireless communication systems. These antennas and arrays are designed with different features to accommodate different application scenarios. The working principle of each antenna is theoretically analyzed. Prototypes of these antennas were fabricated and measured for the performance verification, including S-parameters and radiation patterns.

Wideband and compact base station antennas are presented in Chapter 3. First, a compact dual-polarized antenna based on the sharped-dipoles is illustrated, which features the compact radiator size and wide impedance bandwidth. The second design is a compact dual-polarized antenna based on the crossed shunt loops, which not only has the wide impedance bandwidth covering 1.6-3.0 GHz, but also has high upper out-of-band suppression over 3.35-5.25 GHz. The third design is a dual-polarized antenna with very wide impedance bandwidth. This antenna is designed by using shorted dipoles, and has a wide impedance bandwidth of 74.5% (from 1.69 GHz to 3.7 GHz) for VSWR<1.5 at both ports. The last design is a filtering array antenna, which is realized by using a novel balanced coupling structure. The array antenna features low cross-polarization level, two radiation nulls, low sidelobe level, and high out-of-band suppression.

In Chapter 4, several differentially fed dual-polarized antennas with different performances are presented. First, a wideband and high even mode suppressed six-port power divider is utilized to realize a wideband differentially fed dual-polarized with high common mode suppression. The equivalent circuit under even and odd modes excitations are given for detailed illustration. The second design is a wideband differentially fed dual-polarized antenna with wideband harmonic suppression. The radiating structure is designed based on the open slots, stair-shaped strips, and a square patch. To achieve wideband harmonic suppression, compact stepped impedance resonators are elaborately integrated into this antenna. The last design is a low-cost compact differentially fed dual-polarized array patch antenna. The antenna element is driven by intersected open loop resonators, which is features the high isolation and low cross-polarization level. Beam scanning performances are investigated for this presented array antenna.

Two wideband circularly polarized antennas are presented in Chapter 5. The first one is a wideband series-feed circularly polarized differential antenna, which is designed by using crossed open slot-pairs. This CP antenna is composed of a wide slot-pair and a narrow slot-

pair. In the antenna design, the narrow slot-pair is not only excited as a radiator, but also elaborately loaded to provide wideband half-power output and quadrature phase excitation to the wide slot-pair. Both the proposed half-power phase shifter and CP antenna are illustrated by the corresponding equivalent circuits. The second design is a wideband DCP antenna, which is composed of an OPD with orthogonal input ports, four phase shifters for ±45° phase shift, and four crossed dipoles for DCP radiation. In the integrated feed network, the OPD is formed by the coupled coplanar striplines, and can provide equal magnitude in-phase and out-of-phase outputs. Whereas the ±45° phase shifters are designed by using the lumped element based differential LH-TL unit cell and RH-TL unit cell. Both two CP antennas was design, fabricated, and measured for verification.

6.2 Future Work

Although much work has been done on the design of compact and wideband antennas in this thesis, some new challenges are still existed in the antenna design. The possible future work should be focused on the following new challenges.

- Novel design method of antennas with quasi-elliptic filtering response.

With the development of wireless communication systems, more and more frequency bands have been occupied for different communication systems. Due to increasingly congested available bandwidth for wireless communication, it is meaningful and necessary to reduce these out-of-band interferences, which can transmit serious interference to the other receiver systems and receive the undesired noise from the nearby transmitter systems. If antennas are designed with quasi-elliptic filtering response, the undesired out-of-band interference signals would be deeply suppressed and will have little effect on the communication quality for other systems.

- Novel design method of CP antennas with wide AR bandwidth.

As is known that the bandwidth of CP antennas are always confined by the available AR bandwidth. How to obtain the optimal AR bandwidth is a constant research interest for researchers. It is easy to understand that by using a parasitic strip or patch, the impedance resonances can be increased. However, how to use the parasitic strip or patch to achieve a new CP resonance is still worth the deep research. In details, we can use the equivalent circuit to illustrate the impedance characteristic of wide impedance bandwidth. However, it will become difficult to illustrate why the wide AR bandwidth is obtained by mapping the corresponding equivalent circuit.

- The effect of antenna frequency response with the power amplifier linearity.

Different novel methods of designing antennas and arrays are discussed in this thesis. However, in the practical application scenario, antennas will be connected to the power amplifier with high output power. The working status of the power amplifier can have a significant effect on the performance of antennas. In view of this, the future work will also include following different aspects.

First, because of the high power output form the power amplifier (e.g. >100watts), the antennas are required to withstand the high power output without being destroyed. The presented antenna designs using ordinary substrates may not work. Then, the reflection coefficient of the power amplifier will change as the variance of its output power. So how to balance the optimal output power and obtain the best impedance matching is a challenging work for researchers. Finally, the passive intermodulation of antennas should also be considered. If antennas are not designed properly, these undesired intermodulation products will deteriorate the wireless communication links after the amplification of the power amplifier. Overall, the effect of antenna frequency response with the power amplifier linearity is very important and worth deep consideration in the future practical design work.

References

[1] R. G. Vaughan, "Plarization diversity in mobile communications", *IEEE Trans. Veh. Technol.*, Vol. 39, no. 3, pp. 177-186, Aug. 1990.

[2] J. J. A. Lempiainen and J. K. Laiho-Steffens, "The performance of polarization diversity schemes at a base station in small/micro cells at 1800MHz", *IEEE Trans. Veh. Technol.*, Vol. 47, no. 3, pp. 1087-1092, Aug. 1998.

[3] R. K. Mishra, D. R. Jahagirdar, and G. Kumar, "A review of broadband dual linearly polarized microstrip antenna designs with high isolation", *IEEE Antennas Propag. Mag.*, vol. 56, no. 6, pp. 238-251, Dec. 2014.

[4] S. Gao, Q. Luo, and F. Zhu, Circularly polarized antennas: John Wiley & Sons, 2013.

[5] H. W. Lai and K. M. Luk, "Dual polarized patch antenna fed by meandering probes", *IEEE Trans. Antennas Propag.*, vol. 55, no. 9, pp. 2625–2627, Sep. 2007.

[6] S. Gao, L. W. Li, M. S. Leong and T. S. Yeo, "A broad-band dual-polarized microstrip patch antenna with aperture coupling," *IEEE Trans. Antennas Propag.*, vol. 51, no. 4, pp. 898-900, April 2003.

[7] C. Mao, S. Gao, Y. Wang, F. Qin and Q. Chu, "Multimode resonator-fed dual-polarized antenna array with enhanced bandwidth and selectivity," *IEEE Trans. Antennas Propag.*, vol. 63, no. 12, pp. 5492-5499, Dec. 2015.

[8] Y. X. Guo, K. W. Khoo, and L. C. Ong, "Wideband dual-polarized patch antenna with broadband baluns", *IEEE Trans. Antennas Propag.*, vol. 55, no. 1, pp. 78–83, Jan. 2007.

[9] C. Mao, S. Gao, Y. Wang, Q. Luo and Q. Chu, "A shared-aperture dual-band dual-polarized filtering-antenna-array with improved frequency response," *IEEE Trans. Antennas Propag.*, vol. 65, no. 4, pp. 1836-1844, April 2017.

[10] W. Qiu, C. Chen, H. Zhang, and W. Chen, "A wideband dual-polarized L-probe antenna array with hollow structure and modified ground plane for isolation enhancement", *IEEE Antennas Wireless Propag. Lett.*, vol. 16, pp. 2820–2823, 2017.

[11] Y. Wang and Z. Du, "Dual-polarized slot-coupled microstrip antenna array with stable active element pattern", *IEEE Trans. Antennas Propag.*, vol. 63, no. 9, pp. 4239–4244, Sep. 2015.

[12] S. C. Gao, L. W. Li, M. S. Leong, and T. S. Yeo, "Dual-polarized slot-coupled planar antenna with wide bandwidth," *IEEE Trans. Antennas Propag.*, vol. 51, no. 3, pp. 441-448, March 2003.

[13] J. J. Xie, X. S. Ren, Y. Z. Yin, and J. Ren, "Dual-polarized patch antenna with wide bandwidth using electromagnetic feeds", *Electron. Lett.*, vol. 48, no. 22, pp. 1385–1386, Oct. 2012.

[14] J. Y. Deng, L. X. Guo, Y. Z. Yin, J. Qiu, and Z. S. Wu, "Broadband patch antennas fed by novel tuned loop", *IEEE Trans. Antennas Propag.*, vol. 61, no. 4, pp. 2290–2293, Apr. 2013.

[15] J. J. Xie, Y. Z. Yin, J. H. Wang, and X. L. Liu, "Wideband dual-polarized electromagnetic-fed patch antenna with high isolation and low cross-polarization", *Electron. Lett.*, vol. 49, no. 3, pp. 171–173, Jan. 2013.

[16] J. Li, S. Yang, Y. Gou, J. Hu, and Z. Nie, "Wideband dual-polarized magnetically coupled patch antenna array with high port isolation", *IEEE Trans. Antennas Propag.*, vol. 64, no. 1, pp. 117–125, Jan. 2016.

[17] Y. X. Guo, K. M. Luk, and K. F. Lee, "Broadband dual polarization patch antenna element for cellular-phone base stations", *IEEE Trans. Antennas Propag.*, vol. 50, no. 2, pp. 251–253, Feb. 2002.

[18] K. M. Mak, X. Gao, and H. W. Lai, "Low cost dual polarized base station element for long term evolution", *IEEE Trans. Antennas Propag.*, vol. 62, no. 11, pp. 5861–5865, Nov. 2014.

[19] X. Jiang, Z. Zhang, Z. Tian, Y. Li, and Z. Feng, "A low-cost dual-polarized array antenna etched on a single substrate", *IEEE Antennas Wireless Propag. Lett.*, vol. 12, pp. 265–268, 2013.

[20] X. Jiang, Z. Zhang, Y. Li, and Z. Feng, "A planar wideband dual-polarized array antenna for active antenna system", *IEEE Antennas Wireless Propag. Lett.*, vol. 13, pp. 544–547, 2014.

[21] C. Deng, Y. Li, Z. Zhang, and Z. Feng, "A wideband high-isolated dual-polarized patch antenna using two different balun feedings", *IEEE Antennas Wireless Propag. Lett.*, vol. 13, pp. 1617–1619, 2014.

[22] R. Lian, Z. Wang, Y. Yin, J. Wu, and X. Song, "Design of a low-profile dual-polarized stepped slot antenna array for base station", *IEEE Antennas Wireless Propag. Lett.*, vol. 15, pp. 362–365, 2016.

[23] H. Kähkönen, J. Ala-Laurinaho and V. Viikari, "Dual-polarized Ka-band Vivaldi antenna array," *IEEE Trans. Antennas Propag.*, vol. 68, no. 4, pp. 2675-2683, April 2020.

[24] M. Sonkki, D. Sánchez-Escuderos, V. Hovinen, E. T. Salonen and M. Ferrando-Bataller, "Wideband dual-polarized cross-shaped Vivaldi antenna," *IEEE Trans. Antennas Propag.*, vol. 63, no. 6, pp. 2813-2819, June 2015.

[25] J. Yan, S. Gogineni, B. Camps-Raga and J. Brozena, "A dual-polarized 2–18-GHz Vivaldi array for airborne radar measurements of snow," *IEEE Trans. Antennas Propag.*, vol. 64, no. 2, pp. 781-785, Feb. 2016.

[26] Zhongxiang Shen and Chao Feng, "A new dual-polarized broadband horn antenna," *IEEE Antennas Wireless Propag. Lett.*, vol. 4, pp. 270-273, 2005.

[27] S. Manshari, S. Koziel and L. Leifsson, "Compact dual-polarized corrugated horn antenna for satellite communications," *IEEE Trans. Antennas Propag.*, vol. 68, no. 7, pp. 5122-5129, July 2020.

[28] H. Jin, Y. M. Huang, H. Jin and K. Wu, "E-band substrate integrated waveguide orthomode transducer integrated with dual-polarized horn antenna," *IEEE Trans. Antennas Propag.*, vol. 66, no. 5, pp. 2291-2298, May 2018.

[29] Y. H. Cui, R. L. Li, and H. Z. Fu, "A broadband dual-polarized planar antenna for 2G/3G/LTE base station", *IEEE Trans. Antennas Propag.*, vol. 62, no. 5, pp. 4836–4840, Sep. 2014.

[30] D. Z. Zheng and Q. X. Chu, "A multimode wideband ±45° dual-polarized antenna with embedded loops", *IEEE Antennas Wireless Propag. Lett.*, vol. 16, pp. 633–636, 2017.

[31] H. Huang, Y. Liu, and Shuxi Gong, "A broadband dual-polarized base station antenna with sturdy construction", *IEEE Antennas Wireless Propag. Lett.*, vol. 16, pp. 665–668, 2017.

[32] B. Liu, Y. Cui, and R. Li, "A broadband dual-polarized dual-OAM-Mode antenna array for OAM communication", *IEEE Antennas Wireless Propag. Lett.*, vol. 16, pp. 744–747, 2017.

[33] D. Z. Zheng and Q. X. Chu, "A wideband dual-polarized antenna with two independently controllable resonant modes and its array for base-station applications", *IEEE Antennas Wireless Propag. Lett.*, vol. 16, pp. 2014–2017, 2017.

[34] Y. Luo, Q. X. Chu, and J. Bornemann, "Enhancing cross-polarization discrimination or axial ratio beamwidth of diagonally dual or circularly polarized base station antennas by using parasitic elements", *IET Microw. Antennas Propag.*, vol. 11, iss. 9, pp. 1190–1196, 2017.

[35] Y. Pan, Y. Cui, C. L. Qi, and R. L. Li, "Evaluation of dual-polarized triple-band multi-beam MIMO antennas for WLAN/WiMAX applications", *IET Microw. Antennas Propag.*, vol. 11, iss. 10, pp. 1469–1475, 2017.

[36] Q. X. Chu, D. L. Wen, and Y. Luo, "A broadband ±45° dual-polarized antenna with Y-shaped feeding lines", *IEEE Trans. Antennas Propag.*, vol. 63, no. 2, pp. 483–490, Feb. 2015.

[37] Y. H. Ren, J. Ding, C. J. Guo, Y. Qu, and Y.-C. Song, "A wideband dual-polarized printed antenna based on complementary split-ring resonators", *IEEE Antennas Wireless Propag. Lett.*, vol. 14, pp. 410–413, 2015.

[38] Y. Gou, S. Yang, J. Li, and Z. Nie, "A compact dual-polarized printed dipole antenna with high isolation for wideband base station applications", *IEEE Trans. Antennas Propag.*, vol. 62, no. 8, pp. 4392–4394, Aug. 2014.

[39] A. Elsherbini, J. Wu, and K. Sarabandi, "Dual polarized wideband directional coupled sectorial loop antennas for radar and mobile base-station applications", *IEEE Trans. Antennas Propag.*, vol. 63, no. 4, pp. 1505–1513, Apr. 2015.

[40] Y. H. Cui, R. L. Li, and P. Wang, "A novel broadband planar antenna for 2G/3G/LTE base station", *IEEE Trans. Antennas Propag.*, vol. 61, no. 5, pp. 2767–2773, May 2013.

[41] Y. Luo, Q. X. Chu, and D. L. Wen, "A plus/minus 45 degree dual-polarized base-station antenna with enhanced cross-polarization discrimination via addition of four parasitic elements placed in a square contour", *IEEE Trans. Antennas Propag.*, vol. 64, no. 4, pp. 1514–1519, Apr. 2016.

[42] H. Huang, Y. Liu, and S. Gong, "A broadband dual-polarized base station antenna with anti-interference capacity", *IEEE Antennas Wireless Propag. Lett.*, vol. 16, pp. 613–616, 2017.

[43] Y. H. Huang, Q. Wu, and Q. Z. Liu, "Broadband dual-polarized antenna with high isolation for wireless communicaiton", *Electron. Lett.*, vol. 45, no. 14, pp. 714–715, Jul. 2009.

[44] B. Li, Y. Z. Yin, Y. Zhao, Y. Ding, and R. Zou, "Dual-polarized patch antenna with low cross-polarization and high isolation for WiMAX applications", *Electron. Lett.*, vol. 47, no. 17, pp. 952–953 Aug. 2011.

[45] B. Li, Y. Z. Yin, W. Hu, Y. Ding, and Y. Zhao, "Wideband dual-polarized patch antenna with low cross polarization and high isolation", *IEEE Antennas Wireless Propag. Lett.*, vol. 11, pp. 427–430, 2012.

[46] S.-G. Zhou, P. K. Tan, and T. H. Chio, "Low-profile, wideband dual-polarized antenna with high isolation and low cross polarization", *IEEE Antennas Wireless Propag. Lett.*, vol. 11, pp. 1032–1035, 2012.

[47] D. L. Wen, D. Z. Zheng, and Q. X. Chu, "A dual-polarized planar antenna using four folded dipoles and its array for base stations", *IEEE Trans. Antennas Propag.*, vol. 64, no. 12, pp. 5536–5542, Dec. 2016.

[48] K. M. Luk and H.Wong, "A new wideband unidirectional antenna element," *Int. J. Microw. Opt. Technol.*, vol. 1, no. 1, pp. 35–44, Jun. 2006.

[49] B. Q. Wu and K. M. Luk, "A broadband dual-polarized magneto-electric dipole antenna with simple feeds", *IEEE Antennas Wireless Propag. Lett.*, vol. 8, pp. 60–63, 2009.

[50] L. Siu, H. Wong, and K. M. Luk, "A dual-polarized magneto-electric dipole with dielectric loading", *IEEE Trans. Antennas Propag.*, vol. 57, no. 3, pp. 616–623, Mar. 2009.

[51] L. Ge and K. M. Luk, "A low-profile magneto-electric dipole antenna", *IEEE Trans. Antennas Propag.*, vol. 60, no. 4, pp. 1684–1689, Apr. 2012.

[52] L. Ge and K. M. Luk, "A magneto-electric dipole antenna with low-profile and simple structure", *IEEE Antennas Wireless Propag. Lett.*, vol. 12, pp. 140–142, 2013.

[53] M. Li and K. M. Luk, "Wideband Magnetoelectric dipole antennas with dual polarization and circular polarization", *IEEE Antennas Propag. Mag.*, vol. 57, no. 1, pp. 110-119, Feb. 2015.

[54] L. Ge and K. M. Luk, "Linearly Polarized and dual-polarized magneto-electric dipole antennas with reconfigurable beamwidth in the H-plane", *IEEE Trans. Antennas Propag.*, vol. 64, no. 2, pp. 423–431, Feb. 2016.

[55] C. Ding and K. M. Luk, "Low-profile magneto-electric dipole antenna", *IEEE Antennas Wireless Propag. Lett.*, vol. 15, pp. 1642–1644, 2016.

[56] H. W. Lai, K. K. So, H. Wong, C. H. Chan, and K. M. Luk, "Magnetoelectric dipole antennas with dual open-ended slot excitation", *IEEE Trans. Antennas Propag.*, vol. 64, no. 8, pp. 3338–3345, Aug. 2016.

[57] S. G. Zhou, Z. H. Peng, G. L. Huang, and C. Y. D. Sim, "Design of a novel wideband and dual-polarized magnetoelectric dipole antenna", *IEEE Trans. Antennas Propag.*, vol. 65, no. 5, pp. 2645–2649, May. 2017.

[58] F. Wu and K. M. Luk, "Single-port reconfigurable magneto-electric dipole antenna with quad-polarization diversity", *IEEE Trans. Antennas Propag.*, vol. 65, no. 5, pp. 2289–2295, May. 2017.

[59] Q. Xue, S. W. Liao, and J. H. Xu, "A differentially-driven dual-polarized magneto-electric dipole antenna", *IEEE Trans. Antennas Propag.*, vol. 61, no. 1, pp. 425–430, Jan. 2013.

[60] Y. Luo and Q. X. Chu, "Oriental crown-shaped differentially fed dual-polarized multidipole antenna", *IEEE Trans. Antennas Propag.*, vol. 63, no. 11, pp. 4678–4685, Nov. 2015.

[61] D. L. Wen, D. Z. Zheng, and Q. X. Chu, "A wideband differentially fed dual-polarized antenna with stable radiation pattern for base stations", *IEEE Trans. Antennas Propag.*, vol. 65, no. 5, pp. 2248–2255, May. 2017.

[62] Y. H. Cui, X. Gao, and R. L. Li, "A broadband differentially fed dual-polarized planar antenna", *IEEE Trans. Antennas Propag.*, vol. 65, no. 5, pp. 3231–3234, Jun. 2017.

[63] K. Y. Lam, K. Luk, K. F. Lee, H. Wong, and K. B. Ng, "Small circularly polarized u-slot wideband patch antenna," *IEEE Antennas Wireless Propag. Lett.*, vol. 10, pp. 87-90, 2011.

[64] Y. Guo and D. C. H. Tan, "Wideband single-feed circularly polarized patch antenna with conical radiation pattern," *IEEE Antennas Wireless Propag. Lett.*, vol. 8, pp. 924-926, 2009.

[65] W. Yang, J. Zhou, Z. Yu, and L. Li, "Single-fed low profile broadband circularly polarized stacked patch antenna," *IEEE Trans. Antennas Propag.*, vol. 62, no. 10, pp. 5406-5410, Oct. 2014,.

[66] Q. W. Lin, H. Wong, X. Y. Zhang, and H. W. Lai, "Printed meandering probe-fed circularly polarized patch antenn with wide bandwidth," *IEEE Antennas Wireless Propag. Lett.*, vol. 13, pp. 654-657, 2014.

[67] Ka-Lam Lau, Kwai-Man Luk, and Kai-Fong Lee, "Design of a circularly-polarized vertical patch antenna," *IEEE Trans. Antennas Propag.*, vol. 54, no. 4, pp. 1332-1335, April 2006.

[68] Q. W. Lin, H. Wong, X. Y. Zhang, and H. W. Lai, "Printed meandering probe-fed circularly polarized patch antenna with wide bandwidth," *IEEE Antennas Wireless Propag. Lett.*, vol. 13, pp. 654-657, 2014.

[69] Nasimuddin, Z. N. Chen and X. Qing, "A compact circularly polarized cross-shaped slotted microstrip antenna," *IEEE Trans. Antennas Propag.*, vol. 60, no. 3, pp. 1584-1588, March 2012.

[70] Y. Xu, S. Gong and T. Hong, "Circularly polarized slot microstrip antenna for harmonic suppression," *IEEE Antennas Wireless Propag. Lett.*, vol. 12, pp. 472-475, 2013.

[71] L. Bian, Y.-X. Guo, L. C. Ong, and X. -. Shi, "Wideband circularly-polarized patch antenna," *IEEE Trans. Antennas Propag.*, vol. 54, no. 9, pp. 2682-2686, Sept. 2006.

[72] K. L. Lau and K. M. Luk, "A novel wide-band circularly polarized patch antenna based on L-probe and aperture-coupling techniques," *IEEE Trans. Antennas Propag.*, vol. 53, no. 1, pp. 577-582, Jan. 2005.

[73] Z. Zhang and K. Wu, "A circularly polarized table-like air patch antenna with four grounded metal legs," *IEEE Antennas Wireless Propag. Lett.*, vol. 16, pp. 190-193, 2017.

[74] X. Chen, L. Yang, J. Zhao and G. Fu, "High-efficiency compact circularly polarized microstrip antenna with wide beamwidth for airborne communication," *IEEE Antennas Wireless Propag. Lett.*, vol. 15, pp. 1518-1521, 2016.

[75] K. Ding, C. Gao, D. Qu and Q. Yin, "Compact broadband circularly polarized antenna with parasitic patches," *IEEE Trans. Antennas Propag.*, vol. 65, no. 9, pp. 4854-4857, Sept. 2017.

[76] K. Ding, C. Gao, T. Yu, D. Qu and B. Zhang, "Gain-improved broadband circularly polarized antenna array with parasitic patches," *IEEE Antennas Wireless Propag. Lett.*, vol. 16, pp. 1468-1471, 2017.

[77] K. Li, L. Li, Y. Cai, C. Zhu, and c. liang, "a novel design of low-profile dual-band circularly polarized antenna with meta-surface," *IEEE Antennas Wireless Propag. Lett.*, vol. 14, pp. 1650-1653, 2015.

[78] J. Row and S. Wu, "Circularly-polarized wide slot antenna loaded with a parasitic patch," *IEEE Trans. Antennas Propag.*, vol. 56, no. 9, pp. 2826-2832, Sept. 2008.

[79] W. Yang and J. Zhou, "Wideband circularly polarized cavity-backed aperture antenna with a parasitic square patch," *IEEE Antennas Wireless Propag. Lett.*, vol. 13, pp. 197-200, 2014.

[80] J. Wei, X. Jiang and L. Peng, "Ultrawideband and high-gain circularly polarized antenna with double-y-shape slot," *IEEE Antennas Wireless Propag. Lett.*, vol. 16, pp. 1508-1511, 2017.

[81] J. Pourahmadazar, C. Ghobadi, J. Nourinia, N. Felegari and H. Shirzad, "Broadband cpw-fed circularly polarized square slot antenna with inverted-L strips for UWB applications," *IEEE Antennas Wireless Propag. Lett.*, vol. 10, pp. 369-372, 2011.

[82] H. Zhang, Y. Jiao, L. Lu and C. Zhang, "Broadband circularly polarized square-ring-loaded slot antenna with flat gains," *IEEE Antennas Wireless Propag. Lett.*, vol. 16, pp. 29-32, 2017.

[83] S. Mohammadi, J. Nourinia, C. Ghobadi, J. Pourahmadazar and M. Shokri, "Compact broadband circularly polarized slot antenna using two linked elliptical slots for C-band applications," *IEEE Antennas Wireless Propag. Lett.*, vol. 12, pp. 1094-1097, 2013.

[84] T. Chang and J. Lin, "Circularly polarized antenna having two linked slot-rings," *IEEE Trans Antennas Propag.*, vol. 59, no. 8, pp. 3057-3060, Aug. 2011.

[85] R. Xu, J. Li, J. Liu, S. G. Zhou and K. Wei, "UWB circularly polarised slot antenna with modified ground plane and L-shaped radiator," *Electron. Lett.*, vol. 54, no. 15, pp. 918-920, 26 7 2018.

[86] G. Li, H. Zhai, T. Li, L. Li and C. Liang, "CPW-fed S-shaped slot antenna for broadband circular polarization," I*EEE Antennas Wireless Propag. Lett.*, vol. 12, pp. 619-622, 2013.

[87] G. Feng, L. Chen, X. Xue and X. Shi, "Broadband circularly polarized crossed-dipole antenna with a single asymmetrical cross-loop," *IEEE Antennas Wireless Propag. Lett.*, vol. 16, pp. 3184-3187, 2017.

[88] Y. He, W. He and H. Wong, "A wideband circularly polarized cross-dipole antenna," *IEEE Antennas Wireless Propag. Lett.*, vol. 13, pp. 67-70, 2014.

[89] W. Yang, Y. Pan, S. Zheng and P. Hu, "A low-profile wideband circularly polarized crossed-dipole antenna," *IEEE Antennas Wireless Propag. Lett.*, vol. 16, pp. 2126-2129, 2017.

[90] X. Liang et al., "Wideband circularly polarized antenna with dual-mode operation," *IEEE Antennas Wireless Propag. Lett.*, vol. 18, no. 4, pp. 767-770, April 2019.

[91] H. H. Tran and I. Park, "Wideband circularly polarized cavity-backed asymmetric crossed bowtie dipole antenna," *IEEE Antennas Wireless Propag. Lett.*, vol. 15, pp. 358-361, 2016.

[92] W. Yang, Y. Pan and S. Zheng, "A compact broadband circularly polarized crossed-dipole antenna with a very low profile," *IEEE Antennas Wireless Propag. Lett.*, vol. 18, no. 10, pp. 2130-2134, Oct. 2019.

[93] S. Qu, J. Li, C. H. Chan and Q. Xue, "Cavity-backed circularly polarized dual-loop antenna with wide tunable range," *IEEE Antennas Wireless Propag. Lett.*, vol. 7, pp. 761-763, 2008.

[94] Q. Yang, X. Zhang, N. Wang, X. Bai, J. Li and X. Zhao, "Cavity-backed circularly polarized self-phased four-loop antenna for gain enhancement," *IEEE Trans. Antennas Propag.*, vol. 59, no. 2, pp. 685-688, Feb. 2011.

[95] R. Li, L. Pan and Y. Cui, "A novel broadband circularly polarized antenna based on off-center-fed dipoles," *IEEE Trans. Antennas Propag.*, vol. 63, no. 12, pp. 5296-5304, Dec. 2015.

[96] D. Zheng, Y. Luo and Q. Chu, "Cavity-backed self-phased circularly polarized multidipole antenna with wide axial-ratio beamwidth," *IEEE Antennas Wireless Propag. Lett.*, vol. 16, pp. 1998-2001, 2017.

[97] B. Li, Y. Yin, W. Hu, Y. Ding and Y. Zhao, "Wideband dual-polarized patch antenna with low cross polarization and high isolation," *IEEE Antennas and Wireless Propag. Lett.*, vol. 11, pp. 427-430, 2012.

[98] Y. Cui, X. N. Gao, H. Z. Fu, Q.-X. Chu, and R. L. Li, "Broadband dual-polrized dual-dipole planar antennas," *IEEE Antennas Propag. Mag.*, vol. 59, no. 6, pp. 77–87, Dec. 2017.

[99] Y. He, Z. Pan, X. Cheng, Y. He, J. Qiao and M. M. Tentzeris, "A novel dual-band, dual-polarized, miniaturized and low-profile base station antenna," *IEEE Trans. Antennas Propag.*, vol. 63, no. 12, pp. 5399-5408, Dec. 2015.

[100] Z. Tang, J. Liu, Y. Cai, J. Wang and Y. Yin, "A wideband differentially fed dual-polarized stacked patch antenna with tuned slot excitations," *IEEE Trans. Antennas Propag.*, vol. 66, no. 4, pp. 2055-2060, April 2018.

[101] W. Hong et al., "Multibeam antenna technologies for 5G wireless communications," *IEEE Trans. Antennas Propag.*, vol. 65, no. 12, pp. 6231-6249, Dec. 2017.

[102] P. Jin and R. W. Ziolkowski, "Metamaterial-inspired, electrically small huygens sources," *IEEE Antennas and Wireless Propag. Lett.*, vol. 9, pp. 501-505, 2010.

[103] M. Tang, T. Shi and R. W. Ziolkowski, "A study of 28 GHz, planar, multilayered, electrically small, broadside radiating, huygens source antennas," *IEEE Trans. Antennas Propag.*, vol. 65, no. 12, pp. 6345-6354, Dec. 2017.

[104] M. Tang, B. Zhou and R. W. Ziolkowski, "Low-profile, electrically small, huygens source antenna with pattern-reconfigurability that covers the entire azimuthal plane," *IEEE Trans. Antennas Propag.*, vol. 65, no. 3, pp. 1063-1072, March 2017.

[105] W. Fan, A. Lu, L. L. Wai, and B. K. Lok, "Mixed-mode S-parameter characterization of differential structures," *Proc. 5th Electronics Packaging Tech. Conf. (EPTC 2003).* , pp. 533–537, 2003.

[106] C.A. Balanis, *Antenna Theory: Analysis and Design*, John Wiley, 3rd edition, 2005.

[107] T. Tsukiji and S. Tou, "On polygonal loop antennas," *IEEE Trans. Antennas Propag.*, vol. 28, no. 4, pp. 571-575, July 1980.

[108] S. Ahmed and W. Menzel, "A novel planar four-quad antenna," *2012 6th Europ. Conf. Antennas Propag. (EUCAP)*, Prague, 2012, pp. 1946-1949.

[109] M. A. Aprizal, A. Manda and Edwar, "Design and simulation of multi layer parasitic microstrip biquad patch antenna for WLAN 2.4GHz applications," *2017 IEEE Asia Pacific Conf. Wireless Mobile (APWiMob)*, Bandung, 2017, pp. 72-75.

[110] A. D. Yaghjian and S. R. Best, "Impedance, bandwidth, and Q of antennas," *IEEE Trans. on Antennas Propag.*, vol. 53, no. 4, pp. 1298-1324, April 2005.

[111] A. F. McKinley, T. P. White, I. S. Maksymov, and K. R. Catchpole, "The analytical basis for the resonances and anti-resonances of loop antennas and meta-material ring resonators," *J. Appl. Phys.*, vol. 112, no. 9, pp. 094911, Nov. 2012.

[112] W. K. Roberts, "A new wide-band balun," *Proc. IRE*, vol. 45, pp.1628-1631, Dec. 1957.

[113] H. Sun, C. Ding, B. Jones, and Y. J. Guo, "A wideband base station antenna element with stable radiation pattern and reduced beam squint," *IEEE Access*, vol. 5, pp. 23022–23031, 2017.

[114] Z. Tang, J. Liu, Y. Cai, J. Wang and Y. Yin, "A wideband differentially fed dual-polarized stacked patch antenna with tuned slot excitations," *IEEE Trans. Antennas Propag.*, vol. 66, no. 4, pp. 2055-2060, April 2018.

[115] Z. Tang, J. Liu and Y. Yin, "Enhanced cross-polarization discrimination of wideband differentially fed dual-polarized antenna via a shorting loop," *IEEE Trans. Antennas Propag.*, vol. 17, no. 8, pp. 1454-1458, Aug. 2018.

[116] C. Mao *et al.*, "An Integrated Filtering Antenna Array With High Selectivity and Harmonics Suppression," *IEEE Trans. Microw. Theory Techn.*, vol. 64, no. 6, pp. 1798-1805, May 2016.

[117] C. Mao, S. Gao, Y. Wang, Q. Luo, and Q.-X. Chu, "A Shared-Aperture Dual-Band Dual-Polarized Frequency Response," *IEEE Trans. Antennas Propag.*, vol. 65, no. 4, pp. 1836–1844, Feb. 2017.

[118] J. S. Hong and M. J. Lancaster, *Microstrip Filters for RF/Microwave Applications*. New York, NY, USA: Wiley, 2001.

[119] Y. Ding, Y.-C. Jiao, L. Zhang, and B. Li, "Solving Port Selection Problem in Multiple Beam Antenna Satellite Communication System by Using Differential Evolution Algorithm," *IEEE Trans. Antennas Propag.*, vol. 62, no. 10, pp. 5357–5361, Jul. 2014.

[120] J.-L. Guo and J. Li, "Pattern Synthesis of Conformal Array Antenna in the Presence of Platform Using Differential Evolution Algorithm," *IEEE Trans. Antennas Propag.*, vol. 57, no. 9, pp. 2615–2621, Jul. 2009.

[121] C. Lin, A. Qing, and Q. Feng, "Synthesis of Unequally Spaced Antenna Arrays by Using Differential Evolution," *IEEE Trans. Anteenas Propag.*, vol. 58, no. 8, pp. 2553–2561, May 2010.

[122] S. K. Goudos, K. Siakavara, T. Samaras, E. E. Vafiadis, and J. N. Sahalos, “Self-Adaptive Differential Evolution Applied to Real-Valued Antenna and Microwave Design Problems,” *IEEE Trans. Antennas Propag.*, vol. 59, no. 4, pp. 1286–1298, Jan. 2011.

[123] W. R. Eisenstadt, B. Stengel, and B. M. Thompson, *Microwave Differential Circuit Design Using Mixed-Mode S-Parameters*. Norwood, MA, USA: Artech House, 2006.

[124] Z. Tang, J. Liu, R. Lian, Y. Li and Y. Yin, "Wideband differentially fed dual-polarized planar antenna and its array with high common-mode suppression," *IEEE Trans. Antennas Propag.*, vol. 67, no. 1, pp. 131-139, Jan. 2019.

[125] C. R. White and G. M. Rebeiz, "A differential dual-polarized cavity-backed microstrip patch antenna with independent frequency tuning," *IEEE Trans. Antennas Propag.*, vol. 58, no. 11, pp. 3490-3498, Nov. 2010.

[126] N. Liu, L. Zhu, X. Zhang and W. Choi, "A wideband differential-fed dual-polarized microstrip antenna under radiation of dual improved odd-order resonant modes," *IEEE Access*, vol. 5, pp. 23672-23680, 2017.

[127] Z. L. Ma and C. H. Chan, "Waveguide-based differentially fed dual-polarized magnetoelectric dipole antennas," *IEEE Trans. Antennas Propag.*, vol. 65, no. 8, pp. 3849-3857, Aug. 2017.

[128] V. Radisic, Y. Qian and T. Itoh, "Novel architectures for high-efficiency amplifiers for wireless applications," *IEEE Trans. Microw. Theory Tech.*, vol. 46, no. 11, pp. 1901-1909, Nov. 1998.

[129] E. Babakrpur and W. Namgoong, "A dual-path 4-phase nonuniform wideband receiver with digital mmse harmonic rejection equalizer," *IEEE Trans. Microw. Theory Tech.*, vol. 65, no. 2, pp. 386-395, Feb. 2017.

[130] Z. Tu, K. Jia and Y. Liu, "A differentially fed wideband circularly polarized antenna," *IEEE Antennas Wireless Propag. Lett.*, vol. 17, no. 5, pp. 861-864, May 2018.

[131] L.-H. Hsieh and K. Chang, "Compact elliptic-function low-pass filters using microstrip stepped-impedance hairpin resonators," *IEEE Trans. Microw. Theory Tech.*, vol. 51, no. 1, pp. 193-199, Jan. 2003.

[132] J. T. Ku, M. J. Maa, and P. H. Lu, "A microstrip elliptic function filter with compact miniaturized hairpin resonator", *IEEE Microw. Guided Wave Lett.*, vol. 10, pp. 94-95, Mar. 2000.

[133] S. Biswas, D. Guha and C. Kumar, "Control of higher harmonics and their radiations in microstrip antennas using compact defected ground structures," *IEEE Trans. Antennas Propag.*, vol. 61, no. 6, pp. 3349-3353, June 2013.

[134] C. Sim, M. Chang and B. Chen, "Microstrip-fed ring slot antenna design with wideband harmonic suppression," *IEEE Trans. Antennas Propag.*, vol. 62, no. 9, pp. 4828-4832, Sept. 2014.

[135] W. Li, Y. Wang, B. You, Z. Shi and Q. H. Liu, "Compact ring slot antenna with harmonic suppression," *IEEE Antennas Wireless Propag. Lett.*, vol. 17, no. 12, pp. 2459-2463, Dec. 2018.

[136] H. Li, L. Kang, F. Wei, Y. M. Cai, and Y. Z. Yin, "A low-profile dual-polarized microstrip antenna array for dual-mode OAM applications," *IEEE Antennas Wirel. Propag. Lett.*, vol. 16, pp. 3022–3025, 2017.

[137] H. Nawaz and I. Tekin, "Dual-Polarized, Differential Fed Microstrip Patch Antennas With Very High Interport Isolation for Full-Duplex Communication," *IEEE Trans. Antennas Propag.*, vol. 65, no. 12, pp. 7355–7360, 2017.

[138] T. K. Nguyen, H. H. Tran and N. Nguyen-Trong, "A wideband dual-cavity-backed circularly polarized crossed dipole antenna," *IEEE Antennas Wireless Propag. Lett.*, vol. 16, pp. 3135-3138, 2017.

[139] L. Zhang et al., "Single-feed ultra-wideband circularly polarized antenna with enhanced front-to-back ratio," *IEEE Trans. Antennas Propag.*, vol. 64, no. 1, pp. 355-360, Jan. 2016.

[140] Y. Luo, Q. Chu and L. Zhu, "A low-profile wide-beamwidth circularly-polarized antenna via two pairs of parallel dipoles in a square contour," *IEEE Trans. Antennas Propag.*, vol. 63, no. 3, pp. 931-936, March 2015.

[141] R. Xu, J. Li and W. Kun, "A broadband circularly polarized crossed-dipole antenna," *IEEE Trans. Antennas Propag.*, vol. 64, no. 10, pp. 4509-4513, Oct. 2016.

[142] W. Chen, H. Chen, C. Lee and C. G. Hsu, "Differentially fed wideband circularly polarized slot antenna," *IEEE Trans. Antennas Propag.*, vol. 67, no. 3, pp. 1941-1945, March 2019.

[143] X. Ruan and C. H. Chan, "A circularly polarized differentially fed transmission-line-excited magnetoelectric dipole antenna array for 5G applications," *IEEE Trans. Antennas Propag.*, vol. 67, no. 3, pp. 2002-2007, March 2019.

[144] L. Chi, Y. Qi, Z. Weng, W. Yu, and W. Zhuang, "A compact wideband slot-loop directional antenna for marine communication applications," *IEEE Trans. Veh. Technol.*, vol. 68, no. 3, pp. 2401-2412, March 2019.

[145] C. Mao, S. S. Gao, Y. Wang, and J. T. Sri Sumantyo, "Compact Broadband Dual-Sense Circularly Polarized Microstrip Antenna/Array With Enhanced Isolation," I*EEE Trans. Antennas Propag.*, vol. 65, no. 12, pp. 7073-7082, Dec. 2017.

[146] Y. Yang, J. Guo, B. Sun, Y. Cai, and G. Zhou, "The Design of Dual Circularly Polarized Series-Fed Arrays," *IEEE Trans. Antennas Propag.*, vol. 67, no. 1, pp. 574-579, Jan. 2019.

[147] C. Zhang, X. Liang, X. Bai, J. Geng, and R. Jin, "A Broadband Dual Circularly Polarized Patch Antenna With Wide Beamwidth," *IEEE Antennas Wireless Propag. Lett.*, vol. 13, pp. 1457-1460, 2014.

[148] X. Lai, Z. Xie, Q. Xie, and X. Cen, "A Dual Circularly Polarized RFID Reader Antenna With Wideband Isolation," *IEEE Antennas Wireless Propag. Lett.*, vol. 12, pp. 1630-1633, 2013.

[149] H. Sun, H. Zhu, C. Ding, and Y. J. Guo, "Wideband Planarized Dual-Linearly-Polarized Dipole Antenna and Its Integration for Dual-Circularly-Polarized Radiation," *IEEE Antennas Wireless Propag, Lett.*, vol. 17, no. 12, pp. 2289-2293, Dec. 2018.

[150] C. Ds and S. S. Karthikeyan, "A Novel Broadband Dual Circularly Polarized Microstrip-Fed Monopole Antenna," *IEEE Trans. Antennas Propag.*, vol. 65, no. 3, pp. 1410-1415, March 2017.

[151] R. K. Saini and S. Dwari, "A Broadband Dual Circularly Polarized Square Slot Antenna," *IEEE Trans. Antennas Propag.*, vol. 64, no. 1, pp. 290-294, Jan. 2016.

[152]R. Xu, J. Li, J. Yang, K. Wei, and Y. Qi, "A Design of U-Shaped Slot Antenna With Broadband Dual Circularly Polarized Radiation," *IEEE Trans. Antennas Propag.*, vol. 65, no. 6, pp. 3217-3220, June 2017.

[153] D. M. Pozar, "The active element pattern," *IEEE Trans. Antennas Propag.*, vol. 42, no. 8, pp. 1176-1178, Aug. 1994.

[154] I-Hsiang Lin, M. DeVincentis, C. Caloz, and T. Itoh, "Arbitrary dual-band components using composite right/left-handed transmission lines," *IEEE Trans. Microw. Theory Techn.*, vol. 52, no. 4, pp. 1142-1149, April 2004.